UNIVERSITA' DEGLI STUDI DI CATANIA

DIPARTIMENTO DI FISICA E ASTRONOMIA
DOTTORATO DI RICERCA XXX CICLO

By

CESARE SCALIA

SPECTROPOLARIMETRIC TECHNIQUES AND APPLICATIONS TO STELLAR MAGNETISM

Tutor: Prof. Francesco Leone

a Giacomo Scalia...

Abstract

This dissertation is aimed at the measurement and the characterization of stellar magnetic fields, which are one of the most challenging topics in the modern astrophysics. They are been detected in almost all the stellar evolutionary stages, from pre-main sequence to degenerate stars. They are the keys from the understanding of several phenomena, such as accretion on pre-main sequence stars, stellar activity and spots and they are also important in order to investigate possible false detections of exoplanets and to characterize star-planet interactions. In particular, this thesis focus on the study of upper main sequence, active solar analogs and stars hosting planet, with particular attention on evolved stars.

Stellar magnetic fields can be measured through the polarization and the splitting due to Zeeman effects, from spectropolarimetric observations. In particular, this dissertation employs archive data of Narval and HARPSpol and it is based on observations obtained with the instruments CAOS (Catania Astrophysical Observatory Spectropolarimeter) in more than hundred nights, during the period of the thesis.

Full Stokes observations of the magnetic Ap star β CrB are used in order to determine the transversal component and the angle of the magnetic fields.

The observations of a sample of 22 stars with detected planets are used in order to study the impact of the presence of the field; results show that the 47% of the giants and the 40% of the main sequence stars in the sample host magnetic fields. In particular, the field strenghts of the giant stars show a correlation with the rotational period, which can be connected to the presence of a dynamo process driven by rotation. Measurements are performed throught the Least Square Deconvolution technique, using a code that was implemented and tested during the period of thesis.

Furthermore, a new technique for the measurement of the effective magnetic field from high-resolution observations is introduced. This technique, called multi-line slope method, is tested with synthetic spectra and it is applied to a dataset of spectropolarimetric observations of the active star ϵ Eri, which spans 9 years from 2007 to 2016. The temporal analysis allows to determine a period of variation ($P_1 = 1099 \pm 71$ d) consistent with the variation of the activity index. This measurement represents the first estimation of the period of the cycle of a star obtained from direct measurements of the magnetic field.

ACKNOWLEDGMENTS

I would first like to thank my thesis advisor and mentor Prof. Francesco Leone that guided me since the master and made me a scientist. I would also like to thank Prof. Martin Stift and his wife for the encouraging and Prof. Stefano Bagnulo for his support. I thank Dr. Luca Fossati and Dr. Alex Martin for time working together and all people of Armagh Observatory.

I would like to thank Manuele Gangi and all the group of the instrument CAOS for all the nights spent together at the telescope. I thank Salvo Guglielmino and all the people of the Catania Astrophysical Observatory for the support.

I also thank Giuseppe Marino and all the people of Gruppo Astrofili Catanesi (GAC) for introducing me into the fascinating world of astronomy.

Finally, I thank my mother for her endless support, my family, and my friends.

This research is based on observations collected at the European Organisation for Astronomical Research in the Southern Hemisphere under ESO programmes 079.D-0178(A), 084.D-0338(A), 086.D-0240(A). This research has used the PolarBase database.

TABLE OF CONTENTS

List of Tables

List of Figures

Figure **Page**

CHAPTER 1

INTRODUCTION

Spectropolarimetry is a powerful technique that allows to study several astrophysical phenomena, such as circumstellar envelopes, stellar disks, exoplanets and stellar magnetic fields.

Despite the first application of polarimetry in astrophysics was made by Hale (1908) more than a century ago, a great improvement of the knowledge on stellar spectropolarimetry was possible only in the last few decades, thanks to technological advance and to the introduction of modern spectropolarimeters, which allow to detect the small polarized signals of astrophysical sources.

This work of thesis is devoted to the measure of stellar magnetic fields across the HR diagram. The characteristics of the field changes for different stellar types and they reflect properties of the physical processes which play in stellar atmospheres.

1.1 Overview on the stellar magnetic field

Stellar magnetic fields were detected in almost all the stages of stellar evolution (Fig. 1.1.1), from pre main sequence stars (Johns-Krull, 2007; Hussain & Alecian, 2014) to solar analogue stars (Valenti et al., 1995; Reiners, 2012), upper main sequence stars (Babcock, 1947; Mathys, 2017), giant stars (Konstantinova-Antova et al., 2008; Aurière et al., 2015) and dwarfs (Kemp et al., 1970; Ferrario et al., 2015). A large distinction about the properties of stellar magnetic field can be done according to the presence of a convective envelope at the base of the stellar photosphere. Indeed, stellar convection is

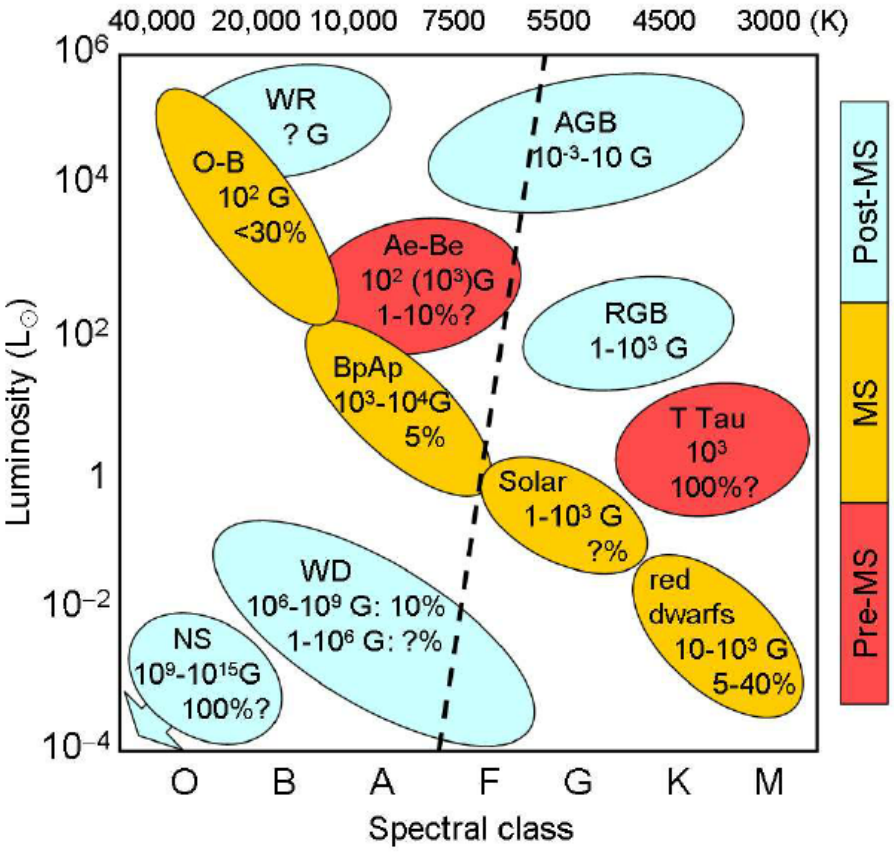

Figure 1.1: Magnetic field over the HR diagram (Berdyugina, 2009). Percentage indicates the fraction of stars with magnetic field; stars with convective and radiative envelopes are respectively at the right and left side of the dashed line.

responsible of phenomena similar to the solar case, such as sunspots, prominences, hot corona and dynamo cycles. Stars without convective envelope possess stable magnetic fields, with large strength values.

1.1.1 Pre-main sequence stars

The study of the magnetic field of pre-main sequence stars is particularly important for stellar evolution, as shown by D'Antona et al. (2000).

Pre main sequence stars are objects in the evolutionary stage of contraction before the zero age main sequence. It is possible to distinguish between:

- T Tauri stars for mass lower than $2M_\odot$
- Herbig Ae/Be stars for mass between $2M_\odot$ and $8M_\odot$.

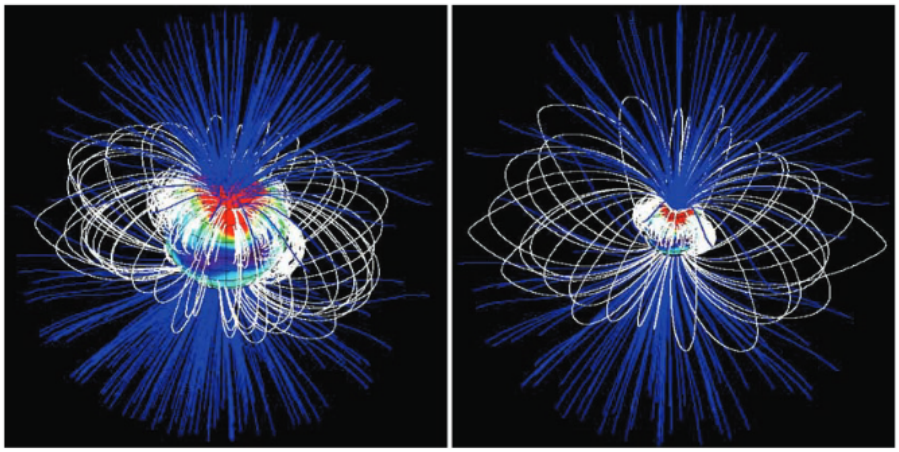

Figure 1.2: Topology of the magnetosphere of the T Tauri BP Tau (Donati et al., 2008).

T Tauri

T Tauri are the progenitors of F, G, K and M stars. They are in the evolutionary stage of the contraction from the Hayashi track, where they are almost fully convective and the energy is released from gravitational collapse.

The magnetic field plays the fundamental role to regulate the accretion of the material on the star. In the *magnetic accretion* model (Uchida & Shibata, 1984), a strong magnetic field couples disk and star and it is responsible for the loss of star's angular momentum so that the material can accrete with a rotation rate lower than the breakup velocity. The field is assumed to be dipolar and it stops the disk, forcing the material to accrete through the magnetic field lines (Shu et al., 1994).

Johns-Krull (2007) measured the magnetic field and showed that it reaches values up to a few kG. This strong field is responsible for flares (Guenther & Emerson, 1997) and strong X-ray emissions (Feigelson & Montmerle, 1999).

The geometry of the magnetic field was studied by Johnstone et al. (2014), who related properties of the magnetic field with the phenomenon of convection. They concluded that, when T Tauri are still fully convective, these stars host strong magnetic fields with a simple dipolar structure. This geometry starts to decay and it becomes more complex when the radiative core develops.

Ae / Be Herbig

Ae / Be Herbig stars are progenitors of B and A stars and they were discovered by Herbig (1960). Differently from the case of T Tauri, Herbig stars are expected to have convective

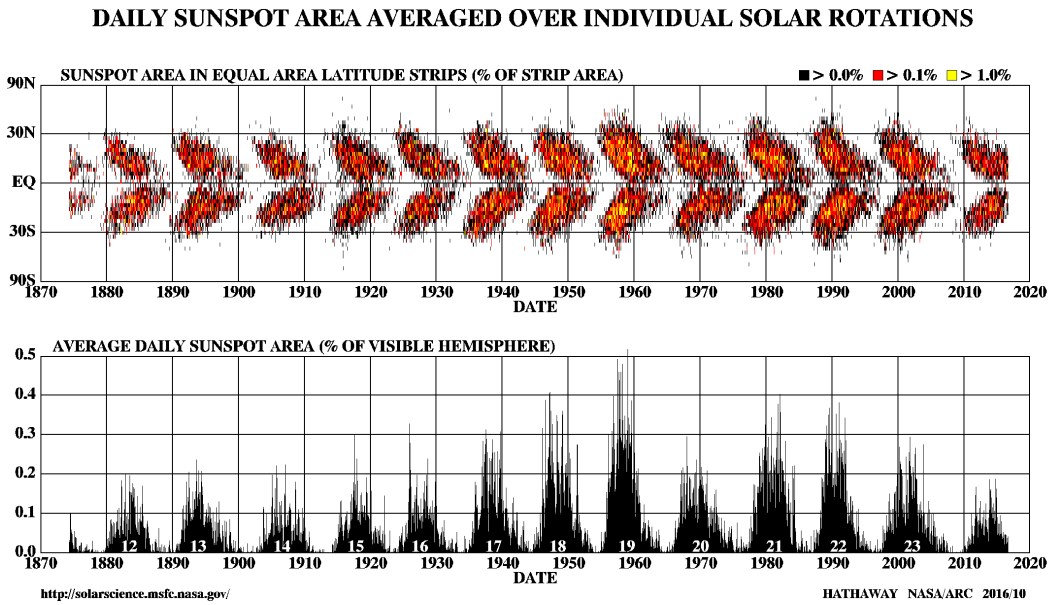

Figure 1.3: Butterfly diagram of sunspots since May 1874. Credits NASA (`https://solarscience.msfc.nasa.gov/SunspotCycle.shtml`).

cores surrounded by radiative sub-photospheric envelopes, as showed by Iben (1965).

The absence of strong and ordered magnetic field (Wade et al., 2007), suggests that the process of accretion of material in these stars is different from T Tauri. However, models of magnetic field generation and accretion processes are still open questions.

1.1.2 Solar magnetic field

The study of the Sun is important for all stellar and plasma astrophysics because it is the only case where several phenomena, assumed to be present also in other stars, can be seen in detail. Examples are spots, flares and chromospheric and coronal emission processes.

The existence of the solar magnetic field was speculated at the end of XIX century by Bigelow (1891), that observed similarities between the solar corona, during a total eclipse, and the field lines of a magnetized sphere.

The first application of spectropolarimetry in astrophysics, that corresponds to the first discovery of an extraterrestrial magnetic field, was performed by Hale (1908), who measured the magnetic field in sunspots.

Spots on the solar surface are known since 350 BC, from the observations of Theophrastus (Mestel, 2012). They were observed also by Chinese in 23 BC and they were rediscov-

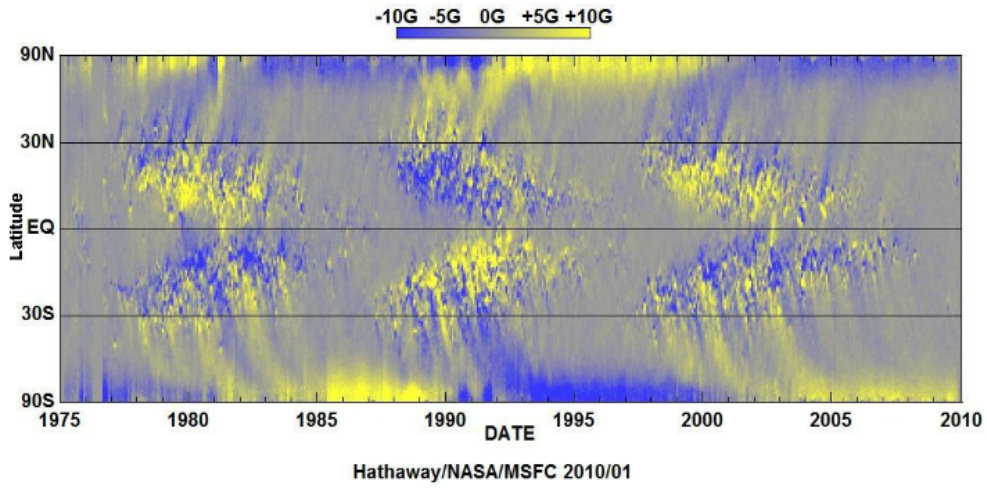

Figure 1.4: Synoptic magnetogram of the radial component of the solar surface magnetic field. Credits NASA (`https://solarscience.msfc.nasa.gov/images/magbfly.jpg`).

ered by Galileo (Wilson, 2003), who noted also that the period of the rotation of the Sun is close to the lunar month and that spots never appear in the polar regions.

A periodicity of 11 yr in the number of sunspots was first reported by Schwabe (1843). Actually, this value is only an average; the period of the spot's number is not strictly constant and it varies between 8 and 15 yr (Foukal, 2004). The magnetic nature of the cycle was supposed also by Sabine (1852), that observed the connection between cycle and geomagnetic storms.

The drifts and the positions of spots were studied by Carrington (1859) and Spoerer (1880). They found that spots lie in a region between -30°and +35°of latitude and they appear at lower latitude during the cycle (Spoerer's law). The plot of the number and the position of the spots, during the cycle, results in the so called *butterfly diagram* (Maunder, 1913), showed in Fig. 1.1.2.

Hale & Nicholson (1925) studied the polarity of the sunspots and they found that regions of strong magnetic fields are grouped in pairs of opposite polarities and active regions, characterized by opposite polarities, are present in opposite hemispheres (Hale's law).

Measurements of the integrated magnetic field of the Sun were performed by Babcock & Babcock (1955), that estimated a field value of $\simeq 1$ G. Babcock (1959) studied also the variation of the weak large scale magnetic field, observing that it reverses with the same period of the cycle. The variation is between 3 G, during the solar minimum, and 20 G, at the maximum (Priest, 2001). An example of polarity reversal is showed in the synoptic

magnetogram of Fig. 1.1.2 where it is possible to note that change of polarity occurs in the polar regions, at the time of the maximum of the cycle (Charbonneau, 2013).

Observations showed that the visible surface of the Sun, called *photosphere*, presents a structure at low scale called, called *granulation*, which is index of the action of stellar convection.

Solar eclipses revealed structures in outer part of the Sun, characterized by an increasing of temperature (Vernazza et al., 1981) and called *chromosphere* and *corona*. Because of the temperature distribution, shown in Fig. 1.1.2, different spectral lines can be used in order to obtain information of different regions of the solar atmosphere. In particular, lines like Ca H & H or calcium infrared triplet are important diagnostic indices for the study of the chromospheric active regions (Hale & Ellerman, 1903), which are connected to the magnetic field at the surface.

The cycle of the number of spots impacts all the regions of the solar atmosphere. It produces a cycle in the intensity of the chromospheric emission lines and in the X-ray emission which can increase of factor 100 during the cycle (Priest, 2001).

1.1.2.1 Solar dynamo

The phenomenology of sunspots, resumed for instance by the laws of Hale and Spoorer, indicates the presence of a strong and well organized toroidal magnetic field. Spots are created from the rise of magnetic flux tubes, due to buoyancy effects related to the magnetic activity (Fan, 2009).

Larmor (1919) proposed the idea that an axisymmetric motion of a conductiong fluid, for instance related to solar rotation, could generate and maintain the toroidal field. However, Cowling (1933) showed that a stable axisymmetric magnetic field can not be generated from an axisymmetric current because it incurs the effects of Ohmic dissipation. The problem was solved by Parker (1955), that showed that the break of symmetry, needed in order to avoid the prediction of Cowling's theorem, could be obtained by the Coriolis twist which raises the material from the convective cells.

Solar dynamo mechanism can be described by the action of two processes:

- differential rotation, which creates the toroidal field from poloidal field, through the shearing of field lines, in a process called Ω effect (Steenbeck & Krause, 1969). Models suppose that this phenomenon is originated in the region at the base of the convective envelope, called tachocline (Charbonneau, 2010);

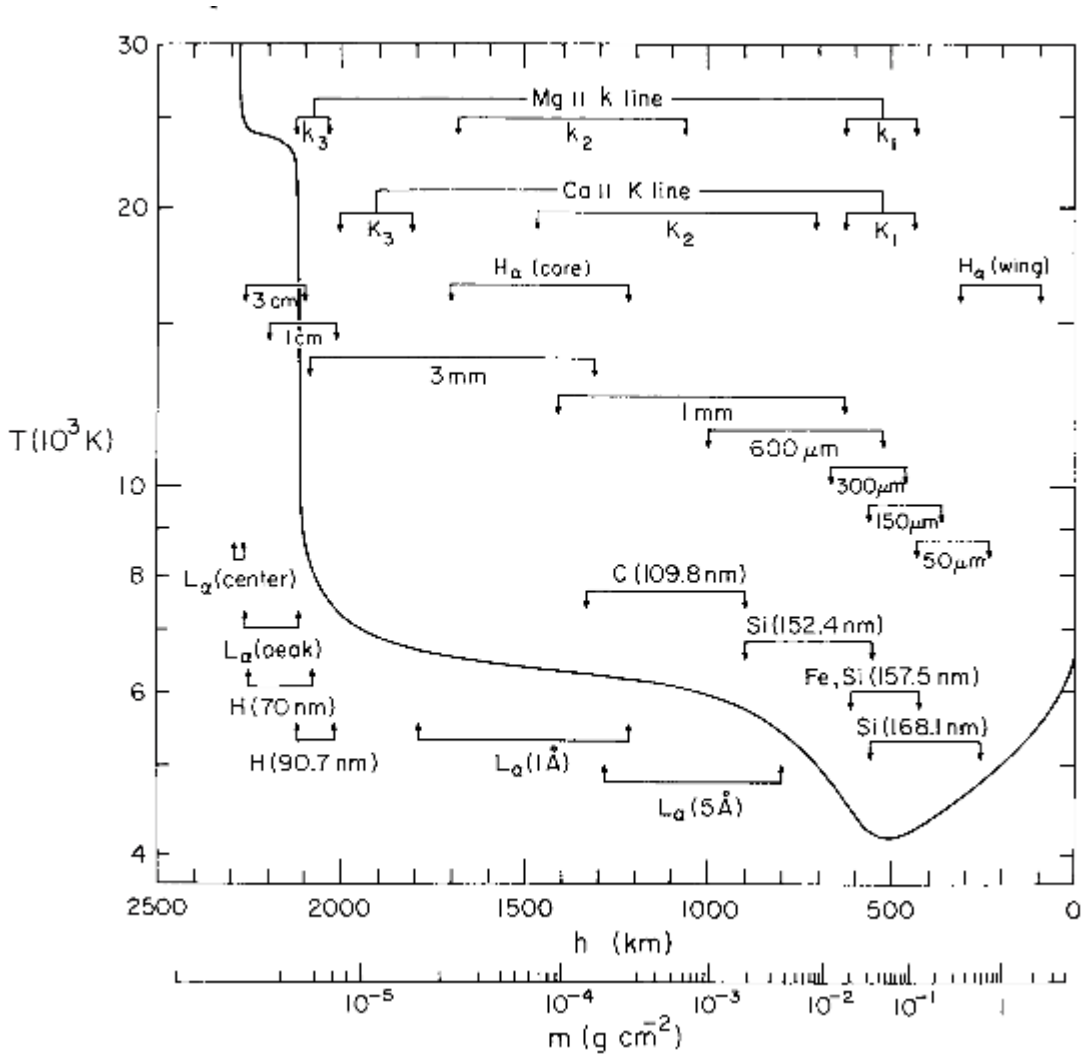

Figure 1.5: The average quiet-Sun temperature distribution .

- helical turbulence, which twists the rising flux tubes by the Coriolis force. The tubes can reconnect and create the poloidal field from the toroidal, in a process called α effect.

1.1.3 Late type stars

Late type main sequence stars are objects with surface temperature $T_s \leq 10^4$ K. Energy in their core is provided by the p-p chain and they are characterized by a radiative core. This results in a stellar envelope which is convectively unstable because of the high opacity due to ionization of hydrogen and helium. This convective sub photospheric envelope generates a magnetism similar to the solar case. For this reason, stellar magnetic fields

of late type main sequence stars are analyzed extending the results of solar physics.

A magnetic field similar to that one of the Sun is very hard to be detected in other stars, because it is characterized by small scale magnetic regions in the stellar surface and their magnetic signals result in a low value, when integrated over the visible stellar hemisphere.

For this reason, indirect indices of magnetism are very important for the study of late type stars. Examples of indicators are the emission chromospheric lines Ca H & K, which can be used in order to detect the presence of magnetic active regions, in analogy of the solar case.

A mile stone on the study of the magnetism of cool stars was the Mt-Wilson survey (Wilson, 1978; Baliunas et al., 1995) which revealed, for the first time, magnetic cycles for stars different from the Sun (Fig. 1.1.3). An other important index of the presence of magnetic field is the X-ray emission which, in analogy to the solar case, is related to the presence of a hot magnetic corona, with temperature close to 10^6 K. X-ray emission of late type stars was measured by Vaiana et al. (1981) and Pallavicini et al. (1981). Schmitt (2001) showed that X-ray emission is present in almost all late type stars, with level also four orders larger than the Sun.

In this context, an important parameter for the magnetism of late type stars is stellar rotation. In particular, magnetic activity showed a correlation with the so called Rossby number $R_o = P_{obs}/\tau_c$ (Noyes et al., 1984), as showed in Fig. 1.1.3; Ω is the rotational velocity and τ_c is the turnover time at the base of the convective envelope.

Magnetic activity for different spectral types was studied by Vaughan & Preston (1980). They found a gap between hot and inactive stars and young, active and fast rotating stars.

1.1.4 Early type stars

Stellar structure of early type stars presents several differences respect to the late type case. These stars are characterized by the presence of a convective core, due to the energy production of the CNO mechanism, and by a radiative stellar envelope.

Following Mestel (2012), the principal properties of the magnetic fields in early type can be resumed in a:

- mean longitudinal component with typical value of few hundred gauss. The largest value for the superficial field is 34kG (Babcock, 1960);

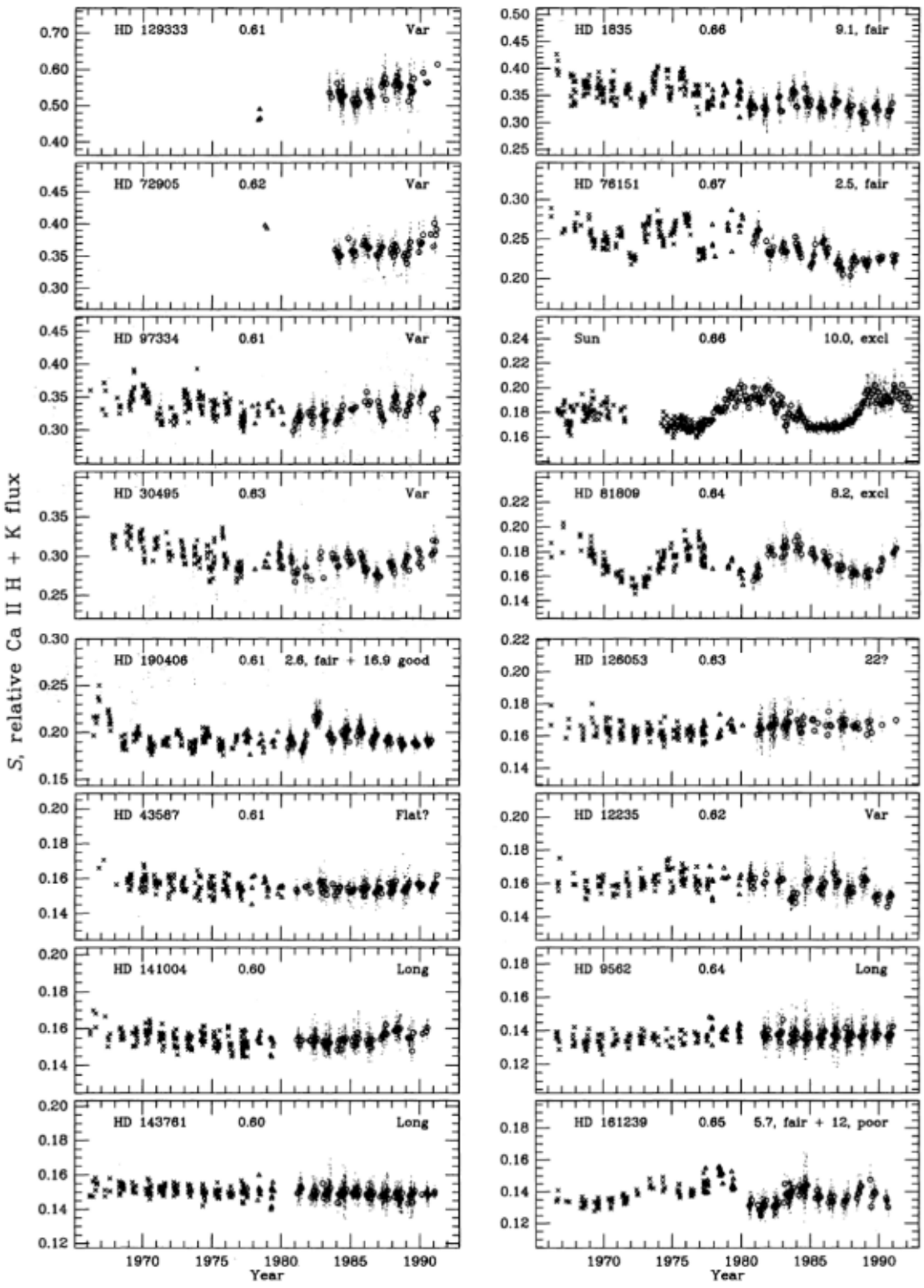

Figure 1.6: Magnetic activity for Sun and other stars (Baliunas et al., 1995).

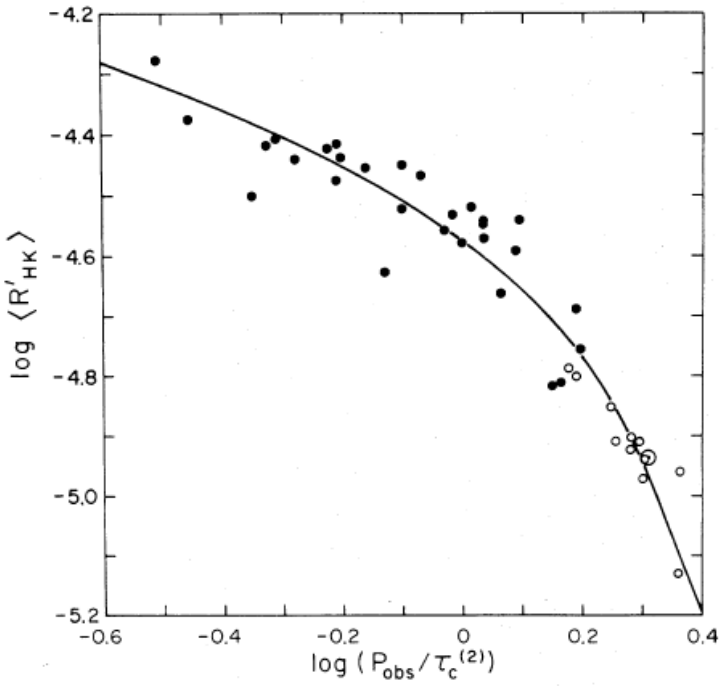

Figure 1.7: Stellar magnetic activity vs rotation (Noyes et al., 1984).

- longitudinal and superficial magnetic fields variations with periods of the order of few days. However, in some cases the variation can be of the order of 100 days, several years or decades, such as the case of γ Equulei which presents a period of the order of a century (P = 97.16 yr) (Bonsack & Pilachowski, 1974; Bychkov et al., 2016);

  or decades! Add some references, for instance gamma Equulei

- chemical peculiarity of magnetic stars of types A or B (Ap or Bp);

- variations are due to stellar rotation;

The statistic of the presence of magnetic fields in early type stars presents also differences respect to the lower main sequence case. While almost all late type stars present magnetic activity, only 10% of upper main sequence stars are magnetic. Furthermore, there is an anti-correlation between magnetism and rotational velocity. Indeed, rapidly rotating early type stars are generally non-magnetic.

Variation of magnetic field is described using the oblique rotator model (Stibbs, 1950), where rotational and magnetic axes differ of an angle β. Observations showed that in

a small sample of stars with a period of about one month, β is in the order of 10°or 20°(Landstreet & Mathys, 2000).

Magnetic fields of early type stars are stable at long term; this suggests a fossil origin for the magnetic field, which can be created in the molecular cloud where the star formed or in a dynamo process at the time of the pre main sequence phase (Mestel, 2012).

1.1.5 White dwarfs

White dwarfs represent one of the final stages of the stellar evolution (Althaus et al., 2010). They are compact objects, with a temperature in a range between 3000 K to 100000 K and a general slow rotation ($\leq 40\,\mathrm{km\,s^{-1}}$). The majority of white dwarfs (about 80%) is hydrogen rich (H-rich) and the remaining part is helium rich (He-rich). About 25% of H-rich and 20% of He-rich white dwarf are polluted by heavy elements.

Ferrario et al. (2015) showed that the distribution of magnetic fields of white dwarfs seems to be bimodal, one mode characterized by high field strength (from 1 to 1000 MG) and one by low field value (< 0.1 MG).

There are several scenarios proposed in order to explain the magnetic field in white dwarfs, for instance:

- fossil field from the evolution of Ap or Bp stars (Angel et al., 1981; Wickramasinghe & Ferrario, 2005);
- evolution of binary systems through a dynamo that operates in a common envelope phase (Nordhaus et al., 2011) or in a hot corona, created in the merging process of two white dwarfs (García-Berro et al., 2012);
- dynamo mechanism created by the convective mantle of a crystallizing white dwarf (Isern et al., 2017). This is produced in the interior of a white dwarf, composed by a mixture of ^{12}C and ^{16}O, when the solid oxygen phase crystallizes and settles down, creating a convective mantle of carbon rich liquid by a Rayleigh-Taylor instability (Isern et al., 1997);
- amplification process during the phase of helium burning (Levy & Rose, 1974);

The first two scenarios can explain the magnetism of the group with strong magnetic field while the last can explain the low field group. However, origin of the magnetism in white dwarf is still unknown.

1.1.6 Giant stars

The study of magnetic fields in giant stars is important for stellar evolution theory because it represents the connection stage between white dwarfs and main sequence stars. The field is strictly connected to the evolution of angular momentum and stellar rotation, as stated by Heger et al. (2005), and it could determine the shape of planetary nebulae, as shown by Blackman et al. (2001). Moreover, the field can inhibit the convection processes, which produce the mixing of elements, and it can impact the chemical evolution of the star.

Magnetic fields are expected in the interiors of red giants, from dynamo process related to differential rotation in radiative core (Spruit, 2002), and they are confirmed by the observations of g-mode by asteroseismology (Fuller et al., 2015).

Magnetic fields on the stellar surface are related to the external convective envelope, more than internal dynamo processes (Brandenburg & Subramanian, 2005). Their presence was expected on active giant stars, in order to explain the brightness variation of their spectra by the presence of spots. For instance, Kron (1947) supposed the presence of spots on binary RS Cvn stars AR Lac, composed by a G-K giant and a less massive G-M main sequence star, which was confirmed by the Doppler imaging of the same class star HR 1099 (Vogt & Penrod, 1983); field was also detected in the rapidly rotating FK Com giant stars.

The expected magnetic field of evolved stars has a very complex topology, concentrated in small-scaled structures (Hubrig et al., 1994). For this reason, direct observations of Zeeman effect are difficult, because the average magnetic field results in a very small polarized signal of the order of 10^{-4}.

Direct measures of magnetic fields on the surface of evolved stars started with the detection of the field in V390 Aurigae, obtained by Konstantinova-Antova et al. (2008). The correlation between field and rotation can be used in order to investigate the origin of the magnetic field and, in particular, the possible indication of a dynamo process driven by stellar rotation. This correlation was found for 37 Com (Tsvetkova et al., 2017), V390 Aur (Konstantinova-Antova et al., 2012) and 31 Com (Borisova et al., 2016).

In the other hands, dynamo mechanism can not easily explain the presence of magnetic field of stars with very long rotational periods. In this case, the magnetic field can be assumed to be a fossil remain from previous evolutionary stages, such as a magnetic main sequence star. Landstreet (2004) showed that a kG field, present on the main sequence stars, is expected to decrease to a few G or less in the giant phase, because of the magnetic flux conservation. An example is the case could be EK Eri (Aurière et al.,

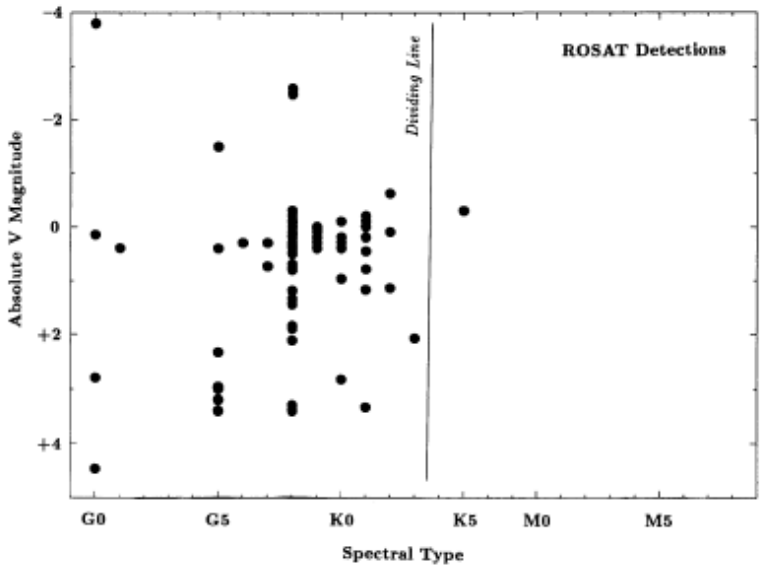

Figure 1.8: Detections of X-rays emission of single stars from ROSAT All-Sky Survey (Haisch et al., 1991).

2008), which has a rotational period of 300 days and it shows a mostly poloidal magnetic field of 100 G (Aurière et al., 2011). Other examples are 14 Cet (Aurière et al., 2012), β Cet (Tsvetkova et al., 2013) and OU And (Borisova et al., 2016).

X-ray activity

Indirect evidence of the magnetism of evolved stars was the measure of the X-ray emissions due to confined and very hot plasma in the corona (Vaiana et al., 1981).

Observations show that the X-ray emission stops for stars later than K3, as reported in Fig. 1.8. This phenomenon, called *X-ray dividing line* (Haisch et al., 1991), is evidence of some change on the dynamo mechanism which drives the magnetic fields in stellar corona.

The idea of a dynamo connected to stellar rotation, as presented by Parker (1955), is confirmed by the correlation between activity and rotation velocity. Pallavicini et al. (1981) found that:

$$L_X \sim (v \sin(i))^2 \tag{1.1}$$

In order to explain this, Pallavicini et al. (1981) concluded that rotation is an important ingredient that maintains the generated magnetic field.

Dynamo theory is also supported by the observation of the decreasing of X-ray emission over the life time of the star. This result can be explained by a rotational spin down, caused by a mass loss connected to a magnetic stellar wind (Skumanich, 1972).

Relation Eq. 1.1 saturates for fast rotators, how shown by Micela et al. (1985) for a sample of K stars members of the Pleiades cluster. The value of saturation is large for later spectral types and it can be related to bolometric luminosity, as showed by Pizzolato et al. (2003):

$$P_{rot}^{sat} \sim L_{bol}^{-1/2} \tag{1.2}$$

This result is another indication of the properties of the convective envelope through the spectral types.

1.2 Magnetic fields and exoplanets

Since the first detection of an exoplanet in the star 51 Peg by Mayor & Queloz (1995), the astrophysical community spent a big effort to find and classify as much as possible exoplanets, with the charming desire to find planets similar to the Earth.

Several techniques are applied for this purpose. One of the most important is the *radial velocity* method, which consists on the measure of variations of the Doppler shift, that is assumed to be related to the gravitational pull due to the presence of a possible orbiting planet. At the moment, 456 extrasolar planets were found with this technique.

However, this method can lead to false detections because of the effects of surface magnetic fields. Indeed, analyzing the case of HD 166435, Queloz et al. (2001) showed that the surface magnetic activity of the star can produce a similar signal, in radial velocity, found in stars with true planetary motions. Other false detections were claimed in the years, such as the case of HD 219542 (Desidera et al., 2004), HD 200466 (Carolo et al., 2014) and HD 99492 (Kane et al., 2016). In this context, the direct detection of stellar magnetic field can be used in order to select cases of possible false exoplanets.

The study of the modulation of the magnetic field can be used directly for test the presence of exoplanets. An important case is Pollux, where a planet was found by Hatzes & Cochran (1993) and it was confirmed by Hatzes et al. (2006) but the spectropolarimetric observations of Aurière et al. (2014) revealed that the period of radial velocity and magnetic field are coincident, as shown in Fig. 1.2. Hence, they claimed that spots, associated with the magnetic poles, explain the variation of radial velocity and they make the hypothesis of exoplanet unnecessary.

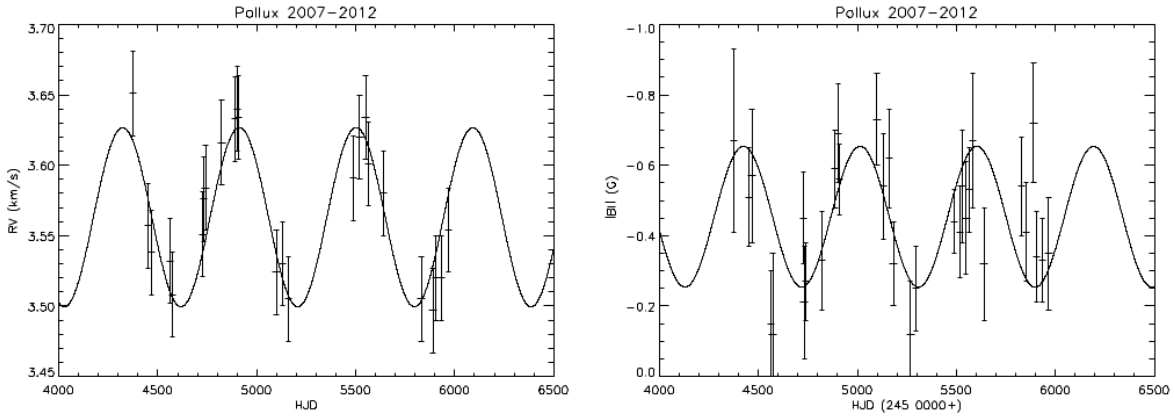

Figure 1.9: Radial velocity (left) and magnetic field (right) variations of Pollux, from Aurière et al. (2014). A sinusoidal fit with P = 589.64 d is showed in both figures.

Magnetic fields are also important in order to study the interaction between stars and planets (Preusse et al., 2006) and the environment around planet-hosting stars (Alvarado-Gómez et al., 2016).

1.3 This work

This work of thesis is devoted to the measurement and the analysis of stellar magnetic fields.

During the work, we described the general techniques for the observation of stellar polarisation and we developed methods of magnetic field diagnostic, in order to study the fields across the HR-diagram, from the main sequence to giant stars.

The aim was to obtain an observational report, in order to characterize the behavior of the magnetic field and to put it in correlation with stellar properties, such as stellar rotation in the case of giant stars, activity index for late type stars or magnetic field geometry in the case of early type magnetic stars.

Furthermore, we showed how the analysis of the temporal variability can be used in order to estimate important stellar parameters. For instance we estimated the radius of the early type stars, the dynamo period of cool stars and we question the detection of one exoplanet.

After a general description of the polarised radiation in Chapt. 2, we introduced the observational techniques used in stellar spettropolarimetry in Chapt. 3, giving particular attention to the description of the instrument *Catania Astrophysical Observatory*

Spectropolarimeter (CAOS), which was also calibrated during the period of the thesis.

Chapt. 4 described the code COSSAM, which was used in order to compute synthetic polarised spectra, representing an important tool for the physical interpretation of the observations. In particular, during the Ph. D. we modified COSSAM in order to include a polynomial expansion for the stellar magnetic field.

The study of the linear polarisation of the early type star β CrB is reported in Chapt. 5, where we showed how it allows to constrain parameters of the magnetic field geometry and, in this way, it is possible to estimate stellar radius and the orientation of the rotational axis in the sky.

Chapt. 6 is devoted to the analysis of a sample of star hosting planet, with a particular attention to the study of magnetic fields in evolved stars. These measurements were performed through the Least Square Deconvolution using a code that was implemented and tested during the work of thesis.

The analysis of the field in cool main sequence stars is showed in Chapt. 7, where we introduced a new technique, called *multi-line slope method*, that was used in order to study the temporal variability of the star ϵ Eri. Final conclusions are reported in Chapt 8.

CHAPTER 2

DESCRIPTION OF POLARIZED LIGHT

The astrophysical investigation of the universe is historically performed by means of the electromagnetic waves. However, because technological limitations, in the past it was mainly performed the analysis of the *direction* (astrometry) and the *intensity* (spectroscopy) of the light.

This chapter is devoted to the description of a third aspect of the electromagnetic radiation, more difficult to measure, called *polarization*: the physical quantity associated with the characteristics of the orientation of the electric field vector in time and space.

2.1 The polarization Ellipse and Stokes Parameters

This description and nomenclature of polarization follows Degl'Innocenti & Landolfi (2006).

In classical physics, it is possible to describe, in a simple way, the idealized case of a pure monochromatic plane wave propagating in vacuum; this treatment can be performed equivalently by the use of the electric or the magnetic field vector. Usually, the representation in terms of the electric field is preferred because detectors are generally build using materials whose interaction with the electromagnetic radiation is dominated by the electric vector.

In a right-handed coordinate system, with the z-axis equal to the direction of propagation and an x-axis pointing to an arbitrary direction in the plane perpendicular to the

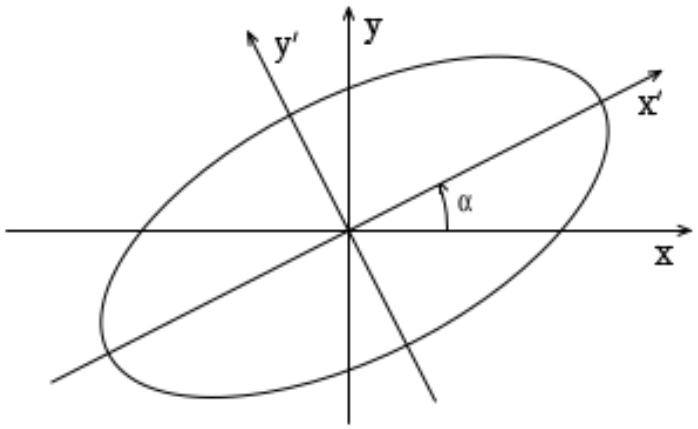

Figure 2.1: Polarization ellipse (Degl'Innocenti & Landolfi, 2006).

direction of propagation, the electromagnetic wave can be described by:

$$E_x(\vec{r},t) = E_1 cos(kz - \omega t + \phi_1) = Re[\varepsilon_1 e^{i(kz-\omega t)}]$$
$$E_y(\vec{r},t) = E_2 cos(kz - \omega t + \phi_2) = Re[\varepsilon_2 e^{i(kz-\omega t)}] \tag{2.1}$$

with:

$$\varepsilon_1 = E_1 e^{i\phi_1}$$
$$\varepsilon_2 = E_2 e^{i\phi_2} \tag{2.2}$$

where E_1, E_2, ϕ_1 e ϕ_2 are four positive constants related to the amplitudes and to the phases of electric field.

In the most general case, the tip of the electric field vector rotates in time in the x-y plane, describing an ellipse called *polarization ellipse* (Fig. 2.1).

Calling (x′,y′) the couple of axes obtained by a rotation of (x,y) of an angle α. The electric field in this system is given by:

$$E_{x'}(t) = (E_1 C\, cos\phi_1 + E_2 S\, cos\phi_2) cos(\omega t) + (E_1 C\, \sin\phi_1 + E_2 S\, \sin\phi_2) \sin(\omega t)$$
$$E_{y'}(t) = (-E_1 S\, cos\phi_1 + E_2 C\, cos\phi_2) cos(\omega t) + (-E_1 S\, \sin\phi_1 + E_2 C\, \sin\phi_2) \sin(\omega t) \tag{2.3}$$

where:

$$\mathrm{C} = \cos\alpha\ ; \mathrm{S} = \sin\alpha \tag{2.4}$$

The angle α in chosen so that (x′,y′) is coincident with the proper axes of the polarization ellipse, with the long axis directed along x′. Calling a the semi-major and b the semi-minor axes, the electric field can be written as:

$$E_{x'}(t) = a\, cos(\omega t - \phi_0)$$
$$E_{y'}(t) = b\, cos(\omega t - \phi_0) \tag{2.5}$$

Comparing Eq. 2.3 and Eq. 2.5, it's possible to derive:

$$\begin{aligned} a\cos\phi_0 &= E_1 C\cos\phi_1 + E_2 S\cos\phi_2 \\ a\sin\phi_0 &= E_1 C\sin\phi_1 + E_2 S\sin\phi_2 \\ b\cos\phi_0 &= -E_1 S\sin\phi_1 + E_2 C\sin\phi_2 \\ b\sin\phi_0 &= E_1 S\cos\phi_1 - E_2 C\cos\phi_2 \end{aligned} \tag{2.6}$$

That is equivalent to:

$$\begin{aligned} a^2 + b^2 &= E_1^2 + E_2^2 \\ ab &= -E_1 E_2 \sin(\phi_1 - \phi_2) \\ a^2 - b^2 &= (E_1^2 - E_2^2)\cos 2\alpha + 2E_1 E_2 \cos(\phi_1 - \phi_2)\sin 2\alpha \\ (E_1^2 - E_2^2)\sin 2\alpha &= 2E_1 E_2 \cos(\phi_1 - \phi_2)\cos 2\alpha \end{aligned} \tag{2.7}$$

The geometrical properties of the polarization ellipse depend on four bilinear combinations of the electric field components. Introducing the so called *Stokes parameters*:

$$\begin{aligned} I &= E_1^2 + E_2^2 \\ Q &= E_1^2 - E_2^2 \\ U &= 2E_1 E_2 \cos(\phi_1 - \phi_2) \\ V &= 2E_1 E_2 \sin(\phi_1 - \phi_2) \end{aligned} \tag{2.8}$$

the angle α is given by:

$$\mathrm{Q}\sin 2\alpha = \mathrm{U}\cos 2\alpha \tag{2.9}$$

with the constraint:

$$\mathrm{a}^2 - \mathrm{b}^2 = \mathrm{Q}\cos 2\alpha + \mathrm{U}\sin 2\alpha \tag{2.10}$$

Choosing the interval $(0,\pi)$ as the interval of definition for α, we obtain for $\mathrm{Q} \neq 0$:

$$\alpha = \frac{1}{2}\arctan(\frac{\mathrm{U}}{\mathrm{Q}}) + \alpha_0 \tag{2.11}$$

where:

$$\alpha_0 = \begin{cases} 0 & if\ Q > 0\ \&\ U > 0 \\ \pi & if\ Q > 0\ \&\ U < 0 \\ \pi/2 & if\ Q < 0 \end{cases} \tag{2.12}$$

and for Q = 0

$$\alpha = \begin{cases} \frac{1}{4}\pi & if\, U > 0 \\ \frac{3}{4}\pi & if\, U < 0 \end{cases} \tag{2.13}$$

In the case Q = U = 0 the angle α is undefined.

After some algebra, the values of the semi-axis of the polarization ellipse are given by:

$$\begin{aligned} a &= \tfrac{1}{2}[\sqrt{I-V} + \sqrt{I+V}] \\ b &= \tfrac{1}{2}[\sqrt{I-V} - \sqrt{I+V}] \end{aligned} \tag{2.14}$$

The four Stokes parameters are not independent, being related by:

$$\mathrm{I}^2 = \mathrm{Q}^2 + \mathrm{U}^2 + \mathrm{V}^2 \tag{2.15}$$

We can introduce also the ellipticity, that is the ratio of the semi-minor and the semi-major axes of the ellipse. We call the angle β so that $-\frac{\pi}{4} \leq \beta \leq \frac{\pi}{4}$. The sign of β is positive in the case of right-handed polarization, while it is negative for the left-handed case.

It can be shown that:

$$\tan 2\beta = \frac{\mathrm{V}}{\sqrt{Q^2 + U^2}} \tag{2.16}$$

Stokes parameters, introduced in Eq. 2.8, can be rewritten as:

$$\begin{aligned} I &= \varepsilon_1^* \varepsilon_1 + \varepsilon_2^* \varepsilon_2 \\ Q &= \varepsilon_1^* \varepsilon_1 - \varepsilon_2^* \varepsilon_2 \\ U &= \varepsilon_1^* \varepsilon_2 + \varepsilon_2^* \varepsilon_1 \\ V &= i(\varepsilon_1^* \varepsilon_2 - \varepsilon_2^* \varepsilon_1) \end{aligned} \tag{2.17}$$

where Eq. 2.2 is used. In this way it is possible to introduce a 2x2 Hermitian matrix, called *polarization tensor*:

$$\mathrm{J_{ij}} = \varepsilon_{\mathrm{i}}^* \varepsilon_{\mathrm{j}} = \frac{1}{2} \begin{pmatrix} I+Q & U-iV \\ U+iV & I-Q \end{pmatrix} \tag{2.18}$$

The more general case of quasi-monochromatic wave can be obtained through the average over a time much longer than the wave period.

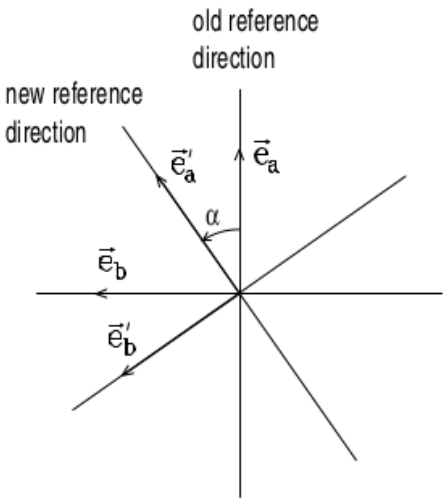

Figure 2.2: Rotation of the reference direction with the angle α (Degl'Innocenti & Landolfi, 2006).

2.1.1 Properties of the Stokes Parameters

Stokes parameters have important characteristics, which are useful for the next sections. We reported the properties of:

- Rotation of the reference direction:

  The Stokes vector in a new system $(\mathrm{I}', \mathrm{Q}', \mathrm{U}', \mathrm{V}')$, obtained by a rotation of an angle α as shown in Fig. 2.2, can be written as:

$$\begin{aligned} I' &= I \\ Q' &= \cos(2\alpha)Q + \sin(2\alpha)U \\ Q' &= -\sin(2\alpha)Q + \cos(2\alpha)U \\ V' &= V \end{aligned} \tag{2.19}$$

  It is possible to note that Stokes I and Stokes V are invariant under rotation, while the linear polarization rotates of an angle 2α in the Q-U plane.

- Addition theorem: any radiation beam can be considered as the incoherent super-

position of an unpolarised beam and a totally polarised beam

$$\begin{pmatrix} I \\ Q \\ U \\ V \end{pmatrix} = \begin{pmatrix} I - \sqrt{Q^2+U^2+V^2} \\ 0 \\ 0 \\ 0 \end{pmatrix} + \begin{pmatrix} \sqrt{Q^2+U^2+V^2} \\ Q \\ U \\ V \end{pmatrix} \tag{2.20}$$

2.2 Zeeman effect

Polarization arises in the presence of asymmetry in the emitted source or in the medium between the source and the observer. Examples of processes which can produce polarization are:

- *reflection*
- *scattering* by grains, molecules and free electrons
- *synchrotron emission*
- *magnetic fields*

This work is concentrated on the measure of the stellar magnetic field, whose effects are connected to Zeeman effect. In this case, the preferential direction of the magnetic field breaks the symmetry of the emission, generating circular and linear polarization.

The first explanation of this process was given by Zeeman (1897), who discovered the splitting of the lines and their polarization characteristics in the presence of magnetic fields. Here we reported a quantum description, following Degl'Innocenti & Landolfi (2006).

In the presence of an external and uniform magnetic field, the Hamiltonian of a system of atoms can be described by the addition of an unperturbed Hamiltonian H_0 and a *magnetic Hamiltonian* H_B, which is given by:

$$H_B = \frac{e_0 h}{4\pi mc}(\vec{L} + 2\vec{S}) \cdot \vec{B} + \frac{e_0^2}{8mc^2}(\vec{B} \times \vec{r})^2 \tag{2.21}$$

where $\vec{L}$ and $\vec{S}$ are the total orbital angular momentum and total spin, $\vec{B}$ is the magnetic field vector and $\vec{r}$ is the position operator. The second term of Eq. 2.21, called *diamagnetic term*, is important only for very strong magnetic fields (for instance for white dwarfs) and it can be neglected for purpose of this work.

Introducing the *Bohr magneton* μ_0 the magnetic Hamiltonian can be written:

$$\mathrm{H_B} = \mu_0(\vec{\mathrm{L}} + 2\vec{\mathrm{S}}) \cdot \vec{\mathrm{B}} \tag{2.22}$$

If magnetic field is so weak that $\mathrm{H_B} \ll \mathrm{H_0}$ (magnetic energy much smaller than the energy interval of the unperturbed Hamiltonian), the effects of the magnetic field can be computed using perturbation theory. In this case, called *Zeeman regime*, the corrections of the unperturbed energy levels $\mathrm{E}_{\alpha \mathrm{J}}$ are given by the diagonalisation of the matrix:

$$\left\langle \alpha \mathrm{JM} \left| \mathrm{H_B} \right| \alpha \mathrm{JM}' \right\rangle = \mu_0 \left\langle \alpha \mathrm{JM} \left| (\vec{\mathrm{L}} + 2\vec{\mathrm{S}}) \cdot \vec{\mathrm{B}} \right| \alpha \mathrm{JM}' \right\rangle = \mu_0 \mathrm{B\,g\,M}\, \delta_{\mathrm{MM}'} \tag{2.23}$$

where J and M are respectively the total angular momentum and his projection on the z-axis, taken with the direction of the magnetic field, and g is the Landé factor:

$$g = 1 + \frac{\left\langle \alpha J \left|\left| \vec{S} \right|\right| \alpha J \right\rangle}{\sqrt{J(J+1)}} \quad (J \neq 0) \tag{2.24}$$

The first order eigenvalues of the total Hamiltonian $(\mathrm{H_0} + \mathrm{H_B})$ are given by:

$$\mathrm{E}_{\alpha \mathrm{J}} + \mu_0 \mathrm{gBM} \quad (\mathrm{M} = -\mathrm{J}, -\mathrm{J}+1, \ldots, \mathrm{J}) \tag{2.25}$$

where it is possible to note that the presence of the magnetic field removes the M degeneracy of the unperturbed Hamiltonian. Moreover, the splitting is proportional to the factor g and to the magnetic field.

2.2.1 Analytical expression of Landé factor

Analytical expressions of Landé factor can be found for the cases of coupling between angular momentums.

The easiest situation is the case of L-S coupling. In this scheme, L and S are good quantum number and, through the projection theorem, it is possible to obtain:

$$\left\langle \beta \mathrm{LSJ} \left|\left| \vec{\mathrm{S}} \right|\right| \beta \mathrm{LSJ} \right\rangle = \frac{\left\langle \beta \mathrm{LSJM} \left|\left| \vec{\mathrm{S}} \cdot \vec{\mathrm{J}} \right|\right| \beta \mathrm{LSJM} \right\rangle}{\sqrt{J(J+1)}} \tag{2.26}$$

where β is the generical quantum number of the electronical configuration and:

$$\vec{\mathrm{S}} \cdot \vec{\mathrm{J}} = \frac{1}{2}[\mathrm{J}^2 + \mathrm{S}^2 - \mathrm{L}^2] \tag{2.27}$$

It is possible to write:

$$\mathrm{g_{LS}} = 1 + \frac{1}{2} \frac{\mathrm{J(J+1)} + \mathrm{S(S+1)} - \mathrm{L(L+1)}}{\mathrm{J(J+1)}} \tag{2.28}$$

and, using the compact notation:

$$\gamma(A,B,C) = \frac{A(A+1)+B(B+1)-C(C+1)}{2A(A+1)} \tag{2.29}$$

Eq. 2.28 can be written as:

$$g_{LS} = 1+\gamma(J,S,L) \tag{2.30}$$

In the case of j-j coupling scheme, it is possible simplify Eq. 2.24 in a similar way. Considering the levels with orbital angular momentum l_1 and l_2 and with angular momentum of spin $s_1 = s_2 = 1/2$, the matrix element can be written as:

$$\left\langle \beta(l_1 s_1) j_1, (l_2 s_2) j_2, J || \vec{S} || \beta(l_1 s_1) j_1, (l_2 s_2) j_2, J \right\rangle \tag{2.31}$$

and the Landé factor is given by:

$$g_{jj} = 1+\gamma(J,j_1,j_2)\gamma(J,\,1/2,\,l_1)+\gamma(J,j_2,j_1)\gamma(J,\,1/2,\,l_2) \tag{2.32}$$

2.2.2 Transition between two atomic levels

In the case of a transition between two atomic levels, with angular momentum J and J' and Landé factor g and g', the unperturbed line will split in a collection of components, with frequencies:

$$\nu_{MM'}^{JJ'} = \nu_0 + \nu_L(g'M' - gM) \tag{2.33}$$

where the term ν_L is called *Larmor frequency* and it is define by:

$$\nu_L = \frac{\mu_0 B}{h} = \frac{e_0 B}{4\pi mc} = 1.3996 \times 10^6 B \tag{2.34}$$

It is possible to write Eq. 2.33 in term of wavelength as:

$$\lambda_{MM'}^{JJ'} = \lambda_0 - \Delta\lambda_B(g'M' - gM) \tag{2.35}$$

where the term $\Delta\lambda_B$ is the splitting and it is given by:

$$\Delta\lambda_B = \lambda_0^2\frac{\nu_L}{c} = \frac{\lambda_0^2 e_0 B}{4\pi mc^2} = 4.6686\,10^{-10}\lambda_0^2 B \tag{2.36}$$

Among all the possible combinations of M, selection rules have to be considered. They depend on the type of interaction, such as electric-dipole, magnetic-dipole, electric-quadrupole and so on. The simplest cases are the electric-dipole transitions, which are also the most probable to observe. In this case, selection rules are given by:

$$\Delta M = M' - M = 0, \pm 1 \tag{2.37}$$

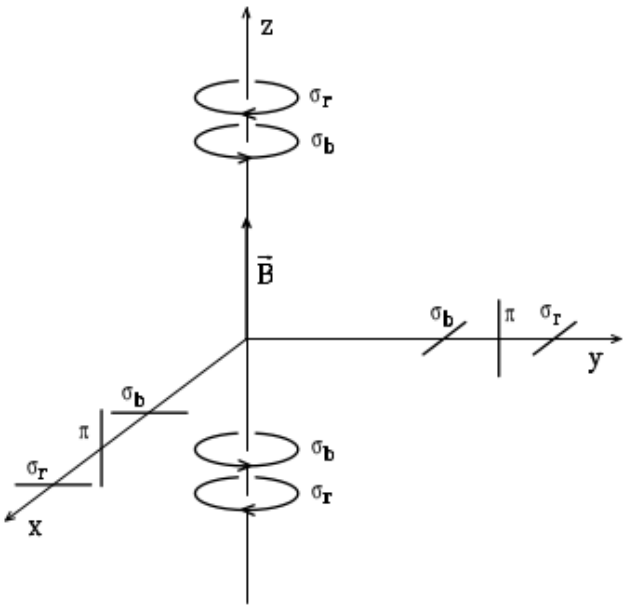

Figure 2.3: Polarization properties of Zeeman effect (Degl'Innocenti & Landolfi, 2006).

The components with $\delta \mathrm{M} = -1$ are called σ_r because they are shifted to longer wavelengths. Their polarisation is generally elliptical and it degenerates into circular, if the components are observed along the direction of the magnetic field, or to linear, if observed along a plane perpendicular to the magnetic field.

The components with $\delta \mathrm{M} = +1$ are called σ_b because they are shifted to shorter wavelengths. The polarization behavior is similar to the case of σ_r, an exception is the sign of the circular polarization which is inverted.

The components with $\delta \mathrm{M} = 0$ are called π and their polarisation is always parallel to the magnetic field.

Properties of the polarization produced by the Zeeman effects are resumed in Fig. 2.3.

We refered to *normal Zeeman effect* or *normal Zeeman triplet*, if the angular momentum of any transition is zero ($\mathrm{J} = \mathrm{J}' = 0$) or if the levels have the same Landé factor ($\mathrm{g} = \mathrm{g}'$). In this case, only three components are present: σ_r at $\lambda_0 + \mathrm{g}\Delta\lambda_\mathrm{B}$, σ_π at λ_0 and σ_b at $\lambda_0 - \mathrm{g}\Delta\lambda_\mathrm{B}$. The other cases are indicated as *anomalus Zeeman effect* and they can be characterized by complex patterns. Examples of splitting are shown in Fig. 2.4. The

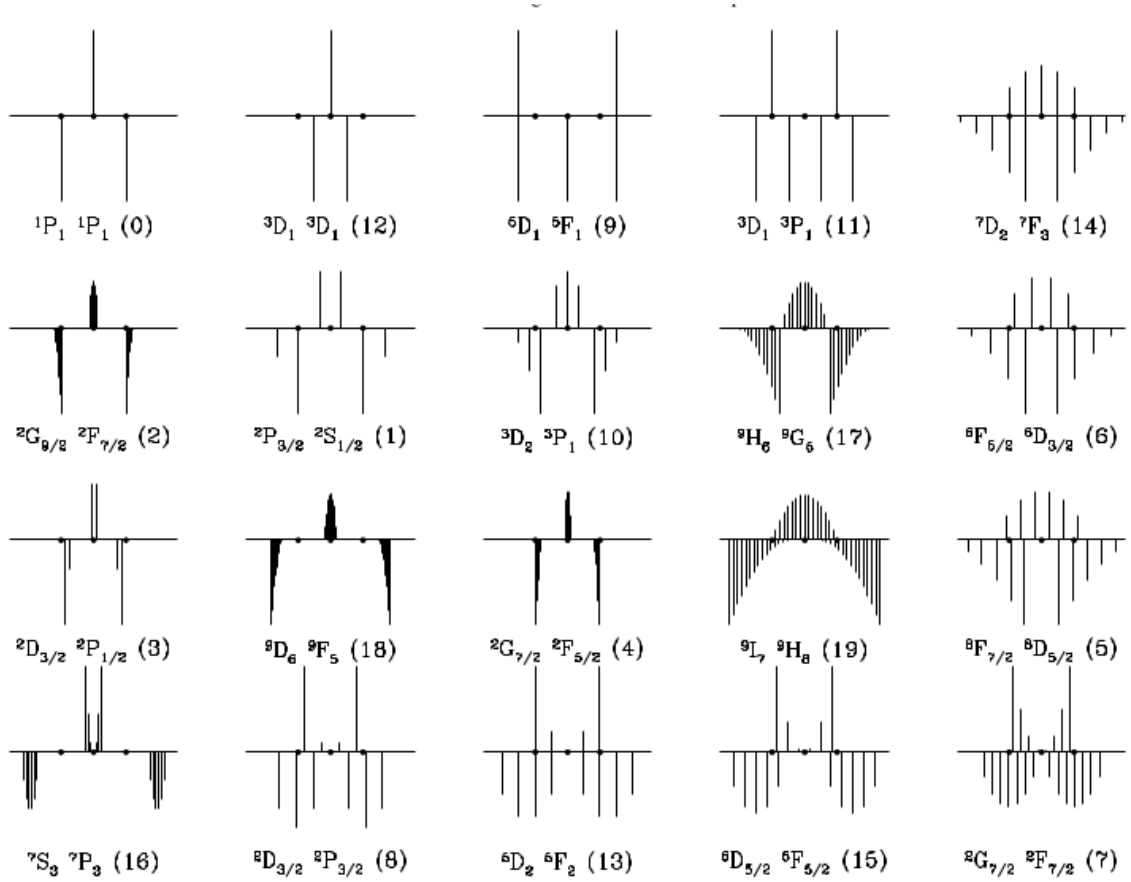

Figure 2.4: Examples of Zeeman patterns (Stift & Leone, 2003).

strengths of components can be computed by:

(2.38)

		$J' = J+1$	$M' = J$	$J' = J-1$
σ_b	$M' = M+1$	$\frac{3(J+M+1)(J+M+2)}{2(J+1)(2J+1)(2J+3)}$	$\frac{3(J-M)(J+M+1)}{2J(J+1)(2J+1)}$	$\frac{3(J-M)(J-M-1)}{2J(2J-1)(2J+1)}$
π	$M' = M$	$\frac{3(J-M+1)(J+M+1)}{2(J+1)(2J+1)(2J+3)}$	$\frac{3M^2}{J(J+1)(2J+1)}$	$\frac{3(J-M)(J+M)}{J(2J-1)(2J+1)}$
σ_r	$M' = M-1$	$\frac{3(J-M+1)(J-M+2)}{2(J+1)(2J+1)(2J+3)}$	$\frac{3(J+M)(J-M+1)}{2J(J+1)(2J+1)}$	$\frac{3(J+M)(J+M-1)}{2J(2J-1)(2J+1)}$

2.2.3 Effective Landé factor

The quantity ($g'M' - gM$) is a property of the particular transition called *effective Landé factor*. It is related to the sensitivity of the line to the magnetic field and it is defined as the separation of the center of gravity of the σ_r respect to the line center, in units of $\Delta\lambda_B$ (Landi Degl'Innocenti, 1982).

Shenstone & Blair (1929) showed that the effective Landé factor g_{eff} can be computed using:

$$g_{eff} = \frac{1}{2}(g_1 + g_2) + \frac{1}{4}(g_1 - g_2)d \tag{2.39}$$

where the term d is given by:

$$d = J_1(J_1 + 1) - J_2(J_2 + 1) \tag{2.40}$$

Typical values of g_{eff} vary from 0.5 to 2.5. Harvey (1973) reported transitions with very large g_{eff} , such as the MnI 4070.278 Å with $g_{eff} = 3.32$, while Sistla & Harvey (1970) reported lines with $g_{eff} = 0$, such as the FeI 5576.089 Å .

2.3 Weak field approximation

In the cases of weak field, when the Zeeman separation $\Delta\lambda_B$ of a Zeeman pattern (assumed as triplet splitting) is small compared to the intrinsic broadening of a spectral line, it is possible to introduce a useful approximation, which is used in order to measure stellar magnetic fields.

In this case, Unno (1956) showed that the circular polarization emerging from a stellar point can be written as:

$$V(\lambda,\theta) = \Delta\lambda_B \cos\phi \frac{dI(\lambda,\theta)}{d\lambda} \tag{2.41}$$

where:

$$\Delta\lambda_B = 4.67\,10^{-13} g_{eff} \lambda^2 B \tag{2.42}$$

and ϕ and θ are respectively the angle between the magnetic field vector and the line of sight and the angle between the local surface normal and the line of sight.

Landstreet (1982) showed that the integration over the unresolved stellar disk presents difficulties related to the effects of stellar rotation, which Doppler shift the profiles of different stellar regions, and to the fact that the angles ϕ and $\Delta\lambda_B$ change over the visible stellar disk.

Assuming that the velocity broadening is small compared to the intrinsic broadening, and neglecting the first effect, Landstreet (1982) showed the relation between the observed Stokes V and the observed Stokes I:

$$\frac{V}{I} = -4.67\,10^{-13} g_{eff} \lambda^2 B_l \frac{dI}{d\lambda}\frac{1}{I} \tag{2.43}$$

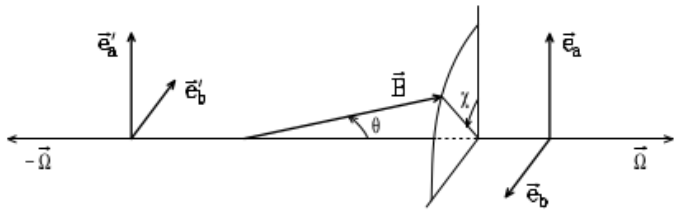

Figure 2.5: Angles θ and χ of the magnetic field direction Degl'Innocenti & Landolfi (2006).

where B_l is the integral over the visible hemisphere of the magnetic field component along the line of sight, called *effective magnetic field* (see Sect. 5.2.1).

2.3.1 Linear polarisation

In the case of weak field approximation (Sect. 2.3), it is possible to obtain equations for linear polarization, similar to Eq. 2.43 for Stokes V (Degl'Innocenti & Landolfi, 2006):

$$\begin{aligned} \frac{Q}{I} &= -5.45\,10^{-26}\bar{G}\,\lambda^4 B^2 \sin^2(\theta)\cos(2\chi)\,\frac{1}{I}\frac{\partial^2 I}{\partial\lambda^2} \\ \frac{U}{I} &= -5.45\,10^{-26}\bar{G}\,\lambda^4 B^2 \sin^2(\theta)\sin(2\chi)\,\frac{1}{I}\frac{\partial^2 I}{\partial\lambda^2} \end{aligned} \tag{2.44}$$

The quantity $B_\perp^2 = B^2\sin^2(\theta)$ is the square root of the transverse component of the magnetic field (see Sect. 5.2.3). The angles θ and χ are showed in Fig. 2.5.

The term $\bar{G}$ is called *second order effective Landé factor*:

$$\bar{G} = g_{\text{eff}}^2 - \delta \tag{2.45}$$

with:

$$\delta = \frac{1}{80}(g_1 - g_2)^2(16\,s - 7\,d^2 - 4) \tag{2.46}$$

where d is defined in Eq. 2.40 and:

$$s = J_1(J_1+1) + J_2(J_2+1) \tag{2.47}$$

g_1, g_2, J_1 and J_2 are respectively the Landé factors and the angular momenta of the levels.

The parameter $\bar{G}$ plays a similar role to g_{eff} for Stokes V. It is possible to note that $\bar{G} \leq g_{\text{eff}}^2$, since δ is equal zero for triplet end non-negative for any Zeeman patter. Moreover, $\bar{G}$ can assume negative values (about 8% of Fe I have $\bar{G} \leq 0$) and the average value is $\langle\bar{G}\rangle = 1.60$ (Degl'Innocenti & Landolfi, 2006).

CHAPTER 3

MEASUREMENT OF POLARIZED LIGHT

The measurement of Stokes parameters is obtained by means of instruments called *polarimeters*, which are composed by *polarizers* and *retarders*. In this chapter, we illustrated the instrumentation and the techniques used to measure, at high resolution, the polarization of stars; in particular, we concentrated on the description of the spectropolarimeter *Catania Astrophysical Observatory Spectropolarimeter* (CAOS), which was calibrated and used during the entire period of the Ph. D.

3.1 Polarizers

The polarizer is an optical device which returns a linearly polarized beam, independently of the polarization state of the incident light (Clarke & Grainger, 1971). The direction of the emergent radiation is called *transmission axis*.

An example of polarizer is the Polaroid, that is characterized by the presence of one single polarized beam at the exit. Mathematically, it can be described by:

$$\begin{pmatrix} \epsilon'_a \\ \epsilon'_b \end{pmatrix} = e^{i\psi} \begin{pmatrix} 1 & 0 \\ 0 & 0 \end{pmatrix} \begin{pmatrix} \epsilon_a \\ \epsilon_b \end{pmatrix} = e^{i\psi} \begin{pmatrix} \epsilon_a \\ 0 \end{pmatrix} \tag{3.1}$$

where ϵ_a and ϵ_b are the components at the entrance of the polariser (along the transmission axis and the orthogonal axis), ϵ'_a and ϵ'_b are the components at the exit of the polariser and ψ is a phase difference.

Polarisers can be obtained by means of one or more birefringent crystals, like calcite or quartz. These devices, called *polarizing beam splitters*, are characterized by the fact

that the incident light splits into two beams, with orthogonal state of polarization. The first is called *ordinary ray* and it passes without any deviation; it is polarized in the parallel direction respect to the unique symmetry axis of the crystal. The second, called *extraordinary ray*, is deviated at the air-crystal interface and it is polarized in the direction perpendicular to the symmetry axis.

Optical properties of crystals depend on the direction of incidence of the light and on the different refractive indices of the crystal for different directions, which in general are characterized by:

$$n_x \neq n_y \neq n_z \tag{3.2}$$

If only one of the refraction indices is different, the crystal is called *uniaxial*.

Uniaxial materials are fundamental for the construction of a polarimeter. The axis with different index of refraction is called the *optic* or *principal axis* and his refractive index is indicated with n_e. In the other hands, we indicated with n_o the other refractive index, which is related to the electric field vector that spans in the plane perpendicular to the optic axis of the crystal.

The difference $\Delta n = n_e - n_o$ is an important properties of the polariser and it is called *birefringence*. Among the material commonly used in astrophysics, calcite ($CaCO_3$) has a negative value $\Delta n = -0.17$ while quartz (SiO_2) has a positive value $\Delta n = 0.009$.

3.1.1 Polarizing beam splitters

In astronomical context, polarizing beam splitters are generally preferred in order to reduce light loss (Clarke & Grainger, 1971). Simple polarisers can be obtained cementing together two prisms composed of quartz or calcite.

The first example is the *Rochon prism* (Fig. 3.1), where two uniaxial crystals are cemented so that the optic axis of the first is parallel to the direction of propagation of the light and the optic axis of the second is perpendicular to it. At the exit, the ordinary beam is transmitted without any deviation while the extraordinary beam is bended two times, at the crystal-crystal and at the crystal-air interface.

Another example is the *Wollaston prism* (Fig. 3.2). In this case, the optic axis of both crystals is perpendicular to each other and to the direction of propagation of the light. This configuration returns a large deviation between the rays respect to the Rochon prism and, for this reason, it is adopted in several instruments, such as the *"Echelle SpectroPolarimetric Device for the Observation of Stars"* (ESPaDOnS) at CFHT (Donati

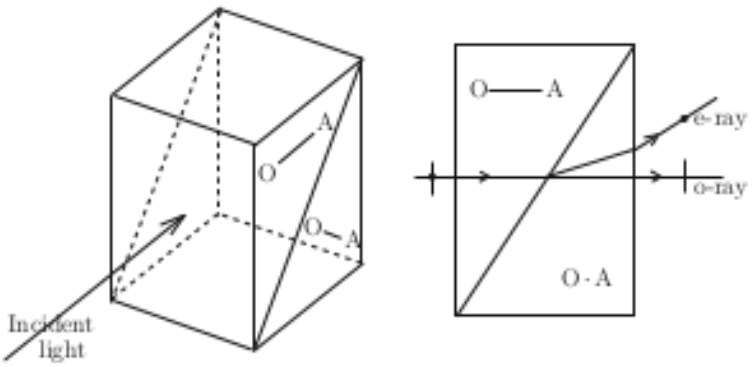

Figure 3.1: Rochon prism (Clarke, 2009).

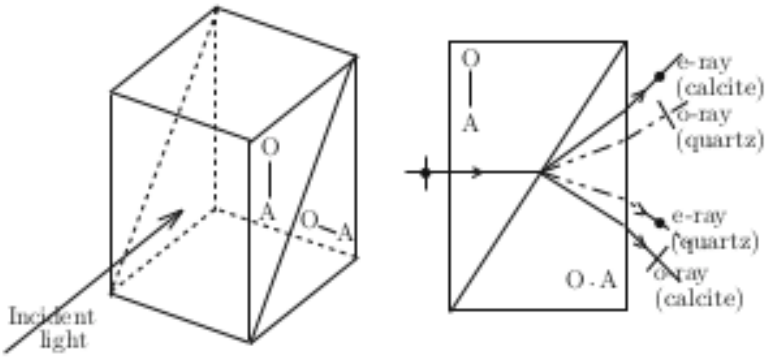

Figure 3.2: Wollaston prism for positive (quartz) or negative (calcite) birefringence (Clarke, 2009).

et al., 2006) and *"Polarimeter Add-On for the LRS Optics"* (PAOLO) at TNG (the use a double Wollaston prism) (Covino et al., 2014).

The total reflection of light is involved in the so called *Glan-Thompson prism* and *Glan-Foucault prism* (Fig. 3.3) and it occurs when a beam hits a surface with an angle larger than a *critical angle*. In this case, the optical axis of the two prisms are parallel but the ordinary ray is totally reflected at the interface while the extraordinary beam passes without any deviation. In Glan-Thompson configuration, the interface is cemented using Canada balsam or polymers. In the case of Glan-Foucault prism there is an air-gap interface.

A similar device is the *Foster prism* (Foster, 1938; Clarke, 1965b). In this case, the two prisms are made of glass and they are separated by a sliver of calcite (Fig. 3.4). This device is adopted in one of the most important high-resolution instrument, the

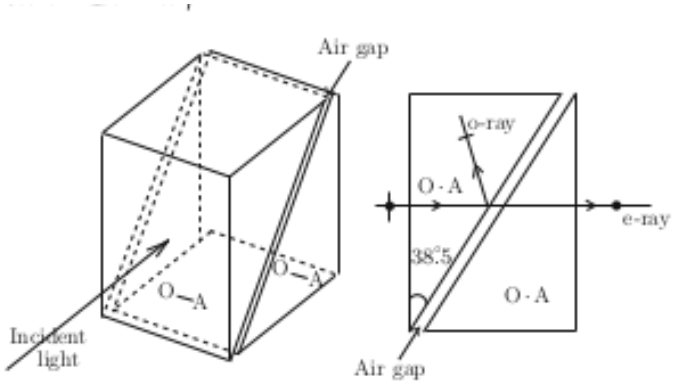

Figure 3.3: Glan-Foucault prism (Clarke, 2009).

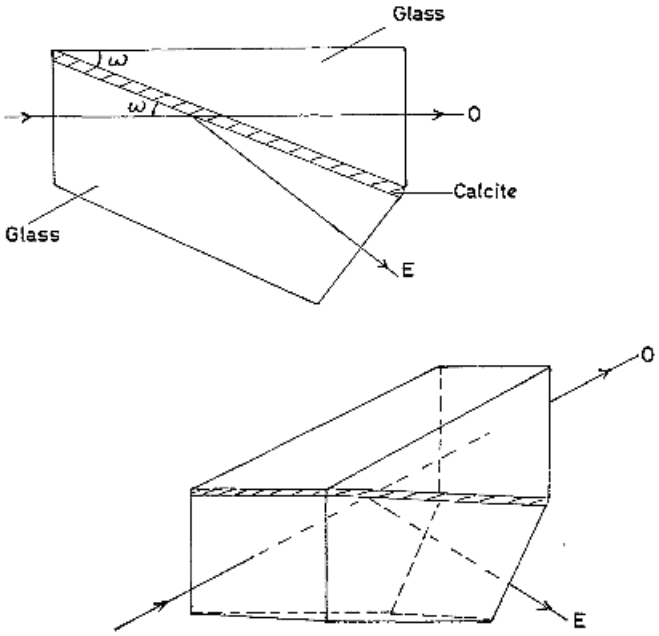

Figure 3.4: Foster prism (Clarke, 1965b).

polarimeter of the *"High Accuracy Radial velocity Planet Searcher"* (HARPSpol) (Snik et al., 2011; Piskunov et al., 2011).

All the previously described devices can not be used in the same focal plane because the angular separation of the beams is different and it could be a source of defocus (Keller, 2002). This problem can be solved by the use of a *Savart plate*, which is adopted for instance in the *"Catania Astrophysical Observatory Spectropolarimeter"* (CAOS) (Leone et al., 2016). The device is composed of two birefringent blocks cemented together, with the same thickness and with optic axes at 45°respect to the normal at the surface and

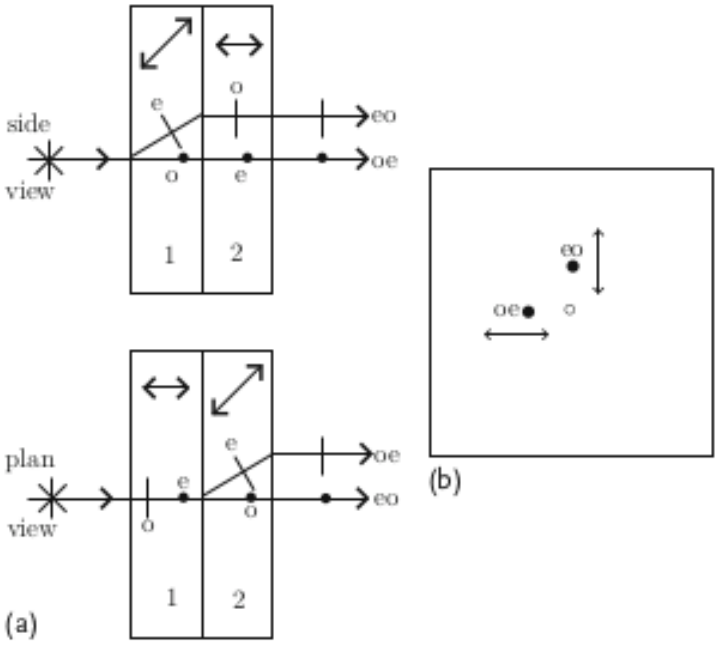

Figure 3.5: Savart plate. a) Two blocks of calcite; b) View of the displacement (Clarke, 2009).

90°respect to each other. At the entrance of the first block, light splits in ordinary and an extraordinary beams, which are switched again at the entrance of the second block. Here, the ordinary became extraordinary and the extraordinary became ordinary. At the exit of the device, the beams will be displaced along a diagonal relative to the edges of the square entrance face, with a displacement 2 times that of each plate (Clarke, 2009), how showed in Fig. 3.5.

3.2 Retarders

Other fundamental devices for the polarimeters are the *retarders*, which can modify the phase relation between orthogonally resolved components the light (Clarke & Grainger, 1971).

Following Landi Degl'Innocenti (1992), the ideal retarded is characterized by two axis, *fast* and *slow*, which have two different indices of refraction n_f and n_s. The electric field inside a retarder, extending between z = 0 and z = l, can be described by:

$$E_f(z,t) = \epsilon_f e^{i(k_f z - \omega t)} \quad 0 \le z \le l$$
$$E_s(z,t) = \epsilon_s e^{i(k_s z - \omega t)} \quad 0 \le z \le l \tag{3.3}$$

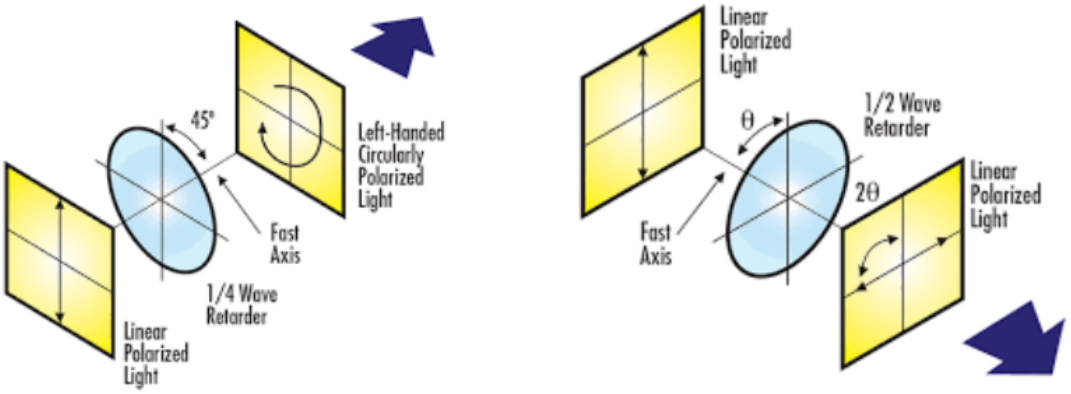

Figure 3.6: General quarter-wave plate (left) and half-wave plate (right). Credits *Edmund Optics* (`https://www.edmundoptics.com/resources/application-notes/optics/understanding-waveplates/`).

where ϵ_s e ϵ_f are complex constants ($\epsilon_f = A_f e^{i\phi_f}; \epsilon_s = A_s e^{i\phi_s}$) and k_f and k_s are given by:

$$k_f = n_f \frac{2\pi}{\lambda} \qquad k_s = n_s \frac{2\pi}{\lambda} \tag{3.4}$$

with the condition $n_s > n_f$. λ is the wavelength in vacuum.

At the exit of the retarder, the electric field can be described by:

$$\begin{pmatrix} \epsilon'_f \\ \epsilon'_s \end{pmatrix} = e^{i\psi} \begin{pmatrix} \epsilon_f \\ \epsilon_s e^{i\delta} \end{pmatrix} \tag{3.5}$$

where ψ is an inessential phase factor and where

$$\delta = (n_s - n_f)\frac{2\pi l}{\lambda} \tag{3.6}$$

is called *retardance* and it represents the phase difference (in radians) introduced by the retarder. If the thickness of the retarder l is such that $\delta = \pi/2$, the retarder is called *quarter-wave plate*; alternatively, if $\delta = \pi$ the retarder is called *half-wave plate*.

The quarter-wave plate is commonly used to measure Stokes V because it converts circularly polarized light ($I = |V|$) into linearly polarized light ($I^2 = Q^2 + U^2$).

Half-wave plate changes right-handed into left-handed circularly polarized light and, in the case of linear polarization, it changes the direction of vibration of the electric field. The general behavior of retarders is resumed in Fig. 3.6.

Retarders based on birefringent materials are highly wavelength sensitive, contrary to birefringent polarizers (Clarke & Grainger, 1971).

In order to correct this dependence, it is possible to combine devices made by materials with opposite variation of δn, changing also their thickness. Combining two materials, it is possible to obtain the so called *achromatic* retarders, which are usually correct at two wavelengths, as shown in Fig. 3.7; typical combinations are quartz and MgF_2.

Combining more materials, it is possible to correct retardance for a broad spectral region. These devices are called *superachromatic* retarders and they can be obtained, for instance, cementing together three pairs of quartz and MgF_2. In this way, it is possible to obtain a difference of $\lambda/2 \pm 0.04\%$ and $\lambda/4 \pm 0.25\%$ for a spectral range from 600 nm to 2700 nm (Fig. 3.8).

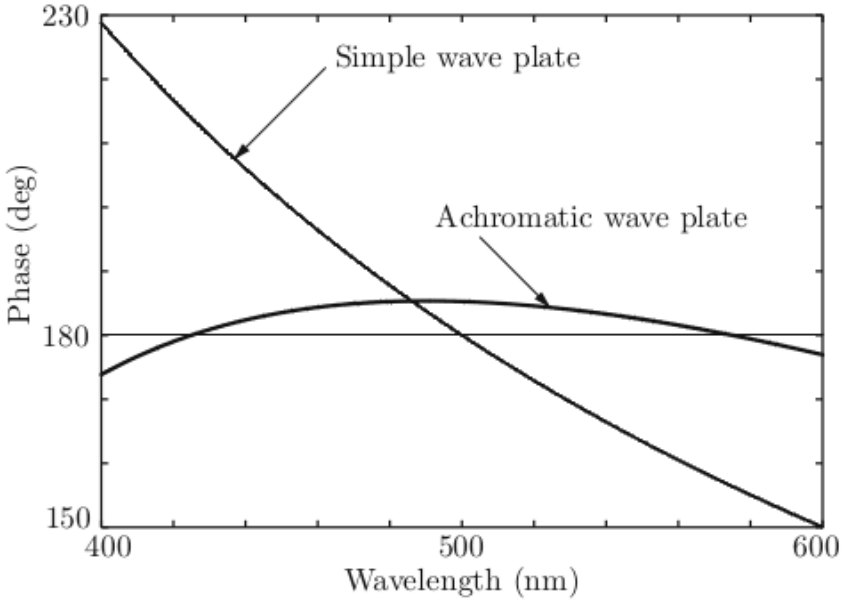

Figure 3.7: The phase delay of a compound half-wave plate made of quartz and MgF_2, designed to be achromatic at 425 and 575 nm, is compared with a simple plate of quartz cut to be half-wave at 500 nm (Clarke, 2009).

3.2.1 TIR retarders

Another physical process which produces phase delay between two orthogonal light components is the total internal reflection (TIR) of one of the components. One example of retarders, which use this physical effect, are the *Fresnel rhombs*. They are used as $\lambda/4$ or as $\lambda/2$, combining two rhombs (Fig. 3.9).

The big advantage of these devices is that they are almost achromatic, as shown in Fig. 3.10. For this reason, they are used for instruments with a broad spectral region, like

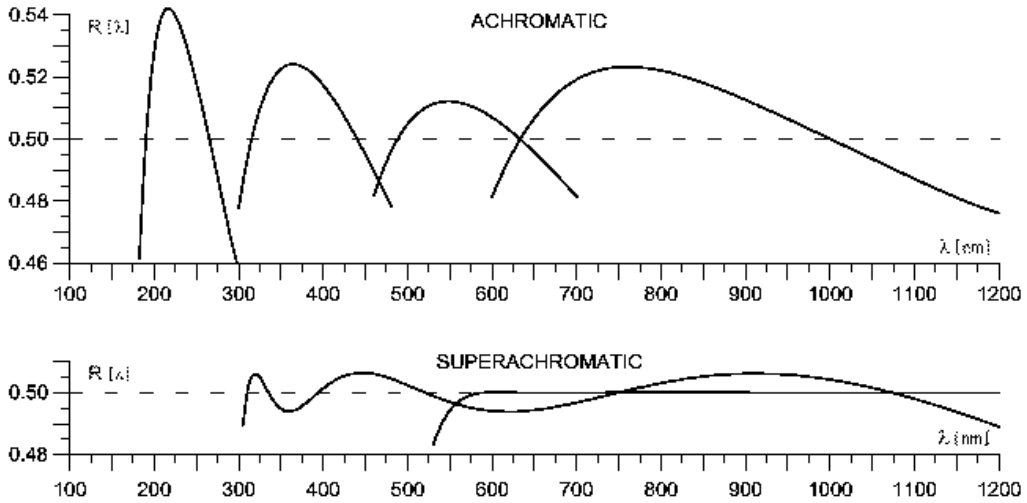

Figure 3.8: Comparison between achromatic and superachromatic retarders. Credits *Bernard Halle Nachfolger GmbH* (`http://www.b-halle.de/EN/Catalog/Retarders/Superachromatic_Quartz_and_MgF2_Retarders.php`).

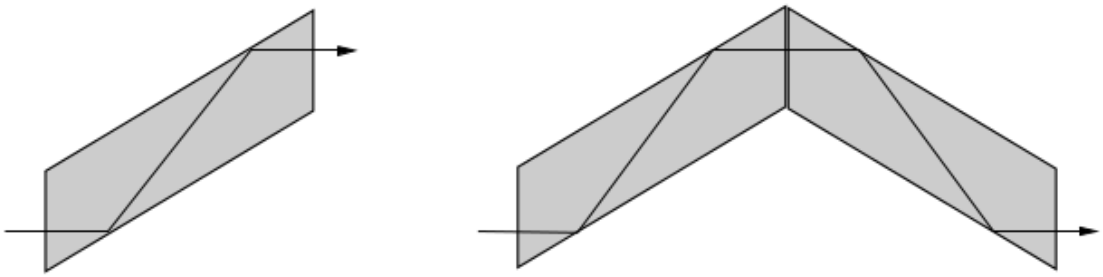

Figure 3.9: Quarter-wave (left) and half-wave (right) Fresnel rhombs (Keller, 2002).

ESPaDOnS. However, they are impossible to be settled in an instrument with reduced space, like CAOS, because of their big dimensions.

Rhombs present disadvantage related to the fact that the light does not emerge along the same axis of the incident beam (for a single $\lambda/4$ retarder) and the delay depends on the incidence angle (Clarke, 2009).

Another example of TIR retarder is the *reversion prism*, known also as *roofless Abbe* or *K prism*. It can be used as rotator, such as the Dove prism, or as $\lambda/4$ retarder, thanks to three internal reflections obtained by an aluminized intermediate face (Moreno, 2004) (Fig. 3.11). In this case, light emerges along the same axis of the incident beam.

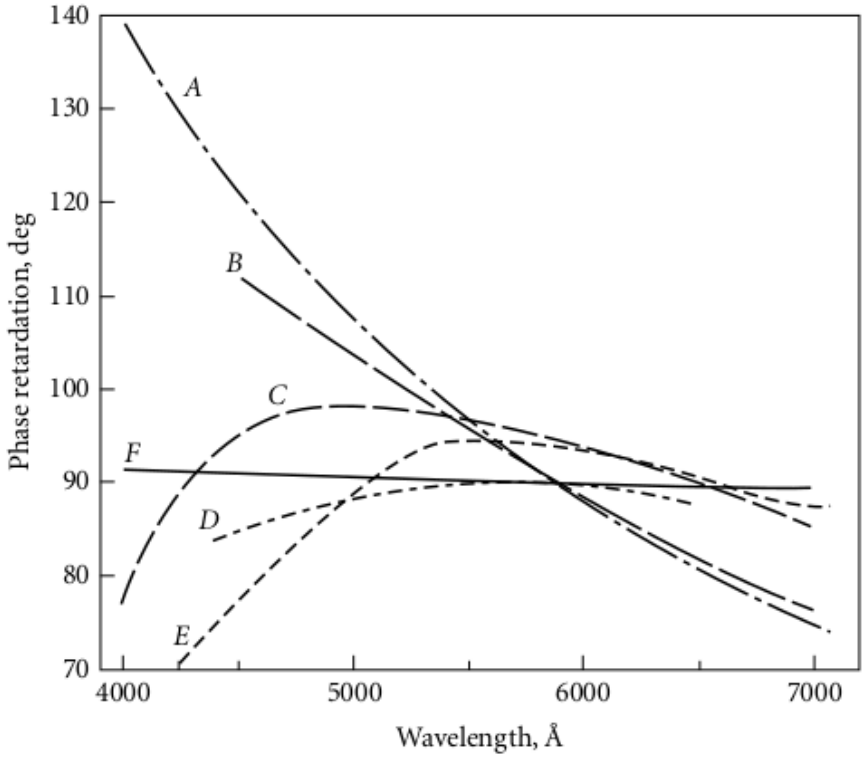

Figure 3.10: Phase retardation vs wavelength for $\lambda/4$ plates: A, quartz; B, mica; C, stretched plastic film; D, apophyllite; and E, quartz-calcite achromatic combination; F, Fresnel rhomb (Bass et al., 2010).

3.3 Prototype of a polarimeter

This general description of a prototype of polarimeter follows Landi Degl'Innocenti (1992). It is possible to build a simple polarimeter combining a wave plate and a linear polarizer, as shown in Fig. 3.12. β is the angle between the transmission direction of the polarizer and the reference axis and α is the angle between the reference direction and the fast axis of the retarder.

At the entrance of the retarder, the components of the electric field, along the unit vectors $\vec{e}_1$ and $\vec{e}_2$, are given by:

$$E_1 = \epsilon_1 e^{-i\omega t} \qquad E_2 = \epsilon_2 e^{-i\omega t} \tag{3.7}$$

while the components along the fast and slow axes of the retard are given by:

$$E_f = (\epsilon_1 cos\alpha + \epsilon_2 sin\alpha) e^{-i\omega t} \qquad E_s = (-\epsilon_1 sin\alpha + \epsilon_2 cos\alpha) e^{-i\omega t} \tag{3.8}$$

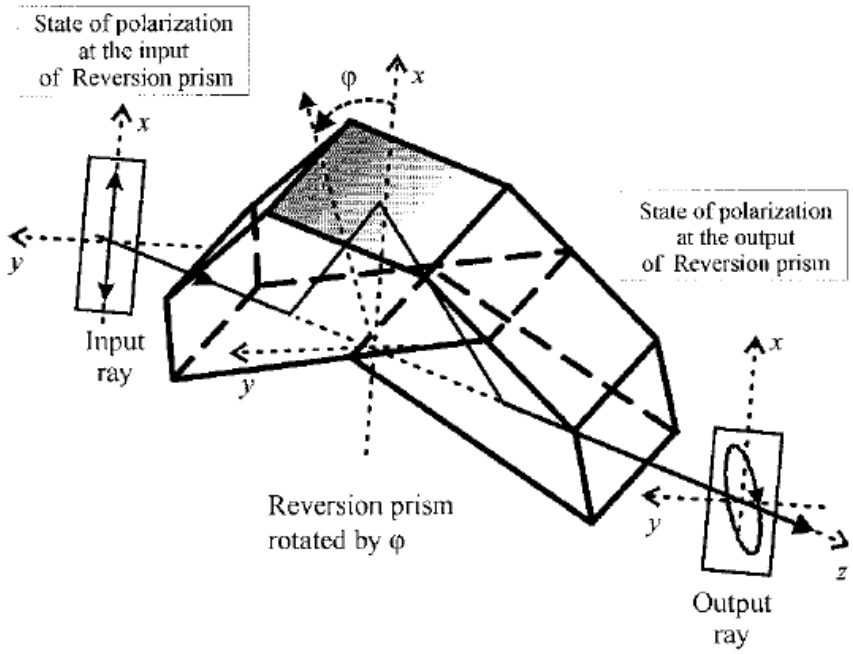

Figure 3.11: K prism retarder (Moreno, 2004).

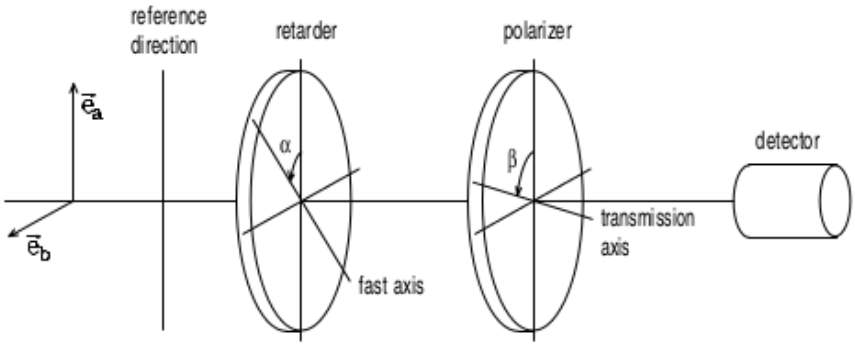

Figure 3.12: Prototype of a polarimeter (Landi Degl'Innocenti, 1992).

Apart the inessential phase factor, at the exit of the retarder the component along the slow axis is retarded by the quantity δ, introduced by the wave plate:

$$E_s = (-\epsilon_1 \sin\alpha + \epsilon_2 \cos\alpha) e^{i\delta} e^{-i\omega t} \tag{3.9}$$

The polarizer transmits only the component along the acceptance axis E_a:

$$\begin{aligned} E_a(t) &= \big(cos(\beta-\alpha)E_f + sin(\beta-\alpha)E_s\big) = \\ &= \{cos(\beta-\alpha)(\epsilon_1 cos\alpha + \epsilon_2 sin\alpha) + \\ &+ sin(\beta-\alpha)[-\epsilon_1 sin\alpha + \epsilon_2 cos\alpha]e^{i\delta}\}e^{-i\omega t} \end{aligned} \tag{3.10}$$

The detector responds with a signal proportional to $\langle E_a^*(t)E_a(t)\rangle$. After some algebra, it is possible to obtain:

$$\begin{aligned} S(\alpha,\beta,\delta) = &\frac{1}{2}\{I + (Q\,cos\,2\alpha + U\,sin\,2\alpha)cos[2(\beta-\alpha)] + \\ &- (Q\,sin\,2\alpha - U\,cos\,2\alpha)sin[2(\beta-\alpha)]cos\delta + \\ &+ V\,sin[2(\beta-\alpha)]sin\delta\}) \end{aligned} \tag{3.11}$$

Stokes parameters can be found setting the polarimeter at particular angles.

3.3.1 Linear polarization

Linear polarization measures are performed removing the retarder ($\delta = 0$) or setting the fast axis to be parallel to the transmission axis of the polarizer ($\alpha = \beta$). In this way, Eq. 3.11 became:

$$S'(\beta) = \frac{1}{2}\{I + Q\,cos\,2\beta + U\,sin\,2\beta\} \tag{3.12}$$

Stokes parameters I, Q and U are given by the combination of four measures with different angles:

$$\begin{aligned} I &= S'(0°) + S'(90°) \\ Q &= S'(0°) - S'(90°) \\ U &= S'(45°) - S'(135°) \end{aligned} \tag{3.13}$$

Eq. 3.13 imply a rotation of the polarizer, which is a dangerous and complicated procedure, especially in the case of spectropolarimetry. This is because grating are usually large and their response is sensitive to the polarization state of the incident radiation (Gray, 2005).

Fixing the polarizer at $\beta = 0°$, it is possible to measure linear polarization using a half-wave plate ($\delta = 180°$). In this case, Eq. 3.11 became:

$$S''(\alpha) = \frac{1}{2}\{I + Q\cos 4\alpha + U\sin 4\alpha\} \tag{3.14}$$

and Stokes parameters can be measured through the following settings of angles:

$$\begin{aligned} I &= S''(\alpha) + S''(\alpha + 45°) \\ Q &= S''(0°) - S''(45°) \\ U &= S''(22°.5) - S''(67°.5) \end{aligned} \tag{3.15}$$

3.3.2 Circular polarization

Circular polarization is measured using a quarter-wave plate ($\delta = 90^{\circ}$), which converts circular to linear polarization. Fixing also in this case the polarizer at $\beta = 0°$, it is possible write Eq. 3.11 as:

$$\mathrm{S}'''(\alpha) = \frac{1}{2}\{\mathrm{I} + \mathrm{Q}\cos^2 2\alpha + \mathrm{U}\sin(2\alpha)\cos(2\alpha) - \mathrm{V}\sin(2\alpha)\} \tag{3.16}$$

Stokes I and Stokes V can be measured by:

$$\begin{aligned} I &= S'''(-45°) + S'''(45°) \\ V &= S'''(-45°) - S'''(45°) \end{aligned} \tag{3.17}$$

3.4 Problems on polarization measurements

The measurements of polarization is a complicated issue not only because the difficulties to reach a good photon statistics, but also for the presence of several systematics, which must be taken into account.

3.4.1 Instrumental sources

The first possible sources of error are the elements of the optical path, which can add polarization through oblique reflections of mirrors (for instance in the case of Nasmyth and Coudé foci), mechanical support structures of the telescope or reflections inside the polarimeter. Each reflection generates linear polarization on the order of 5%.

The telescope itself can be a source of polarization because inhomogeneities in the shape of the mirrors, which brake the rotational symmetry that compensates for polarizations due to reflections from different parts of mirrors. These effects could be caused by temperature or by internal stress at the moment of the manufacturing process; they are always present at some level.

The polarization produced by the optics is generally called *Instrumental Polarization*. It is usually evaluated by calibration through unpolarized sources, although the intrinsic level of polarization of standard source is unknown at high level.

3.4.2 Atmospheric sources

Another source of spurious polarization is the atmosphere of the Earth. Although atmospheric extinction does not add any polarization (Clarke, 2009), scattering by aerosols

and molecules in the Earth's atmosphere can yield to spurious signals (Kemp et al., 1987); for instance, Hough et al. (2006) reported how the dichroic behavior of the Saharan dust is strongly dependent on the zenith distance.

Induced polarization is expected because of the continuously changing of refractive index in the atmosphere. The polarization of the sky background was analyzed by Fox (1992), who discovered that one of the most contributors is the scattered moonlight, that impacts the accuracy of the measures.

Atmospheric turbulence impacts measurement breaking the rotational symmetry of the optical systems. This is because it creates a distortions of the wave front in the system pupil and, in this way, different parts of the mirrors are weighted in differently. These effects disappear if they are averaged over long exposure, as stated by Tinbergen (2005). Guiding errors have similar effects.

Faraday rotation, due to the earth magnetic field, rotates the plane of oscillation of the electric field vector and it impacts measures of linear polarization. This effect was quantified by Hsu & Breger (1982), who demonstrated, that in the case of a star at 5°above the horizon, the rotation is about $40'$ and it became negligible (less than 0.1°) for airmass 1.5.

3.5 Instrumental implementation: two beam analyser

The expected polarization of astronomical sources is usually very small, of about a few per cent of the signal (Clarke, 1965a; Tinbergen, 2005).

For this reason, applications of spectropolarimetric techniques were limited in the past and a big step forward was possible only during the last decade, thanks to the technological advancement and to the introduction of larger telescopes and modern CCD detectors.

One of the most important innovation was the introduction of the two beam technique by Tinbergen & Rutten (1992). This method allowed to reach a higher accuracy, extracting the information of the Stokes parameters from the ratio between the intensities of two exposures with opposite sign of the polarization, obtained by the rotation of the wave-plate.

For instance, Stokes Q can be obtained with an exposure at 0°and another obtained rotating the half-wave plate by 45°, while Stokes U can be measured with two exposures

at 22.5°and 67.5°. The case of circular polarization is similar, with the use of quarter wave plate at angles with a difference of 90°.

The technique can be described parametrizing in a function G the time-independent effects (efficiency of the system), and in a function F, the time-dependent effects (atmospheric transmission, seeing and variations in shutter time). The intensities of the four spectra of the two exposures are given by:

$$\begin{aligned} i_{1,\parallel} &= \tfrac{1}{2}(I+S)G_{\parallel}F_1 \\ i_{1,\perp} &= \tfrac{1}{2}(I-S)G_{\perp}F_1 \\ i_{2,\parallel} &= \tfrac{1}{2}(I-S)G_{\parallel}F_2 \\ i_{2,\perp} &= \tfrac{1}{2}(I+S)G_{\perp}F_2 \end{aligned} \tag{3.18}$$

where $\parallel$ and $\perp$ are related to ordinary and extraordinary beam. The ratio R is given by:

$$\mathrm{R}^2 = \frac{\mathrm{i}_{1,\parallel}/\mathrm{i}_{1,\perp}}{\mathrm{i}_{2,\parallel}/\mathrm{i}_{2,\perp}} \tag{3.19}$$

and it can be used to extract the generic Stokes parameter S of the degree of polarization P_S using:

$$\mathrm{P_S} = \frac{\mathrm{S}}{\mathrm{I}} = \frac{\mathrm{R}-1}{\mathrm{R}+1} \tag{3.20}$$

Another important information can be computed using the ratio:

$$\mathrm{R}_{\mathrm{N}}^2 = \frac{\mathrm{i}_{1,\parallel}/\mathrm{i}_{2\perp}}{\mathrm{i}_{2,\parallel}/\mathrm{i}_{1,\perp}} \tag{3.21}$$

which can be used to compute the so called the *Noise* or *Null* (Donati et al., 1997), given by:

$$\frac{\mathrm{N}}{\mathrm{I}} = \frac{\mathrm{R_N}-1}{\mathrm{R_N}+1} \tag{3.22}$$

In the ideal case, with a perfect signal extraction and a perfect wavelength calibration of the spectra, the parameter N/I is flat. Any deviations may reflect the presence of a systematic spurious polarization signal related to errors caused by observations or wrong data reduction. For instance, typical causes of signals on the Null spectrum are shifts between spectral lines observed in orthogonal polarizations, which can be created by not optimal wavelength calibration.

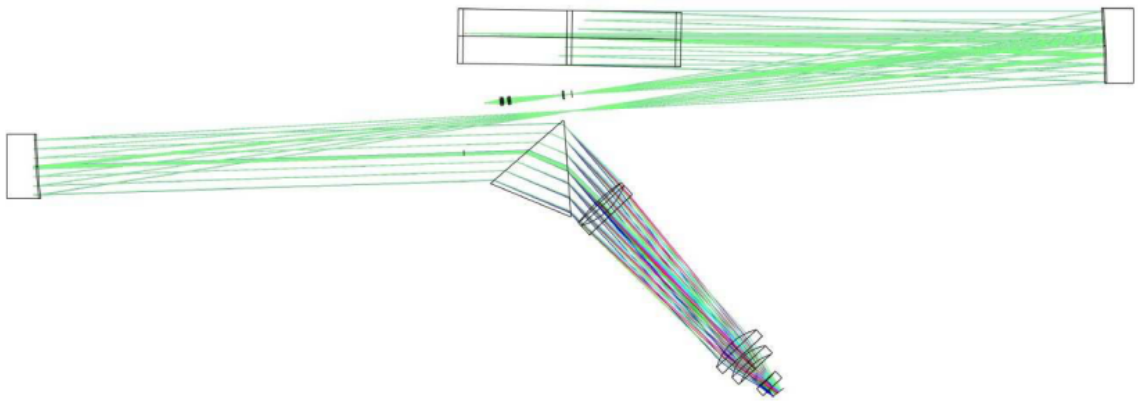

Figure 3.13: Optical layout of CAOS as seen from the top (Leone et al., 2016).

3.5.1 Four beam procedure

In order to reach higher accuracy on the measure, it is possible to use four exposures per Stokes parameter, taking two more images with different angles of the wave-plate. In this case:

$$\begin{aligned} i_{3,\parallel} &= \tfrac{1}{2}(I-S)G_{\parallel}F_3 \\ i_{3,\perp} &= \tfrac{1}{2}(I+S)G_{\perp}F_3 \\ i_{4,\parallel} &= \tfrac{1}{2}(I+S)G_{\parallel}F_4 \\ i_{4,\perp} &= \tfrac{1}{2}(I-S)G_{\perp}F_4 \end{aligned} \tag{3.23}$$

with the ratios:

$$\mathrm{R}_{\mathrm{V}}^{4} = \frac{\mathrm{i}_{1\mathrm{o}}}{\mathrm{i}_{2\mathrm{o}}}\frac{\mathrm{i}_{2\mathrm{s}}}{\mathrm{i}_{1\mathrm{s}}}\frac{\mathrm{i}_{4\mathrm{o}}}{\mathrm{i}_{3\mathrm{o}}}\frac{\mathrm{i}_{3\mathrm{s}}}{\mathrm{i}_{4\mathrm{s}}} \; ; \; \mathrm{R}_{\mathrm{N}}^{4} = \frac{\mathrm{i}_{1\mathrm{o}}}{\mathrm{i}_{2\mathrm{o}}}\frac{\mathrm{i}_{2\mathrm{s}}}{\mathrm{i}_{1\mathrm{s}}}\frac{\mathrm{i}_{3\mathrm{o}}}{\mathrm{i}_{4\mathrm{o}}}\frac{\mathrm{i}_{4\mathrm{s}}}{\mathrm{i}_{3\mathrm{s}}} \tag{3.24}$$

3.6 CAOS

A big effort during the PhD was made in order to perform observations with the instrument CAOS (Leone et al., 2016). It is an high resolution (R ≈ 55000) échelle spectropolarimeter with a spectral coverage from 388 nm to 725 nm.

The optical layout is reported in Fig. 3.13 and it shows a collimated beam of 10 cm, dispersed by a R4 (blaze angle of 76°) échelle grating in a white pupil configuration (Dekker et al., 2000). A F/2.1 camera of five lenses focused the dispersed spectrum into an E2V42-40 Thinned and Back Illuminated High-Performance CCD, with 2048 x 2048 pixel format. The focal plane was tilted in order to correct the axial chromatism, as shown in

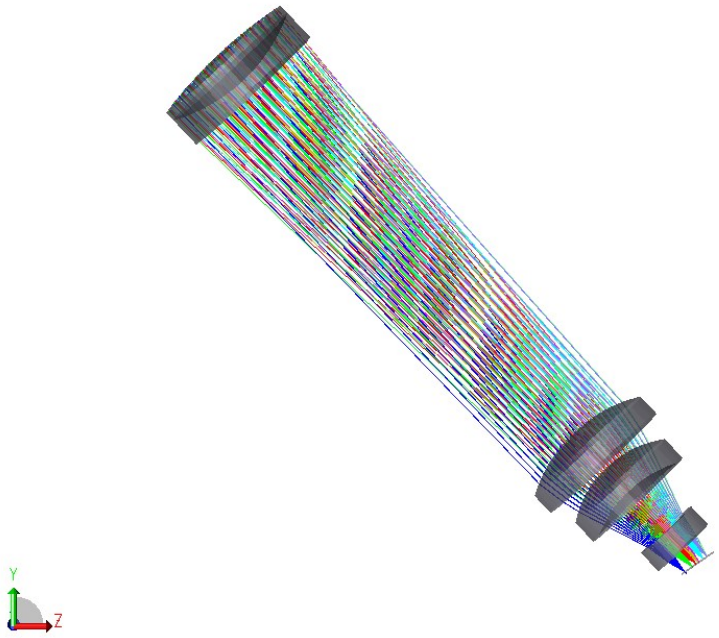

Figure 3.14: CAOS camera (Leone et al., 2016).

Fig. 3.14. The read-out noise is 3.5 e^- reading at 100kHz, 4 e^- reading at 200kHz and 6 e^- reading at 400kHz.

The grating was made by *SPECTRA PHYSICS Richardson* and it presents 41, 59 rules mm^{-1}, an area of 102x408 mm with an aluminum reflection coating and it works on Littrow configuration, with an off-plane angle of 0.9°. The cross disperser used is a 140x160x160 mm prism with an aperture angle of 53.1°and it is made of Schott SF1 glass.

CAOS uses two 100 μm multimode optical fibers with high-OH radicals. The F/15 pupil of the telescope is projected into a F/4 beam of the fibers through a couple of gradient-index lenses, glued on the input of the fibers. This configuration corrects for the *focal ratio degradation* and it improves the stability of the shape of the spectral lines during the exposures (Avila et al., 1998).

One of the most important characteristics for a spectropolarimeter is the stability of the echellogram in time. A 2.4 x 1.2 m TMC optical table, with a dry pumping system for vibration cancellation, avoid the vibration noise which is due, for instance, to the

continuous seismic activity of Etna volcano.

Variations of temperature in the optical path within the spectropolarimeter have impacts on the measure. It can cause a transverse movement of the echellogram, in the CCD, and a longitudinal variation, which results into a defocus (Leone et al., 2016). If the thermal variations are longer than exposure time, they can be, in principle, corrected through telluric lines. Variations shorter than exposure time are more problematic and they can reduce the accuracy of the wavelength calibration and decrease the spectral resolution. However, these effects should be visible into a spurious polarized signal in the null profile. In order to reduce temperature related effects, CAOS is settled in a thermal isolated room with a temperature stable within a rms ≤ 0.01 K.

3.6.1 The polarimeter

The design of the polarimeter for CAOS follows the design of the polarimeter build for the instrument SARG, at the *Telescopio Nazionale Galileo* (Leone et al., 2003). It is located on the converging F/15.5 beam of the telescope and it is based on the dual beam technique.

The polarizer is a Savart plate made of calcite, with a total length of 32 mm, a beam separation of 2.5 mm (in the visible) and an AR coating for the 350-900 nm interval range. This optical device has the advantage to give the same optical path to ordinary and extraordinary beams, in the converging beam.

The retarders are achromatic optical devices produced by *Bernard Halle Nachfolger GmbH*. They induce a retardance of ± 3 % in a range of 450-700 nm, with a correct value at 488 nm and 633 nm (Fig. 3.15). In principle, super-achromatic retarders should be more suitable, considering the broad spectral range covered by CAOS (380-850 nm), but they are a source of ripples for resolution higher than R $\approx$ 35000 (Donati et al., 1999). Fresnel rhombs and K-prism were impossible to settle in the beam because of their dimensions.

The alignment of the fast axis of the retarder, respect to the acceptance axis of the polarizer, follows Goodrich et al. (1995).

Fig. 3.16 shows a comparison between the spectra of the magnetic star βCrB obtained with CAOS and ESPaDOnS and it demonstrates the quality of the instrument.

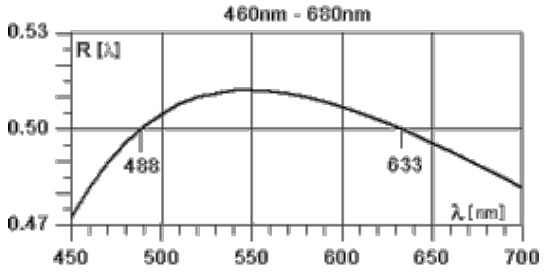

Figure 3.15: Retardance of CAOS wave plates.

3.7 CAOS Calibration

The calibration of a high-resolution spectropolarimeter, such CAOS, is a complicated procedure because the difficulties to make a measure of the absolute value of polarization, which can be compared with standard polarized stars. Indeed, in the case of low resolution instruments, absolute flux is easier to measure, using slits larger than the image which collect all the light of the source.

High-resolution observations are usually performed by small slits (smaller than the image) or by fibres. In this way, it is not possible to collect all the flux of the star during the exposure, which results to be split because of the atmospheric refraction. Another issue is that the ratio between the fluxes in the two beams does not keep constant during the exposures of a series because of a not constant transmission of the fibres or of a change of the way in which they are illuminated as the retarder rotates (Bagnulo et al., 2012). Moreover, objects are guided at a given wavelength region and errors in the guiding process can mix the flux measured. For these reasons, standard polarized stars can not be used for the calibration.

In order to calibrate CAOS, we introduced a new technique based on the use of magnetic early type stars. This method follows the technique used by Kuhn et al. (1994) for the calibration of the Solar Observatory Vacuum Tower Telescope, which was performed using sunspots.

In general, characteristics of the instrument can be mathematically described by a Muller matrix M_λ, which connects the input Stokes vector with the observed:

$$[I, Q, U, V]_{obs} = M_\lambda [I, Q, U, V]_{inp} \tag{3.25}$$

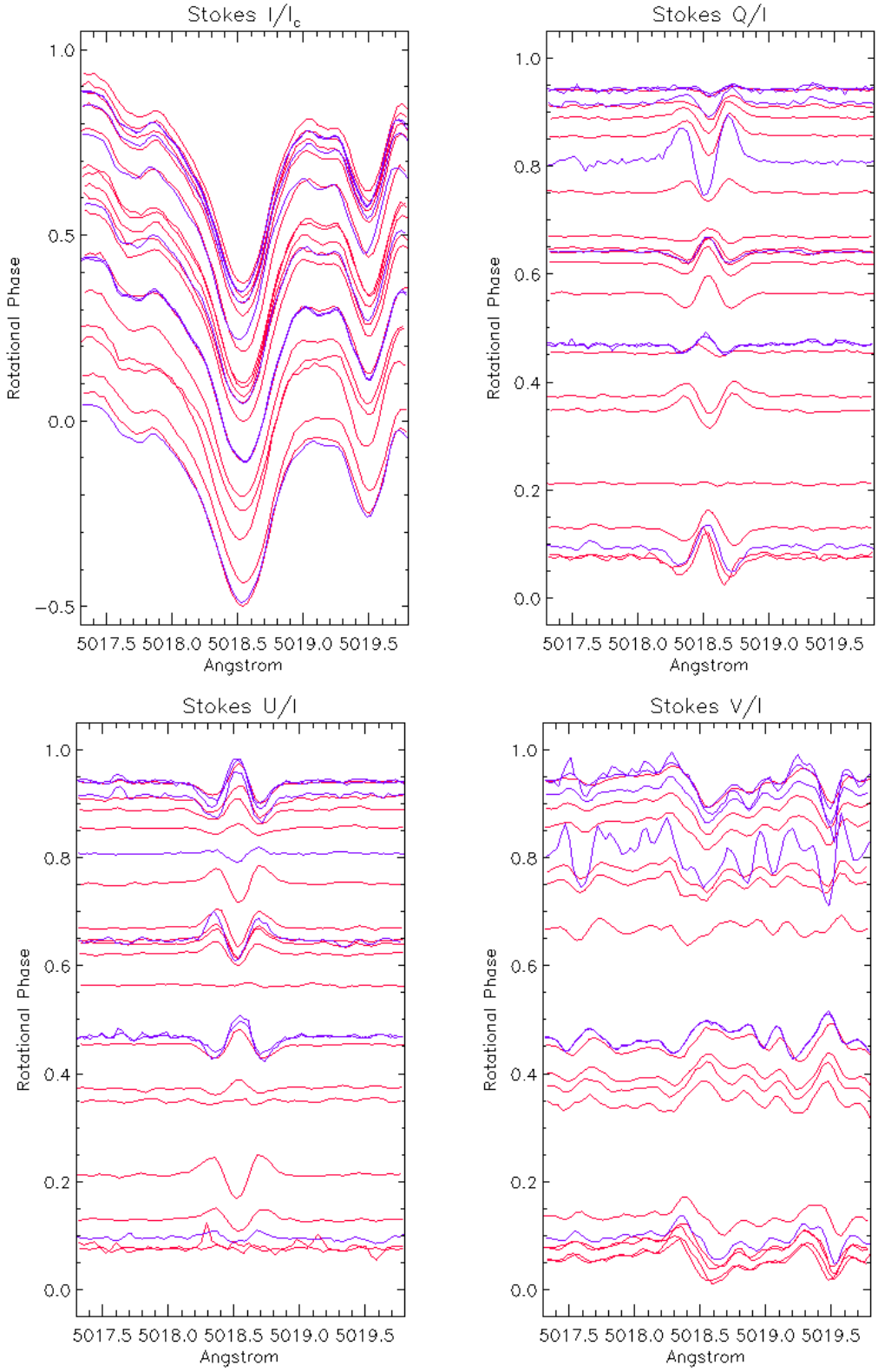

Figure 3.16: Variation of Stokes profiles of Fe II 5018 Å of βCrB. The red curves are obtained with CAOS while the blue are obtained with ESPaDOnS.

where the inverse of M_λ can be written as (Kuhn et al., 1994):

$$\mathrm{M}_\lambda^{-1} = \begin{pmatrix} 1 & 0 & 0 & 0 \\ 0 & 1+a_\lambda c_\lambda & a_\lambda d_\lambda & -a_\lambda \\ 0 & c_\lambda b_\lambda & 1+d_\lambda b_\lambda & -b_\lambda \\ 0 & -c_\lambda & -d_\lambda & 1 \end{pmatrix} \tag{3.26}$$

Parameters of Eq. 3.26 were estimated using spectropolarimetric observation of the magnetic stars γ Equ and β CrB.

The terms c_λ and d_λ were determined assuming that Stokes Q and Stokes U of γ Equ are null; this was done excluding lines with large second order Landé factor, such as the FeII 5018.44 Å.

The terms a_λ and b_λ were determined assuming that Stokes V of π components of β CrB are null; this allows to estimate the cross-talk from linear to circular polarization and it was made after the correction for the cross-talk from circular to linear.

Final values of the parameters are:

$$\begin{aligned} a_\lambda &= -0.161 + 5.55\times10^{-5}\lambda - 4.60\times10^{-9}\lambda^2 \\ b_\lambda &= -0.131 + 4.80\times10^{-5}\lambda - 4.42\times10^{-9}\lambda^2 \\ c_\lambda &= +0.031 - 8.13\times10^{-6}\lambda + 5.04\times10^{-10}\lambda^2 \\ d_\lambda &= -0.370 + 1.33\times10^{-4}\lambda - 1.18\times10^{-8}\lambda^2 \end{aligned} \tag{3.27}$$

This shows that the cross-talk of CAOS is almost negligible. We noted that about the 0.4% of Stokes Q and U are converted in Stokes V. This dependence is similar to a typical trend for retardance in the case of achromatic retarder found by Leone et al. (2003) and, for this reason, we attribute this behaviour to the waveplates.

3.8 Data reduction

Data reduction process consists on the conversion of the 2D image, captured by the detector, into a 1D spectrum calibrated in wavelength.

The reduction of spectropolarimetric data is similar to the case of classical spectroscopy. In addition, Stokes profiles can be measured by the combination of the exposures taken with different angles.

3.8.1 Calibration

The first step of each data reduction procedure is the creation of the calibration frames. They are:

- the *master Bias*, which contains the zero level of the detector due to electronic and read out noise. The master frame is computed as the simple average of several bias frames, which are obtained through a zero second exposure. In the case of CAOS, the level of the master bias is on the order of 9700 ADU.

- the *Dark frame*, which contains the electronic noise due to thermal effects, called *dark current*. This term is almost negligible for modern CCD detectors, that are also cooled using liquid nitrogen. For instance, the CCD of CAOS is cooled at -135° C.

- the *master Flat*, which contains the pixel to pixel variation caused by the optics (for instance given by a not uniform transmission of the light across the field of view), vignetting, dust on the CCD itself or the glass CCD cover, fringing effects of the wave-plate and differences on pixel sensitivities. Master flat is computed as the median of several flat field frames obtained observing a continuous light source, with no spectral lines. In the case of CAOS, a 100W halogen lamp is used in order to have signal in the wide wavelength range covered by the instrument. The master flat is normalized around the unit by dividing for its maximum value.

- the *ThAr frame*, which is used for the wavelength calibration. It is obtained by exposures of a lamp with known spectral lines, such as a Thorium Argon lamp.

3.9 Reduction of the images

The procedure of data reduction of each image starts with the subtraction of the master bias.

The second step consists in the selection and in the tracing of the apertures, for the ordinary and extraordinary beam. This operation is performed by a recentering of the apertures from a reference frame.

Known issue of spectroscopy is the presence of internal reflections, caused by elements of the system. This additional radiation, called *scattered light*, alters the zero level and it can impact the measures of the equivalent width of spectral lines. It is subtracted by a bi-dimensional fit of the image. Fig. 3.17 shows a section of CAOS frames where a value smaller than 1% of scattered light has been measured. This low value indicates the high quality of the optics and the mechanical parts of the instrument.

After the subtraction of the scattered light, the extraction of the orders can be performed. Wavelength coverage of each order of CAOS is listed in Table 3.9.

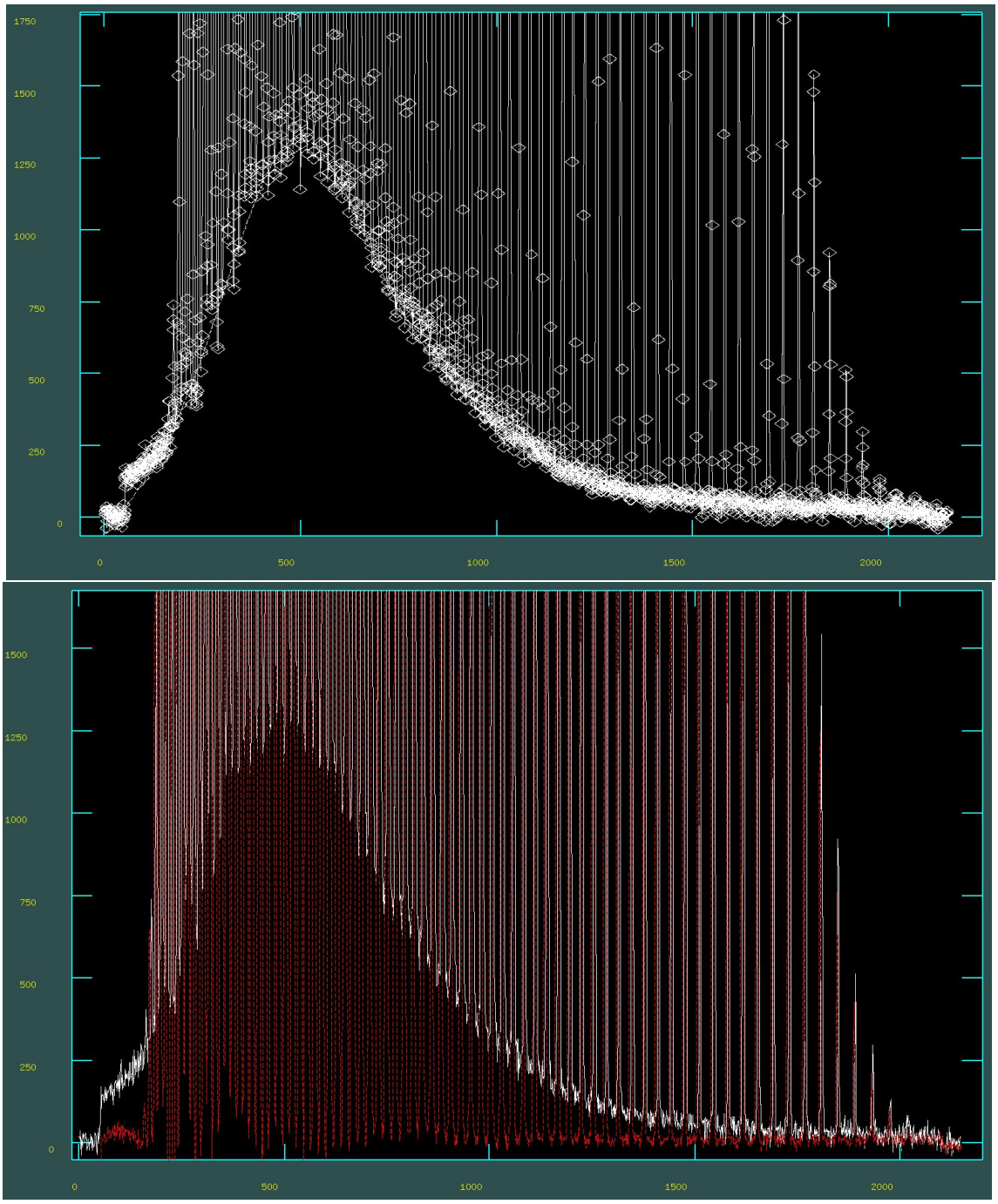

Figure 3.17: Top: section of CCD frame showing the 1% scattered light level and its fitting with a polynomial function. Bottom: comparison after scattered light subtruction.

Table 3.1: Order by order wavelength coverage. Columns report aperture numbers (A), diffraction orders (O), first and last wavelengths.

A	O	λ_{min}	λ_{max}	A	O	λ_{min}	λ_{max}
1	42	10776.6	10950.6	41	82	5581.6	5673.7
2	43	10531.9	10702.0	42	83	5515.1	5606.2
3	44	10298.0	10464.4	43	84	5450.1	5540.2
4	45	10074.2	10237.1	44	85	5386.7	5475.8
5	46	9859.9	10019.4	45	86	5324.7	5412.9
6	47	9654.4	9810.8	46	87	5264.1	5351.3
7	48	9457.4	9610.6	47	88	5204.9	5291.2
8	49	9268.2	9418.5	48	89	5147.0	5232.4
9	50	9086.4	9233.9	49	90	5090.4	5174.9
10	51	8911.6	9056.3	50	91	5034.9	5118.6
11	52	8743.4	8885.5	51	92	4980.7	5063.6
12	53	8581.4	8720.9	52	93	4927.7	5009.7
13	54	8425.3	8562.4	53	94	4875.7	4957.0
14	55	8274.8	8409.5	54	95	4824.8	4905.3
15	56	8129.5	8262.0	55	96	4775.0	4854.8
16	57	7989.3	8119.5	56	97	4726.2	4805.2
17	58	7853.8	7981.9	57	98	4678.4	4756.7
18	59	7722.9	7848.9	58	99	4631.5	4709.1
19	60	7596.2	7720.2	59	100	4585.6	4662.5
20	61	7473.6	7595.7	60	101	4540.5	4616.8
21	62	7354.9	7475.1	61	102	4496.3	4571.9
22	63	7239.9	7358.3	62	103	4453.0	4528.0
23	64	7128.5	7245.1	63	104	4410.5	4484.8
24	65	7020.4	7135.3	64	105	4368.8	4442.5
25	66	6915.6	7028.8	65	106	4327.9	4401.0
26	67	6813.8	6925.4	66	107	4287.7	4360.2
27	68	6715.0	6825.1	67	108	4248.2	4320.2
28	69	6619.0	6727.5	68	109	4209.5	4281.0
29	70	6525.8	6632.8	69	110	4171.5	4242.4
30	71	6435.1	6540.7	70	111	4134.1	4204.5
31	72	6346.9	6451.1	71	112	4097.4	4167.3
32	73	6261.0	6363.9	72	113	4061.3	4130.7
33	74	6177.5	6279.0	73	114	4025.9	4094.8
34	75	6096.1	6196.4	74	115	3991.0	4059.5
35	76	6016.9	6115.9	75	116	3956.7	4024.8
36	77	5939.7	6037.5	76	117	3923.0	3990.7
37	78	5864.5	5961.1	77	118	3889.9	3957.1
38	79	5791.1	5886.5	78	119	3857.2	3924.1
39	80	5719.5	5813.9	79	120	3825.1	3891.7
40	81	5649.7	5742.9	80	121	3793.5	3859.8
				81	122	3762.3	3828.3

The successive step is the wavelength calibration. This is an important point because it can impact directly the measure of Stokes profiles, because a wrong wavelength calibration can cause a misalignment of the spectra in the process of combination of the exposures and it can result in profile in the null spectrum. The Thorium-Argon reference lamp is calibrated with a precision of 10^{-4} Å.

Each wavelength calibrated imaged is corrected by the effects of heliocentric velocity. Since we are not in an inertial system, measured wavelengths are shifted for the effects due to Earth's rotation around his axis, Earth's motion respect to Earth-Moon and Sun barycenters and motion respect the Local Standard of Rest. This value depends on the coordinates of observed star and observatory, time and date of the observation.

3.10 Computation of the Stokes parameters

After the data reduction of each exposures, Stokes parameters and null spectrum are computed following Eq. 3.20 and Eq. 3.22.

We pointed out how the computation of the Stokes profiles from the ratio method can be done without the correction of the flat field. This is because its effects are eliminated by the ratio of the spectra. Flat correction is necessary for the computation of Stokes I.

In order to compute Stokes I, we first computed the ratios:

$$\begin{aligned} boa1 &= \frac{i_{1,\parallel}}{i_{2,\parallel}} \\ boa2 &= \frac{i_{2,\perp}}{i_{1,\perp}} \end{aligned} \tag{3.28}$$

Then we fitted their continuum, called rat1 and rat2, in order to add the intensity of the spectra with a common level:

$$\mathrm{I} = \frac{1}{2}\left(\frac{\mathrm{i}_{1,\parallel}}{\mathrm{rat1}} + \mathrm{i}_{2,\parallel} + \frac{\mathrm{i}_{2,\perp}}{\mathrm{rat2}} + \mathrm{i}_{1,\perp}\right) \tag{3.29}$$

CHAPTER 4

COSSAM

Modern high resolution spectropolarimeters allowed the detection of magnetic fields in almost all the stellar evolutionary stages. In this context, theoretical models of polarized light have become important in order to interpret the results and to understand the physics of the emitting sources.

Computation of theoretical Stokes profiles is a complicated issue. It includes all the difficulties of the calculation of synthetic unpolarized spectra, such as the knowledge of atomic information, non-LTE effects and opacities calculation; in addition, it involves complications related to the magnetic field and to the description of polarization, such as the parametrization of the magnetic field and the knowledge of additional atomic data, like the Landé factors (Wade et al., 2001).

This chapter is devoted to the description of the code "Codice per la Sintesi Spettrale nelle Atmosfere Magnetiche" (COSSAM), which was used in order to compute synthetic spectra in circular and linear polarized light in the Stokes parametrisation.

An application of COSSAM for the measurement of chemical elements of open clusters is reported in Appendix A.

4.1 Radiative transfer for polarized radiation

The problem of the computation of synthetic Stokes profile in a stellar magnetic atmosphere requires the solution of a set of linear differential equations. In this section,

we derived the Radiative transfer equations for polarized radiation, following Landi Degl'Innocenti (1992).

The generation and the transfer of polarized radiation is a very complicated issue, that involves quantum mechanics and plasma description of the stellar atmosphere. For simplicity, a semi classical derivation of the transfer equation is presented, using only some consideration of quantum mechanics. Classically, the properties of the propagation of a wave inside a medium are parametrized by the refractive index n. If the medium is anisotropic, the index of refraction depends on the direction of oscillation of the electric field. In this case, it is possible to define three mutually orthogonal unit vectors $\vec{u}_\alpha(\alpha = 1,2,3)$ related to the component of the electric field along the vector $\vec{u}$ propagates with a different value of n_α of the index of refraction:

$$\vec{E}(\vec{r},t) = \sum_\alpha \epsilon_\alpha \vec{u}_\alpha e^{2\pi i \frac{\nu}{c}(n_\alpha \vec{r}\cdot\vec{\Omega} - ct)} \tag{4.1}$$

where ϵ_α are constants and where the unit vectors $\vec{u}_\alpha$ are such that $\vec{u}^*_\alpha \cdot \vec{u}_\beta = \delta_{\alpha\beta}$

As settled in Eq. 2.8, the Stokes parameters are related to the electric field along two orthogonal unit vectors ($\vec{e}_1$ and $\vec{e}_2$) perpendicular to the direction of propagation:

$$\vec{E}(\vec{r},t) = \sum_k \epsilon_k(\vec{r},t)\vec{\epsilon}_k \tag{4.2}$$

Using Eq. 4.1, it is possible to write:

$$\sum_k \epsilon_k(\vec{r},t)\vec{\epsilon}_k = \sum_\alpha \epsilon_\alpha \vec{u}_\alpha e^{2\pi i \frac{\nu}{c}(n_\alpha \vec{r}\cdot\vec{\Omega} - ct)} \tag{4.3}$$

taking the scalar product between Eq. 4.3 and $\vec{e}_j$:

$$\epsilon_j(\vec{r},t) = \sum_\alpha \epsilon_\alpha C_{\alpha j} e^{2\pi i \frac{\nu}{c}(n_\alpha \vec{r}\cdot\vec{\Omega} - ct)} \tag{4.4}$$

and $\vec{u}^*_\beta$:

$$\sum_k C^*_{\beta k} \epsilon_k(\vec{r},t) = \epsilon_\beta e^{2\pi i \frac{\nu}{c}(n_\alpha \vec{r}\cdot\vec{\Omega} - ct)} \tag{4.5}$$

where C_{ij} is the cosine director $C_{\alpha j} = \vec{u}_\alpha \cdot \vec{\epsilon}_j$.

Deriving Eq. 4.4 respect to the coordinate $s = \vec{r}\cdot\vec{\Omega}$:

$$\frac{d\epsilon_j(s,t)}{ds} = 2\pi i \frac{\nu}{c} \sum_\alpha \epsilon_\alpha n_\alpha C_{\alpha j} e^{2\pi i \frac{\nu}{c}(n_\alpha \vec{r}\cdot\vec{\Omega} - ct)} \tag{4.6}$$

where:

$$G_{jk} = -2\pi i \frac{\nu}{c} \sum_\alpha n_\alpha C_{\alpha j} C^*_{\alpha k} \tag{4.7}$$

it is possible to obtain:

$$\frac{\mathrm{d}\epsilon_{\mathrm{j}}(\mathrm{s},\mathrm{t})}{\mathrm{ds}} = -\sum_{\mathrm{k}} \mathrm{G}_{\mathrm{jk}}\epsilon_{\mathrm{k}}(\mathrm{s},\mathrm{t}) \tag{4.8}$$

that is related to the *transfer equation*:

$$\frac{\mathrm{d}}{\mathrm{ds}}\mathrm{I}_{\mathrm{jk}} = \frac{\mathrm{d}}{\mathrm{ds}}\left\langle \epsilon_{\mathrm{j}}^{*}\epsilon_{\mathrm{k}} \right\rangle = \sum_{\mathrm{l}} (\mathrm{G}_{\mathrm{jl}}^{*}\mathrm{I}_{\mathrm{lk}} + \mathrm{G}_{\mathrm{kl}}\mathrm{I}_{\mathrm{jl}}) \tag{4.9}$$

It is possible to rewrite Eq. 4.8 as:

$$\begin{aligned}
\tfrac{d}{ds}I_{11} &= -[(G_{11}^{*}+G_{11})I_{11} + G_{12}^{*}I_{12} + G_{12}I_{12}] \\
\tfrac{d}{ds}I_{22} &= -[(G_{22}^{*}+G_{22})I_{22} + G_{21}^{*}I_{12} + G_{21}I_{12}] \\
\tfrac{d}{ds}I_{12} &= -[(G_{11}^{*}+G_{22})I_{12} + G_{12}^{*}I_{22} + G_{21}I_{11}] \\
\tfrac{d}{ds}I_{21} &= -[(G_{22}^{*}+G_{11})I_{11} + G_{21}^{*}I_{11} + G_{12}I_{22}]
\end{aligned} \tag{4.10}$$

reminding Eq. 2.17 and Eq. 2.18, one gets:

$$\frac{\mathrm{d}}{\mathrm{ds}}\begin{pmatrix} I \\ Q \\ U \\ V \end{pmatrix} = \begin{pmatrix} \eta_I & \eta_Q & \eta_U & \eta_V \\ \eta_Q & \eta_I & \rho_Q & -\rho_U \\ \eta_U & -\rho_V & \eta_I & \rho_Q \\ \eta_V & \rho_U & -\rho_Q & \eta_I \end{pmatrix}\begin{pmatrix} I \\ Q \\ U \\ V \end{pmatrix} \tag{4.11}$$

with the positions:

$$\begin{aligned}
\eta_I &= Re(G_{11}+G_{22}) & & \\
\eta_Q &= Re(G_{11}-G_{22}) & \rho_Q &= -Im(G_{11}-G_{22}) \\
\eta_U &= Re(G_{12}+G_{21}) & \rho_U &= -Im(G_{12}+G_{21}) \\
\eta_V &= Im(G_{12}-G_{21}) & \rho_V &= Re(G_{12}-G_{21})
\end{aligned} \tag{4.12}$$

Eq. 4.11 can be rewritten, decomposing the matrix into a diagonal matrix and two off-diagonal matrices:

(4.13)

$$\frac{\mathrm{d}}{\mathrm{ds}}\begin{pmatrix} I \\ Q \\ U \\ V \end{pmatrix} = -\begin{pmatrix} \eta_I & 0 & 0 & 0 \\ 0 & \eta_I & 0 & 0 \\ 0 & 0 & \eta_I & 0 \\ 0 & 0 & 0 & \eta_I \end{pmatrix} - \begin{pmatrix} 0 & \eta_Q & \eta_U & \eta_V \\ \eta_Q & 0 & 0 & 0 \\ \eta_U & 0 & 0 & 0 \\ \eta_V & 0 & 0 & 0 \end{pmatrix} - \begin{pmatrix} 0 & 0 & 0 & 0 \\ 0 & 0 & \rho_V & -\rho_U \\ 0 & -\rho_V & 0 & \rho_Q \\ 0 & \rho_U & -\rho_Q & 0 \end{pmatrix}\begin{pmatrix} I \\ Q \\ U \\ V \end{pmatrix}$$

The first diagonal matrix is called *absorption matrix* and it is proportional to η_{I}, the second symmetrical matrix is called *dichroism matrix* and the third one is an antisymmetric matrix called *dispersion matrix*.

The parameters of the matrix can be written as function of the absorption profiles ϕ_p, ϕ_r, ϕ_b and dispersion profiles ψ_{p},ψ_{b} and ψ_{r}.

Considering the case when the atoms follow a Maxwell distribution of the velocities, with an rms ω_{T} and a bulk velocity of the medium along the line of sight ω_{M}, it is possible to write:

$$\begin{aligned} \phi_p &= \tfrac{1}{\sqrt{\pi}}\tfrac{1}{\Delta\nu_D} H(\nu-\nu_m,a)\,;\, \phi_p = \tfrac{1}{\sqrt{\pi}}\tfrac{1}{\Delta\nu_D} L(\nu-\nu_M,a) \\ \phi_b &= \tfrac{1}{\sqrt{\pi}}\tfrac{1}{\Delta\nu_D} H(\nu-\nu_m+\nu_B,a)\,;\, \phi_b = \tfrac{1}{\sqrt{\pi}}\tfrac{1}{\Delta\nu_D} L(\nu-\nu_M+\nu_B,a) \\ \phi_r &= \tfrac{1}{\sqrt{\pi}}\tfrac{1}{\Delta\nu_D} H(\nu-\nu_m-\nu_B,a)\,;\, \phi_r = \tfrac{1}{\sqrt{\pi}}\tfrac{1}{\Delta\nu_D} L(\nu-\nu_M-\nu_B,a) \end{aligned} \tag{4.14}$$

where H and L are respectively the Voigt function and the associated dispersion function:

$$\begin{aligned} H(v,a) &= \tfrac{a}{\pi}\int e^{-y^2}\tfrac{1}{(v-y)^2+a^2}dy \\ L(v,a) &= \tfrac{1}{\pi}\int e^{-y^2}\tfrac{v-y}{(v-y)^2+a^2}dy \end{aligned} \tag{4.15}$$

with:

$$\begin{aligned} \Delta\nu_D &= \nu_0\tfrac{\omega_T}{c}\,;\, \Delta\lambda_D = \lambda_0\tfrac{\omega_T}{c} \\ v &= \tfrac{\nu_0-\nu_D}{\Delta\nu_D} = \tfrac{\lambda-\lambda_0}{\Delta\lambda_D}\,;\, a = \tfrac{\Gamma}{\Delta\nu_D} \end{aligned} \tag{4.16}$$

As stated in Sect. 2.2, any level, characterized with angular momentum quantum number J, is split by a magnetic field in 2J+1 sublevels with magnetic quantum number M, which assumes all values from -J to J in integer steps. For this reason, the quantities ϕ_{p}, ϕ_{r}, ϕ_{b}, ψ_{p},ψ_{b} and ψ_{r}, can be replaced by a sum of as many absorption or dispersion profiles as the number of components π and σ centred at the shift $\nu_{\mathrm{MM'}}$ and weighted by $\mathrm{S_{MM'}}$:

$$\begin{aligned} \nu_{MM'} &= (gM - g'M')\nu_L \\ S_{MM'} &= 3\begin{pmatrix} J & J' & 1 \\ M & -M' & M'-M \end{pmatrix}^2 \end{aligned} \tag{4.17}$$

where J and M are related to the upper level and J′ and M′ to the lower. For instance:

$$\begin{aligned} \phi_b &= \textstyle\sum_{M-M'=1} S_{MM'}\tfrac{1}{\pi}\tfrac{\Gamma}{(\nu_0+\nu_{MM'}-\nu)^2+\Gamma^2} \\ \psi_b &= \textstyle\sum_{M-M'=1} S_{MM'}\tfrac{1}{\pi}\tfrac{\nu_0+\nu_{MM'}-\nu}{(\nu_0+\nu_{MM'}-\nu)^2+\Gamma^2} \end{aligned} \tag{4.18}$$

The expression for ψ_{p} and ϕ_{p} are equal for $\mathrm{M}-\mathrm{M}' = 0$, while in the case of ψ_{r} and ϕ_{r} we have $\mathrm{M}-\mathrm{M}' = -1$.

In the hypothesis of *Local Thermodynamic Equilibrium* (LTE), the transfer equation can be written as:

$$\frac{\mathrm{d}}{\mathrm{d}\tau}\begin{pmatrix} I \\ Q \\ U \\ V \end{pmatrix} = \begin{pmatrix} \eta_I & \eta_Q & \eta_U & \eta_V \\ \eta_Q & \eta_I & \rho_Q & -\rho_U \\ \eta_U & -\rho_V & \eta_I & \rho_Q \\ \eta_V & \rho_U & -\rho_Q & \eta_I \end{pmatrix}\begin{pmatrix} I - B_T \\ Q \\ U \\ V \end{pmatrix} \tag{4.19}$$

where $\mathrm{d}\tau = -\kappa_\mathrm{c}\,\mathrm{ds}$ is the optical depth measured in the continuum close to the line, and where:

$$\begin{aligned} \eta_I &= 1 + \tfrac{\eta_0}{2}\left[\phi_p sin^2\theta + \tfrac{\phi_b+\phi_r}{2}\left(1+cos^2\theta\right)\right] \\ \eta_Q &= \tfrac{\eta_0}{2}\left[\phi_p - \tfrac{\phi_b+\phi_r}{2}\right] sin^2\theta\, cos2\chi \qquad & \rho_Q &= \tfrac{\eta_0}{2}\left[\psi_p - \tfrac{\psi_b+\psi_r}{2}\right] sin^2\theta\, cos2\chi \\ \eta_U &= \tfrac{\eta_0}{2}\left[\phi_p - \tfrac{\phi_b+\phi_r}{2}\right] sin^2\theta\, sin2\chi \qquad & \rho_U &= \tfrac{\eta_0}{2}\left[\psi_p - \tfrac{\psi_b+\psi_r}{2}\right] sin^2\theta\, sin2\chi \\ \eta_V &= \tfrac{\eta_0}{2}\left[\phi_r - \phi_b\right] cos\theta \qquad & \rho_V &= \tfrac{\eta_0}{2}\left[\psi_r - \psi_b\right] cos\theta \end{aligned} \tag{4.20}$$

θ and χ are showed in Fig. 2.5 and η_0 is given by:

$$\eta_0 = \frac{\kappa_\mathrm{l}}{\kappa_\mathrm{c}} = \frac{\pi\,\mathrm{e}_0^2\mathrm{fN}}{\mathrm{m\,c}\,\kappa_\mathrm{c}} \tag{4.21}$$

4.2 ADA for astrophysical computation

COSSAM code is written in the programming language ADA [1], which is a powerful object oriented language designed for the UNITED STATES DEPARTMENT OF DEFENSE (DOD) and used also by important brands such as AIRBUS and BOEING.

COSSAM descends from the FORTRAN code ADRS3 (Chmielewski, 1979), that was modified by Stift (1985) in order to compute theoretical Stokes I and Stokes V for rotating and pulsating magnetic stars. ADRS3 originate in turn by the ALGOL60 code ANALYSE65 (Baschek et al., 1966).

The conversion from FORTRAN to ADA happened in 1993 thanks to the Stift's student G. Könighofer. It was due to the necessities of the computation of heavy blended spectra of CP2 stars, for a diagnostic of the linear polarization (Landolfi et al., 1993). This problem requested changes that would require an almost rewrite of the FORTRAN code, which was not easily editable.

The choose of ADA has related to the advantage of easy modification thanks to the possibility of encapsulating in packages the big routines, which can be used in different

[1] `http://www.adaic.org/`

programs. Another important characteristic of ADA was the possibility to perform easily parallelization, that needs only 20 expressions in 3500 line of code (Stift, 1998b). Additionally, the use of protected objects allows a safer way for the synchronization.

Other informations about ADA and COSSAM can be found in Stift & Dubois (1998) and Stift (1998a).

4.3 Numerical solver of Stokes profiles

Numerical solvers for the radiative transfer equation are:

- Zeeman Feautrier (Auer et al., 1977; Alecian & Stift, 2004)
- Diagonal Element Lambda Iteration (DELO) (Rees et al., 1989; Socas-Navarro et al., 2000)
- Matrix Attenuation Operator (Landi Degl'Innocenti, 1987)

The first two are implemented in COSSAM.

Zeeman Feautrier is the most stable and accurate method. It is based on the extension to the polarized case (Auer et al., 1977) of the Feautrier solver for radiative transfer unpolarized spectra. This method is based on the work of Feautrier (1964), who showed how the first-order radiative transfer equation is equivalent to a second-order differential equation, splitting the intensity into ingoing and outgoing intensity.

Feautrier methods can be in principle applied only for symmetric profiles, in the case of macroscopic velocity; for this reason, they can not be applied in case of blends. This extension was made in the version of Alecian & Stift (2004), which is numerically implemented in COSSAM.

DELO methods represent an easiest and faster alternative to Zeeman Feautrier, in the cases where extreme accuracy is not required.

Tests performed by Stift (1998b) revealed that the results of Zeeman Feautrier solver are more accurate respect to DELO, of a factor up of 5 when blends are present.

4.4 Cossam extensions

The simple version of COSSAM allows the computation of Stokes profiles in the case of centered and de-centered dipolar large scale magnetic field.

The code was extended to the case of a spotted stellar atmosphere by Stift et al. (2012). This version, called COSSAMMULTI, allows to takes into account up to 10 spots with different model atmosphere or to compute Stokes profiles dividing the star up to 90 rings.

During the PhD, we worked to an extension of COSSAM, in order to compute Stokes parameters for a magnetic field described as the sum of spherical harmonics. This work was performed in a direct collaboration with Prof. Martin Stift.

We implemented the spherical harmonics parametrisation of the geomagnetic field used by Yokoyama & Yukutake (1991), which is given by:

$$\begin{aligned} B_r(\phi_i,\theta_i) &= \sum_{l=1}^{\infty}\sum_{m=0}^{l}\{(l+1)[g_l^m\, cos(m\phi_i)+h_l^m\, sin(m\phi_i)]\}P_n^m(\theta_i) \\ B_\theta(\phi_i,\theta_i) &= -\sum_{l=1}^{\infty}\sum_{m=0}^{l}\{[g_l^m\, cos(m\phi_i)+h_l^m\, sin(m\phi_i)]\}\frac{dP_n^m(\theta_i)}{d\theta_i} \\ B_\phi(\phi_i,\theta_i) &= \frac{1}{sin(\theta_i)}\sum_{l=1}^{\infty}\sum_{m=0}^{l} m\,\{(l+1)[g_l^m\, sin(m\phi_i)-h_l^m\, cos(m\phi_i)]\}P_n^m(\theta_i) \end{aligned} \tag{4.22}$$

where B_r, B_θ and B_ϕ are respectively the radial, meridional and azimuthal components of the magnetic field, $P_n^m(\theta_i)$ are the spherical harmonics (Press et al., 1992), the radius is taken equal to the unity and h_l and g_l are the so called *Gauss coefficients* (Blakely, 1995), in the case of internal source of the magnetic field.

The total magnetic field and the orientation angle can be written as:

$$\begin{aligned} B_{tot} &= \sqrt{B_r^2+B_\theta^2+B_\phi^2} \\ \gamma &= arccos\left(\frac{B_{rad}}{B_{tot}}\right) \end{aligned} \tag{4.23}$$

For instance, in this notation, the dipole moment is connected to the Gauss coefficients by:

$$m = \sqrt{m_x^2+m_y^2+m_z^2} = \frac{4\pi}{\mu_0}\sqrt{\left(g_1^0\right)^2+\left(g_1^1\right)^2+\left(h_1^1\right)^2} \tag{4.24}$$

We reported in Fig. 4.1, Fig. 4.2 and Fig. 4.3 examples of magnetic field configurations with l = 1, l = 2 and l = 3.

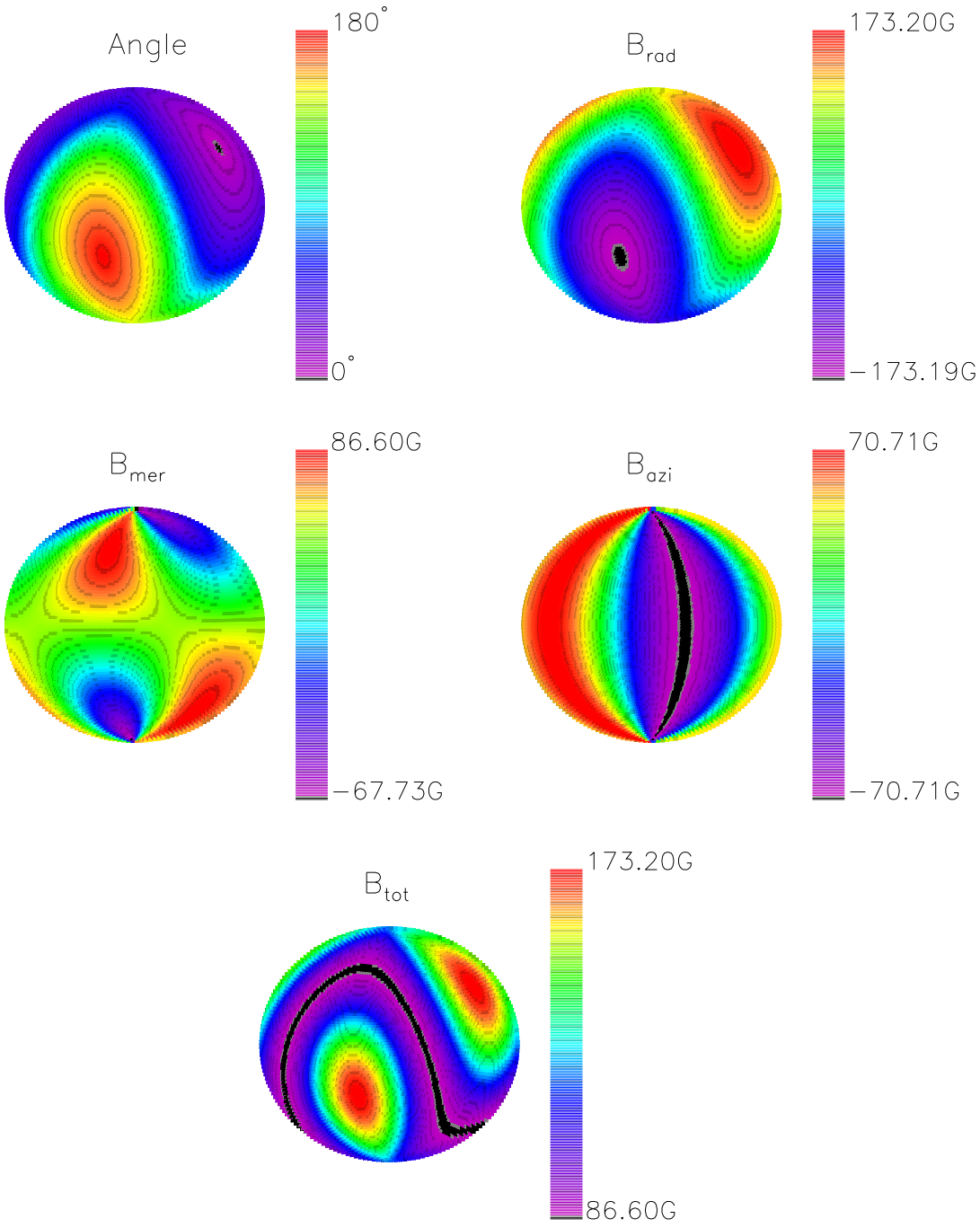

Figure 4.1: Polynomial magnetic field configuration with l = 1.

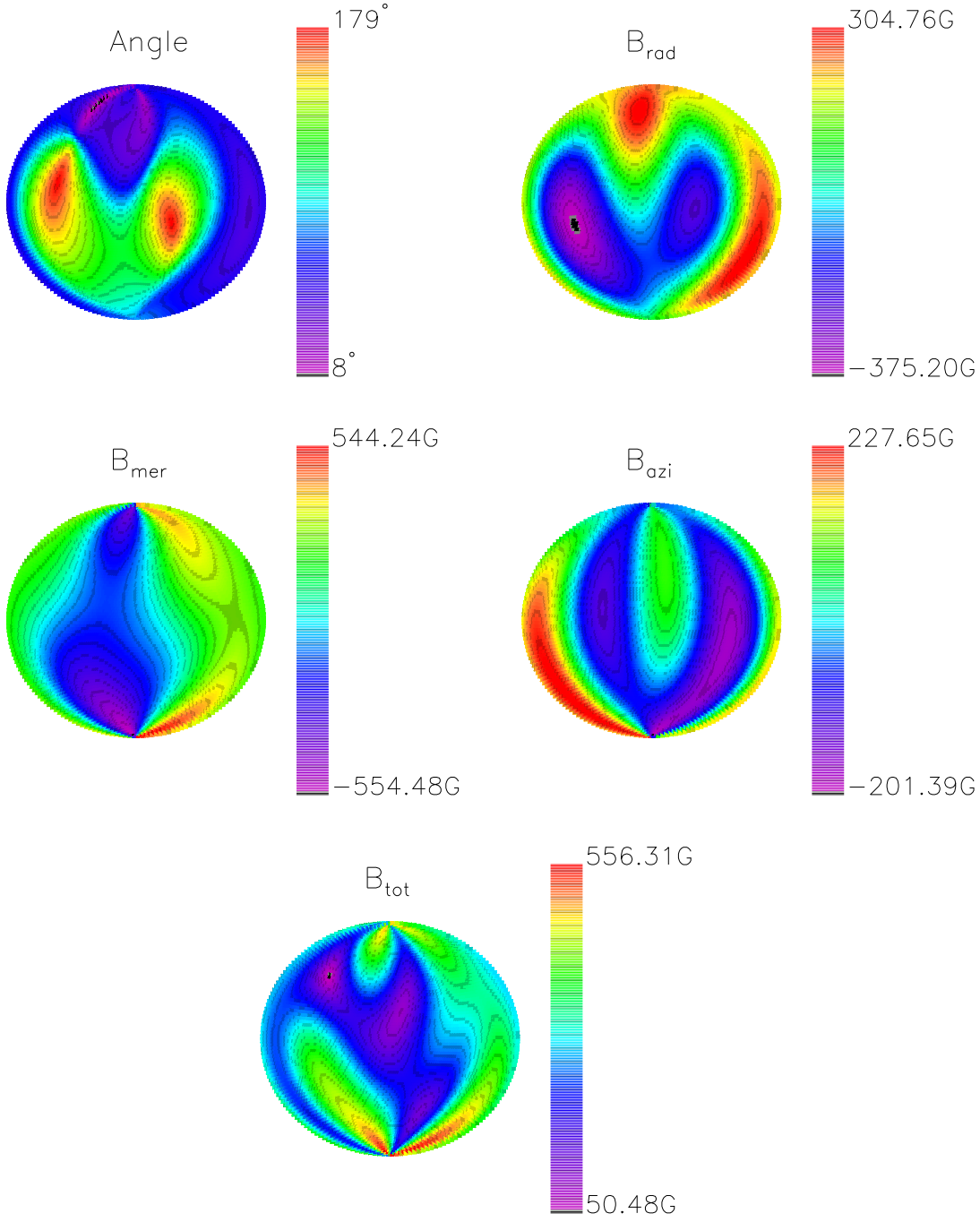

Figure 4.2: Polynomial magnetic field configuration with l = 2.

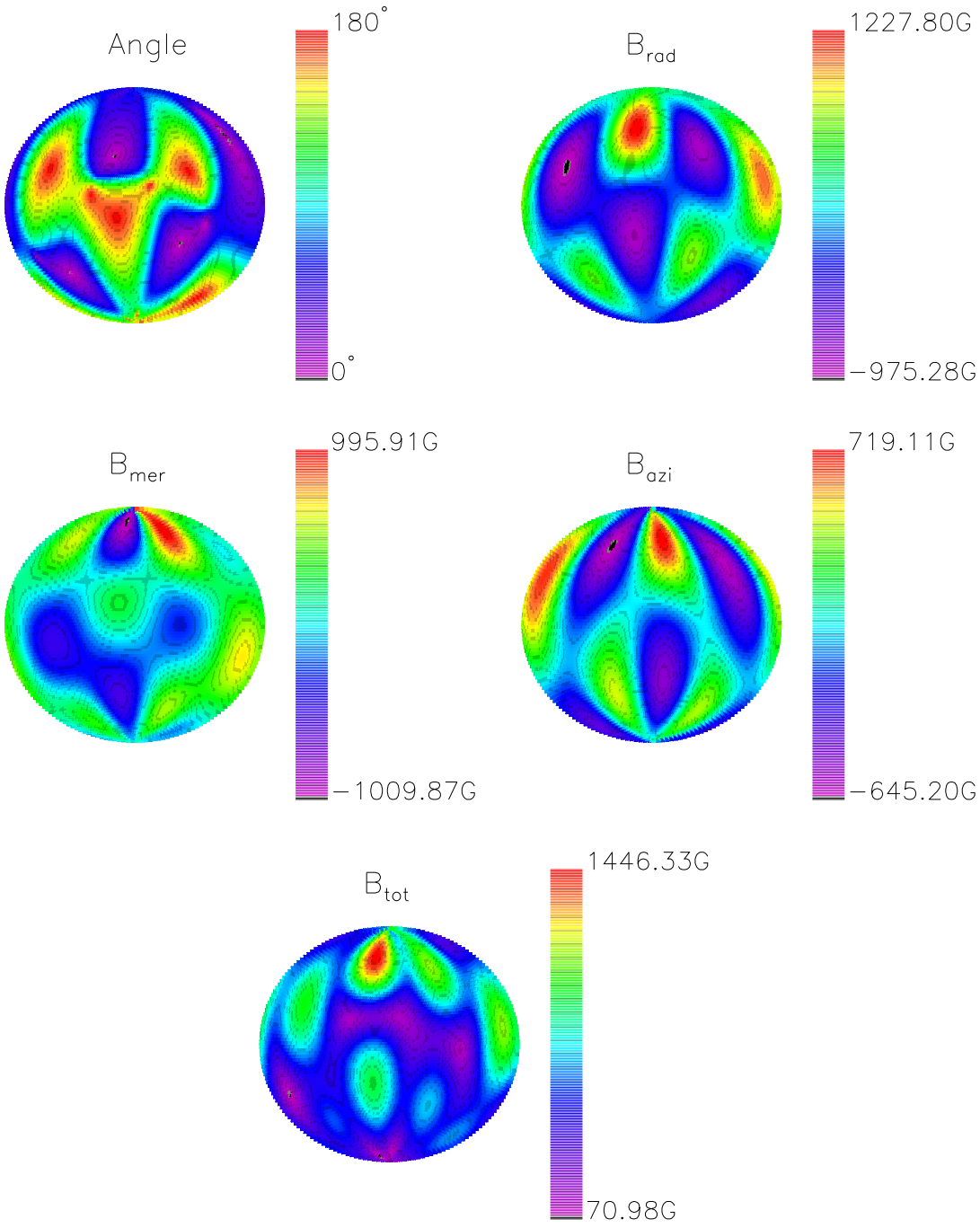

Figure 4.3: Polynomial magnetic field configuration with l = 3.

CHAPTER 5

THE TRASVERSAL MAGNETIC FIELD OF βCRB

Stars in the upper main sequence, at T_{eff} above 6600K, can present peculiarities on their spectra and on their photometric variations (Kurtz & Martinez, 2000). Among these, a group presents large scale magnetic fields, with strength values from hundreds to tens of thousands Gauss. Following Preston (1974), these stars are called magnetic CP2 stars. They are characterized by common properties, such as:

- strong anomalous overabundances of the Fe-peak, rare earth and lanthanide elements (up to a factor of 10^5), considered to be caused by magnetic diffusion. In particular, radiative levitation can push to the surface these elements, because they have many absorption lines near the flux maximum, at the temperature of the radiative zone (Kurtz & Martinez, 2000);

- very slow rotation, $v \sin i < 125\,km\,s^{-1}$, considered to be the result of magnetic braking;

- magnetic fields that vary on a time-scale from days to decades, corresponding to the rotational period;

- brightnesses that vary in correlation with the magnetic and spectrum variations.

Citing Bidelman (1967), magnetic CP2 stars are:

"stars of unusual spectrum are doing unusual thing"

The prototype is the bright star α^2 CVn (M_V=2.88), where peculiarities were reported since the work of Maury & Pickering (1897). A period of 5.5 d for the spectral variation of this object was provided by Belopolsky (1913), that explained it supposing the presence of a gaseous satellite or ring, with a condensation of matter at one point, surrounding the star.

The first detection of magnetic fields in CP2 stars was reported by Babcock (1947), on the star 78 Vir.

The aim of this chapter is to take advantage of the measurement of linear polarisation in order to estimate the transversal component of the magnetic field and the orientation of the rotational axis of magnetic Ap stars. The results of this chapter are published in Leone et al. (2017).

5.1 Oblique rotator model

In order to model spectral and magnetic field variations, Babcock (1949) introduced the *rigid rotator model*, which was later extended by Stibbs (1950) into the *oblique rotator model*.

The idea at the base of the models is that the magnetic axis of the star (assumed dipolar) is tilted respect to the rotation axis, in analogy of the solar and Earth cases. Moreover, the distributions of chemical elements and the magnetic field are assumed to be frozen on the star, in a non symmetrical configuration respect to the rotation axis (Bagnulo et al., 2001). In this way, as the star rotates, different line shape and polarization are showed to the observer, caused by different aspects of the chemical abundances and magnetic field on the visible stellar hemisphere. This model is supported by the observational fact that the variability corresponds to the rotational period of the star (Fig. 5.1).

Stibbs (1950) showed that the surface integrated field, produced by a magnetic dipole located at the center of the star, can be represented considering the magnetic axis inclined by an angle β respect to the rotational axis, inclined in turn of an angle i respect to the line of sight. This quantity is given by:

$$\delta(\alpha, \mathrm{u}) = \mathrm{a}\,\frac{\mathrm{M}\cos\alpha}{\mathrm{I_0\,R^3}}\,\frac{15+\mathrm{u}}{3-\mathrm{u}} \tag{5.1}$$

where u is the coefficient of limb darkening, M is the moment of the magnetic dipole and:

$$\cos\alpha = \cos(\mathrm{i})\cos(\beta) + \sin(\mathrm{i})\sin(\beta)\cos(\theta) \tag{5.2}$$

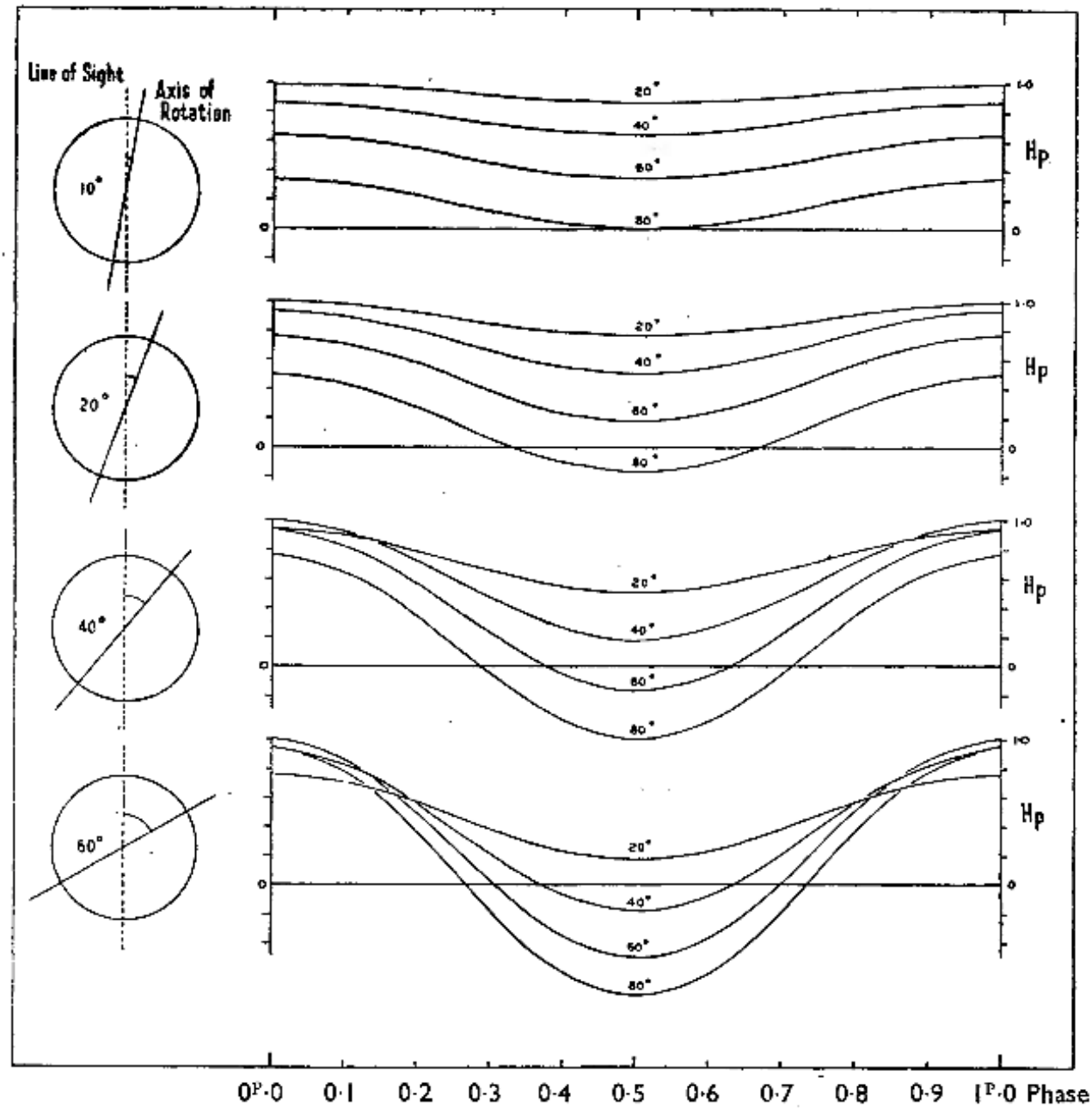

Figure 5.1: Magnetic field variations described by the oblique rotator model. Four curves relative to co-latitude of 20°, 40°, 60°and 80°are shown for each inclination respect to the line of sigh (Stibbs, 1950)

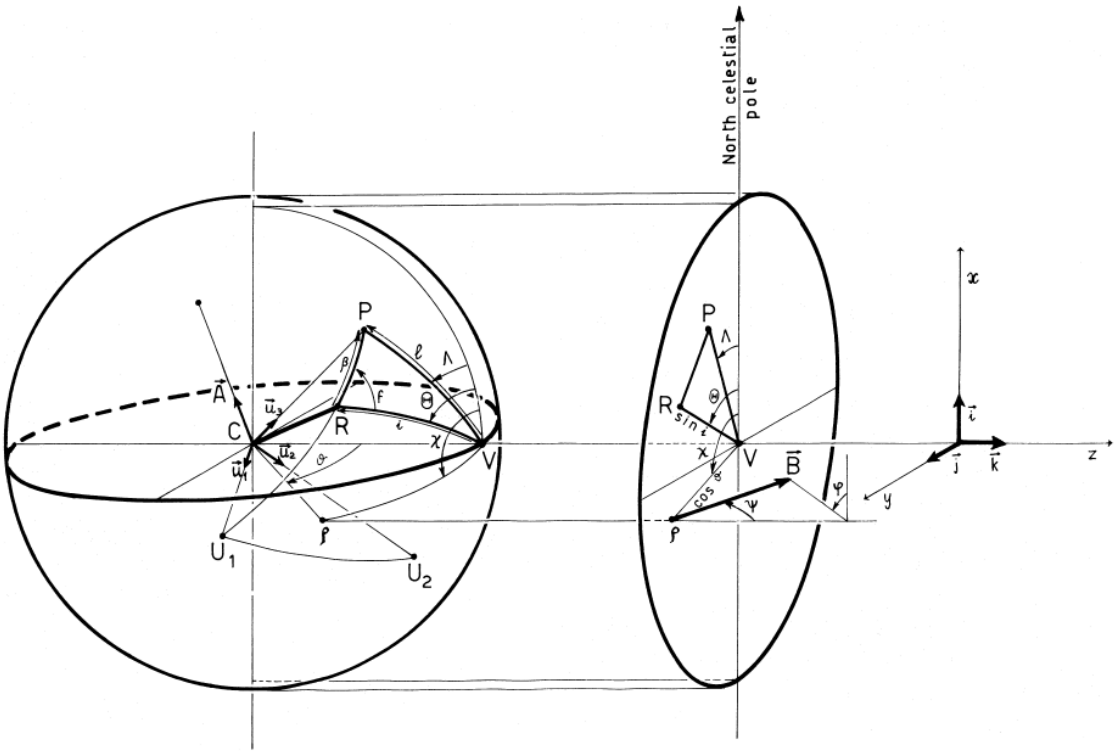

Figure 5.2: Geometry of a rotating magnetic star following Landi Degl'Innocenti et al. (1981).

where θ is an angle related to the rotational phase. The geometrical model of the oblique rotator is reported in Fig. 5.2.

In the case of rigid rotator, it is possible to estimate the stellar radius from (Wolff, 1983):

$$R \sin i = \frac{P v \sin i}{50.6} \tag{5.3}$$

where R is expressed in units of the solar radius, P is the period in days and v is the equatorial rotation velocity in km s^{-1}.

5.2 Integrated quantities

Observations of magnetic fields of magnetic early type stars allow the measurement of quantities integrated over the visible stellar hemisphere. They are the manifestation of the Zeeman effect and its polarimetric properties, described in Sect. 2.2.

5.2.1 Effective magnetic field

The first integrated quantities, called effective field strength B_{eff}, is related to the component of the magnetic field in the line of sight, averaged over the visible hemisphere (Babcock & Babcock, 1958). It is given by:

$$B_{eff} = \frac{\int\int B_\zeta I \, d\xi \, d\eta}{\int\int I \, d\xi \, d\eta} \tag{5.4}$$

where B_ζ is the magnetic component in the line of sight, I is the surface brightness and $d\xi \, d\eta$ are the surface elements of the stellar disk.

The system (ξ, η, ζ) is oriented so that ζ is parallel to the line of sight. Transformation equations into a system (x,y,z), such that z is parallel to the magnetic axis and $x^2 + y^2 + z^2 = 1$, can be written as:

$$x = \zeta \sin i + \xi \cos i \quad y = \eta \quad z = \zeta \cos i - \xi \sin i \tag{5.5}$$

Introducing the limb darkening effects, given by:

$$I = 1 - u + u\zeta \tag{5.6}$$

the integration over ξ and η returns the relations found by Schwarzschild (1950), which are given by:

$$\begin{array}{ll} B_{eff} = \frac{15+u}{15-5u} \frac{B_p}{4} \cos i & dipole \\ B_{eff} = \frac{u}{3-u} \frac{B_p}{4} \frac{1+3\cos 2i}{4} & quadrupole \end{array} \tag{5.7}$$

It is possible to note that the effective field depends on the inclination i with a simple harmonic shape.

In the case of oblique dipole rotator, Stibbs (1950) showed that Eq. 5.7 can be written as:

$$B_{eff} = \frac{1}{20} \frac{15+u}{3-u} B_p \left[\cos\beta \cos i + \sin\beta \sin i \cos\left(\frac{2\pi t}{P}\right) \right] \tag{5.8}$$

where B_p is the field strength at the pole.

5.2.2 Magnetic field strength

In the case when the magnetic field is strong and the rotation slow enough to observe resolved Zeeman patterns, magnetic field strength can be measured directly from the

Zeeman splitting, which is given by the average displacement of the σ components from λ_0:

$$\Delta\lambda = \pm 4.67\,10^{-13}\,\mathrm{z\,B}\,\lambda_0^2 \tag{5.9}$$

Examples of stars which show Zeeman patterns are HD215441 (Babcock, 1960), 53 Cam (Preston, 1969) and β CrB (Wolff & Wolff, 1970).

Preston (1971) showed that Zeeman splitting is visible when the splitting $\Delta\lambda$ is greater than the Doppler (or instrumental) width $\Delta\lambda_d$. These cases are characterised by:

$$\frac{1.4\times 10^{-4}\lambda \mathrm{Bz}}{\mathrm{v}} > 1 \tag{5.10}$$

where B is expressed in kG, λ in Angstrom, the Doppler width v in km s^{-1} and z is the mean displacement of the σ components.

It is possible to note that Eq. 5.9 does not depend on the line of sight. For this reason, it is possible to define a scalar magnetic field, averaged over the visible hemisphere of the star, following Wolff (1983):

$$\mathrm{B_s} = \frac{\int |\mathrm{B}|\,\mathrm{I\,dA}}{\int \mathrm{I\,dA}} \tag{5.11}$$

In the case of dipolar field, Preston (1971) showed that $\mathrm{B_s} \approx 0.80\mathrm{B_p}$ if the star is viewed pole on or $\mathrm{B_s} \approx 0.64\mathrm{B_p}$ in the equator-on cases.

5.2.3 Transverse magnetic field

Despite the huge literature on stellar magnetic field measurement, only the longitudinal magnetic field (related to Stokes V) and the field strength (related to the Zeeman splitting) are usually analyzed.

Linear polarisation on magnetic early type stars was first detected by Kemp & Wolstencroft (1974) in 53 Cam and α^2 CVn.

Theoretical modelling started with the work of Landi Degl'Innocenti et al. (1981), who computed the net flux of linear polarization in broad spectral regions:

$$\begin{aligned} F_Q &= R_0 \int_0^{2\pi} d\chi \int_0^1 d\mu\,\mu^2 \Pi(v_H,\Psi)\cos\left\{2\left[\phi+\Phi(v_H,\psi\right]\right\}\sum_{lines} W_0 \\ F_U &= R_0 \int_0^{2\pi} d\chi \int_0^1 d\mu\,\mu^2 \Pi(v_H,\Psi)\sin\left\{2\left[\phi+\Phi(v_H,\psi\right]\right\}\sum_{lines} W_0 \end{aligned} \tag{5.12}$$

where ϕ and ψ are the angles that specifies the magnetic field (Fig. 5.2), $\mathrm{W_0}$ is the total amount of radiation, Π and Φ are respectively the fractional linear polarization and the

direction of the maximum of the polarization. These quantities, defined by Calamai et al. (1975), can be written as:

$$\Pi = \frac{\sqrt{(\int Q\,dv)^2+(\int U\,dv)^2}}{W} \qquad \Phi = \frac{1}{2} arctg\left(\frac{\int U\,dv}{\int Q\,dv}\right) + \Phi_0 \tag{5.13}$$

Using Eq. 4.16, it is possible to write v_H as:

$$v_H = \frac{e_0 g_{eff} B}{4\pi m_e c\,\Delta v_D} \tag{5.14}$$

The analytical evaluation of Eq. 5.13 is a complex issue. The problem was simplified in the case weak field approximation by Landolfi et al. (1993), that introduced the so called *canonical model*. In this case, it is possible to describe analytically the linear polarization, in the case of dipolar magnetic field, through (Bagnulo et al., 1995):

$$P_Q = k\,\sin^2(l(t))\,[\cos(2\Lambda(t)) + \epsilon\,\cos(l(t))\,\sin(2\Lambda(t))] \qquad P_U = k\,\sin^2(l(t))\,[\sin(2\Lambda(t)) - \epsilon\,\cos(l(t))\,\sin(2\Lambda(t))] \tag{5.15}$$

where Λ(t) is the angle between the projection of the magnetic field and the north celestial pole and l(t) is the time dependent angle between the line of sight and the magnetic axis (Fig 5.2). k and ϵ are given by:

$$k = \frac{105-17u}{560(3-u)}\frac{\xi}{1-\xi}c_1 B_p^2 \qquad \epsilon = \frac{105-41u}{4(105-17u)}c_2 B_p \tag{5.16}$$

where c_1 and c_2 are constants (Landolfi et al., 1993), ξ is the fraction of the continuum subtracted by the line and B_p is the magnetic field at the positive pole.

5.3 Magnetic field modelling and parametrization

In order to extract information about the magnetic field of early type stars, it is necessary to model the structure of the large scale magnetic field.

First observations showed that the magnetic field topology is basically dipolar. In fact, a large integrated longitudinal field can not be easily produced by a toroidal fields and, in addition, the integrated effects of higher order multipoles are small (Preston, 1971).

In particular, model dependent information about the parameters of the oblique rotator could be extracted from the curves of the magnetic field variations with the rotational period. For instance, Preston (1967) defined the parameter r, which connects the angles β and i with the extremes of variation of B_{eff}:

$$r = \frac{B_{eff}(min)}{B_{eff}(max)} = \frac{\cos\beta\cos i - \sin\beta\sin i}{\cos\beta\cos i + \sin\beta\sin i} = \frac{1-\tan(\beta)\tan(i)}{1+\tan(\beta)\tan(i)} \tag{5.17}$$

these values can be connected to the polar value of the magnetic field by (Borra & Landstreet, 1980):

$$\mathrm{B_{eff}(min,max)} = 0.316\,\mathrm{B_p}\,\cos(\beta \pm \mathrm{i}) \tag{5.18}$$

Mathys (1993) pointed out how dipolar configuration alone is not sufficient to reproduce all the details of the curves and, in particular, models beyond the cylindrical symmetry are needed. Departures from simple dipole are even more evident if shapes and polarisation of spectral lines are considered, instead of integrated quantities such magnetic curves.

Extensions beyond the dipolar configuration were presented by several authors, in terms of polynomial expansion (Deutsch, 1970; Monaghan, 1973), decentred dipole (Stift, 1974, 1975) or multi-polar expansions, such as dipole+quadrupole (Landolfi et al., 1998) or dipole+quadrupole+octupole (Landstreet & Mathys, 2000).

Gregory et al. (2010) showed that the multi-polar expansion of a magnetic field, stopped at the octupolar term, can be written as:

$$\begin{gathered} B_r = \tfrac{2\mu}{r^3}\cos\theta\,; \quad B_\theta = \tfrac{\mu}{r^3}\sin\theta \quad Dipole \\ B_r = \tfrac{3Q}{2r^4}(3\cos^2\theta - 1)\,; \quad B_\theta = \tfrac{3Q}{r^4}\cos\theta\sin\theta \quad Quadrupole \\ B_r = \tfrac{2\Omega}{r^5}(5\cos^5\theta - 3)\cos\theta\,; \quad B_\theta = \tfrac{3\Omega}{2r^5}(5\cos^2\theta - 1)\sin\theta \quad Octupole \end{gathered} \tag{5.19}$$

In order to transform spherical coordinates of Eq. 5.19 into the Cartesian, it is possible to apply the matrix:

$$\begin{bmatrix} A_x \\ A_y \\ A_z \end{bmatrix} = \begin{bmatrix} \sin\theta\cos\phi & \cos\theta\cos\phi & -\sin\phi \\ \sin\theta\sin\phi & \cos\theta\sin\phi & \cos\phi \\ \cos\theta & -\sin\theta & 0 \end{bmatrix} \begin{bmatrix} A_r \\ A_\theta \\ A_\phi \end{bmatrix} \tag{5.20}$$

where:

$$\begin{aligned} x &= r\,\sin\theta\,\cos\phi \\ y &= r\,\sin\theta\,\sin\phi \\ z &= r\,\cos\theta \end{aligned} \tag{5.21}$$

In this way, it is possible to obtain the components of magnetic fields:

$$\begin{aligned} B_x &= 3\mu xz/r^5 \\ B_y &= 3\mu yz/r^5 \qquad dipole \\ B_z &= \mu(3z^2 - r^2)/r^5 \end{aligned} \tag{5.22}$$

$$\begin{aligned} B_x &= \tfrac{3Q}{r^5}(\tfrac{5}{2}\tfrac{z^2}{r^2} - \tfrac{1}{2})x \\ B_y &= \tfrac{3Q}{r^5}(\tfrac{5}{2}\tfrac{z^2}{r^2} - \tfrac{1}{2})y \quad quadrupole \\ B_z &= \tfrac{3Q}{r^5}(\tfrac{5}{2}\tfrac{z^2}{r^2} - 1)z \end{aligned} \tag{5.23}$$

$$\begin{aligned} B_x &= \tfrac{\Omega}{2r^7}(35\tfrac{z^2}{r^2} - 15)xz \\ B_y &= \tfrac{\Omega}{2r^7}(35\tfrac{z^2}{r^2} - 15)yz \qquad octupole \\ B_z &= \tfrac{\Omega}{2r^5}(35\tfrac{z^4}{r^{\cdot 4}} - 30\tfrac{z^2}{r^{\cdot 2}} + 3) \end{aligned} \tag{5.24}$$

In the case $x^2 + y^2 + z^2 = 1$, Eq. 5.22 and Eq. 5.23 agree with the results of the computation of Schwarzschild (1950), which are given by:

$$\begin{array}{lll} B_x = x(\frac{3}{2}z)B_p & B_y = y(\frac{3}{2}z)B_p & B_z = (\frac{3}{2}z^2 - \frac{1}{2})B_p \qquad dipole \\ B_x = x(\frac{5}{2}z^2 - \frac{1}{2})B_p & B_y = y(\frac{5}{2}z^2 - \frac{1}{2})B_p & B_z = z(\frac{5}{2}z^2 - \frac{1}{2})B_p \quad quadrupole \end{array} \tag{5.25}$$

where $B_p = 2\mu/R^3$ is the field strength at the pole and μ is the moment of the magnetic dipole (quadrupole).

5.4 Measurement of the transverse magnetic field

We introduced the possibility to estimate the transverse magnetic field component through Eq. 2.44, obtained in the case of weak field approximation.

We indicated with the quantities S_Q and S_U respectively the slopes of Stokes Q and Stokes U, respect to the second derivative of Stokes I:

$$\begin{aligned} S_Q &= \zeta B_\perp^2 \cos(2\chi) \\ S_U &= \zeta B_\perp^2 \sin(2\chi) \end{aligned} \tag{5.26}$$

with the position $\zeta = -5.45\,10^{-26}\bar{G}\,\lambda^4\,\frac{1}{I}$.

Using Eq. 2.44, it is possible to determine $B_\perp$ and χ through:

$$\begin{aligned} B_\perp &= \sqrt[4]{\frac{S_Q^2 + S_U^2}{\zeta^2}} \\ \chi &= \tfrac{1}{2}\arctan(\tfrac{S_U}{S_Q}) \end{aligned} \tag{5.27}$$

In general, the measurement of the slopes of Eq. 5.26 is complicated for several reasons, such as:

- polarization signals of Stokes Q and Stokes U are usually small and for this reason high S/N observations are needed.

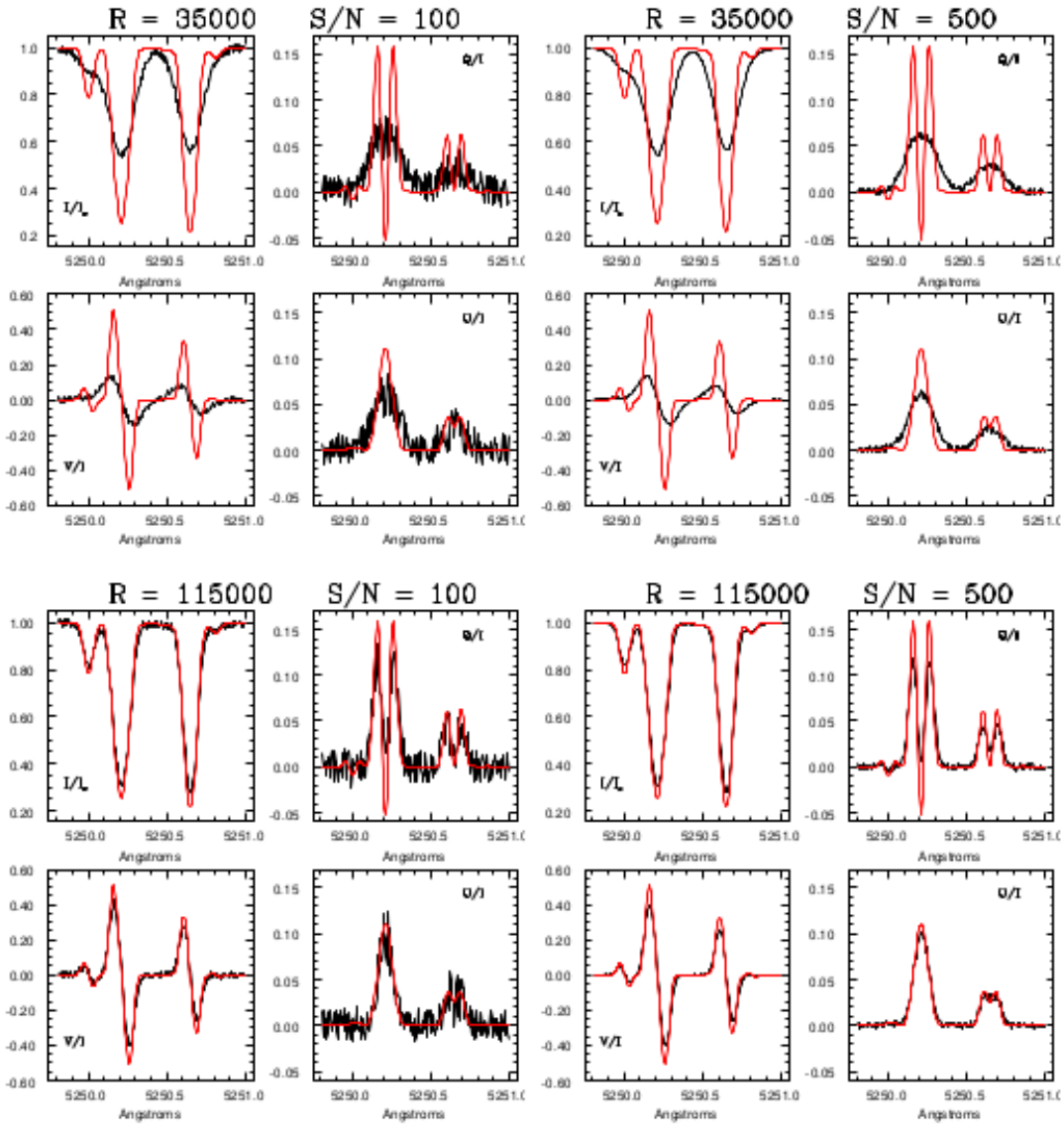

Figure 5.3: Simulated Stokes parameters (red) for an uniform 1 kG magnetic field, as observed at R = 35000 and S/N = 100 (top-left panel), at R = 35000 and S/N = 500 (top-right panel), at R = 115000 and S/N = 100 (bottom-left panel) and R = 115000 and S/N = 500 (bottom-right panel).

- the signals of Stokes Q and Stokes U suffer the effects of the instrumental smearing more than Stokes V and Stokes I (Leone et al., 2003), as showed in Fig. 5.3.

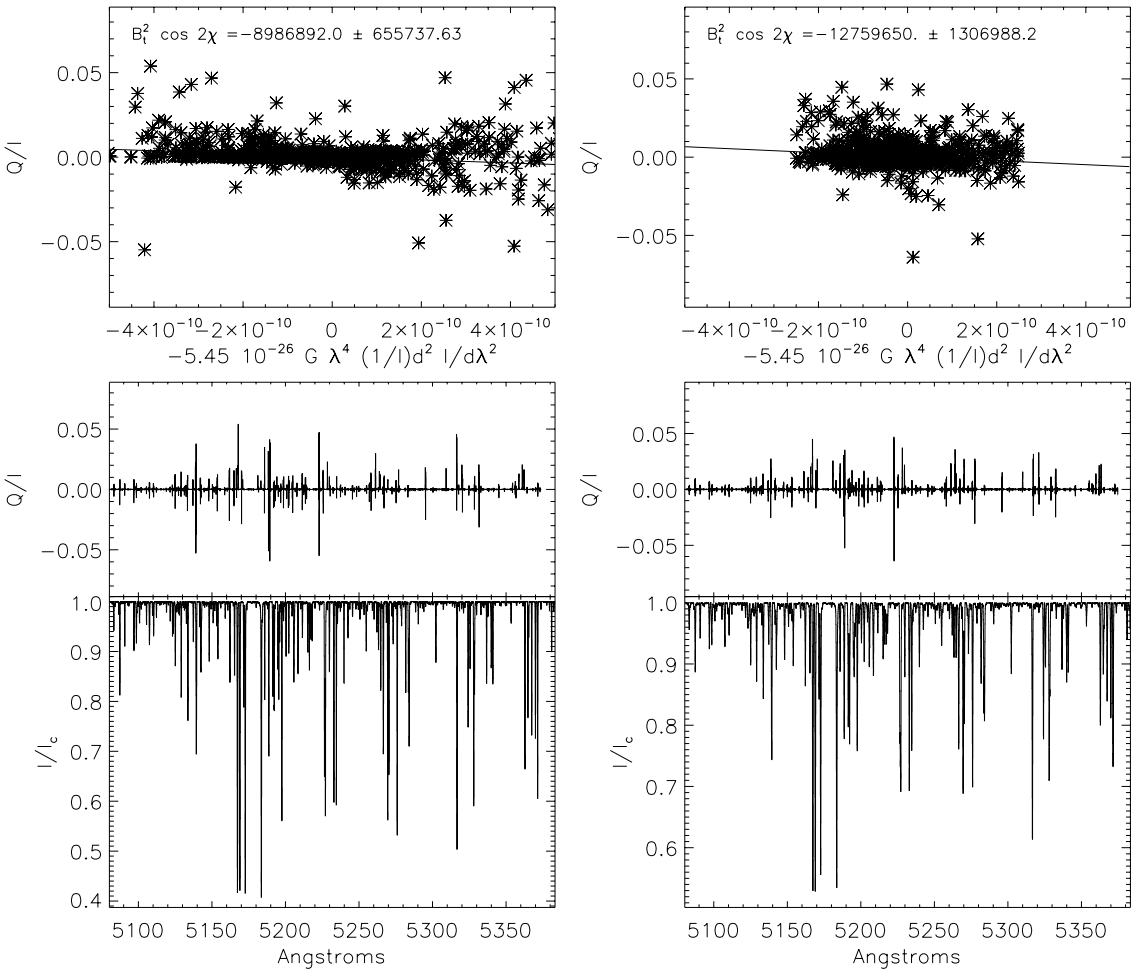

Figure 5.4: Measurements of S_Q from COSSAM simulations with B=1 T orthogonal to the rotational axis and along E-W direction, considering a rotational velocity of 3 km s^{-1} (left panel) and 18 km s^{-1} (right panel).

5.4.1 Disk integrated relation

In principle, Eq. 2.44 is valid only for single points of the stellar surface.

The integration over the stellar disk introduces difficulties in the computation of the Stokes profiles because the Doppler effect due to stellar rotation mixes the profiles of different stellar regions.

Martínez González & Asensio Ramos (2012) analyzed theoretically the problem, in the case of a large scale dipolar magnetic field configuration. They showed that the relations of weak field approximation can be extended to a disk integrated rotating star, if the rotation velocities is not larger than 8 times the Doppler width of the local absorption profiles.

Table 5.1: Ratio between the measured transverse field and the expected value. The equatorial velocity is equal to the projected velocity.

		v_{eq} [km s^{-1}]				
		0	3	6	12	18
B_p[G]	10	1.93	1.18	1.17	0.79	3.51
	100	0.96	1.13	1.13	1.13	3.37
	1000	0.93	1.06	1.08	1.15	3.32
	10000	0.81	0.84	1.02	1.07	1.21

Despite this theoretical result, which supports the application of Eq. 2.44 to observed disk integrated spectra of β CrB, we decided to perform numerical simulation using COSSAM. We considered a dipolar magnetic field geometry, with dipole axis orthogonal to rotation axis, taking both tangents to the celestial sphere.

In this context, the sampling of the stellar surface is a critical issue because all the small effects into the shape of Stokes I are enlarged by the second derivative of the synthetic profiles. We computed synthetic spectra with the maximum sampling allowed by CAOS, although this computation was time-consuming.

Table 5.1 reports the results of the measurements from synthetic spectra while examples of measurements are reported in Fig. 5.4.

Simulations show that the transverse magnetic field can be determined with an accuracy of about 20% respect to the correct value, in the case of velocity lower than 12 km s^{-1} and at the spectral resolution of CAOS (R≈55000). We pointed out how the anomalous values obtained for a velocity of 18 km s^{-1} at low magnetic field are probably related to the fact that, in this case, the line profile is dominated by the instrumental smearing, which impacts the second derivative of Stokes I.

5.5 HD 137909

As an example of magnetic field study of early type stars, we reported the case of β CrB (HD 137909, HIP 75695, HR 5747), which is one of the most bright and studied F0p chemically peculiar CP2 stars, with m_V=3.68 mag Ducati (2002).

Babcock (1958) detected for the first time the presence of magnetic field in this star while Zeeman patterns were observed by Preston & Sturch (1967), who measured also the variation of the longitudinal field. The surface field was measured by Wolff & Wolff (1970). The results of these measures are showed in Fig. 5.5; it is possible to note that

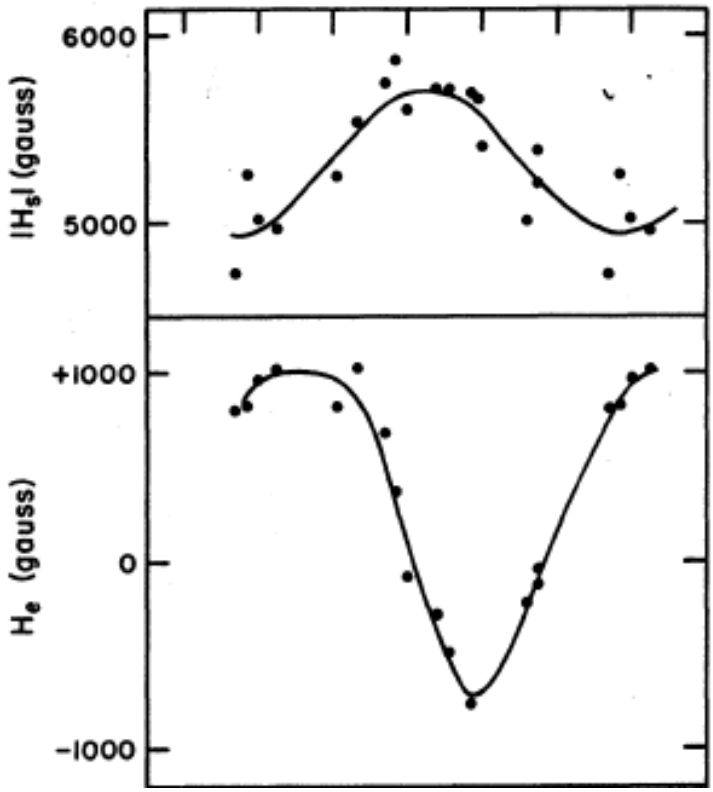

Figure 5.5: Variation of the total surface field $|B_S|$ and longitudinal field B_{eff} of β CrB (Preston & Sturch, 1967).

the total amplitude of the variation of $|B_S|$ is about 800 G and with a maximum value of about 5700 G.

According to the oblique rotator model, in the case of dipolar field geometry (where the field has a maximum at each pole) a double wave is expected on the curve of $|B_S|$, every time that B_{eff} has an extreme. However, this is not the case displayed in Fig. 5.5. This is an observational evidence that modelings more sophisticated than the simple dipole are required. For instance, Wolff & Wolff (1970) tried to explain Fig. 5.5 considering one magnetic pole to be stronger than the other.

Borra & Vaughan (1976) detected for the first time the linear polarisation of β CrB, measuring also the rotation of the electric field vector on the plane of the sky. The variation of broadband linear polarization is reported in Fig. 5.6.

Bagnulo et al. (2000) studied the magnetic configuration of the star, concluding that it can be more complicated than the quadrupolar term.

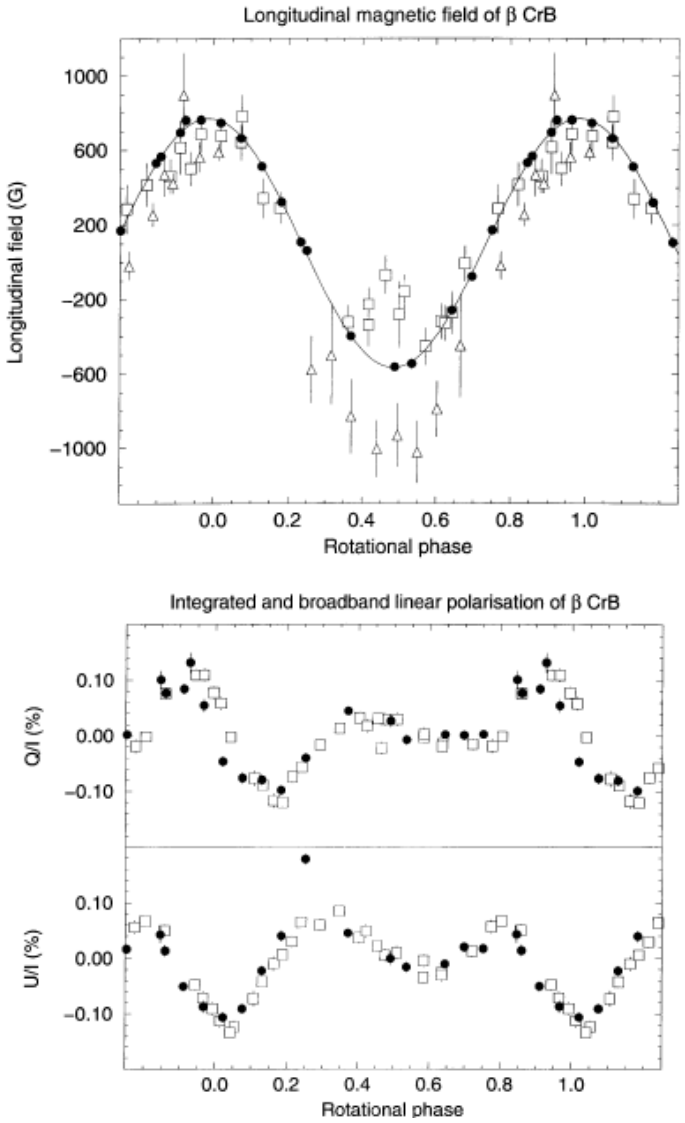

Figure 5.6: Top: B_{eff} measures of HD137909 obtained by Wade et al. (2000) (solid circles), Borra & Landstreet (1980) (open squares), Mathys (1991) and Mathys & Hubrig (1997) (open triangles). Bottom: scaled net linear polarization measurements obtained from LSD profiles by Wade et al. (2000) and broad-band polarization obtained by Leroy (1995). Credits Wade et al. (2000).

Table 5.2: Data set of CAOS observation of βCrB.

MJD [d]	S/N$_V$	S/N$_Q$	S/N$_U$
56778.539	290	302	271
56787.528	345	419	731
56788.585	298	742	488
56799.498	445	385	537
56807.530	352	435	394
56809.475	515	527	372
56815.500	265	177	191
56816.488	322	792	554
56820.499	226	457	309
56822.404	292	625	590
56826.379	430	655	602
56830.510	487	448	500
56831.394	537	493	453
56833.449	168	127	298
56835.379	422	351	347
56836.378	416	512	548
56848.380	629	678	436
57129.589	369	438	421
57189.426	541	723	663
57190.380	318	447	484
57191.376	439	476	532
57193.398	379	445	514

5.6 Transverse magnetic field of β CrB

We observed β CrB with CAOS between 2014 and 2015, collecting a total of 22 full Stokes spectra of the star (Table 5.2). Examples of observed spectral variations are showed in Fig. 5.7, relative to two FeII lines centred at 4923.93 Å and 5018.44 Å.

Measurements of $B_\perp$ and χ from Eq. 5.26 and Eq. 5.27 were obtained from a section of 50 Å in the 500-600 nm interval and from a region of the Fe II 5018.44 Å, which has a known $\bar{G}$ = 3.67 and it presents clear Stokes profiles; they are reported in Table **??**. Examples S_Q and S_U are showed in Fig. 5.8 and Fig. 5.9, for the spectral region around the FeII 5018.44 Å.

We pointed out that line-by-line differences in the second order Landé factors (Eq. 2.45) are larger than differences in the effective Landé factors (Eq. 2.39) and the linear polarized signal is present just in few lines. In this context, the application of the method to broad spectral region impacts the result of the measure, because it includes

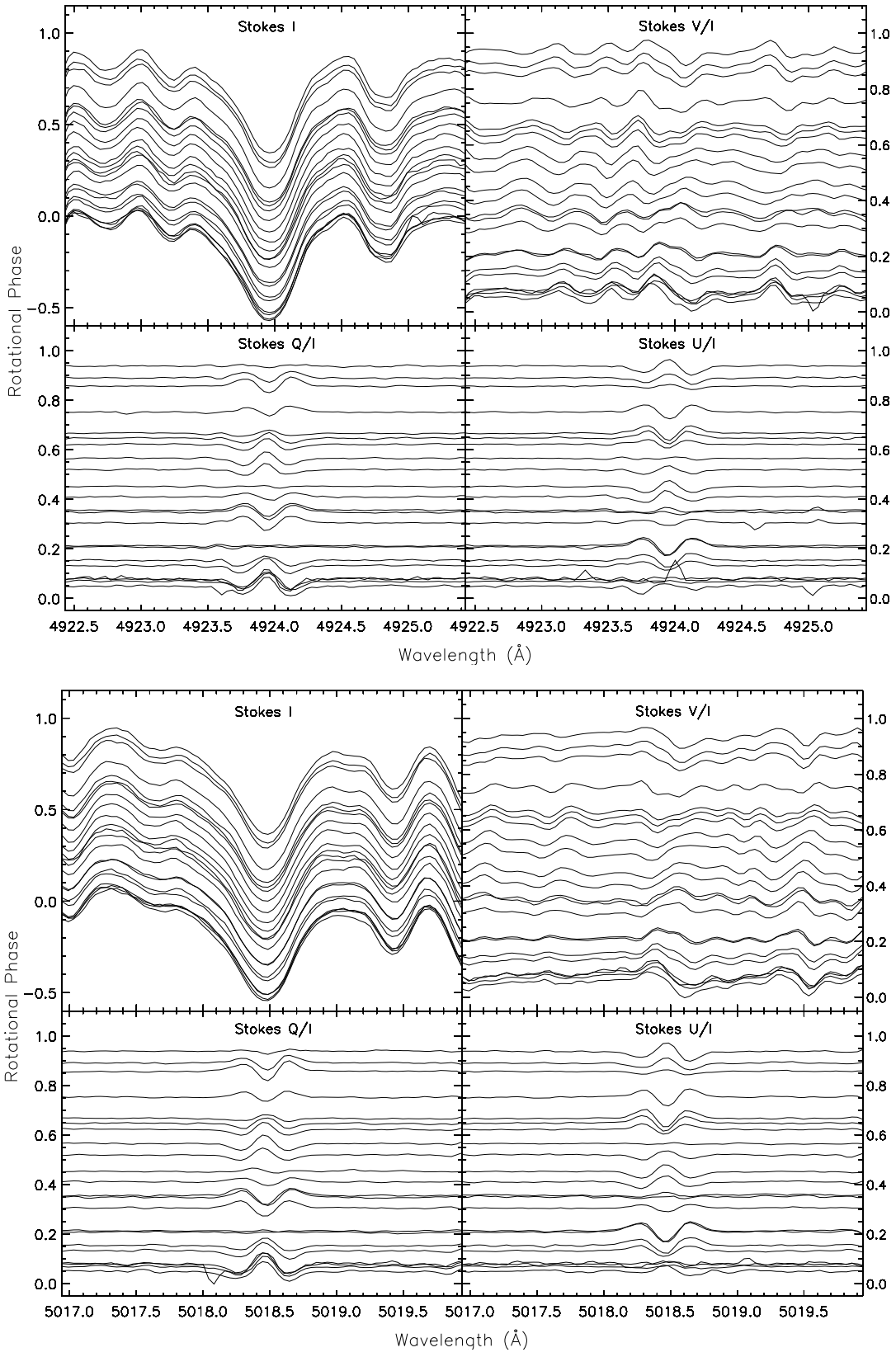

Figure 5.7: Stokes I, V, Q and U of β CrB for the FeII 4923.93 Å (top) and 5018.44 Å (bottom) observed with CAOS.

Table 5.3: Measured transverse magnetic field of βCrB. Eq 5.27 was applied to CAOS spectra in the range 5000 to 6000 Å and to a single iron line.

	5000 - 6000 Å		FeII 5018.44 Å	
HJD 2450000	$B_\perp \pm \sigma$ kG	$\chi \pm \sigma$ °	$B_\perp \pm \sigma$ kG	$\chi \pm \sigma$ °
6787.511	1.117±0.084	85± 5	0.930±0.012	88± 1
6788.560	0.923±0.160	69± 5	0.877±0.015	70±20
6799.481	0.907±0.223	48±12	0.841±0.015	45±43
6802.471	0.737±0.123	147±11	0.564±0.025	148±31
6807.515	1.109±0.162	63± 6	0.897±0.019	63±27
6809.448	1.138±0.167	34± 5	0.982±0.016	37±35
6815.452	1.217±0.147	106± 6	11207±0.019	101±13
6816.436	1.005±0.149	89± 8	0.995±0.015	84± 5
6820.484	0.849±0.082	22±16	0.794±0.021	12± 9
6822.429	0.735±0.108	117±11	0.608±0.022	127±40
6826.417	1.073±0.122	55± 3	0.960±0.014	55±36
6829.409	1.155±0.153	3± 4	1.010±0.013	1± 1
6830.474	1.237±0.155	161± 6	1.094±0.015	160±20
6831.422	1.311±0.124	144± 5	1.152±0.013	143±37
6833.478	1.289±0.129	108± 6	1.134±0.020	108±20
6835.405	1.000±0.098	81± 7	0.949±0.019	75±14
6836.408	0.873±0.180	51±24	0.703±0.019	44±41
6844.369	1.246±0.136	60± 3	1.030±0.014	60±30
6848.338	1.139±0.134	171±17	1.000±0.014	173± 7
6849.343	1.004±0.094	152± 5	0.976±0.021	150±29
7129.556	1.144±0.142	103± 9	1.129±0.014	96± 7
7189.467	0.798±0.130	15±20	0.691±0.017	5± 3
7190.426	0.766±0.128	163± 6	0.733±0.020	169±12
7191.416	0.619±0.102	118±17	0.483±0.024	135±41
7193.425	0.757±0.112	90± 9	0.657±0.018	93± 7

points with no information about the transverse field, adding just noise.

We found that β CrB presents a variation of the transverse field and χ with the rotation period, with an average value about 1 kG and an amplitude as large as 0.250 kG. χ is limited by definition to the range 0-180°and it shows saw-tooth behavior.

5.7 Modelling magnetic curves

We performed numerical modeling of magnetic curves, including measurements of effective magnetic field obtained by Mathys (1994) and measurements of superficial field

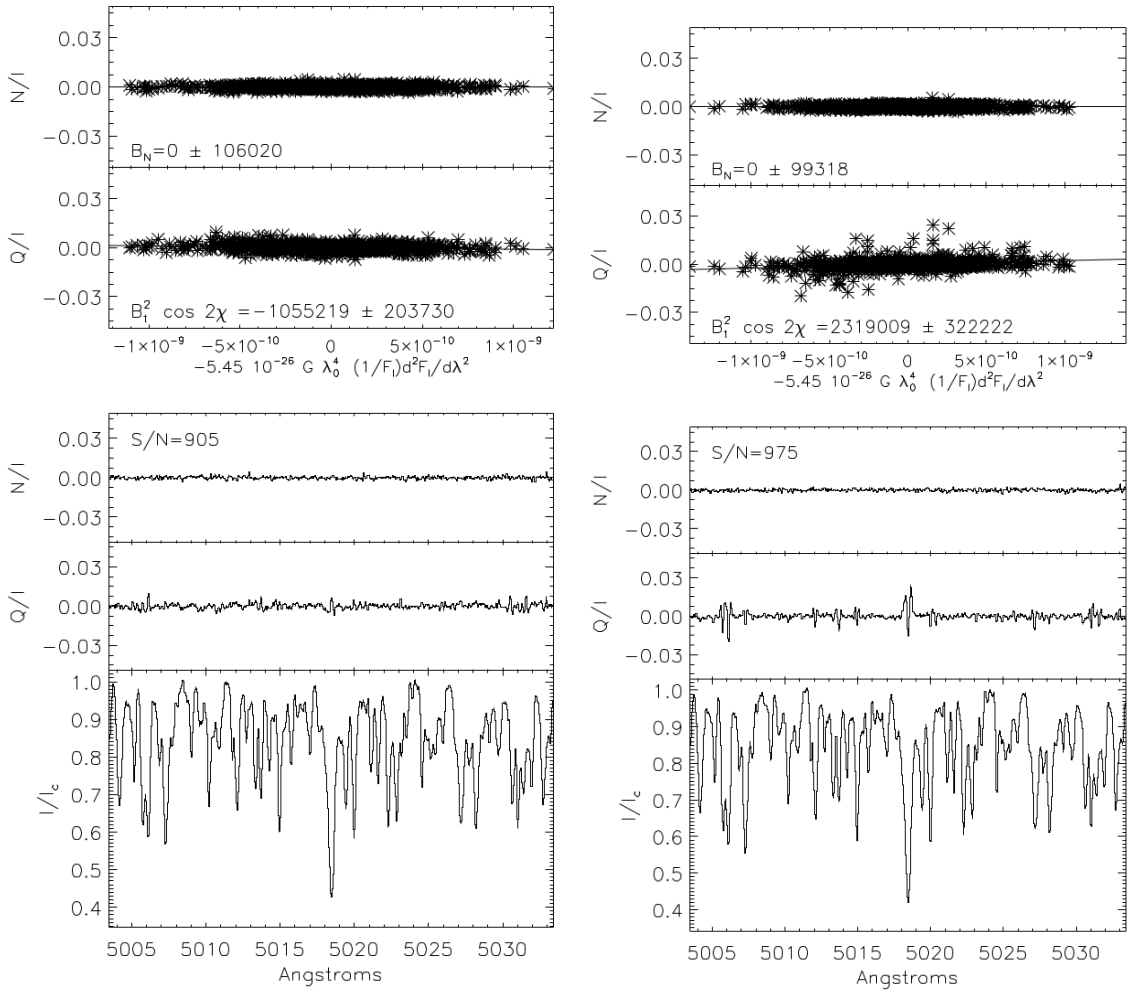

Figure 5.8: Exemples of measures S_Q of HD137909.

strength made by Mathys et al. (1997). Literature values are reported respectively in Table 5.4 and Table 5.5.

We chose to represent the magnetic field geometry as the addition of a dipole, a quadrupole and an octupole, with axes of symmetry with different directions respect to the rotation axis and respect to each other. The reference plane was identified by the rotation axis and the line of sight. We defined the zero rotation phase when the axis of the dipole corresponded to the reference plane.

The model needed 10 parameters:

- i inclination angle respect to the line of sight;
- m1 moment of the dipole;

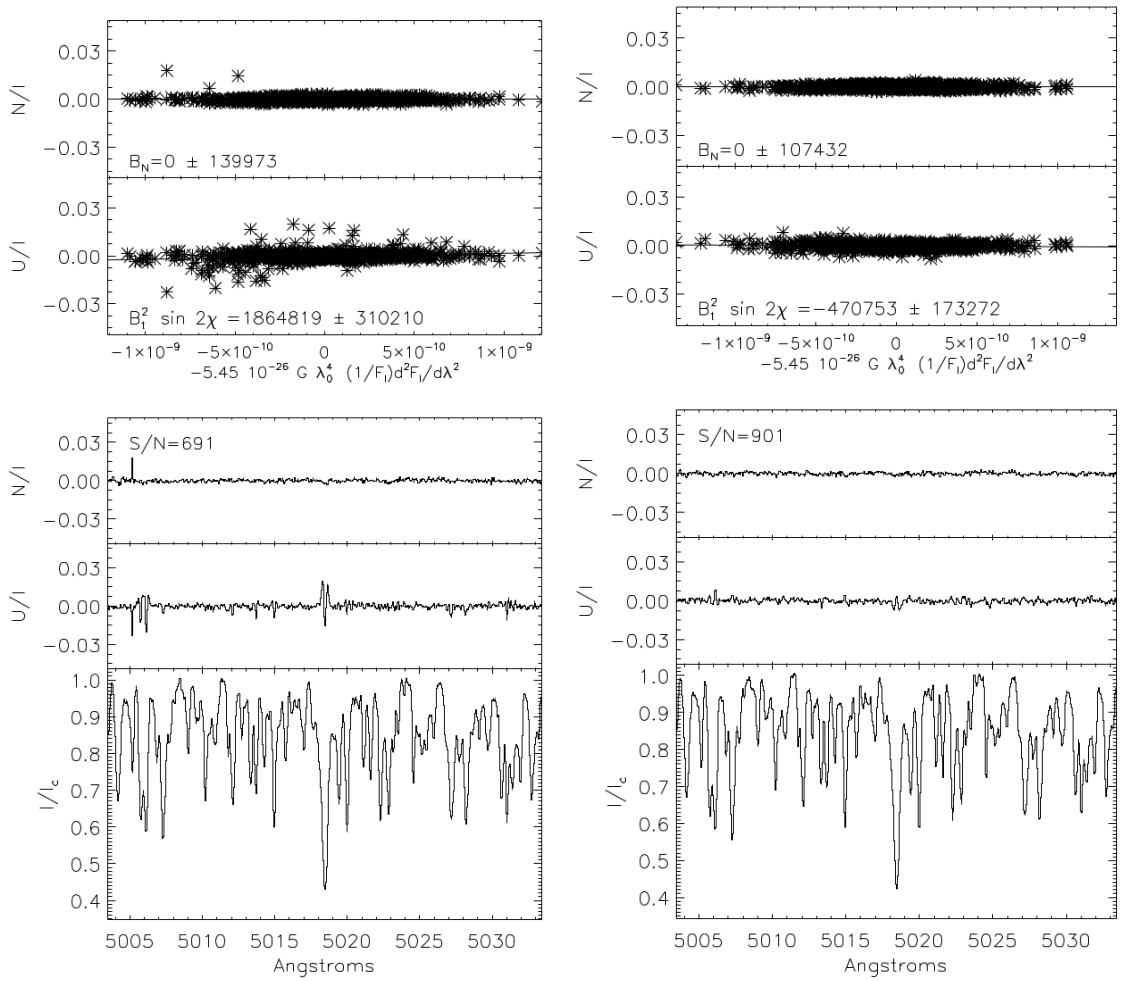

Figure 5.9: Exemples of measures S_U of HD137909.

- β angle between dipole and rotational axis;
- m2 moment of the quadrupole;
- β_q angle between quadrupole and rotational axis;
- ϕ_q angle between dipole and quadrupole axis;
- m3 moment of the octupole;
- β_o angle between octupole and rotational axis;
- ϕ_o angle between dipole and octupole axis;

We found a solution, showed in Fig. 5.10, with:

Table 5.4: Effective magnetic field of β CrB (Mathys, 1994).

HJD (2440000+)	B_{eff} [G]
6218.617	486 ± 114
6219.613	897 ± 223
6547.717	-450 ± 278
6549.708	-19 ± 73
6894.800	-1005 ± 153
6895.834	-932 ± 170
6896.813	-1023 ± 167
6897.805	-790 ± 149
7279.738	-579 ± 180
7280.731	-502 ± 263
7281.723	-830 ± 200

- i = 153°
- m1 = +6.1 kG, β = 86°
- m2 = +3.9 kG, β_q = 88°, β_q = 64°
- m3 = -10.7 kG, β_o = 20°, β_o = 40°

It was found using *genetic algorithms* (Charbonneau, 1995), which are particularly useful in order to find a global solution of the problem. However, the investigation of the uniqueness for this ill-posed mathematical problem is hard and it is out of the scope of this work. For the implementation, we used the IDL code *SOLution BreedER*[1] (SOLBER).

This solution is important in order to evince that a multipolar expansion is needed in order to represent the transverse and the surface fields, even if the dipolar field can fit the variation of the effective magnetic field and χ, as shown in Fig. 5.11.

We noted that the knowledge of transverse field and χ can be used to solve the ambiguity between the angles i and β of Eq. 5.17 and Eq. 5.18, as pointed out also by Leroy et al. (1993). For instance, Fig. 5.12 shows how two magnetic configurations with the same transverse and longitudinal field can be distinguished with the different variations of the angle χ; in particular, the configuration with i larger than β results in an amplitude of the variation of χ lower than 180°.

[1] http://www.ast.cam.ac.uk/ vasily/solber/index.htm.12012009

Table 5.5: Surface field of β CrB (Mathys et al., 1997).

HJD (2440000+)	$\langle B_S \rangle$ [G]
8167.257	5705
8478.344	5570
8480.365	5736
9108.567	5721
9110.472	5730
9111.433	5675
9112.478	5661
9113.395	5531
9114.438	5510
9157.637	5371
9158.642	5271
9159.636	5247
9160.445	5378
9160.638	5294
9161.655	5350
9162.354	5480
9162.644	5466
9163.362	5663
9163.643	5594
9164.361	5694
9165.356	5742
9166.355	5705
9576.396	5443
9577.399	5434
9578.323	5375
9580.321	5279
9581.318	5277
9600.314	5321
9601.299	5292
9603.282	5352
9605.293	5445
9607.284	5669

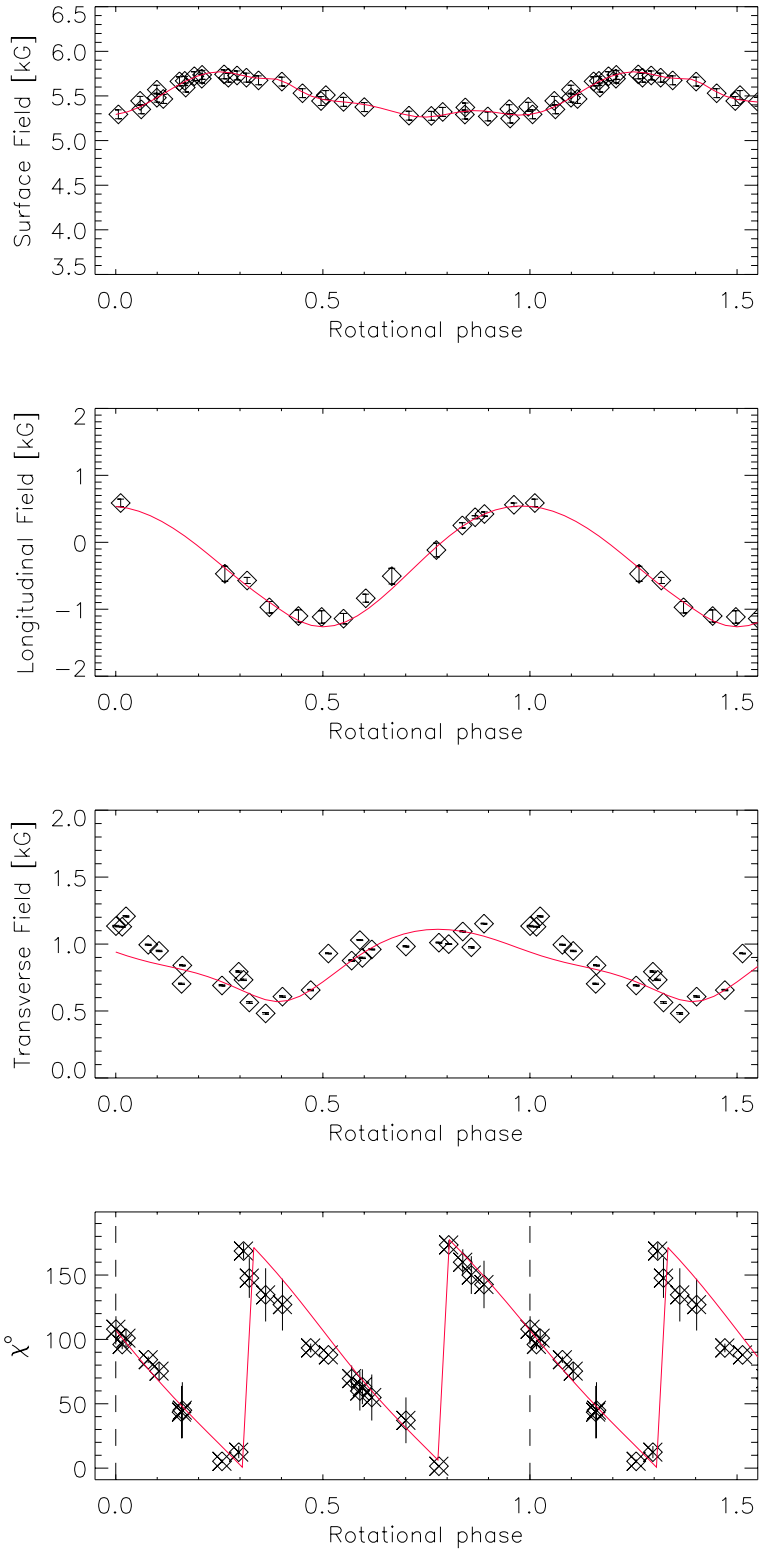

Figure 5.10: Genetic fit with multipolar magnetic field.

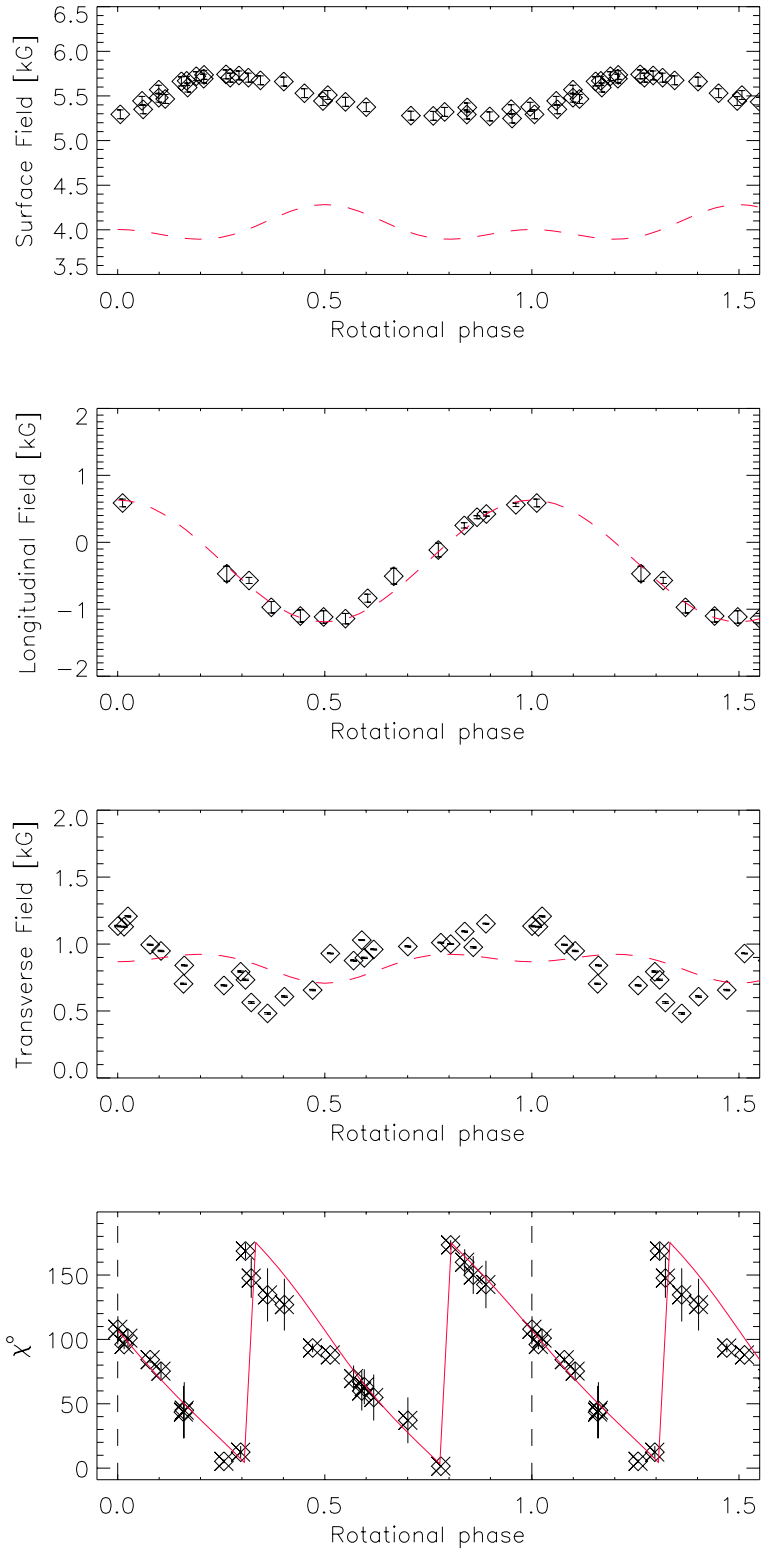

Figure 5.11: Genetic fit with dipolar magnetic field.

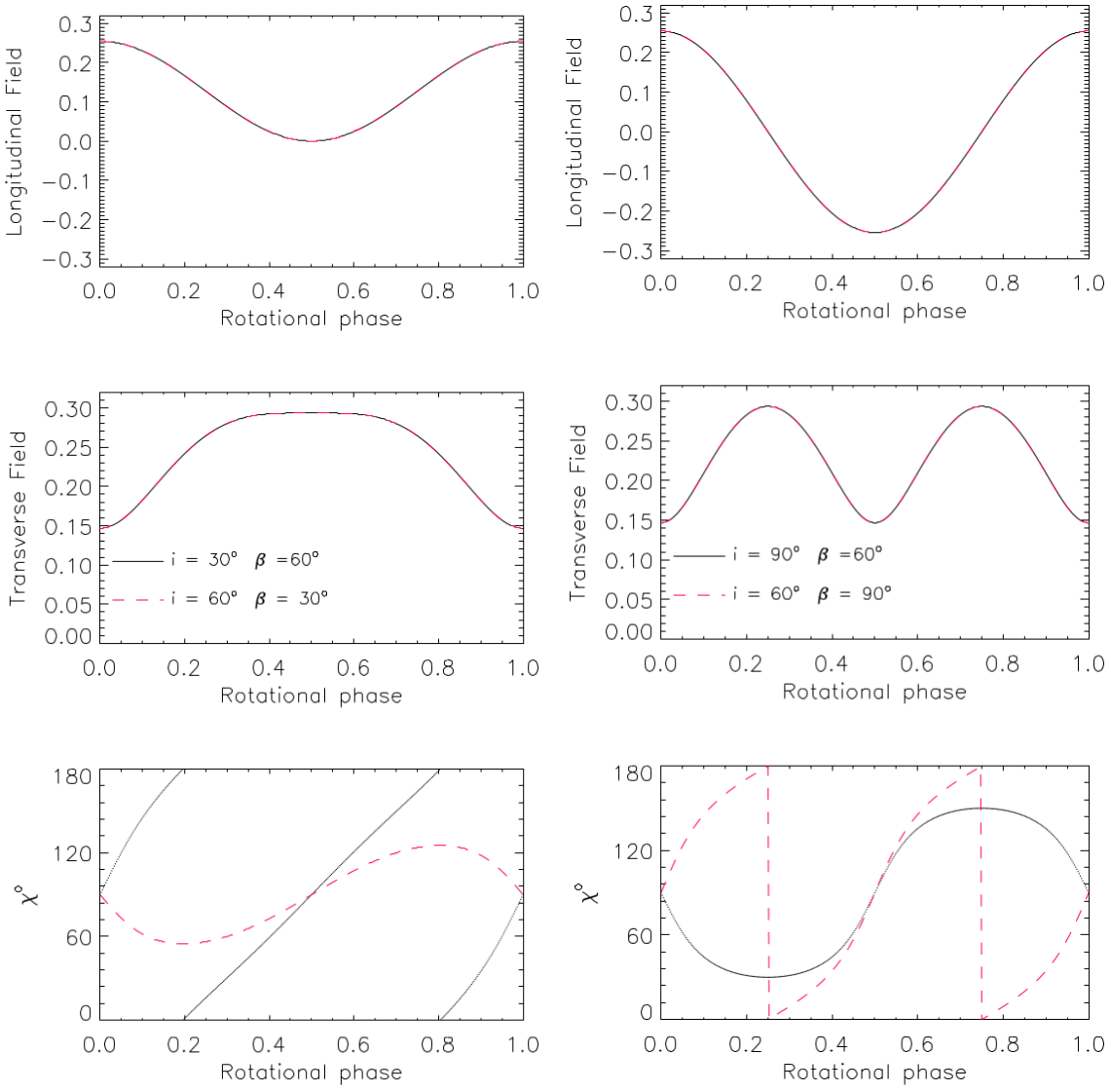

Figure 5.12: Examples of configurations with same transverse and longitudinal field but different variations of χ. Field values are given in units of the polar magnetic field.

Disentangling the angles i and β can be useful in order to estimate the stellar radius R, through Eq. 5.3. Kurtz et al. (2007) evaluated the v sin(i) of β CrB in a range from 3.0 to 3.8 km s^{-1}, with a value of 3.5 km s^{-1} for the Fe II 6149 Å. Considering the degeneracy (i = 153°, β_d = 86°) or (i = 86°, β_d = 153°), two values would be possible for the stellar radius: $1.25 \pm 0.15\,R_\odot$ or $2.75 \pm 0.30\,R_\odot$. The determination of i = 153°implies R = $2.75\,R_\odot$, which is confirmed by the interferometric value of $2.6\,R_\odot$ obtained by Bruntt et al. (2010).

5.8 The orientation of the stellar rotational axis

From Fig. 5.10 and Fig. 5.11, it is possible to evince that it is possible to estimate the angle χ of HD137909 from the dipolar component, while the quadrupolar and octupolar component has only negligible effects.

The measure of the value of the angle χ at the extreme of the longitudinal field is an estimation of the angle between the rotational axis and the N-S direction in the sky. This is because at the extreme, dipole axis, rotational axis and line of sight are in the same plane.

We can conclude that the rotational axis of HD137909 is tilted of θ=110°respect to the N-S direction and the resulting magnetic field will draw a cone in the sky. This value is consistent with the results of the modeling of broadband linear polarimetry of Leroy (1995), who found θ=135°and Bagnulo et al. (2000) that found θ=110°.

CHAPTER 6

MAGNETIC FIELD OF STARS HOSTING PLANET

As stated in Sect. 1.2, magnetic fields are important for the study of exoplanets, because they can lead to false detections and they can play a role in the interaction between stars and planets.

Since the discovery of the first exoplanet in giant stars, Iota Draconis b (Hypatia) by Frink et al. (2002) (the biggest found on the basis of radial velocities (Butler et al., 2006)), planets in evolved stars were detected in RV surveys (Niedzielski & Wolszczan, 2008) and on the basis of transit method (Huber et al., 2013). They represent the 3% of the total number of exoplanets (in September 2016) (Hrudková et al., 2017).

This chapter is devoted to study of the magnetic fields for a sample of stars hosting planet. In particular, we posed attention to the case of exoplanets in evolved stars, which is important in order to evince the planet survivor after the hydrogen burning phase. Moreover, the study of the magnetic field in giant stars is important for stellar evolution theory. Measurement are performed using the method of the Least Square Deconvolution. We implemented the technique and we tested the code using synthetic spectra, computed with COSSAM, and real observations previous analysed by other authors.

6.1 Least square deconvolution

The expected polarized signal, due to the presence of magnetic fields in giant stars, is very low and, in order to find it, a noise level on Stokes V of about 10^{-4} is needed. However, this value can not be obtained from a single line, which can reach a maximum of 10^{-3}

(Donati et al., 1997) with the current instrumentation. For this reason, sophisticated techniques are required in order to reduce the noise level.

Semel & Li (1996) proposed the idea to add several spectral lines and compute a pseudo profile with higher S/N. Several techniques were implemented in order to do this sum, such as the *Least Squares Deconvolution* (LSD) (Donati et al., 1997), the *Principal Components Analysis* (Semel et al., 2009) and the *Zeeman component decomposition* (Sennhauser & Berdyugina, 2010).

Among all these techniques, the LSD is probably the most used and, for this reason, we decided to numerically implement it in IDL, following Kochukhov et al. (2010).

The method is based on the assumptions of:

- weak-field regime of magnetic field (Eq. 2.43);
- each line can be approximately described by the same line shape, scaled by a certain factor, both in Stokes I and Stokes V;
- limb darkening is wavelength-independent;

in this way, the observed spectrum can be described as the sum of scaled and shifted identical profiles Z(v):

$$\mathrm{Y(v)} = \sum_{\mathrm{i}} \mathrm{w_i}\delta(\mathrm{v}-\mathrm{v_i})\mathrm{Z(v_i)} \tag{6.1}$$

where Y(v) can be posed equal to the residual Stokes I $(1-\mathrm{I/I_c})$ or the normalized Stokes V $(\mathrm{V/I_c})$, $\mathrm{w_i}$ is a weight and $\mathrm{v_i} = \mathrm{c}\,\Delta\lambda_\mathrm{i}/\lambda_\mathrm{i}$ is the position in the velocity space respect to the i line. Introducing the line pattern function:

$$\mathrm{M(v)} = \sum_{\mathrm{i}} \mathrm{w_i}\delta(\mathrm{v}-\mathrm{v_i}) \tag{6.2}$$

the entire spectrum can be written as the convolution between the line pattern and the common profile:

$$\mathrm{Y} = \mathrm{M} * \mathrm{Z} \tag{6.3}$$

which is equivalent to a linear system:

$$\mathrm{V} = \mathrm{M} \cdot \mathrm{Z} \tag{6.4}$$

It is possible to find the common profile Z(v) as the solution of the least-square problem:

$$\mathrm{Z} = ({}^{\mathrm{t}}\bar{\mathrm{M}} \cdot \mathrm{S}^2 \cdot \bar{\mathrm{M}})^{-1\,\mathrm{t}}\bar{\mathrm{M}} \cdot \mathrm{S}^2 \cdot \mathrm{Y} \tag{6.5}$$

where S is the square diagonal matrix of the inverse error bar $1/\sigma_{ij}$.

The term M is called *line mask matrix* (Donati et al., 1997) and it collects all the information related to the lines. Its dimensions are:

$$\bar{M} = n_{pixel} \times n_{vel} \tag{6.6}$$

where n_{pixel} are the number of the points of the spectrum used for the computation and n_{vel} are the number of points which sample the velocity space. This sampling is performed considering the spectral resolution of the instrument and the characteristics of the detector. In the cases of the spectropolarimeters used in this work, these values are setted to:

$$incr_{vel} = \begin{cases} 0.825\,[km\,s^{-1}] & HARPSpol \\ 1.845\,[km\,s^{-1}] & Narval/Espadon \\ 2.38\,[km\,s^{-1}] & CAOS \end{cases} \tag{6.7}$$

Each l line corresponds to a bidiagonal term in the line mask matrix, given by:

$$\begin{aligned} \bar{M}_{i,j} &= \omega_l (v_{j+1} - v_i)/(v_{j+1} - v_j) \\ \bar{M}_{i,j+1} &= \omega_l (v_i - v_j)/(v_{j+1} - v_j) \end{aligned} \tag{6.8}$$

where ω_l is a weight and v is the velocity:

$$v_i = c(\lambda_i - \lambda_l) \quad v_j \leq v_i \leq v_{j+1} \tag{6.9}$$

with λ_l equal to the central wavelength of the line.

Different weights are used for the computation of the LSD Stokes I and Stokes V. They are given by:

$$\begin{aligned} \omega_I &= d \\ \omega_V &= d\,\lambda_l\,g_{eff,l} \end{aligned} \tag{6.10}$$

where d is the depht and $g_{eff,l}$ is effective Landé factor of the transition.

The list of the lines used for the computation of the LSD profiles is an important issue. Line selection started with a synthetic spectrum computed with SYNTHE (Kurucz, 1993a; Sbordone et al., 2004), using the T_{eff} and $\log g$ of the star. In order to avoid saturated line, that can not be used because their depth did not simply scale up with the local line central depth, we restricted the computation only to line with $d < 0.7$.

We performed a cutoff from a central depth at the level of 0.1. Kochukhov et al. (2010) pointed out how the choice of the cutoff value is important and it can impact the profiles, causing, for instance, a depression of the LSD Stokes I respect to the continuum.

Normalization of the LSD profiles is another important issues, in order to interpret the results. Several authors chose different normalization criteria for the profiles obtained with their code; for instance, Donati et al. (1997) normalized the profiles to a line centred at $\lambda_0 = 500\,\mathrm{nm}$, setting to unity the Landé factor and the depth. We decided to normalize the profiles to the mean value of depth for Stokes I, and to the mean value of the product between depth, Landé factor and central wavelength for Stokes V:

$$Z_I = \overline{d}\ Z_I$$

(6.11)

$$Z_V = \overline{d\,\lambda\,g_{eff}}\ Z_V$$

In principle, Z(v) can be also computed by a simple line addition, which is simpler to implement. Semel et al. (2009) and Paletou (2012) found similarities between the results of the simple average and the LSD. However, Kochukhov et al. (2010) pointed out that the LSD profiles are less dependent on line blends.

6.2 Effective magnetic field measurement

Stellar effective magnetic field (see Sect. 5.2.1) can be computed, from a given spectral line, through the *first order moment* of Stokes V ($\mathrm{R_V^{(1)}}$) respect the line centre λ_I (Mathys, 1991, 1994), which is given by:

$$\mathrm{B_{eff}} = \frac{\mathrm{R_V^{(1)}}}{4.67\,10^{-13}\,\mathrm{g_{eff}}\,\lambda_0^2} \tag{6.12}$$

where $\mathrm{R_V^{(1)}}$ is equal to:

$$\mathrm{R_V^{(1)}} = \frac{\int \frac{\mathrm{V}}{\mathrm{I_c}}(\lambda - \lambda_\mathrm{I})\,\mathrm{d}\lambda}{\int [1 - \mathrm{I_c}]\,\mathrm{d}\lambda} \tag{6.13}$$

and the line centre is computed through:

$$\lambda_\mathrm{I} = \frac{\int [1 - \mathrm{I}]\lambda\,\mathrm{d}\lambda}{\int [1 - \mathrm{I}]\,\mathrm{d}\lambda} \tag{6.14}$$

In order to apply the equations of the moment techniques to the profiles computed with the LSD, they have to be re written in the velocity frame. Following Kochukhov et al. (2010), they are given by:

$$\mathrm{B_{eff}} = -7.145 \times 10^6 \frac{\int \mathrm{v Z^v dv}}{\lambda_0 \bar{\mathrm{g}} \int \mathrm{Z^I dv}} \tag{6.15}$$

where Z^V is Stokes V LSD profile, Z^I is the residual Stokes I LSD profile, λ_0 and $\bar{g}$ are the quantities adopted for the normalization of weights of the Stokes V LSD profile.

In order to compute the effective magnetic field from the profiles obtained with our code, we followed the relations given by Chen & Johns-Krull (2013), that reported Eq. 6.15 in the case of the discrete velocity frame, given also a relation for the estimation of the error. They can be written as:

$$B_{eff} = -\frac{7.145 \times 10^6}{\lambda_0 \bar{g}} \frac{\sum_{i=n}^{m} v_i Z_i^v}{\sum_{i=n}^{m} Z_i^I}$$
$$\sigma_{B_{eff}} = \left|B_{eff}\right| \sqrt{\frac{\sum_{i=n}^{m} v_i^2 \sigma_V^2}{\left|\sum_{i=n}^{m} v_i Z_i^v\right|^2} + \frac{\sum_{i=n}^{m} \sigma_I^2}{\left|\sum_{i=n}^{m} Z_i^I\right|^2}} \tag{6.16}$$

where σ_V is computed from the scatter of the LSD null profile and σ_I is computed from the scatter of the continuum of the LSD Stokes I. We selected the spectral region for the computation of the moment through the standard deviation of the Gaussian fit of the LSD Stokes I.

6.3 LSD tests

The measure of small magnetic fields from the LSD profiles is a delicate procedure, which can be affected by several systematic errors. They can be related to the implementation of the code itself or to errors in the instrumental setup, which are difficult to individuate at the level required for this measure.

Tests of the code can be performed by the comparison with results previously obtained by similar codes. In order to do it, we applied our LSD procedure to the dataset of the magnetic cool star ϵ Eri, observed by HARPSpol in January 2010 and previously published by Piskunov et al. (2011) and Kochukhov et al. (2011) (numerical values are taken from Olander (2013)). We downloaded the raw data from the ESO archive and we reduced it following the procedure described in Sect. 3.8.

Fig. 6.1 shows the results of the effective magnetic field measurements of ϵ Eri obtained with our code and with the code used by Kochukhov et al. (2011). It is possible to note a general agreement between the measurements; we pointed out that difference can be caused by the different data reduction and the use of a different line list.

These data were also used by Chen & Johns-Krull (2013) to test their numerical implementation of the LSD code. A comparison between the profiles obtained with our code and the profiles obtained by Chen & Johns-Krull (2013) and Kochukhov et al. (2011) is reported in Fig. 6.2. It is possible to note that the shape of the profiles obtained with

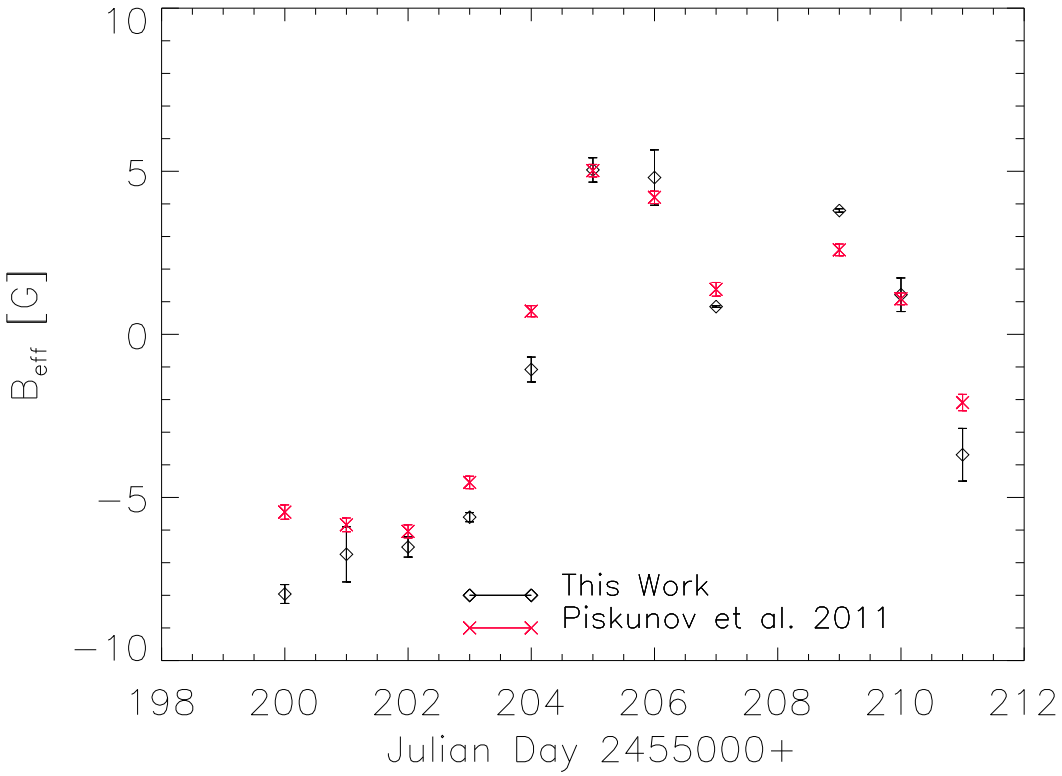

Figure 6.1: Comparison between the measurements of the effective magnetic field of ϵ Eri observed with HARPSpol in 2010 (Kochukhov et al., 2011; Olander, 2013). The black points are obtained with our LSD code (black) and red points are the values obtained by Kochukhov et al. (2011).

our LSD code is similar to the results obtained by the other authors. The level of the profiles presents differences that can be explained considering the different criteria of normalization and the different list of lines used. It is possible to note that Chen & Johns-Krull (2013) and Kochukhov et al. (2011) used the same data and the same line list.

A test, independent from the data reduction, can be performed analyzing synthetic spectra computed with COSSAM. This allowed to test the behavior of the code with respect to the rotational velocity and the effective magnetic field strength.

Results are showed in Table 6.1. It is possible to note that differences between result and input value generally increase with the increasing of rotational velocity, while they decrease at higher spectral resolution. This can be explained considering that:

- the weak field relations (see Sect. 2.3) are obtained for a single point of the stellar surface. These relations can be considered valid also for the disk integrated case

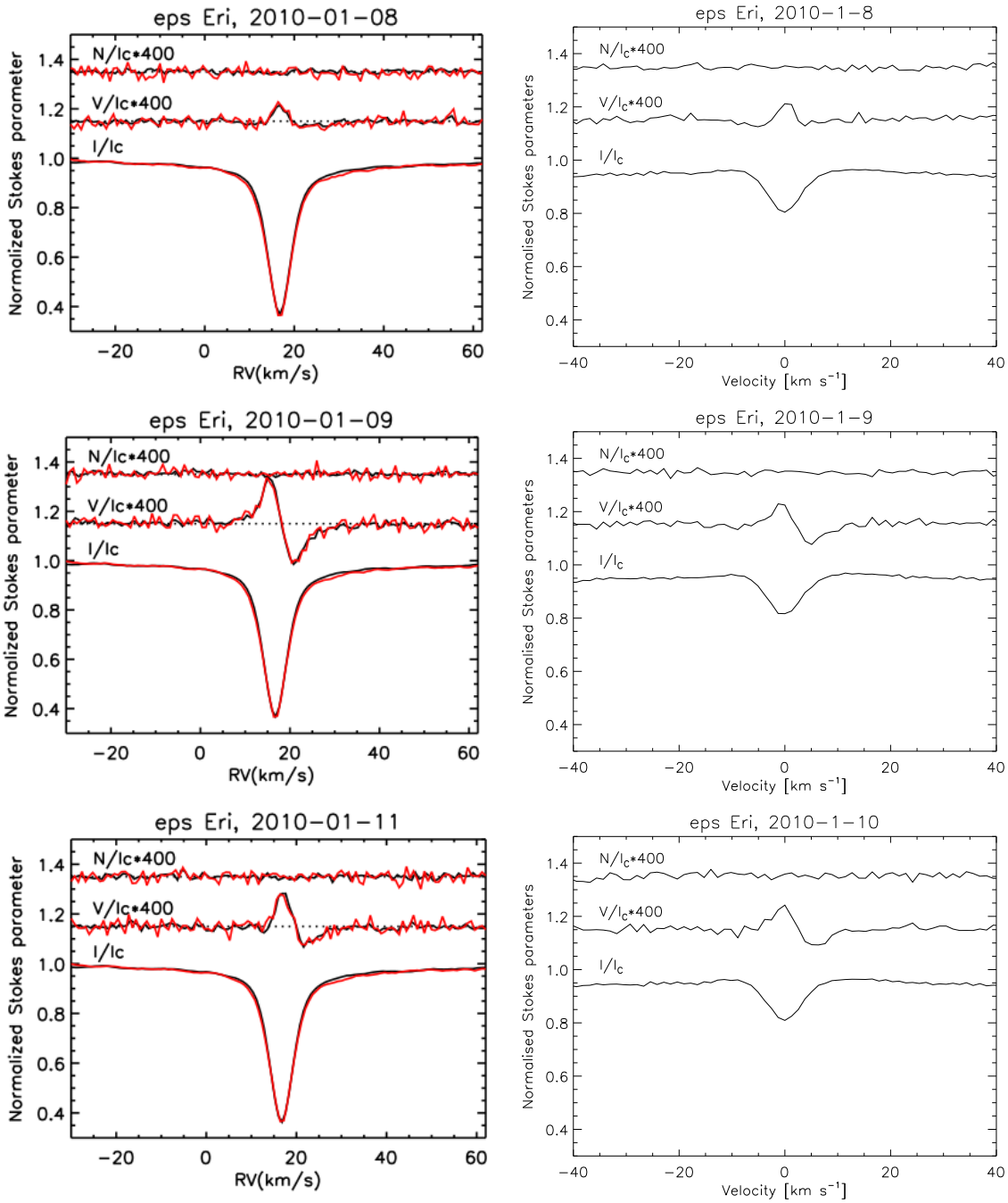

Figure 6.2: Comparison between the LSD profiles of the magnetic star ϵ Eri observed with HARPSpol in 2010. On the left, the LSD profiles obtained by Chen & Johns-Krull (2013) (red) and Kochukhov et al. (2011) (black).

Table 6.1: Results of effective magnetic field measurement from the Least Square Deconvolution profiles obtained by COSSAM simulations for different values of rotational velocity and effective magnetic field. The percentages are computed as the difference between the measured and the syntetic values.

	CAOS R=55000 2.5 px per FWHM				NARVAL R=65000 2.5 px per FWHM				HARPSpol R=115000 4.1 px per FWHM			
v sin(i)	B_{inp}				B_{inp}				B_{inp}			
[km s^{-1}]	-0.64 G	-3.22 G	-6.45 G	-32.25 G	-0.64 G	-3.22 G	-6.45 G	-32.25 G	-0.64 G	-3.22 G	-6.45 G	-32.25 G
3	-0.45 31%	-3.20 1%	-6.12 5%	-31.18 3%	-0.70 9%	-3.25 1%	-6.35 1%	-32.34 0%	-0.64 1%	-3.29 2%	-6.26 3%	-31.97 1%
6	-0.53 18%	-3.33 3%	-7.07 10%	-34.39 7%	-0.76 18%	-2.72 16%	-6.00 7%	-29.98 7%	-0.58 11%	-3.28 2%	-6.77 5%	-32.84 2%
12	-0.80 24%	-3.83 19%	-6.84 6%	-34.13 6%	-0.78 21%	-3.41 6%	-5.74 11%	-29.36 9%	-0.66 3%	-2.98 7%	-6.16 4%	-29.80 8%
18	-0.50 22%	-3.43 6%	-5.38 17%	-29.38 9%	-1.89 193%	-2.91 10%	-5.43 16%	-29.03 10%	-0.43 33%	-3.11 4%	-5.99 7%	-30.91 4%

Table 6.2: Effective magnetic field measures of ϵ Eri observed with CAOS.

Star	JD (2400000+)	Null [G]	Field [G]
EpsEri	56921.572	0.69 ± 0.59	8.73 ± 0.59
	56922.578	-0.63 ± 0.93	0.34 ± 0.93
	56946.504	-0.46 ± 0.99	-2.84 ± 0.99
	56947.504	3.83 ± 1.82	2.53 ± 1.82
	57630.549	0.35 ± 0.66	-10.26 ± 0.66
	57634.617	1.12 ± 0.91	-3.15 ± 0.91
	57724.413	-2.48 ± 1.53	-10.44 ± 1.53

only for rotation velocities not larger than 8 times the Doppler width of the absorption line (Martínez González & Asensio Ramos, 2012), as stated in Sect. 5.4.1.

- at higher resolution the sampling in the velocity space is higher and these results in a well-defined LSD profile.

In the case of CAOS resolution, the difference between computed and synthetic value was at maximum about the 30% of the input value.

The presence of systematic errors due to the instrument can be checked by observations of stars with detected magnetic fields. Results of the application of the LSD to spectropolarimetric data of ϵ Eri, obtained with CAOS, are reported in Table 6.2 and Fig. 6.3. They demonstrate the capabilities of the code and of the instrumental setup to measure the magnetic field signals of cool stars.

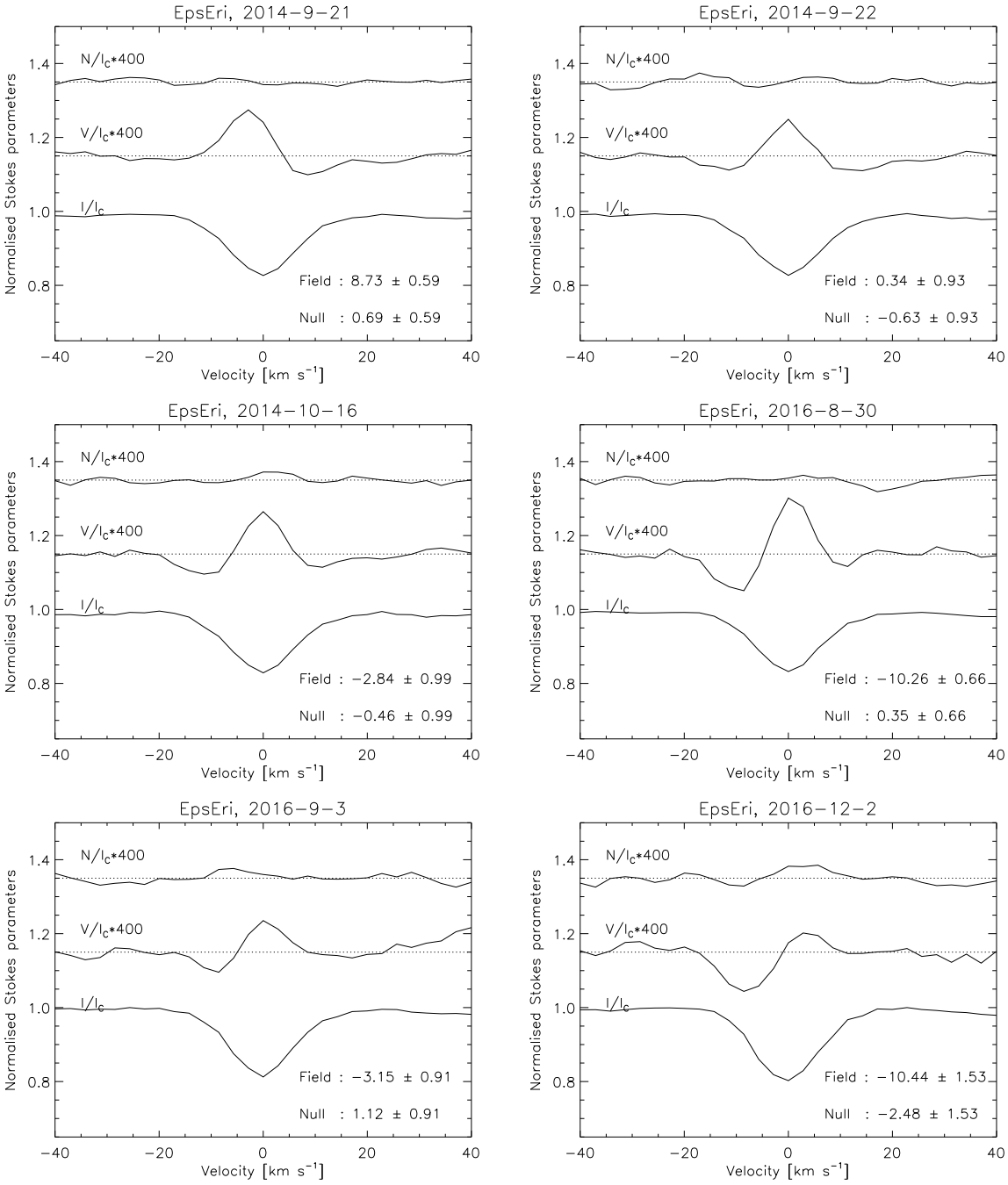

Figure 6.3: LSD profiles of the active cool star ϵ Eri observed with CAOS.

Table 6.3: Table of stars observed with CAOS. The reference are respectively: [1] (Valenti & Fischer, 2005), [2] (Jofré et al., 2015), [3] (Takeda et al., 2008), [4] (Trifonov et al., 2014), [5] (Soubiran et al., 2016), [6] (Wu et al., 2011), [7] (Mortier et al., 2013), [8] (Sato et al., 2012), [9] (Massarotti et al., 2008), [10] (Zoghbi, 2011), [11] (de Medeiros & Mayor, 1999), [12] (De Medeiros et al., 2002), [13] (Hoffleit & Warren, 1995), [14] (Richichi et al., 2005), [15] (Richichi & Percheron, 2002), [16] (Baines et al., 2008), [17] (Borde et al., 2002), [18] (Bourges et al., 2017), [19] (ESA, 1997), [20] (Simpson et al., 2010) and [21] (Kane et al., 2010). The symbol * is used for indicate values estimated from the interferometric diameter (see text).

Star	V [mag]	Spec. Type	T_{eff} [K]	log g	$\frac{[Fe]}{[H]}$ [dex]	v sin(i) [km s^{-1}]	θ_{UD} [mas]	θ_{LD} [mas]	Parallax [mas]	Radius [R/$R_\odot$]	Period [d]
α Ari	2.01	K1III	4636[2]	2.74[2]	-0.24[2]	0.5[10]	6.5[14]	6.9[14]	49.80[19]	14.9*	187.2*
4 Uma	4.61	K1III	4471[2]	2.23[2]	-0.37[2]	2.1[10]	2.1[17]	2.2[17]	12.92[19]	18.3*	54.8*
51 Peg	5.46	G2.5IV	5787[1]	4.45[1]	0.20[1]	2.6[10]	0.7[14]		65.10[19]	1.2*	29.0[20]
11 Com	4.74	G8III	4670[2]	2.38[2]	-0.51[2]	3.0[10]			9.04 [19]		
70 Vir	4.97	G4V	5559[2]	4.05[2]	-0.06[2]	1.4[10]	1.0[15]		55.22[19]	1.9*	35.7[20]
ι Dra	3.29	K2III	4504[2]	2.52[2]	0.03[2]	1.9[10]	3.6[17]	3.7[17]	31.92[19]	12.5*	434 [21]
42 Dra	5.51	K1.5III	4446[2]	2.13[2]	-0.480[2]	1.8[10]	2.0[17]	2.0[17]	10.28[19]	20.9*	73.0*
HD190360	5.71	G7IV	5552[1]	4.38[1]	0.21[1]	2.2[10]	0.7[16]	0.7[16]	62.92[19]	1.2*	3.4*
HD167042	5.95	K1III	5021[2]	3.51[2]	-0.01[2]	0.7[10]			20.00[19]		
ξ Aql	4.71	G9.5III	4807[2]	2.82[2]	-0.25[2]	3.4[10]	1.6[17]	1.7[17]	15.96[19]	11.5*	21.2*
omi Uma	3.42	G5III	5215[6]	2.52[6]	-0.13[6]	3.8[8]	2.4[15]		17.76[19]	14.5*	24.0*
ϵ Crb	4.13	K2III	4532[7]	2.10[7]	-0.23[7]	2.4[9]	2.7[15]	2.8[15]	14.20[19]	21.2*	55.5*
κ CrB	4.82	K0III	4803[2]	3.23[2]	0.17[2]	1.4[9]			32.13[19]		
ϵ Tau	3.53	K0III	5016[2]	2.97[2]	0.10[2]	2.7[9]	2.5[14]	2.7[14]	21.04[19]	13.8*	32.1*
γ Cep	3.22	K1III	4794[2]	3.18[2]	-0.05[2]	1.6[9]	3.1[14]	3.2[14]	72.50[19]	4.7*	18.6*
18 Del	5.51	G6III	5071[2]	3.00[2]	0.10[2]	1.6[10]	0.9[18]	1.0[18]	13.68[19]	7.9*	30.9*
HD210702	5.93	K0III	4957[2]	3.51[2]	-0.05[2]	2.3[9]			17.88[19]		
HD3651	5.88	K0V	5221[1]	4.45[1]	0.16[1]	1.1[9]	0.8[16]	0.8[16]	90.03[19]	1.0*	44.1[20]
HD38529	5.92	G8III	5573[2]	3.81[2]	0.37[2]	1.6[9]	0.6[16]	0.6[16]	23.57[19]	2.7*	37.8[20]
υ And	4.10	F9V	6213[1]	4.25[1]	0.15[1]	9.6[9]	1.1[16]	1.1[16]	74.25[19]	1.6*	1.0*
6 Lyn	5.88	K0III	4964[6]	3.17[6]	-0.18[6]	1.3[10]			17.56[19]		
β Umi	2.08	K4III	4076[6]	1.70[6]	-0.13[6]	1.7[11]	9.6[14]	10.3[14]	25.79[19]	42.9*	158.7*
HD6860	2.05	MOIII	3789[5]	1.60[5]	-0.01[5]	7.2[9]	13.9[14]	14.4[14]	16.36[19]	94.6*	82.6*

6.4 Target stars

We observed a sample of giant and main sequence stars with a confirmed presence of planets, using the spectropolarimeter CAOS in a period between 2014 and 2017.

Targets were selected according to their brightness in V, choosing only stars brighter than 6 mag in order to obtain spectra with a S/N ratio of at least 300 in a reasonable exposure time, considering the small aperture of the telescope of 91 cm.

In order to infer the nature of the magnetic fields, the rotational period of the star is an important parameter. It was not possible to find a rotational period in literature for all the stars in our sample. We found in Simpson et al. (2010) the values for 4 stars: 51 Peg, 70 Vir, HD3651 and HD38529. Moreover, we found in Kane et al. (2010) the orbital period of ι Dra.

The rotational period for all the other cases was determined from the interferometric apparent diameter θ, using the parallax values determined by Hipparcos (ESA, 1997). When possible, it was preferred the use of the limb darkening value θ_{LD} instead than the uniform disk value θ_{UD}. This is because the value of θ_{LD} takes into account the effects of limb darkening and this allows a more accurate determination of the angular diameters of the star (Davis et al., 2000).

Rotational periods were computed using the equation:

$$P_{rot} = \frac{2\pi R_*}{v \sin(i)} \sin(i) \tag{6.17}$$

where the radius R_* was estimated by:

$$R_* = \frac{1}{2} \frac{a * b * 1000}{\pi_p} \frac{1}{R_\odot} \tag{6.18}$$

where a is the constant for the conversion from milliarcsecond to radiant, b is the constant for the conversion from parsec to kilometre, π_p is the parallax in milliarcsecond and $R_\odot$ is the solar radius in km. It is possible to note that period derived in this way is just a lower value estimation, because the uncertain on the inclination angle in v sin(i). The information about the observed stars is reported in Table 6.3

6.5 Results

The results of the effective magnetic field measurements of our sample are reported in Table 6.5.

Table 6.4: Effective magnetic field measurements on the sample of stars observed with CAOS.

Star	JD (2400000+)	Null [G]	Field [G]	N. Lines
		Giant stars with planet		
α Ari	57038.243	0.47 ± 0.87	-2.74 ± 0.87	2131
	57723.407	1.46 ± 0.93	-3.57 ± 0.93	1057
4 Uma	57723.659	1.57 ± 0.84	-6.20 ± 0.84	1337
11 Com	57129.434	0.58 ± 0.52	1.51 ± 0.52	1395

Continued on next page

Table 6.4 – *Continued from previous page*

Star	JD (2400000+)	Null [G]	Field [G]	N. Lines
ι Dra	57131.551	-0.25 ± 0.17	-0.99 ± 0.17	3301
	57203.419	-0.33 ± 0.94	4.37 ± 0.94	1066
	57577.382	0.18 ± 0.87	8.70 ± 0.87	1014
	57584.299	1.19 ± 0.77	0.66 ± 0.77	2184
	57589.349	0.44 ± 0.28	1.03 ± 0.28	1054
42 Dra	57172.560	-0.18 ± 1.79	-3.07 ± 1.79	1492
	57282.283	-5.30 ± 2.60	-3.28 ± 2.60	2956
HD167042	57224.445	-0.65 ± 2.93	2.46 ± 2.93	934
ξ Aql	57221.495	2.69 ± 1.22	3.15 ± 1.22	705
omi Uma	57129.377	-0.85 ± 0.65	-4.79 ± 0.65	1024
ϵ Crb	57185.489	1.09 ± 0.60	-7.66 ± 0.61	935
	57224.330	-0.68 ± 1.52	-0.52 ± 1.52	956
κ CrB	57131.612	-0.31 ± 0.56	-0.29 ± 0.56	887
	57583.379	-2.78 ± 1.53	11.26 ± 1.53	852
ϵ Tau	57039.374	6.24 ± 3.03	-11.97 ± 3.03	1360
γ Cep	56889.603	-2.01 ± 1.02	-0.47 ± 1.02	1751
	56904.551	-0.73 ± 1.53	2.36 ± 1.53	711
18 Del	56921.473	0.17 ± 1.19	26.19 ± 1.19	1011
HD210702	56949.351	4.31 ± 1.76	1.13 ± 1.76	3475
HD38529	57038.431	-2.22 ± 1.54	-0.89 ± 1.54	1913
6 Lyn	57044.410	-3.65 ± 1.76	-4.39 ± 1.76	1270
β Umi	57555.401	1.36 ± 1.55	-9.48 ± 1.55	2357
	Main sequence stars with planet			
51 Peg	57282.443	3.47 ± 2.04	10.68 ± 2.04	700
70 Vir	57132.438	4.32 ± 1.80	-2.32 ± 1.80	1749
HD190360	57222.528	0.15 ± 1.94	-2.95 ± 1.94	675
HD3651	56949.456	1.77 ± 0.95	5.58 ± 0.96	789
υ And	57038.275	5.09 ± 2.71	-5.95 ± 2.72	407

Continued on next page

Table 6.4 – *Continued from previous page*

Star	JD (2400000+)	Null [G]	Field [G]	N. Lines
		M Giant stars		
HD6860	56900.605	2.13 ± 0.97	2.95 ± 0.97	2662
	56904.589	2.66 ± 1.05	-0.28 ± 1.05	1011

LSD Stokes profiles of the observed giant stars with planet are reported in Fig. 6.4, Fig. 6.5, Fig. 6.7, Fig. 6.6 and Fig. 6.5.

A clear magnetic field signal was detected in the case of α Ari, 4 Uma, ι Dra, Omi Uma, ϵ Crb, ϵ Tau, 18 Del and β Umi. They correspond to the 47% of the observed giants with a planet. The presence of a magnetic field of 1.3 ± 0.3 G in ϵ Tau was reported by Aurière et al. (2015), who did not detect any signal in the spectra of α Ari.

Fig. 6.5 shows the LSD profiles for the sample of the main sequence stars hosting planets. Magnetic field signal was detected in the 40% of the cases, in particular for 51 Peg and HD3651.

We reported in Fig. 6.10 the computed LSD profiles of the M star HD6860 (β And), which shows the presence of a very weak magnetic field. We measured also a reversion of the magnetic field for our two observations. This result represents the confirmation of the presence of the magnetic field in this post AGB star, which was marginally detected by Konstantinova-Antova et al. (2010) using the spectropolarimeter NARVAL.

6.5.1 Magnetic field strength vs rotational period

The origin of the magnetic field can be estimated analyzing possible correlations between magnetic field strength and stellar rotation.

In order to consider a larger sample of observations, we included into the analysis the measures of effective magnetic fields on giant stars reported by Aurière et al. (2015) and on main sequence stars obtained by Folsom et al. (2016).

Fig. 6.11 shows the absolute value of the maximum effective magnetic field versus the rotational period.

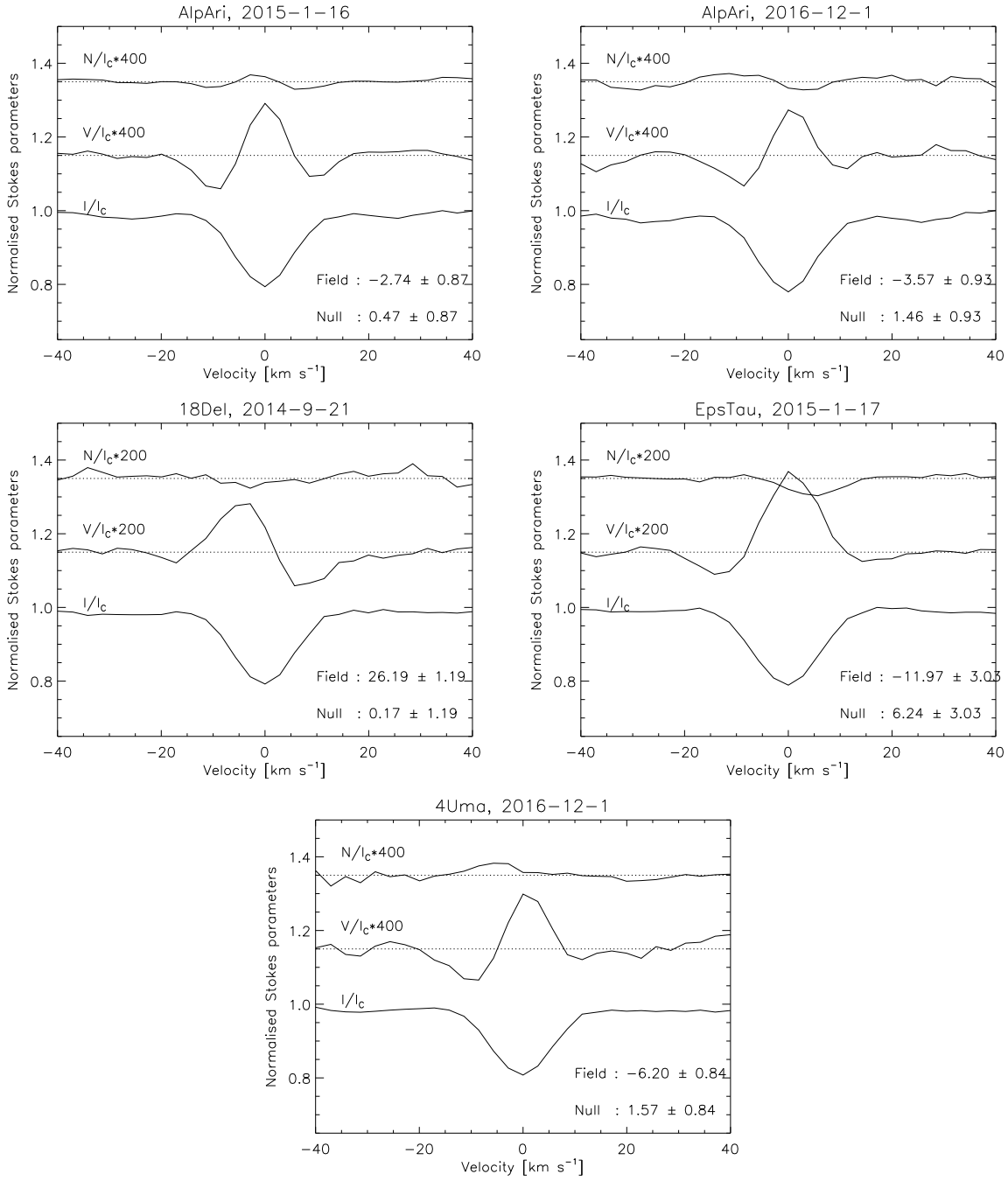

Figure 6.4: LSD profiles of giant stars with planet: α Ari (top), 18 Del (center left), ϵ Tau (center right) and 4 Uma (bottom).

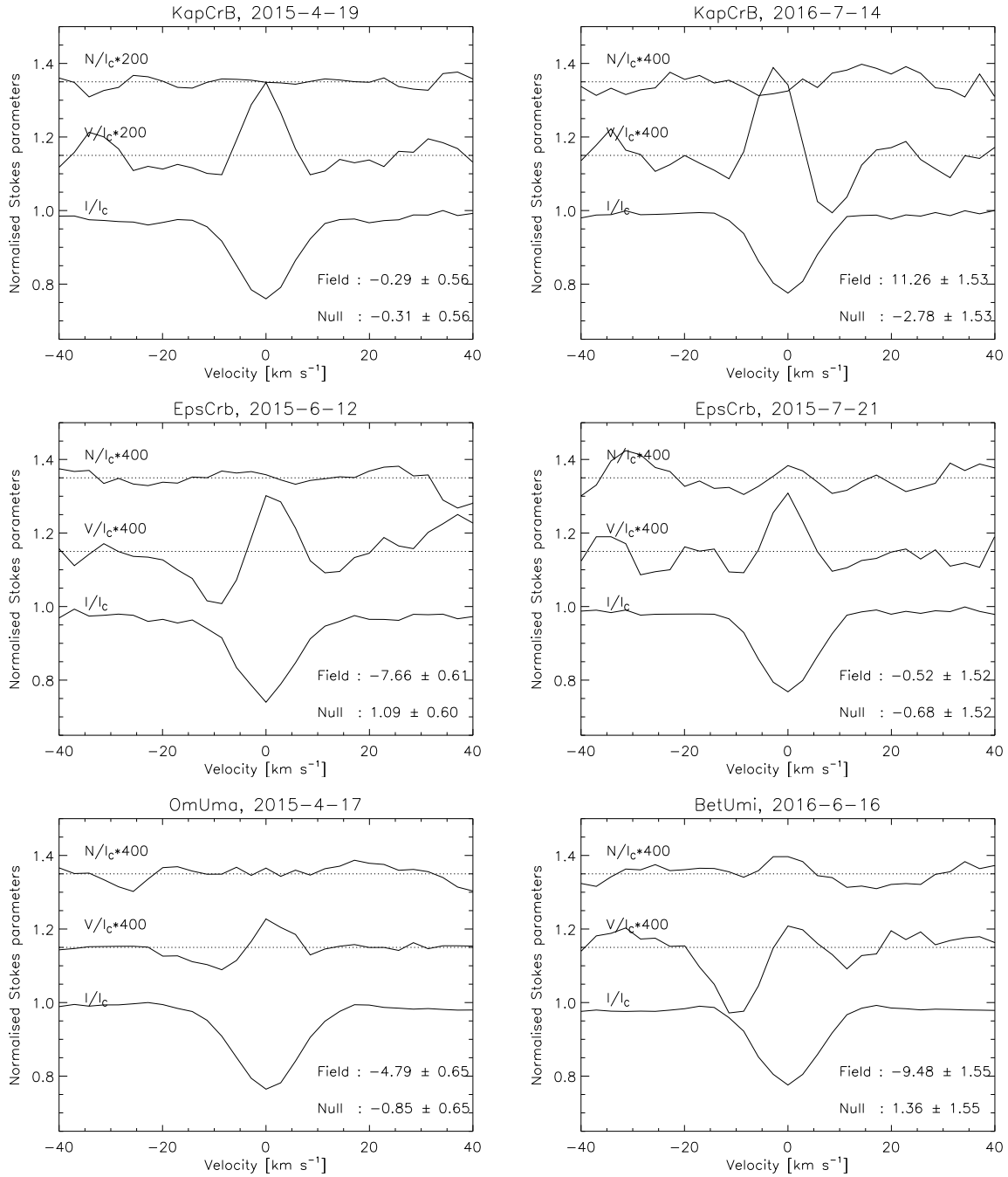

Figure 6.5: LSD profiles of giant stars with planet: κ CrB (top), ϵ CrB (center), Omi Uma (bottom left) and β Umi (bottom right).

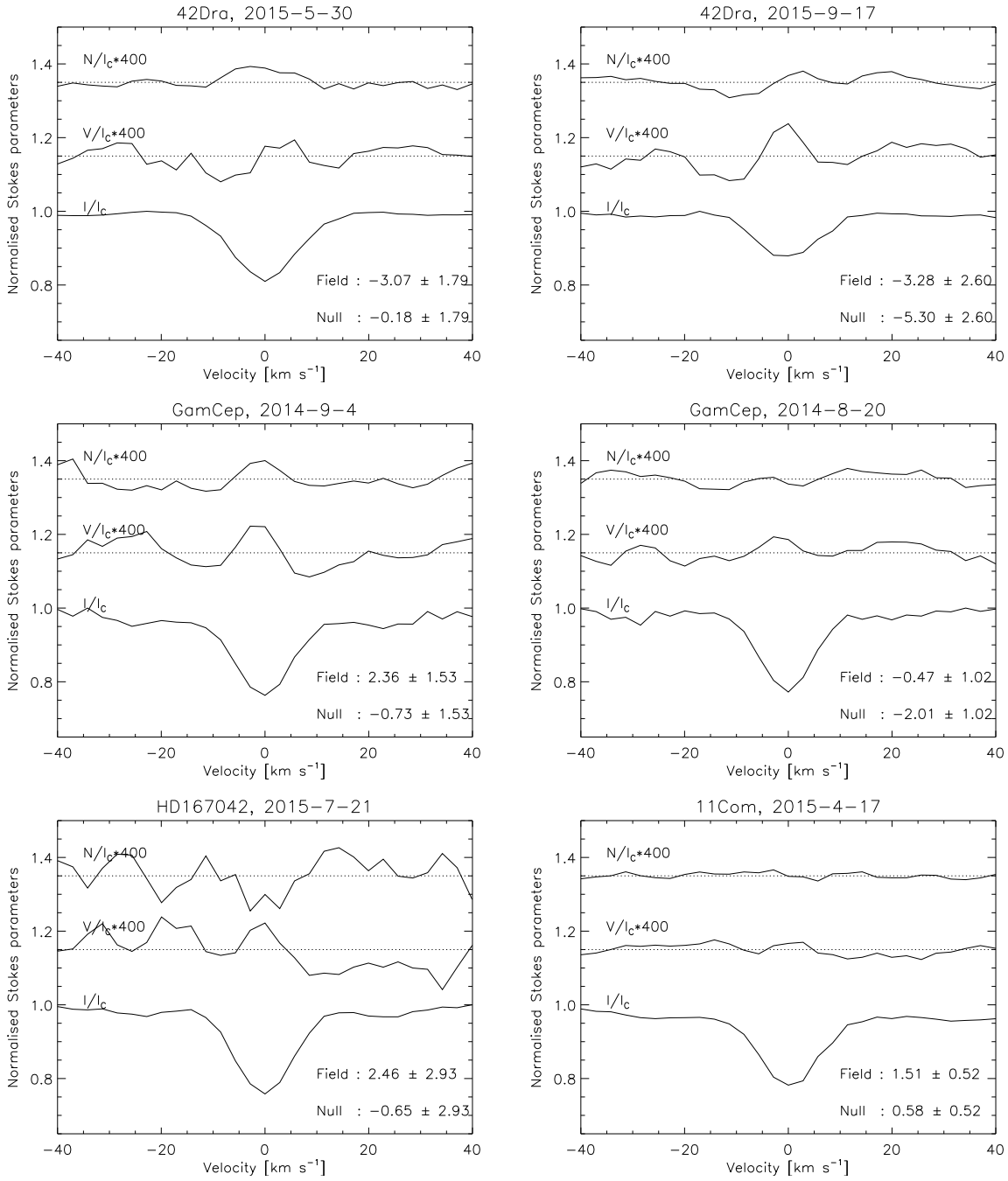

Figure 6.6: LSD profiles of giant stars with planet: 42 Dra (top), γ Cep (center), HD167042 (bottom left) and 11 Com (bottom right).

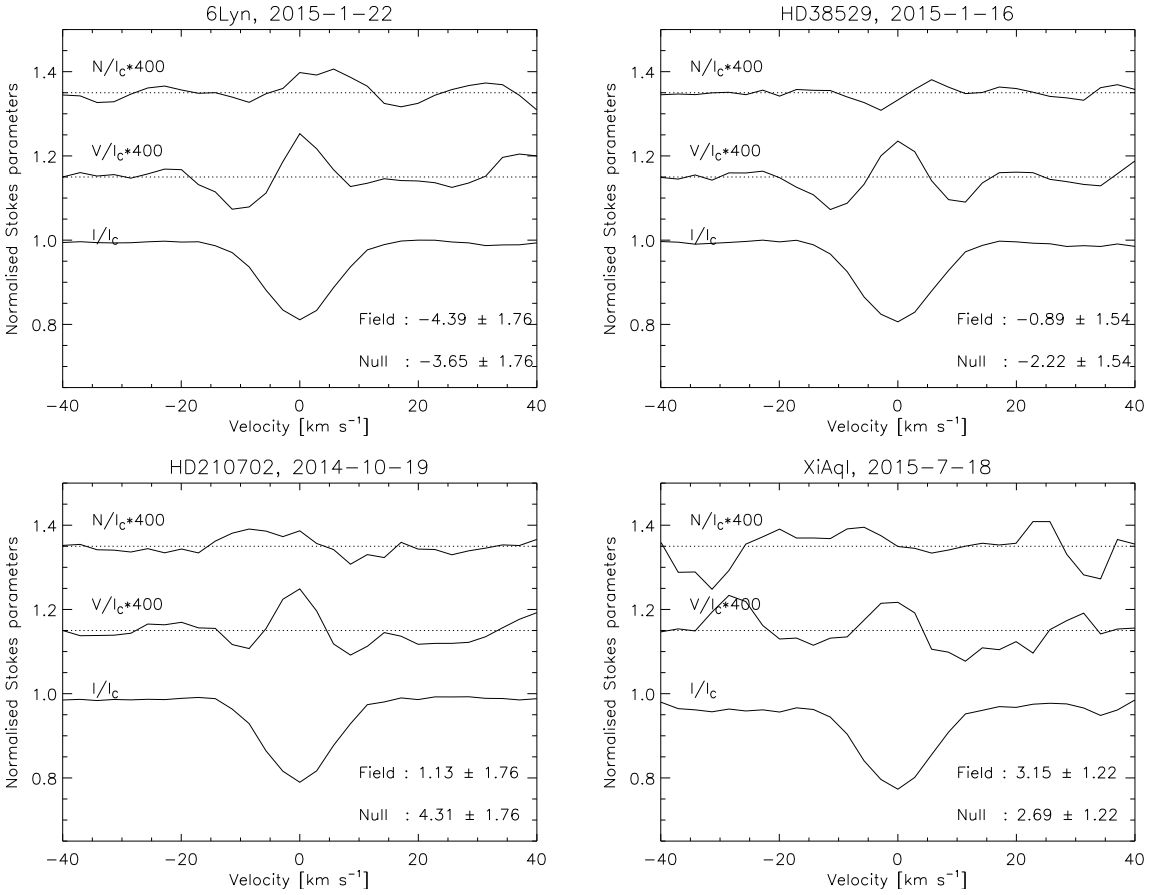

Figure 6.7: LSD profiles of giant stars with planet: 6 Lyn (top left), HD38529 (top right), HD210702 (bottom left) and ξ Aql (bottom right).

It is possible to see a correlation between magnetic field and rotational period similar to Aurière et al. (2015), who explained it considering an operating α-ω dynamo (Durney & Latour, 1978) driven by rotation, like the solar case.

Analysing their sample, Aurière et al. (2015) evaluated the stars OU And, Ek Eri and β Cet as probable Ap descendent, in order to explain their position in Fig. 6.12. However, considering the correlation that we found, only the magnetic field of Ek Eri is uncorrelated with the rotational period.

Another exception in Fig. 6.11 is the AGB M0III giant HD6860. Its position can be explained assuming a wrong estimation of the period or considering different dynamo mechanisms operating in this star, such as an α^2-ω dynamo driven by turbulence (Brandenburg, 2001; Soker & Zoabi, 2002). This could be also the case of the star Pollux, observed by Aurière et al. (2015).

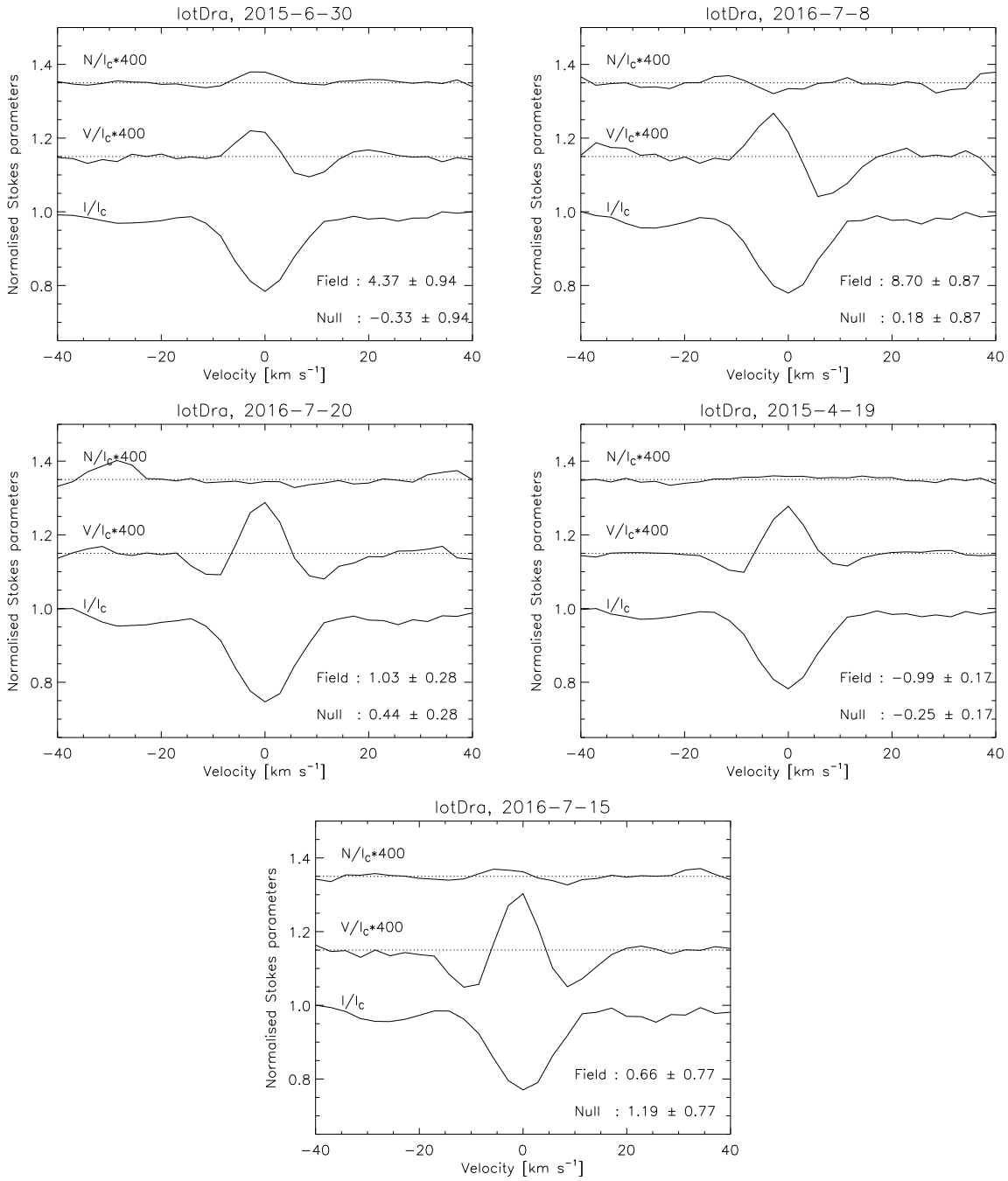

Figure 6.8: LSD profiles of giant star with planet ι Dra.

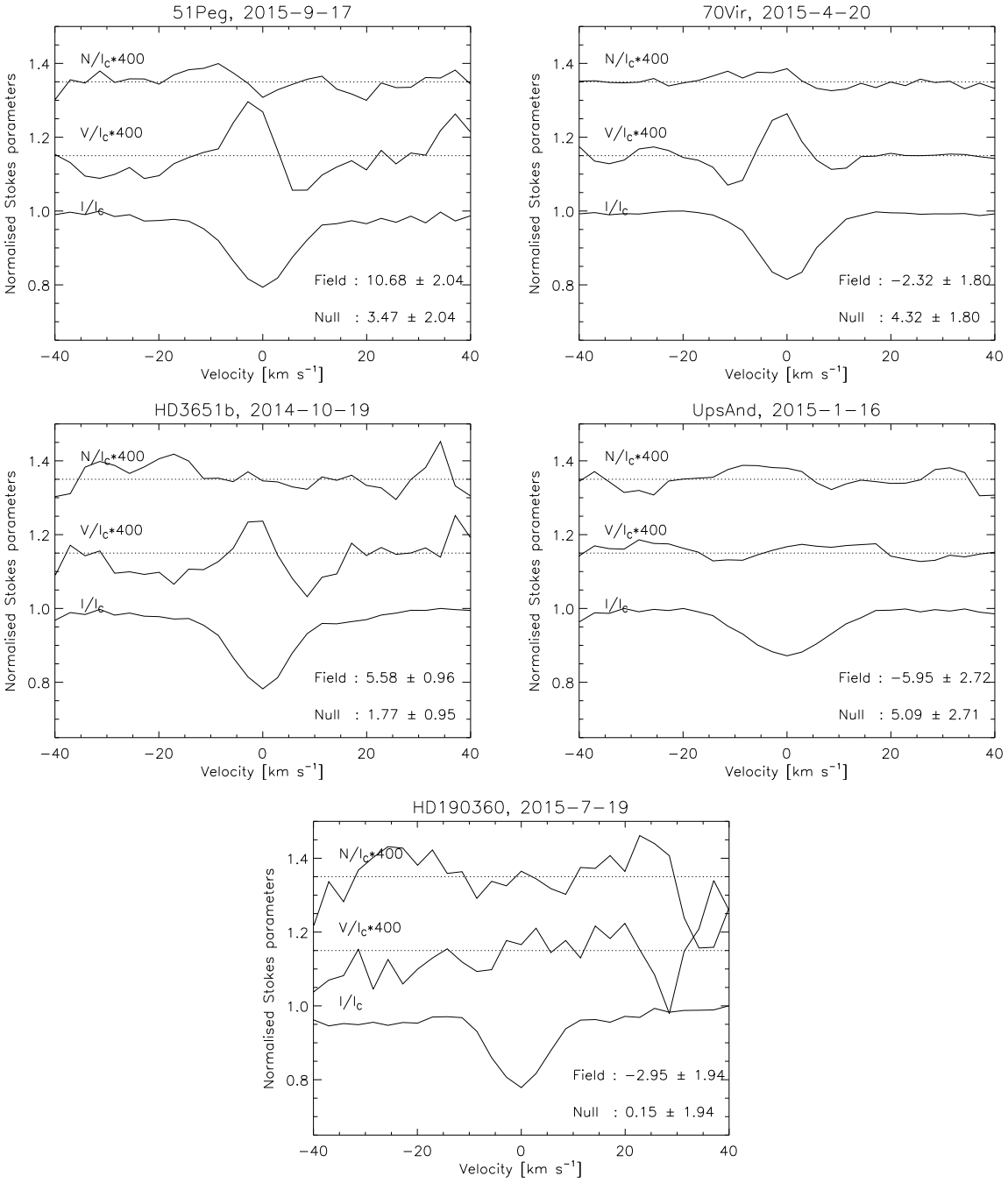

Figure 6.9: LSD profiles of main sequence stars with planet: 51 Peg (top left), 51 Peg (top right), HD3651 (center left), υ And (center right) and HD190360 (bottom).

Figure 6.10: LSD profiles of the MIII stars HD6860 (β And).

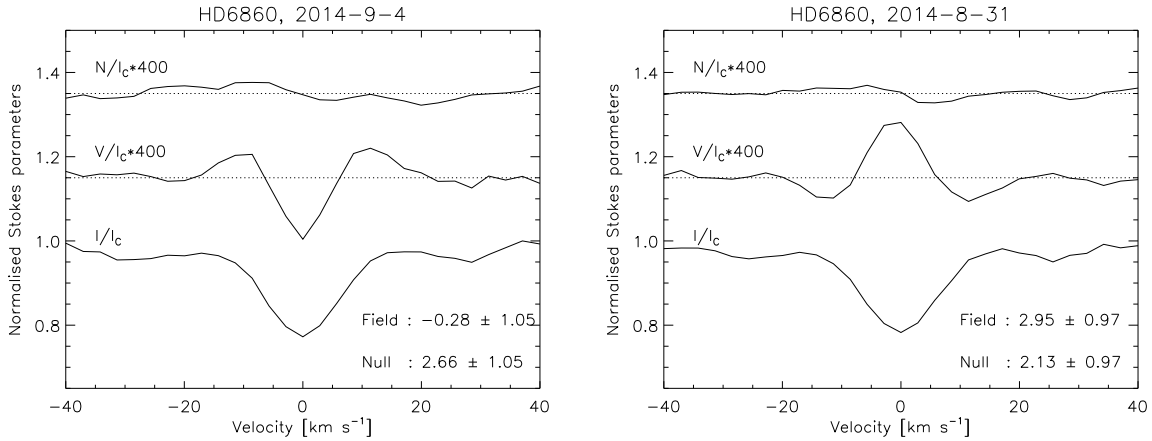

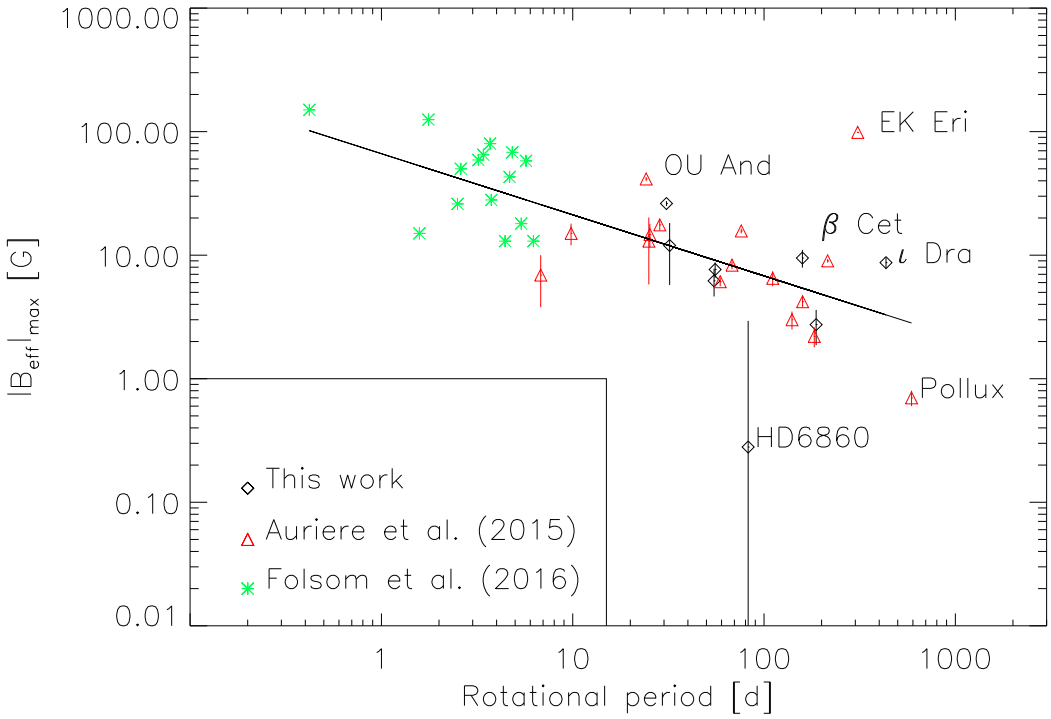

Figure 6.11: Magnetic field strength vs rotational period.

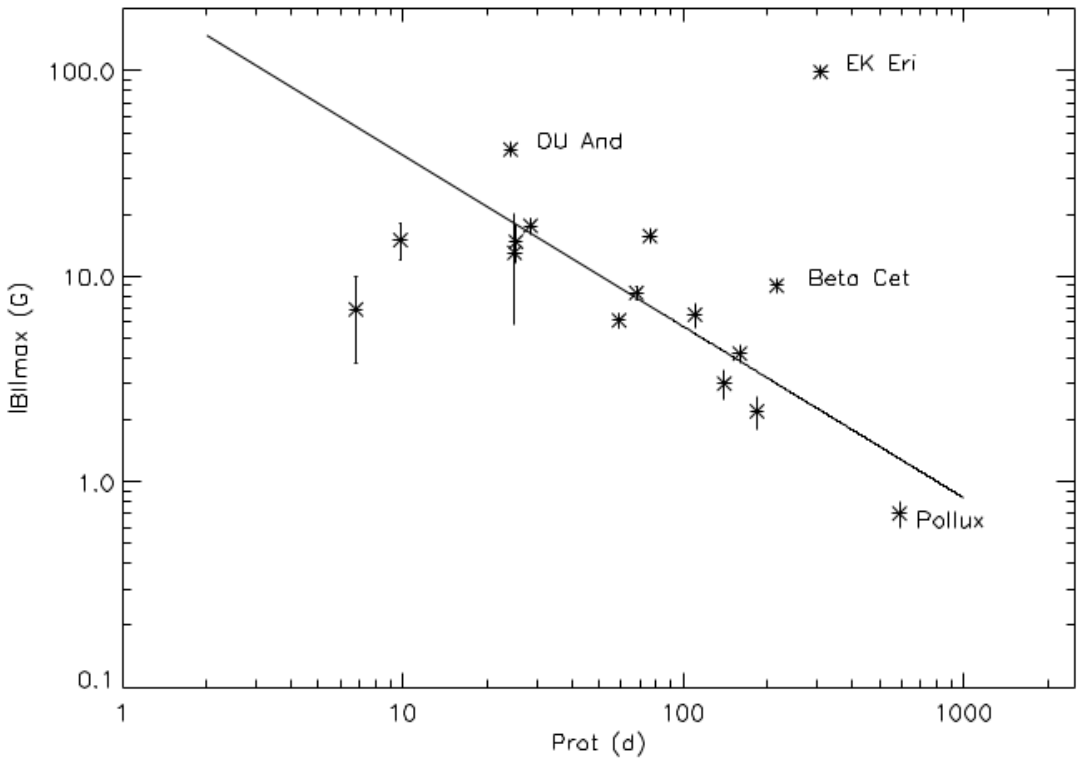

Figure 6.12: Magnetic field strength vs rotational period in the work of Aurière et al. (2015).

6.5.2 Questioning of the exoplanet of ι Dra

The presence of a planet orbiting around ι Dra was first reported by Frink et al. (2002), who presented orbital solutions with large uncertainties because they measured only a single cycle of orbit.

The presence of planet was confirmed by the measures of Zechmeister et al. (2008) and Kane et al. (2010), that reported an orbital period $P_{orbital} = 510.72 \pm 0.07$ d. A mass of $M = 8.82 \pm 0.72\, M_J$ was reported by Butler et al. (2006) and it is one of the biggest planet ever found with the radial velocity technique.

Fig. 6.13 reports the measures of the effective magnetic field of ι Dra folded with the orbital period of the planet. It is possible to note that this period could be compatible with the variation of the magnetic field. However, due to the narrow sampling, the amplitude of the sinusoidal fit is unrealistically large. In order to study possible correlations between the variation of the radial velocity (which are explained by the presence of a planet) and the variation of the magnetic field, more observations are required.

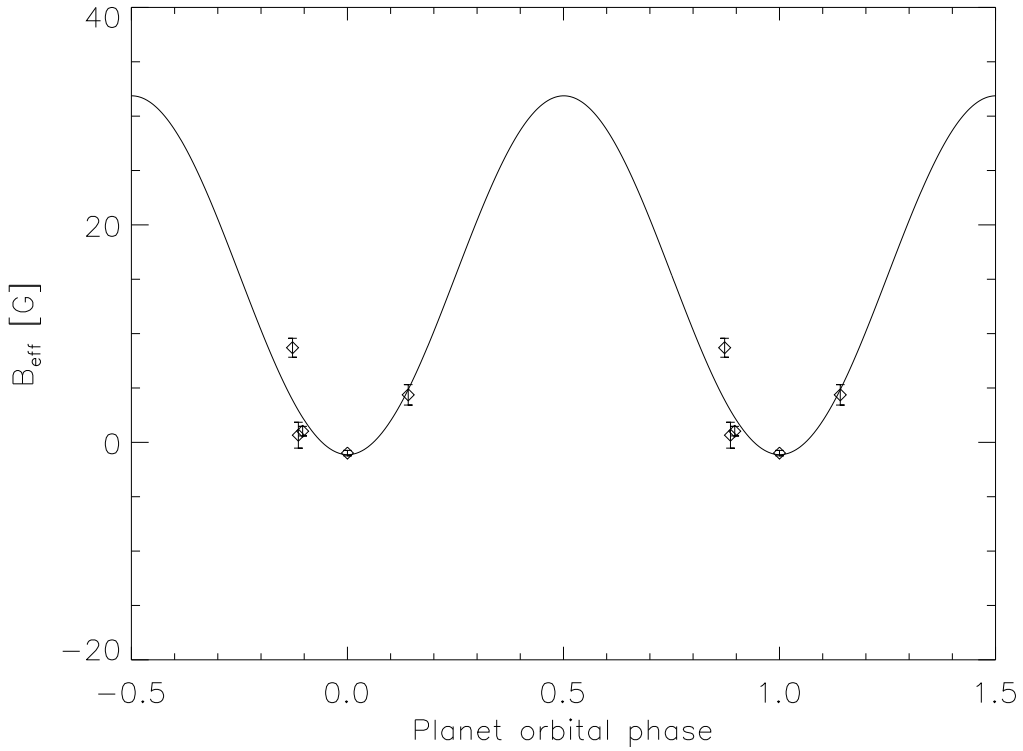

Figure 6.13: Effective magnetic field of ι Dra folded with the rotational period of the planet ι Dra b $P_{orbital} = 510.72$ d (Kane et al., 2010).

CHAPTER 7

THE SLOPE METHOD FOR THE MEASURE OF THE EFFECTIVE MAGNETIC FIELD OF COOL STARS

Magnetic field plays important role in cool stars. It is the key to explain several physical phenomena, such as spots, flares, chromospheric and coronal heating. It is also important for the physics of material accretion on the star (Bouvier et al., 2007), for the formation of exoplanets and for the interaction between stars and planets (Preusse et al., 2006; Strugarek et al., 2015).

One of the first attempt of direct measurement of magnetic fields on cool stars started with the work of Vogt (1980) which was inconclusive because the low level of the signal; it is so low that it is not possible to be detected in individual spectral lines even with the current instrumentation (Reiners, 2012).

Another important pioneering work was performed by Robinson (1980), who attempted to measure the line broadening due to Zeeman splitting in Stokes I. This technique was criticized by several authors, that claimed the difficulties to disentangle the broadening due to the presence of the magnetic field respect to other broadening or small blends. For instance, Anderson et al. (2010) showed how measures of magnetic field from Stokes I are subject to large uncertainties. However, this method is more reliable in the near-infrared region, where the Zeeman splitting is larger (Valenti et al., 1995).

The aim of this chapter is the introduction of a new technique for the measurement of the effective magnetic field from high-resolution spectra of cool stars in polarised light. We extend a technique applied by Bagnulo et al. (2002) for the measure of the magnetic

field of early type stars from low-resolution spectropolarimetric data, called *slope method*. The results of this chapter are published in Scalia et al. (2017).

7.1 The slope method

The slope method measures the longitudinal net field strength from the inclination of Stokes V as a function of the first spectral derivative of Stokes I. The technique is based on Eq. 2.43, which is generally valid in the case of weak fields and for unblended lines.

It is important to note that Eq. 2.43 can be applied only if the shape of the line is given by the magnetic field and it is not dominated by instrumental or rotational broadening.

Bagnulo et al. (2002) applied Eq. 2.43 in order to measure effective magnetic field of magnetic stars from low resolution data (R≤5000) (Fig. 7.1). Early type magnetic stars analyzed on their work present spectral lines with a shape dominated by the magnetic field even in low resolution. In particular, Balmer lines of A and B type stars are suitable for the measure of effective magnetic fields from low-resolution spectra because their large broadening and because weak field regime can be assumed for Hydrogen lines also for magnetic field strengths of the order of 10 kG (Bagnulo et al., 2002). For this reason, Bagnulo et al. (2002) measured the field from individual Balmer lines, considering all the Balmer lines simultaneously and considering all the data point in a range from 370 nm to 575 nm. They pointed out how the use of metallic lines is problematic because they are blended in low-resolution spectra.

The slope method was applied by other authors on stars whose spectra are also dominated by Balmer lines. For instance, RR-Lyr stars were analyzed by Kolenberg & Bagnulo (2009) who did not found any magnetic signal at a level of significance; Leone (2007) applied this technique on chemical peculiar stars observed with the William Hershel telescope in order to test the polarimetric capabilities of the instrument and Leone et al. (2011) estimated and upper limit for the magnetic field on the central stars of planetary nebulae.

7.2 The multi-line slope method

The simultaneous application of the slope method to several spectral lines returns, in principle, a sensitive measure of the effective magnetic field, analogously to the case of radial velocity where thousand of spectral lines are used for the computation of the cross-correlation function.

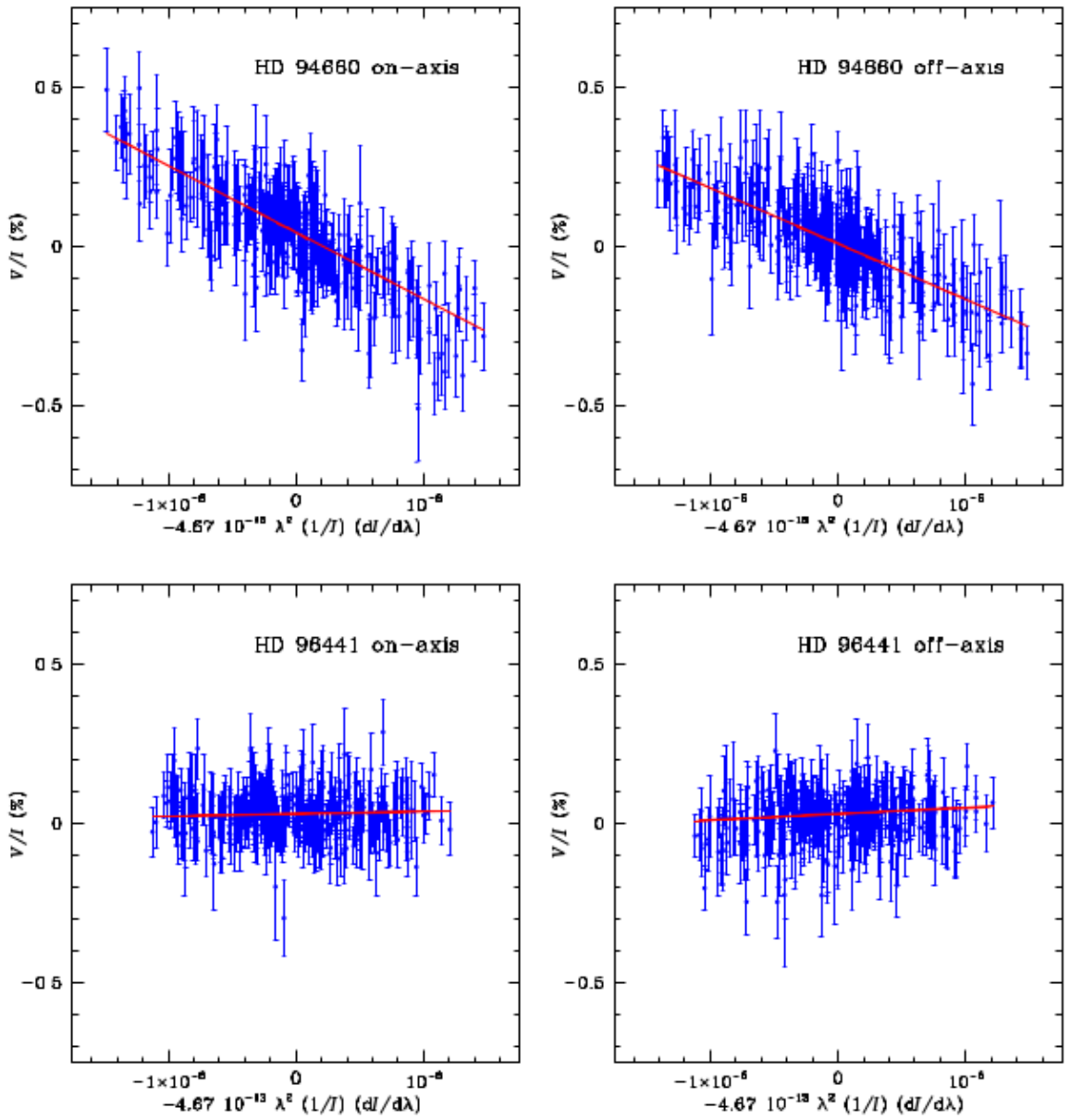

Figure 7.1: Slope method applied to the magnetic star HD 94660 (top) and to a non magnetic star (bottom) observed with the low resolution instrument FORS1 (Bagnulo et al., 2002). Observations were performed on-axis (at centre of the CCD) and off-axis (at the edges of the CCD) in order to exclude systematics on the measurement.

We proposed a new technique, called *multi-line slope method*, as a multi line extension of the slope method for the measurement of the effective magnetic field from high resolution observations. This approach presents the advantage of the use of the correct value of g_{eff} for each line. Indeed, average Landé factors were used by several authors, such as Leone (2007), although it limits the accuracy of the measure. An estimation of the uncertainties due to the use of a not correct Landé factors was made by Bagnulo et al. (2012), that showed how the circular polarization can vary from the average by a factor of 25%.

As all the multi line techniques, the selection of spectral lines is a critical issue. The first line list is obtained by a synthetic spectrum of the star computed by SYNTHE (Kurucz, 1993a; Sbordone et al., 2004) using a given value of T_{eff} and $\log g$. Atomic parameters are taken from VALD database (Piskunov et al., 1995). From this list, we excluded all the transitions in the region of strong lines, like Hα and Hβ, telluric lines and lines weaker than the noise level. Broad and strong spectral lines were excluded in order to avoid line cores that are dominated by saturation rather than magnetic field. We excluded also lines with effective Landé factor lower than 0.7 in order to avoid regions with no information about the magnetic field.

A big effort of the line selection was the removal of line blends. Several algorithms were tried for this purpose. First, we tried to use a multi-gaussian fit to estimate the blends. However, this approach resulted to be not efficient because the slowness of the computation for thousand of spectral lines and the inability to choose a priori the number of Gaussians to use. A faster method was found analyzing the width of the lines in the velocity space. Taking advantage on the fact that data were taken with echelle spectrograph, where $\frac{\Delta\lambda}{\lambda} \approx$ constant, we evaluated the position of the centroid and the FWHM (in $\mathrm{km\,s^{-1}}$) of each line through a Gaussian fit, excluding all the transitions whose radial velocity and FWHM was distant more than 3σ from the averaged value. Fig. 7.2 shows examples of selected and unselected lines on the case of a spectra of ϵ Eri obtained by HARPSpol ($R \approx 115000$) on 5^{th} January 2010.

Another source of uncertainties on the measure is the normalization for the pseudo continuum level which impacts Stokes I and his derivative (Bagnulo et al., 2012). It was evaluated by a linear fit of the highest ten point in a a region of 3 Å respect to the central wavelength, half on the left and half on the right (Fig. 7.3).

The presence of spikes due to cosmic rays and spurious points on the spectra are removed by a 5σ clipping on the null profile (Bagnulo et al., 2006). This is possible assuming that the presence of systematic errors in the spectra is evinced by a not flat

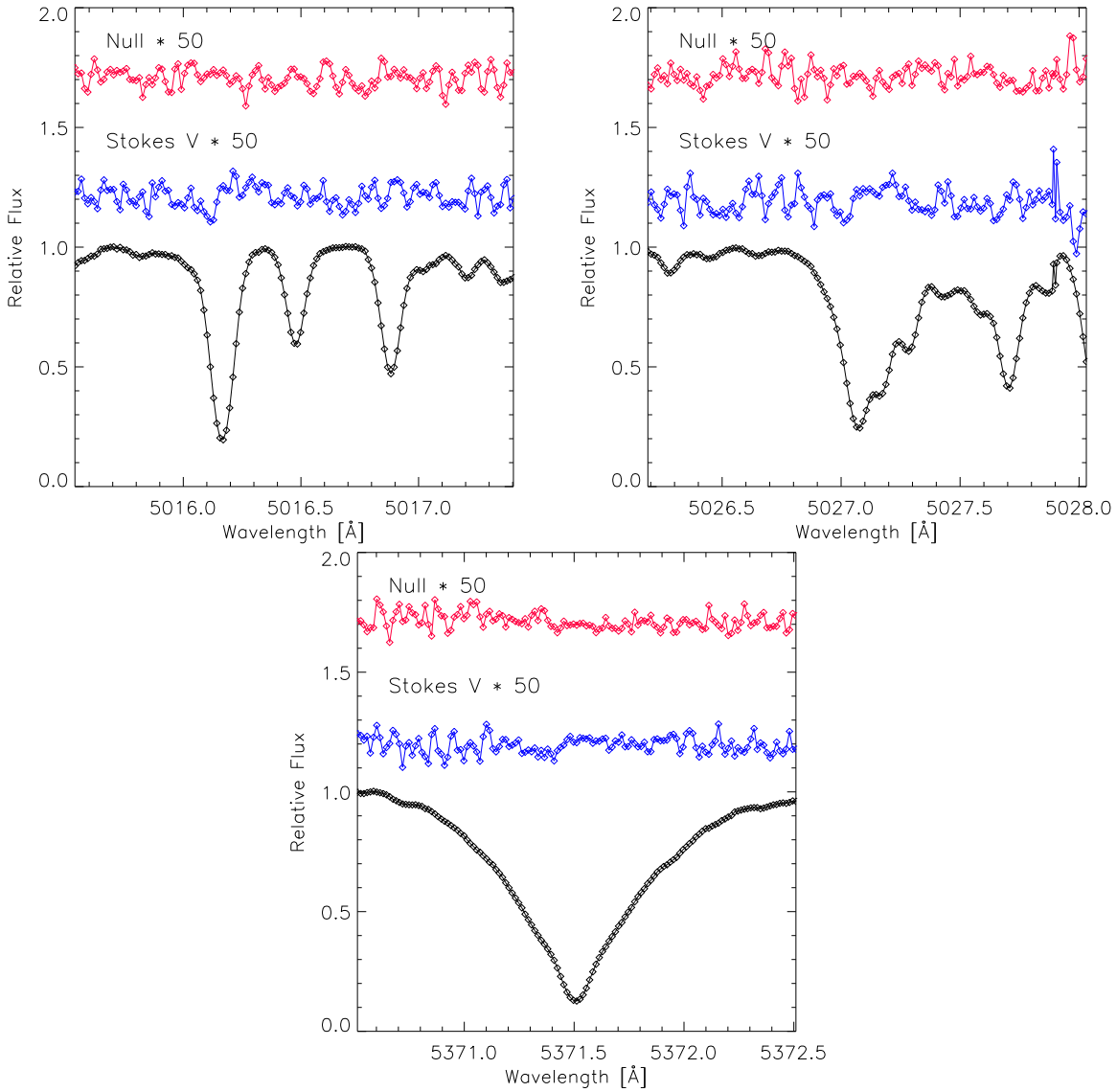

Figure 7.2: Examples of selected unblended lines (top left), unselected blend lines (top right) and unselected strong lines (bottom) for a spectra of ϵ Eri observed with HARPSpol on 5^{th} January 2010.

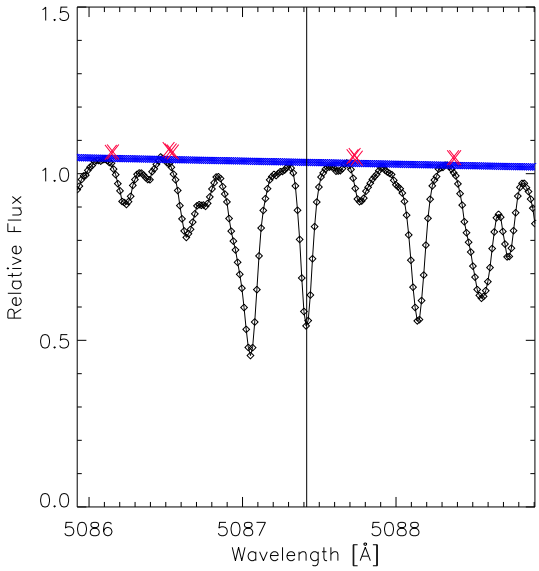

Figure 7.3: Example of normalisation of Stokes I. The red crosses refer to the points used for the computation of the linear fit, which is reported in blue.

distribution of the null profile.

We computed the quantity x_{ij}:

$$x_{ij} = -4.67\,10^{-13}\,\lambda_{0j}^2\,g_{eff_j}\,\frac{1}{I_{ij}(\lambda)}\,\frac{dI_{ij}(\lambda)}{d\lambda_{ij}} \tag{7.1}$$

where i spans over the pixels and j spans over the line. We computed the quantity $\frac{dF_{I_{ij}}(\lambda)}{d\lambda_{ij}}$ using a 3-point Lagrangian interpolation (Bevington & Robinson, 2003).

The effective magnetic field was measured by the minimization of the χ^2:

$$\chi^2 = \sum_{ij} \frac{\left(y_{ij} - \langle B_l \rangle\, x_{ij} - b\right)^2}{\sigma_{ij}^2} \tag{7.2}$$

where b is a constant term related to the residual instrumental polarization (Bagnulo et al., 2002)

We used $y_{ij} = \frac{V_{ij}}{I_{ij}}$ for the measurement of the magnetic field and $y_{ij} = \frac{N_{ij}}{I_{ij}}$ for the estimation of systematic errors (see Sect. 3.5). The total error was computed as the quadratic sum of the systematic error and standard error of the fit.

We reported on Fig. 7.4 examples of magnetic field measures obtained by the multi-line slope method using the high resolution observations of ϵ Eri obtained by HARPSpol.

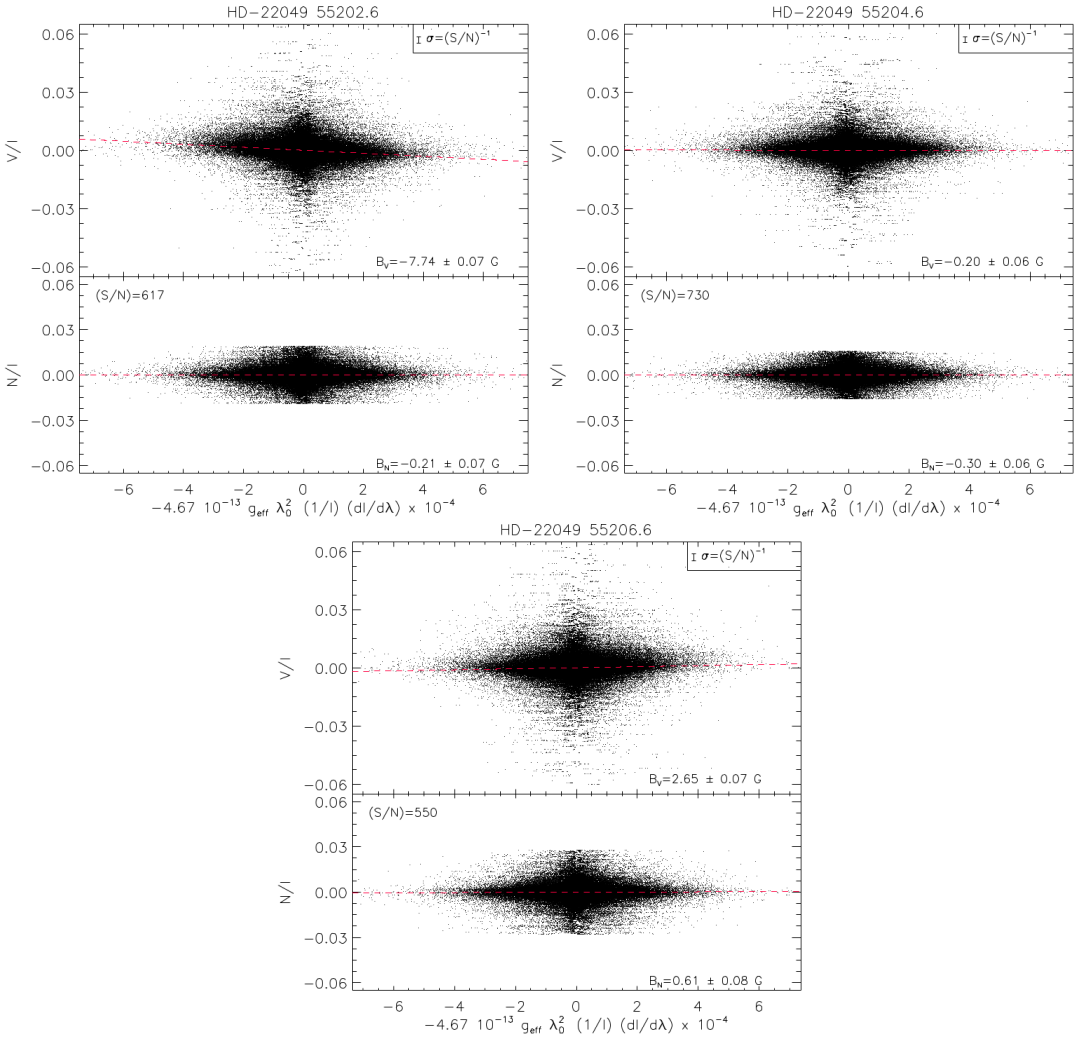

Figure 7.4: Magnetic field measurements of ϵ Eri from HARPSpol data. Top and bottom panels report respectively Stokes V and the null profiles as a function of the spectral derivative of Stokes I. It is possible to note that the presence of the field is evinced by the slope of the distribution of Stokes V. A flat distribution of the null profile indicates a good quality of the measure. The figure refers, from top to the bottom, to the observation made on the nights of 5, 7 and 9 January 2010. The sizes of the typical error bars are shown in the figures and the S/N is calculated from the standard deviation of the points of the null profile. About 3900 lines are used in the measures.

Table 7.1: Results of effective magnetic field measurements from the multi-line slope method ($B_{\rm ms}$) and from the slope method and from the slope method applied on all the simulated data points in the spectral region ($B_{\rm slope}$) vs rotational velocity. The input effective magnetic field is $B_{\rm inp}$ = -6.45 G.

	CAOS R=55000 2.5 px per FWHM					NARVAL R=65000 2.5 px per FWHM					HARPSpol R=115000 4.1 px per FWHM				
v sin(i) [kms^{-1}]	$B_{\rm ms}$ [G]	$\Delta B_{\rm inp-ms}$ (%)	Lines	$B_{\rm slope}$ [G]	$\Delta B_{\rm inp-slope}$ (%)	$B_{\rm ms}$ [G]	$\Delta B_{\rm inp-ms}$ (%)	Lines	$B_{\rm slope}$ [G]	$\Delta B_{\rm inp-slope}$ (%)	$B_{\rm ms}$ [G]	$\Delta B_{\rm inp-ms}$ (%)	Lines	$B_{\rm slope}$ [G]	$\Delta B_{\rm inp-slope}$ (%)
0	-6.59	2	697	-8.60	33	-6.69	4	697	-8.46	31	-6.33	-2	697	-7.72	20
3	-7.28	13	688	-9.18	42	-7.21	12	688	-9.12	41	-7.08	10	688	-8.83	37
6	-8.13	26	615	-10.04	56	-8.24	28	615	-10.15	57	-8.20	27	615	-10.17	58
9	-8.49	32	537	-10.57	64	-8.66	34	537	-10.67	65	-8.57	33	537	-10.53	63
12	-8.53	32	411	-10.72	66	-8.51	32	411	-10.70	66	-8.44	31	411	-10.48	63
15	-8.74	35	301	-10.74	66	-8.69	35	301	-10.67	65	-8.50	32	301	-10.43	62
18	-8.85	37	236	-10.80	67	-8.64	34	236	-10.57	64	-8.54	32	236	-10.43	62
21	-8.99	39	187	-10.74	67	-9.08	41	187	-10.66	65	-8.80	36	187	-10.39	61
24	-9.43	46	146	-10.77	67	-9.31	44	146	-10.57	64	-9.17	42	146	-10.31	60
27	-9.29	44	104	-10.60	64	-9.40	46	104	-10.67	65	-9.23	43	104	-10.29	60
30	-9.92	54	61	-10.58	64	-10.37	61	61	-10.65	65	-10.02	55	61	-10.29	60
33	-10.79	67	48	-10.76	67	-10.31	60	48	-10.80	67	-10.25	59	48	-10.34	60

7.3 Numerical tests

The multi-line slope method was tested using synthetic spectra computed by COSSAM. Simulated spectra were convolved for the spectral resolution of the instruments CAOS (R ≈ 55000), NARVAL (R ≈ 65000) and HARPSpol (R ≈ 115000). We considered a pixel sampling per FWHM of 2.5 for CAOS and NARVAL and 4.1 for HARPSpol[1].

Synthetic spectra were computed considering a large scale dipolar magnetic field centered on the star, with i = 135°, β = 50°and zero phase.

Simulations were computed in order to test:

- the effects of the magnetic field strength on the measure;
- the capabilities of the technique to retrieve the result in presence of a finite S/N ratio;
- the impact of the magnetic field geometry;

The first simulation tested the effects of rotational velocity on the measurements. This is particularly important in order to numerically verify the validity of Eq. 2.43 at the increasing of the rotational velocity since the relation was obtained in the approximation of low rotational velocity. Results are showed in Table 7.1. For values of the rotational

[1] http://www.eso.org/sci/facilities/lasilla/instruments/harps/inst/description.html

Table 7.2: Results of effective magnetic field measurements from the multi-line slope method (B_{ms}) and from the slope method applied on all the simulated data points in the spectral region from 500 nm to 600 nm (B_{slope}) vs effective magnetic field strength. The rotational velocity is v sin(i) =3 km s^{-1}.

	CAOS R=55000 2.5 px per FWHM					NARVAL R=65000 2.5 px per FWHM					HARPSpol R=115000 4.1 px per FWHM				
B_{inp} [G]	B_{ms} [G]	ΔB_{inp-ms} (%)	Lines	B_{slope} [G]	$\Delta B_{inp-slope}$ (%)	B_{ms} [G]	ΔB_{inp-ms} (%)	Lines	B_{slope} [G]	$\Delta B_{inp-slope}$ (%)	B_{ms} [G]	ΔB_{inp-ms} (%)	Lines	B_{slope} [G]	$\Delta B_{inp-slope}$ (%)
0.63	0.66	5	1344	0.91	43	0.72	13	1344	0.93	46	0.70	10	1344	0.89	40
6.35	7.37	16	1342	9.23	45	7.17	13	1342	9.09	43	7.07	11	1342	8.87	40
65	75	18	1348	91	44	75	18	1348	91	43	73	15	1348	88	39
635	684	8	1341	819	29	681	7	1341	815	28	649	2	1341	788	24
3175	2323	-27	675	2740	-14	2155	-32	675	2495	-21	1516	-52	675	1697	-47

Table 7.3: Results of the effective magnetic field measurements from the multi-line slope method (B_{ms}) and from the slope method applied on all the simulated data points in a region from 500 nm to 550 nm (B_{slope}) in the case of a dipole shifted from the centre of the star.

	CAOS R=55000 2.5 px per FWHM					NARVAL R=65000 2.5 px per FWHM					HARPSpol R=115000 4.1 px per FWHM				
B_{inp} [G]	B_{ms} [G]	ΔB_{inp-ms} (%)	Lines	B_{slope} [G]	$\Delta B_{inp-slope}$ (%)	B_{ms} [G]	ΔB_{inp-ms} (%)	Lines	B_{slope} [G]	$\Delta B_{inp-slope}$ (%)	B_{ms} [G]	ΔB_{inp-ms} (%)	Lines	B_{slope} [G]	$\Delta B_{inp-slope}$ (%)
-1.45	-1.34	-7	350	-1.77	22	-1.34	-8	362	-1.78	23	-1.26	-13	384	-1.70	17

Table 7.4: Results of effective magnetic field measurements from the multi-line slope method (B_{ms}) vs S/N ratio. The input effective magnetic field is B_{inp} = 6.35 G and v sin(i) = 3 km s^{-1}. σB_{ms} is the standard deviation of the measures in the simulation (details in the text). The spectral region is between 500 nm to 600 nm.

	CAOS R=55000 2.5 px per FWHM				NARVAL R=65000 2.5 px per FWHM				HARPSpol R=115000 4.1 px per FWHM			
S/N	B_{ms} [G]	σB_{ms} [G]	ΔB_{inp-ms} (%)	Lines	B_{ms} [G]	σB_{ms} [G]	ΔB_{inp-ms} (%)	Lines	B_{ms} [G]	σB_{ms} [G]	ΔB_{inp-ms} (%)	Lines
100	4.18	5.50	-34	1274	6.13	4.88	-3	1348	5.98	1.66	-6	1537
250	8.13	1.88	28	1310	7.34	2.21	16	1375	6.90	0.63	9	1512
500	7.18	1.62	13	1322	7.14	0.66	12	1382	6.76	0.34	6	1517
1000	7.41	0.50	17	1333	7.13	0.34	12	1389	6.92	0.18	9	1519

velocity lower than $5\,\mathrm{km\,s^{-1}}$, the results of the multi-line slope method differ respect to the input by the order of 20%. Increasing the rotational velocity, the difference increase and it is up to 50% for $\mathrm{v\sin(i)} \geq 25\,\mathrm{km}\ s^{-1}$. We explained it by the fact that large rotational velocity values impact the shape of the line profile and its derivative in a non-negligible way; moreover, the number of blends increases with the rotational velocity and, consequently, the number of lines used decrease and it results in a lower accuracy of the measure.

The second simulation tested the effects of the effective magnetic field strength in the measure in the case of low rotational velocity, set at $\mathrm{v\sin(i)} = 3\,\mathrm{km\,s^{-1}}$. Table 7.2 shows the results. The multi-line slope method gave results that differ by some 20% from the input value for field strength less than 1000 G. We found that the method tends to underestimate the field for values larger than 1 kG and the discrepancy increases with the spectral resolution. These behaviors can be explained considering that Zeeman splitting dominates at large field value and it impacts the shape of Stokes I and his first derivative. This effect is smeared in the case of low resolution and it impacts larger high-resolution observations.

In order to test the impact of a different magnetic field geometry on the simulations, we considered also the case of a measure of the effective magnetic field resulting from a decentered dipole model (Stift, 1974, 1975), shifting the dipole from the center of the star. Measures are reported in Table 7.3 and they show that the simulations are not impacted by the choice of the large scale magnetic field geometry.

Resuming, we found that the multi-line slope method can be used in the case of:

- rotational velocity lower than $5\,\mathrm{km\,s^{-1}}$
- effective magnetic field strength lower than 1 kG

Moreover, Table 7.1 and Table 7.2 show the advantage of the line selection respect to the use of the entire spectral region with an average Landé factor. It is possible to note that the results of the multi-line slope method are closer to the input better than 20% and this behavior is systematic except for the case of large field strengths, that is outside of the range of validity of this technique.

7.4 Noise simulations

Previous simulations were performed without the inclusion of the effects of degradation due to the finite integration time of real exposures.

The impact of the S/N ratio was taken into account generating random numbers, from a normal distribution with a mean zero and a standard deviation of one, and dividing they by the wanted value of S/N and by the square root of the synthetic Stokes I. This noise η was added on the combination of Stokes profiles:

$$\begin{aligned} s_1 &= (I+S)+\eta \\ s_2 &= (I-S)+\eta \end{aligned} \tag{7.3}$$

that was used to compute the noise synthetic profiles $\widetilde{\mathrm{I}}$ and $\widetilde{\mathrm{S}}$ through:

$$\begin{aligned} \widetilde{I} &= \tfrac{s_1+s_2}{2} \\ \widetilde{S} &= \tfrac{s_1-s_2}{2} \end{aligned} \tag{7.4}$$

For each synthetic spectra, we measured the field 100 times changing the random numbers used for the noise and we computed the average $\mathrm{B_{ms}}$ and a standard deviation $\sigma\mathrm{B_{ms}}$. Results are showed in Table 7.4. It is possible to note that, in the case of a low effective magnetic field, the errors and the differences between input and results decrease with the resolution. Moreover, we found that a minimum S/N of 250 is needed in Stokes V in order to measure the effective magnetic field with a significance level of 3σ in the case of CAOS resolution.

7.5 Comparison with the Least Square Deconvolution technique

As showed in Sect. 6.1, one of the most used technique for measure magnetic fields in cool stars is the *Least Squares Deconvolution* which consists in the addition of thousand of spectral lines in one pseudo profile that can be used for the estimation of the effective magnetic field from Eq. 6.15.

In order to compare results of the two techniques, we applied the multi-line slope method to the spectropolarimetric data set of ϵ Eri obtained by HARPSpol in January 2010, previously published by Piskunov et al. (2011) and whose numerical values are reported in Olander (2013).

Results of the comparison are showed in Fig. 7.5. The results of the two methods are in general agreement; however, the multi-line slope method returns values systematically lower than the values of the LSD. The reason of it is not clear and it can be explained by different data reduction procedure because we did not found the reduced data in the ESO archive.

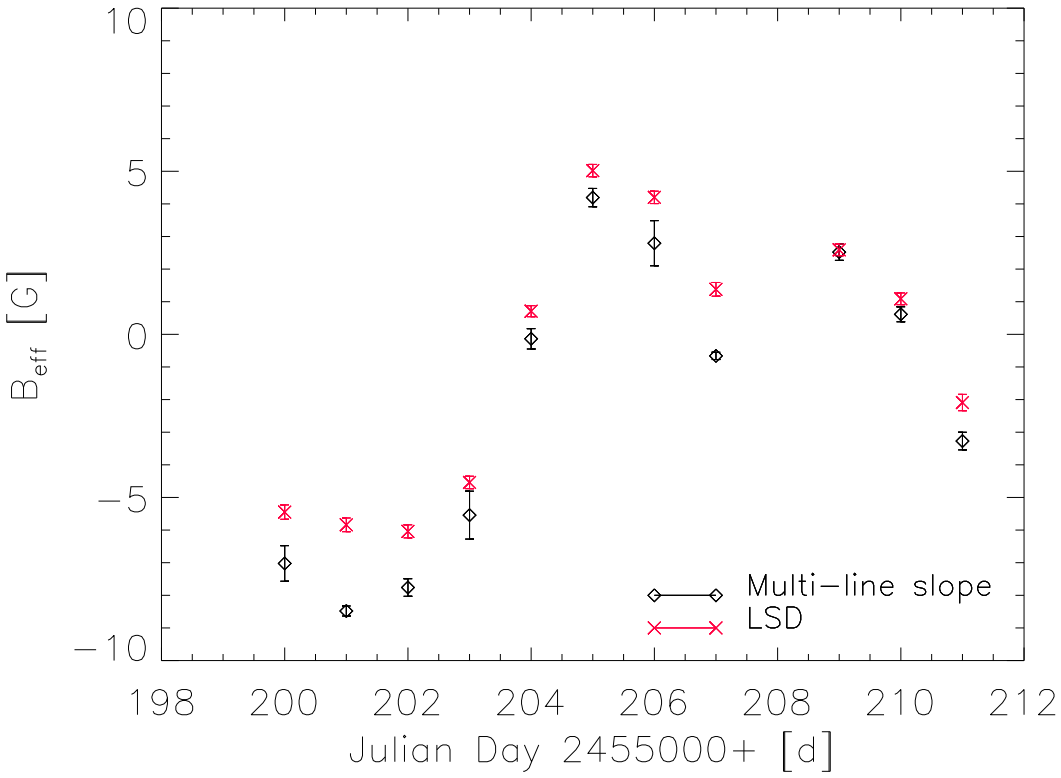

Figure 7.5: Comparison between the multi-line slope method (black) and LSD (red) for the ϵ Eri HARPSpol observations from the year 2010 (Piskunov et al., 2011; Kochukhov et al., 2011; Olander, 2013).

We concluded that the multi-line slope method can be an alternative to the LSD for the measure of the effective magnetic field of late type stars. It has the advantage to be easier to implement and faster to compute although LSD can retrieve the shape of the profile, which allows to detect the field also in stars with magnetic configurations with zero average value. At least in principle, the slope method can also point out a zero average field when the V/I scatter is larger than N/I scatter, as showed in Fig. 7.6.

7.6 Magnetic field of Epsilon Eridani

Epsilon Eridani (HD 22049, HIP 16537) is a bright (M_V=3.73 mag Ducati (2002)) K2V star (Keenan & McNeil, 1989) and one of the most studied solar analogue. It has an effective temperature of 5146 K, a mass of 0.856 $M_{\odot}$ and a v sin(i)= 2.4 km s^{-1} (Valenti & Fischer, 2005).

The long term variation of the magnetic field of ϵ Eri was studied by Jeffers et al.

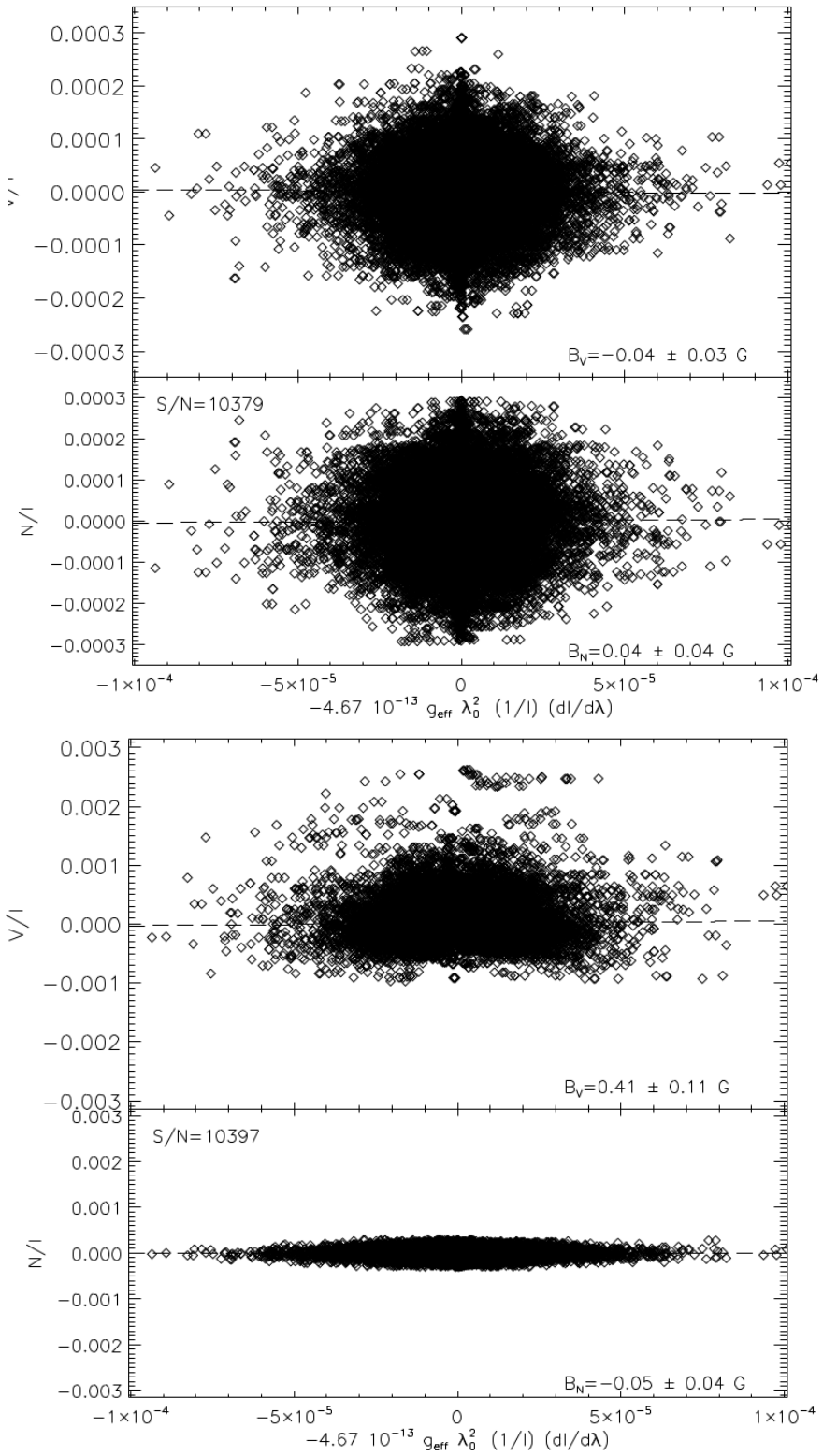

Figure 7.6: Comparison between the multi-line slope method (black) and LSD (red) for the ϵ Eri HARPSpol observations from the year 2010 (Piskunov et al., 2011; Olander, 2013).

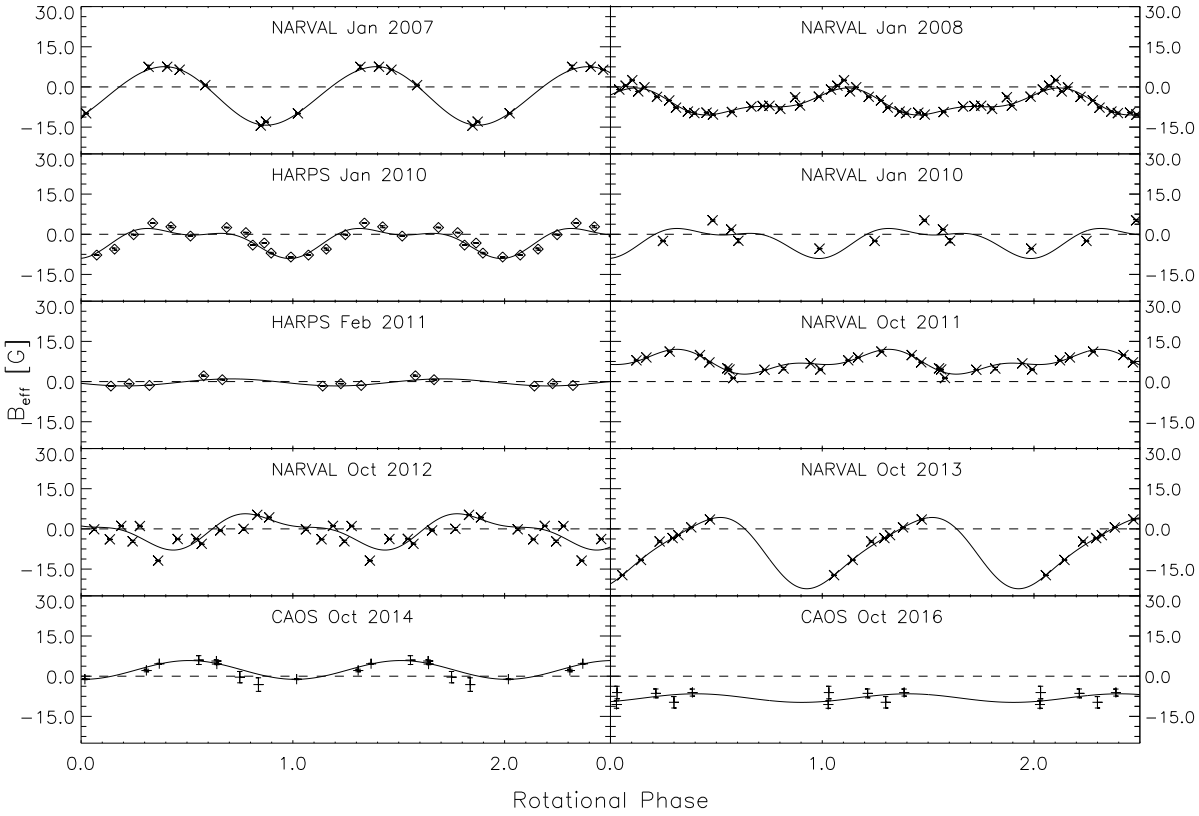

Figure 7.7: Magnetic curves of ϵ Eri folded with the period of rotation of the star P_{rot}= 11.35 d (Fröhlich, 2007). Cross, diamonds and plus refer to observations obtained respectively with NARVAL, HARPSpol and CAOS. Zero phase is equal to MJD 54101 (Jeffers et al., 2014). Magnetic curves are obtained by a fitting through Eq. 7.5 (see text).

(2014), who collected spectropolarimetric observation of Stokes V for six different epochs using NARVAL and HARPSpol, from 2007 to 2013. They did not find any common patterns of the large scale magnetic field.

Activity measures of ϵ Eri were collected for more than 45 years. This huge data set was analyzed by Metcalfe et al. (2013), who found two main periods of variation of the magnetic field, ascribing it to a dynamo mechanism acting in the star. Using a wavelet analysis, they found a short cycle period of 2.95 yr modulated by a long cycle of 12.7 yr (Fig. 7.8).

7.6.1 Questioning about the presence of planets

The existence of exoplanets in the system of ϵ Eri is a still open question. Hatzes et al. (2000) found the presence of a planet analysing the long-period variation of the radial

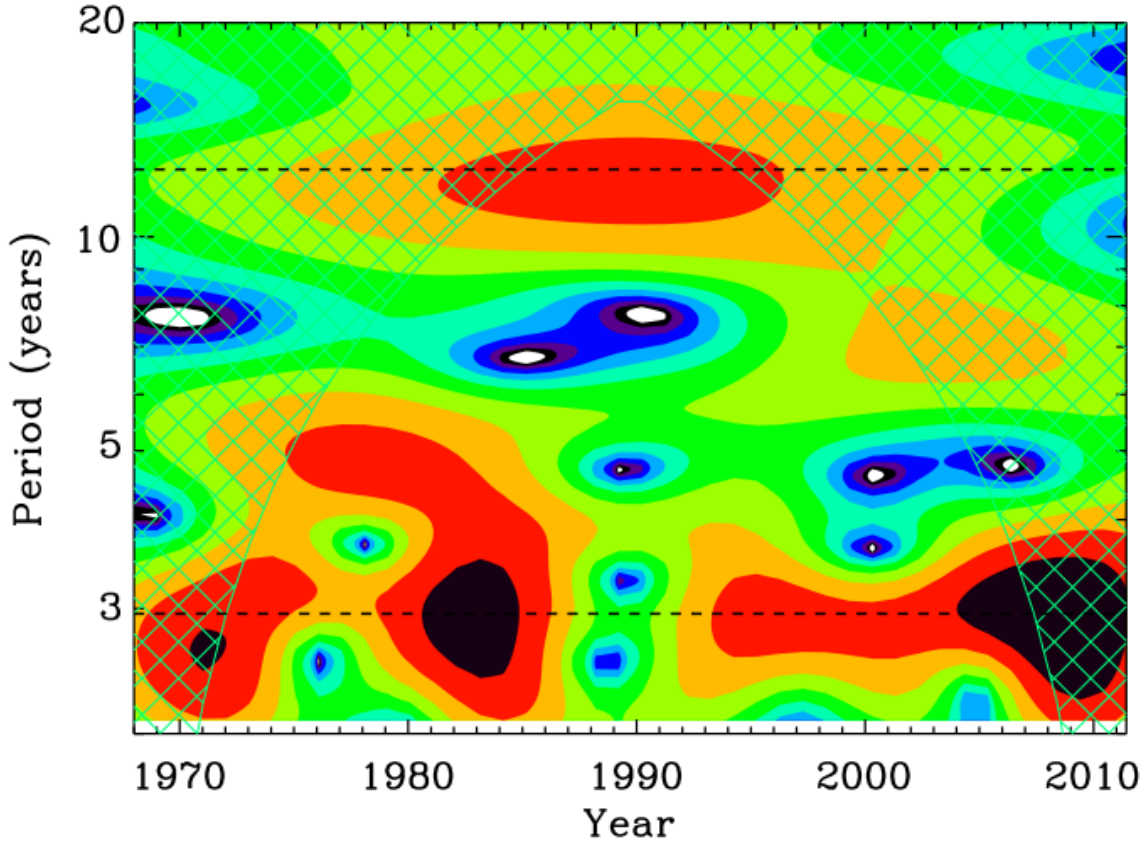

Figure 7.8: Wavelet spectrum of S-index measurements from 1968 to 2012 (Metcalfe et al., 2013). The level of significance is indicated by the color scale; the weakest are white and blue while the strongest are black and red.

velocity and Benedict et al. (2006) confirmed the detection, finding an orbital period of $P_{orbital} = 6.85 \pm 0.03$ yr and a mass of $M = 1.55 \pm 0.24\, M_J$. Backman et al. (2009) ascribed the existence of exoplanets as a possible explanation for the inhomogeneities in the debris disk of ϵ Eri, previously found by Greaves et al. (2005).

On the other hands, Anglada-Escudé & Butler (2012) measured radial velocity of the star using HARPS concluding that the variability is probably due to stellar activity cycles – non-strictly periodic – rather than to the presence of a planet. Planets were not confirmed also by the measures of Zechmeister et al. (2013) and by the imaging (Janson et al., 2015; Mizuki et al., 2016).

7.6.2 Observations

We applied the multi-line slope method to all available spectropolarimetric observations of ϵ Eri, combining archive data of HARPSpol and NARVAL with new observations obtained by CAOS from 2014 to 2017.

It was not possible to obtain reduced HARPSpol data. For this reason, we downloaded the raw files from the ESO archive[2] and we performed the data reduction with the same procedures used with CAOS data (see Sect. 3.8).

NARVAL data were downloaded in reduced form from PolarBase database[3] (Petit et al., 2014). They contain data from six different epochs: January 2007, January 2008, January 2010, October 2011, October 2012 and October 2013.

7.6.3 Measurements

Measures of the multi-line slope method of ϵ Eri are reported in Table 7.6.3 and they are plotted in Fig. 7.7, folded with the rotational period of $P_{rot} = 11.35$ d (Fröhlich, 2007) and a zero phase fixed at MJD 54101 in analogy of Jeffers et al. (2014). We noted that effective magnetic field is highly variable; some curves present polarity reversal (Narval 2007, HARPSpol 2010 and Narval 2013) while other presents the same sign as in the case of NARVAL 2011.

Table 7.5: Effective magnetic field measures of ϵEri.

MJD [d]	B_{eff} [G]	Instrument	MJD [d]	B_{eff} [G]	Instrument
54122.256	-12.97 ± 0.21	NARVAL	55605.505	2.15 ± 0.25	HARPS
54127.316	7.49 ± 0.60	NARVAL	55606.504	0.72 ± 0.16	HARPS
54128.313	7.53 ± 0.31	NARVAL	55836.623	6.80 ± 0.05	NARVAL
54130.354	0.69 ± 0.26	NARVAL	55838.638	7.94 ± 0.10	NARVAL
54133.326	-14.41 ± 0.11	NARVAL	55843.622	4.53 ± 0.14	NARVAL
54135.316	-9.87 ± 0.18	NARVAL	55845.503	4.39 ± 0.09	NARVAL
54140.328	6.43 ± 0.12	NARVAL	55846.521	4.85 ± 0.44	NARVAL
54485.380	-3.83 ± 0.37	NARVAL	55850.517	9.00 ± 0.12	NARVAL

Continued on next page

[2] http://archive.eso.org/eso/eso_archive_main.html
[3] http://polarbase.irap.omp.eu/

Table 7.5 – *Continued from previous page*

MJD [d]	B_{eff} [G]	Instrument	MJD [d]	B_{eff} [G]	Instrument
54487.305	-1.00 ± 0.06	NARVAL	55866.516	1.32 ± 0.14	NARVAL
54488.321	-1.69 ± 0.06	NARVAL	55874.464	11.18 ± 0.12	NARVAL
54489.325	-3.68 ± 0.21	NARVAL	55876.594	7.16 ± 0.15	NARVAL
54490.345	-7.72 ± 0.21	NARVAL	55877.552	4.95 ± 0.13	NARVAL
54491.328	-9.77 ± 0.33	NARVAL	55882.540	4.54 ± 0.19	NARVAL
54492.327	-10.31 ± 0.29	NARVAL	55887.432	9.88 ± 0.08	NARVAL
54493.339	-9.36 ± 0.08	NARVAL	56202.533	1.14 ± 0.07	NARVAL
54494.383	-7.37 ± 0.06	NARVAL	56203.533	1.07 ± 0.23	NARVAL
54495.352	-7.01 ± 0.08	NARVAL	56205.556	-3.79 ± 0.17	NARVAL
54499.348	2.53 ± 0.17	NARVAL	56206.543	-3.74 ± 0.10	NARVAL
54501.331	-5.01 ± 0.06	NARVAL	56214.494	-4.65 ± 0.39	NARVAL
54502.330	-9.18 ± 0.17	NARVAL	56224.617	-3.89 ± 0.13	NARVAL
54503.330	-9.60 ± 0.14	NARVAL	56229.541	-5.57 ± 0.26	NARVAL
54506.339	-7.12 ± 0.08	NARVAL	56230.540	-0.56 ± 0.19	NARVAL
54507.284	-8.19 ± 0.27	NARVAL	56232.517	5.25 ± 0.07	NARVAL
54508.342	-6.94 ± 0.07	NARVAL	56238.554	-11.85 ± 0.14	NARVAL
54509.347	-3.64 ± 0.20	NARVAL	56244.508	4.31 ± 0.16	NARVAL
54510.343	0.45 ± 0.29	NARVAL	56246.476	-0.15 ± 0.38	NARVAL
54511.350	-0.11 ± 0.07	NARVAL	56254.483	0.02 ± 0.49	NARVAL
54512.341	-2.49 ± 0.16	NARVAL	56555.500	-3.44 ± 0.05	NARVAL
55199.609	-4.04 ± 0.04	HARPS	56556.500	0.56 ± 0.06	NARVAL
55200.593	-7.02 ± 0.27	HARPS	56557.500	3.50 ± 0.23	NARVAL
55201.650	-8.48 ± 0.08	HARPS	56575.500	-17.29 ± 0.10	NARVAL
55202.593	-7.76 ± 0.13	HARPS	56576.500	-11.61 ± 0.14	NARVAL
55203.550	-5.54 ± 0.37	HARPS	56577.500	-4.70 ± 0.28	NARVAL
55204.569	-0.14 ± 0.16	HARPS	56578.500	-2.34 ± 0.13	NARVAL
55205.593	4.19 ± 0.14	HARPS	56921.608	6.02 ± 1.64	CAOS
55206.570	2.79 ± 0.35	HARPS	56922.557	5.67 ± 0.42	CAOS
55207.617	-0.66 ± 0.06	HARPS	56922.578	4.52 ± 0.20	CAOS
55209.558	2.52 ± 0.13	HARPS	56941.499	2.12 ± 0.49	CAOS

Continued on next page

Table 7.5 – *Continued from previous page*

MJD [d]	B_{eff} [G]	Instrument	MJD [d]	B_{eff} [G]	Instrument
55210.587	0.62 ± 0.11	HARPS	56946.504	-0.36 ± 2.12	CAOS
55211.575	-3.27 ± 0.14	HARPS	56947.504	-3.12 ± 2.54	CAOS
55224.311	-5.36 ± 0.08	NARVAL	56949.551	-1.12 ± 0.16	CAOS
55231.306	-2.42 ± 0.72	NARVAL	57044.323	4.65 ± 0.15	CAOS
55241.276	5.21 ± 0.31	NARVAL	57630.549	-10.58 ± 1.39	CAOS
55242.271	1.78 ± 0.12	NARVAL	57630.580	-6.10 ± 2.34	CAOS
55600.534	-1.66 ± 0.05	HARPS	57634.617	-6.12 ± 1.31	CAOS
55601.509	-0.78 ± 0.09	HARPS	57723.443	-6.41 ± 1.64	CAOS
55602.599	-1.44 ± 0.04	HARPS	57724.413	-9.74 ± 2.13	CAOS

Fig. 7.7 reports sinusoidal fits of the effective magnetic field variation during the stellar rotation. They are obtained by a fit procedure with the relation:

$$f(t) = A_0 + A_1 \sin\left(2\pi \frac{t - t_0}{P} + A_2\right) + A_3 \sin\left(4\pi \frac{t - t_0}{P} + A_4\right) \tag{7.5}$$

where t is the time in days, t_0 is a reference time (equal to the zero phase time), P is the rotational period, A_1 and A_3 are amplitudes (expressed in Gauss), A_2 and A_4 are phase shifts and A_0 represents the level of the variation of the curves (in Gauss); in the case of CAOS and HARPS 2011 magnetic curves are obtained form single wave fit ($A_3 = A_4 = 0$) because the few points of measure and in the case of the curves of Jan 2010 the measures of NARVAL and HARPSpol were combined.

7.7 Periodicities of effective magnetic field

The analysis of the periodicities of the effective magnetic field of ϵ Eri was performed using the Fourier transform generalized for unequally sampled data by Deeming (1975). Moreover, the frequency domain was deconvolved, using the CLEAN algorithm developed by Roberts et al. (1987), in order to avoid spurious effects due to the incompleteness of the sampling.

FT of the measurements is showed in Fig. 7.9. The positions of the main peaks are estimated using a Gaussian fit and the error on the periods was assumed as large as the

Table 7.6: Table of the values of A_0.

$MJD_{average}$ [d]	A_0 [G]
54131.030	-3.15 ± 0.21
54498.337	-6.08 ± 0.03
55205.339	-2.19 ± 0.04
55603.330	-0.31 ± 0.04
55860.543	7.12 ± 0.03
56225.684	-0.58 ± 0.04
56568.214	-8.27 ± 0.67
56949.516	2.34 ± 0.67
57668.720	-8.17 ± 0.67

FWHM of the Gaussian. We found two main peaks at $P_1 = 976 \pm 70$ d and $P_2 = 555 \pm 22$ d. The period P_1 is very important because it is close to the 2.95 yr period found by Metcalfe et al. (2013) for the activity variation. This is an important result that connects direct estimations of the magnetic field to indirect indicators, such as the chromospheric emissions. This period was also confirmed by the measures of Lehmann et al. (2015), that analyzed the variation of Zeeman broadening from Stokes I. The variation of S-index measures (Metcalfe et al., 2013) folded with the period P_1 is reported in Fig. 7.10.

Another analysis of periodicities can be performed separating the shots-time sinusoidal modulation – due to the stellar rotation – from long-term variations. This can be archived analyzing the variation of the level of oscillation of each magnetic curves, represented by the term A_0 of Eq. 7.5 and reported in Table 7.6. This process can be considered analogue to the subtraction of the frequency due to the rotation of the star.

Fig. 7.11 displays the Cleaned Fourier transform of A_0. We found periods close to that of effective magnetic fields at $P_1 = 1099 \pm 71$ d and $P_2 = 517 \pm 17$ d.

We tested the best period by the computation of the χ^2 for a sinusoidal fit of the A_0 folded with the two periods (Fig. 7.11); we found that P_1 is the best period. The variation of A_0 over the time is showed in Fig. 7.12.

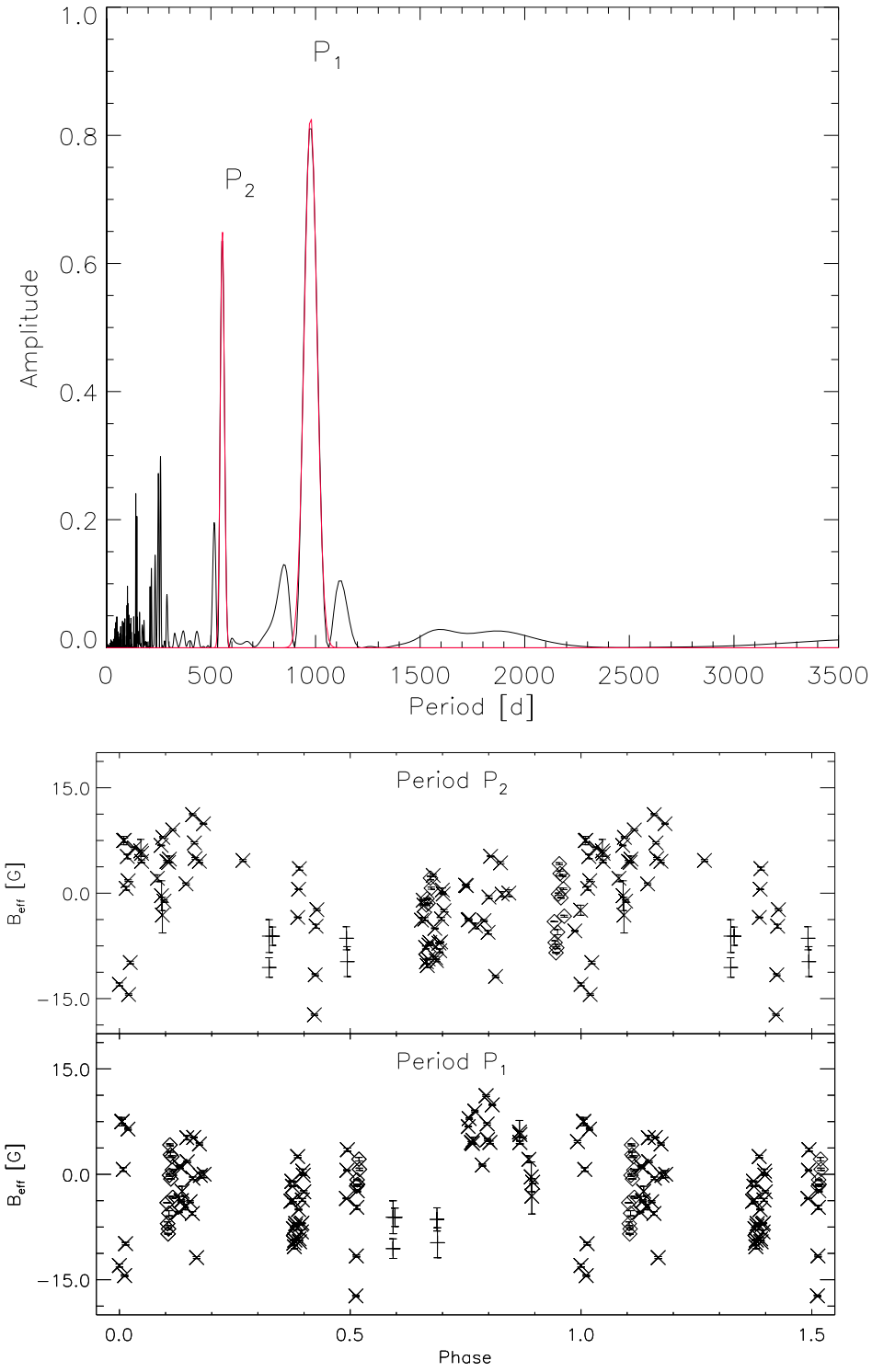

Figure 7.9: Top: Cleaned Fourier transform of the effective magnetic field of ϵ Eri (black) (Deeming, 1975; Roberts et al., 1987) and gaussian fit of the main periods (red). Bottom: Effective magnetic field measures (Table 7.6.3) folded with the two periods. Cross, diamonds and plus refers to observations obtained respectively with NARVAL, HARPSpol and CAOS.

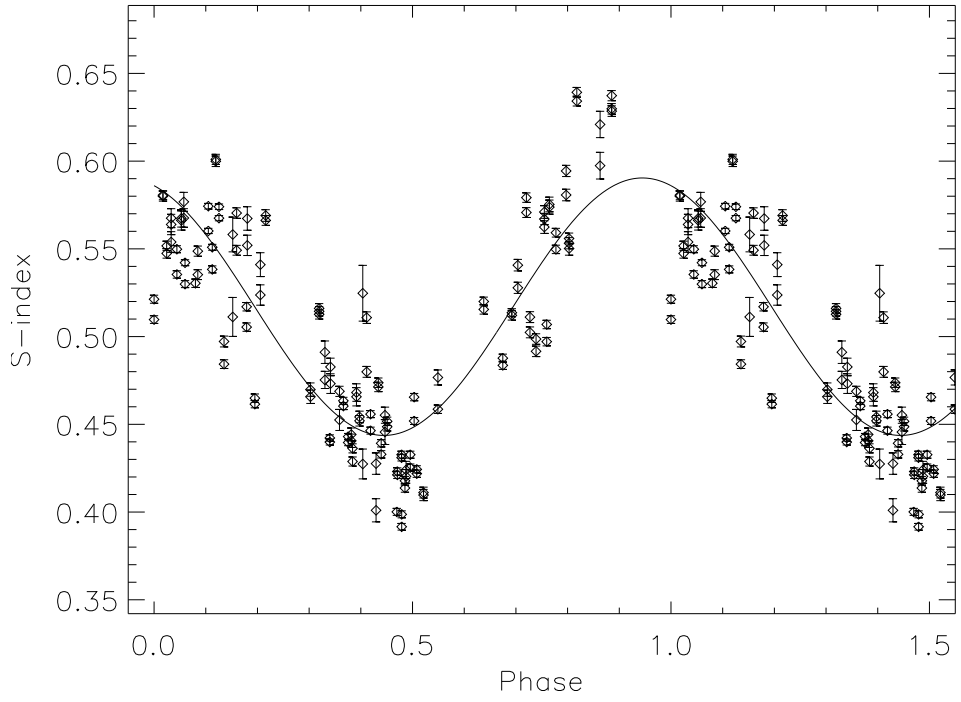

Figure 7.10: S-index measures (Metcalfe et al., 2013) folded with the period P_1.

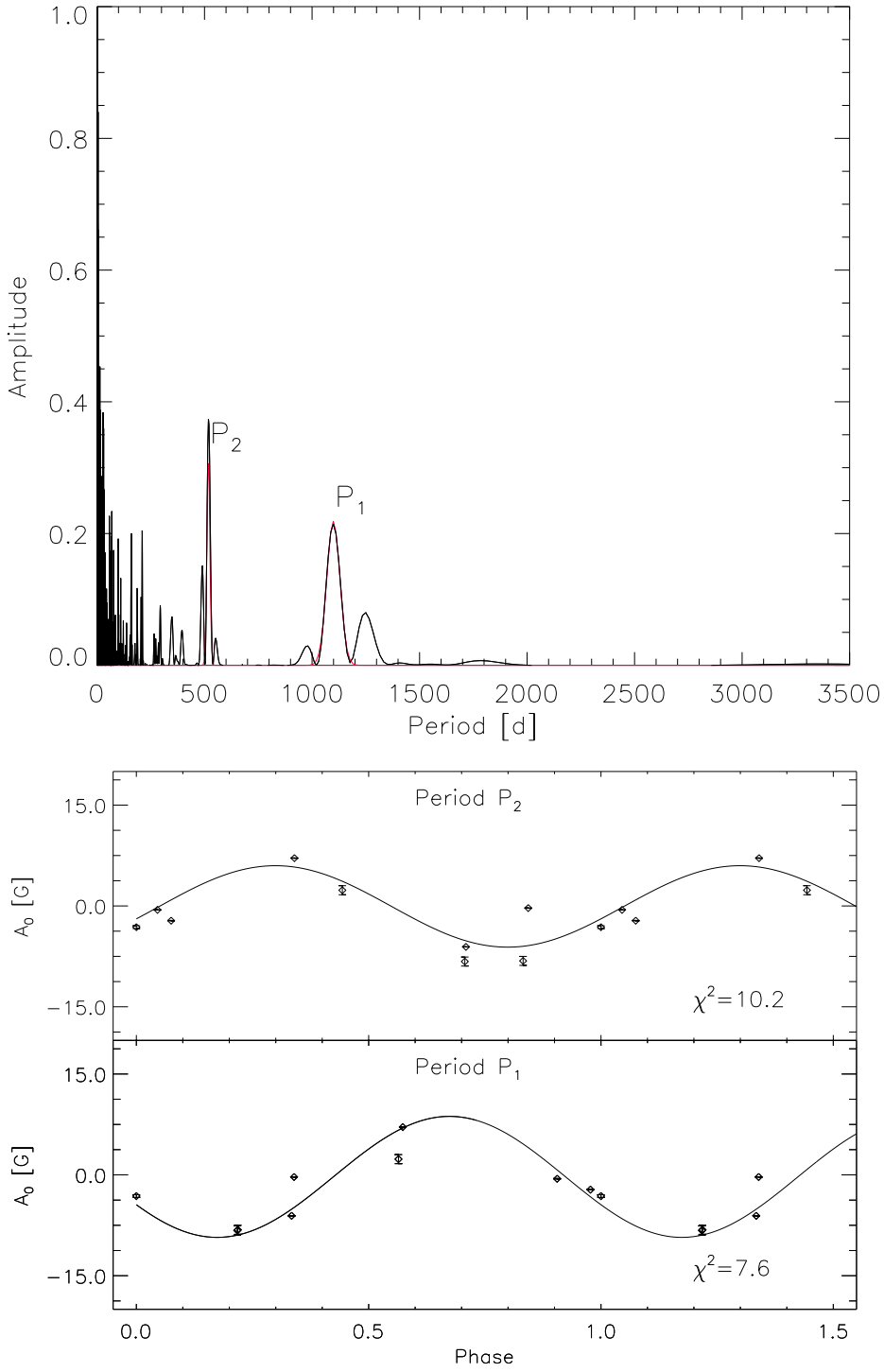

Figure 7.11: Top: Cleaned Fourier transform of A_0 (black) (Deeming, 1975; Roberts et al., 1987) and gaussian fit of the main periods (red). Bottom: A_0 folded with the two periods.

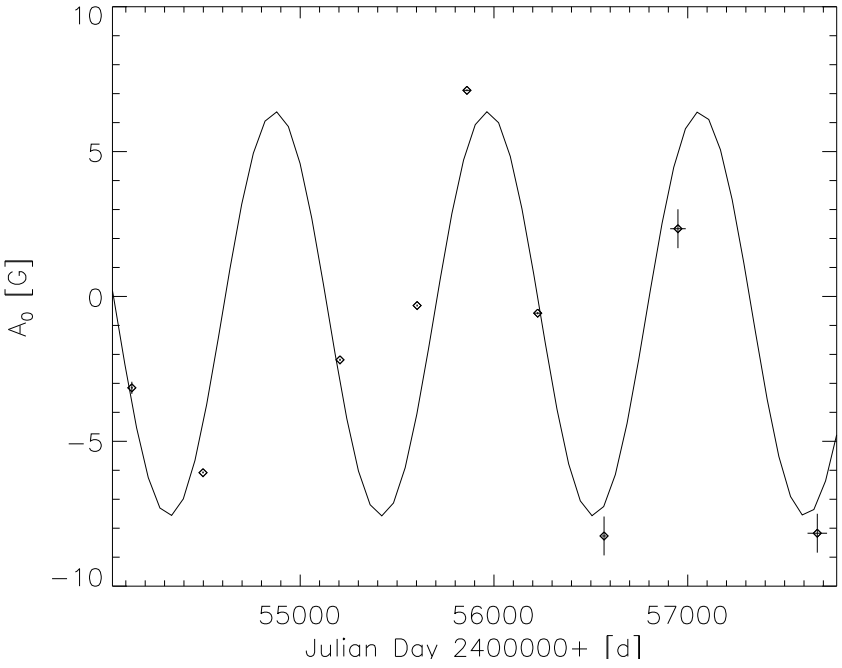

Figure 7.12: Temporal variation of A_0.

CHAPTER 8

CONCLUSION

This work of thesis was devoted to the detection and the analysis of stellar magnetic fields.

Data were obtained in large part through the spectropolarimeter *Catania Astrophysical Observatory Spectropolarimeter* (CAOS), which is attached at the 91 cm telescope located in Serra La Nave, Mt. Etna, Italy. During the work, it was possible to calibrate the instrument with a new method based on the observations of magnetic early type stars. We showed that the cross-talk of the polarimeter is almost negligible and we noted that about the 0.4% of Stokes Q and Stokes U are converted in Stokes V, attributing this behavior to the retardance properties of the achromatic waveplates used.

We obtained full Stokes spectra of the early type magnetic star β CrB, covering the entire rotational period. We proposed a new technique in order to measure the transversal component and the angle of the magnetic field, taking advantage of the slope of the distribution of Stokes Q and Stokes U respect to the second derivative of the Stokes I, in the approximation of weak field regime. We showed that through linear polarimetry it is possible to distinguish magnetic configurations which produce the same signal in circular polarisation and this allowed to obtain stronger constraints to geometrical parameters. In this way, it was possible to give an estimation of the stellar radius of $R = 2.75\,R_{\odot}$, which agrees with the interferometric value obtained by Bruntt et al. (2010). Furthermore, we showed that the angle between the rotational axis and the N-S direction in the sky can be estimated from the extreme of the variation of the angle of the magnetic field. We found a value of θ=110°which agrees with the results of

Leroy (1995) and Bagnulo et al. (2000), obtained from the modelling of the broadband linear polarimetry.

In order to study the impact of magnetic fields in star hosting planet, we observed a sample of 22 stars where planets were detected. The sample was composed of 17 giant stars; in this way, it was possible to study the magnetism on evolved stars, in order to obtain observational constraints. We observed also the M0III AGB star HD6860.

Detections were obtained implementing a version of the *Least Square Deconvolution*, which is the most used technique for the measure of small signals due to the presence of a stellar magnetic field. We tested the code with synthetic spectra computed by COSSAM and real observations of HARPSpol and CAOS.

We found magnetic fields for the 47% of the giant and for the 40% of the main sequence stars. Moreover, we showed that the few observations of ι Dra could be folded with the orbital period of the planet. However, more observations are required in order to question its presence.

The detected magnetic field of the sample of giant stars shows a correlation with the rotational period, which is consistent with the measures on giant stars reported by Aurière et al. (2015) and on main sequence stars obtained by Folsom et al. (2016). This correlation can be explained considering a surface magnetic field originated by a dynamo process driven by stellar rotation. The M0III AGB star β And do not follow the correlation. We ascribe this as a possible wrong estimation of the period or as the effect of a different dynamo process acting in this star and driven by turbulence.

We proposed a new technique, called multi-line slope method, as an easier alternative to the Least Square Deconvolution for the measure of the effective magnetic field of cool stars. We tested this method using the synthetic spectra computed by COSSAM and comparing our results with previous one obtained with the LSD. We concluded that the multi-line slope method can be an alternative to LSD, in the case of low rotational velocities ($v \sin(i) \leq 5\,\mathrm{km\,s^{-1}}$) and low field strengths ($B_{\mathrm{eff}} \leq 1\,\mathrm{kG}$). Finally, we applied this technique to all the available spectropolarimetric data of the star ϵ Eri. We used archive data from HARPSpol and NARVAL and new observation obtained with CAOS, collecting data which covers a period of 9 yr. The long-term variation of the magnetic field was separated by the short-time variation, due to stellar rotation, through a coefficient A_0 (defined in Eq. 7.5). The Fourier transform of the variation of A_0 showed that the best-fit period ($P_1 = 1099 \pm 71$ d) corresponds to the short cycle period of the S-index found by Metcalfe et al. (2013). This result represents a connection between the direct measure of the magnetic field and the indirect estimation through chromospheric emission lines.

Moreover, it confirms that direct measurements of the effective magnetic field allows to determine the periods of the cycles of active cool stars.

APPENDIX A

APPENDIX A: COSSAM APPLICATIONS TO OPEN CLUSTERS

During the Ph. D., we worked on the implementation of the inversion code SPARTI (Spectro Polarimetric Analysis by Radiative Transfer Inversion) (Martin et al., 2017), which combines the capability of calculus offered by COSSAM with the efficiency of the Levenberg Marquardt algorithm (Levenberg, 1944; Marquardt, 1963), in order to infer properties of the magnetic field geometry of magnetic early type stars.

In order to test the capabilities of the code, we performed chemical abundance analysis of stars member of open clusters using the unpolarized version SPARTI_SIMPLE. These studies represent an important tool for the constraints of diffusion models (Michaud, 1970), stellar evolution theory and galactic chemical evolution (Lambert & Reddy, 2016).

Members can be assumed to have the same age and the same initial chemical composition and to differ for the initial mass, rotational velocity and duplicity (Fossati et al., 2008).

Open clusters have also the advantage that the age can be estimated with higher accuracy with respect to single stars, through the fit of the color-magnitude diagram with isochrones (Bagnulo et al., 2006).

This analysis is part of a large project whose intent is the study of chemical abundances of stars belonging to bright open clusters. Previous works include the analysis of Praesepe cluster (Fossati et al., 2007, 2008, 2010), NGC5460 (Fossati et al., 2011), Hyades cluster (Gebran et al., 2010), Coma Berenices cluster (Gebran et al., 2008), NGC6475 (Villanova et al., 2009) and NGC6405 (Kılıçoğlu et al., 2016).

Table A.1: Gratings employed for the FLAMES/GIRAFFE observations.

Grating setting	Resolving Power	Spectral Region (Å)
L479	7500	4500 – 5077
H525	25900	5139 – 5355
H572	24200	6438 – 6822

We analyzed stars belonging to the open clusters NGC6250 and NGC6633. The results of the first cluster are published in Martin et al. (2017).

This appendix is mainly devoted to the study of the diffuse intermediate age open cluster NGC6633, that is one of the oldest observed in the project. Williams & Bolte (2007) and Smiljanic et al. (2009) determined a cluster age of $\log t = 8.75 \pm 0.05$ and $\log t = 8.65$, respectively. Kharchenko et al. (2005) estimated an isochrone-based distance to the cluster of 388 pc and (Hiltner et al., 1958) reported a cluster reddering of E(B-V) =0.17 using UBV photometry of early-type stars. The cluster includes dozen of early-type stars (Levato & Abt, 1977), which are interesting for the study of stellar diffusion.

A.1 Observations

Observations of NGC6633 were obtained on the 27th of June 2007 with the *Fibre Large Array Multi Element Spectrograph* (FLAMES), which is located at the UT2 of the ESO Very Large Telescope (VLT) and it is described in Pasquini et al. (2002). It can retrieve simultaneously more than 130 low or medium resolution spectra (R =7500 – 30000) with the MEDUSA fibers connected to GIRAFFE spectrograph and up to 8 high-resolution spectra (R = 47000) with the UVES fibers linked to the red arm of the UVES spectrograph.

Data were obtained through a UVES setting centered at 520 nm, in order to cover a spectral region from 4140 Å to 6120 Å. This spectral range contains a large number of metal lines and two hydrogen lines, the H_β and H_γ, which can be used for the estimation of fundamental stellar parameters.

Because of the higher resolution, UVES spectra needed a longer exposure time respect to the GIRAFFE spectra. For this reason, three GIRAFFE spectra with different gratings were obtained during each UVES exposure. GIRAFFE gratings were chosen in a wavelength range centered at 520 nm (the central wavelength used for the guide of UVES) in order to avoid light loss due to different atmospheric refraction.

The three GIRAFFE settings were the low resolution $L479$ and the medium resolution

$H525$ and $H572$, whose characteristics are reported in Table A.1. The low resolution grating $L479$ was selected in order to include the $H\beta$ line and several Fe, Cr and Si; the grating $H525$ was useful because it contains elements of Fe-peak, such as iron and titanium and the Mg triplet centered at 5172Å; the grating $H572$ contains lines of iron, sodium and scandium, which is important for the classification of Am chemically peculiar stars (Fossati et al., 2008).

UVES spectra were reduced by a IRAF pipeline, which follows all the procedures described in Sect. 3.8. GIRAFFE spectra were reduced with the available ESO pipeline, as described in Fossati et al. (2011).

A.2 Abundance Analysis

A.2.1 Cossam Simple

We performed the chemical abundance analysis fitting the observed spectra with synthetic spectra, computed assuming plane-parallel atmosphere and a local thermodynamic equilibrium (LTE). In order to do it, we used a simpler version of COSSAM for the unpolarised cases, which is called COSSAM SIMPLE (Martin et al., 2017). We computed model atmospheres with ATLAS9 (Kurucz, 1993a), using Opacity Distribution Function (ODF) tables for solar abundances (Kurucz, 1993b). Hydrogen lines were computed following Hubeny et al. (1994) and Hubeny & Lanz (1995) and atomic line information, including radiation damping, Stark broadening and Van Der Waals broadening constants, were taken from VALD database (Piskunov et al., 1995).

A.2.2 Determination of stellar parameters

Effective temperature T_{eff} and log$g$ were estimated comparing synthetic and observed Hydrogen lines. We used H_β for GIRAFFE stars and H_β and H_γ for UVES stars. This is possible because Balmer lines are sensitive to temperature variation below 8000K while, for higher temperature, they are sensitive to log$g$ variation; in this case, temperature effects are still visible in the part of the wing close to the line core (Fossati et al., 2011). Fig. A.1 shows examples of fitted H_β lines for a sample of stars.

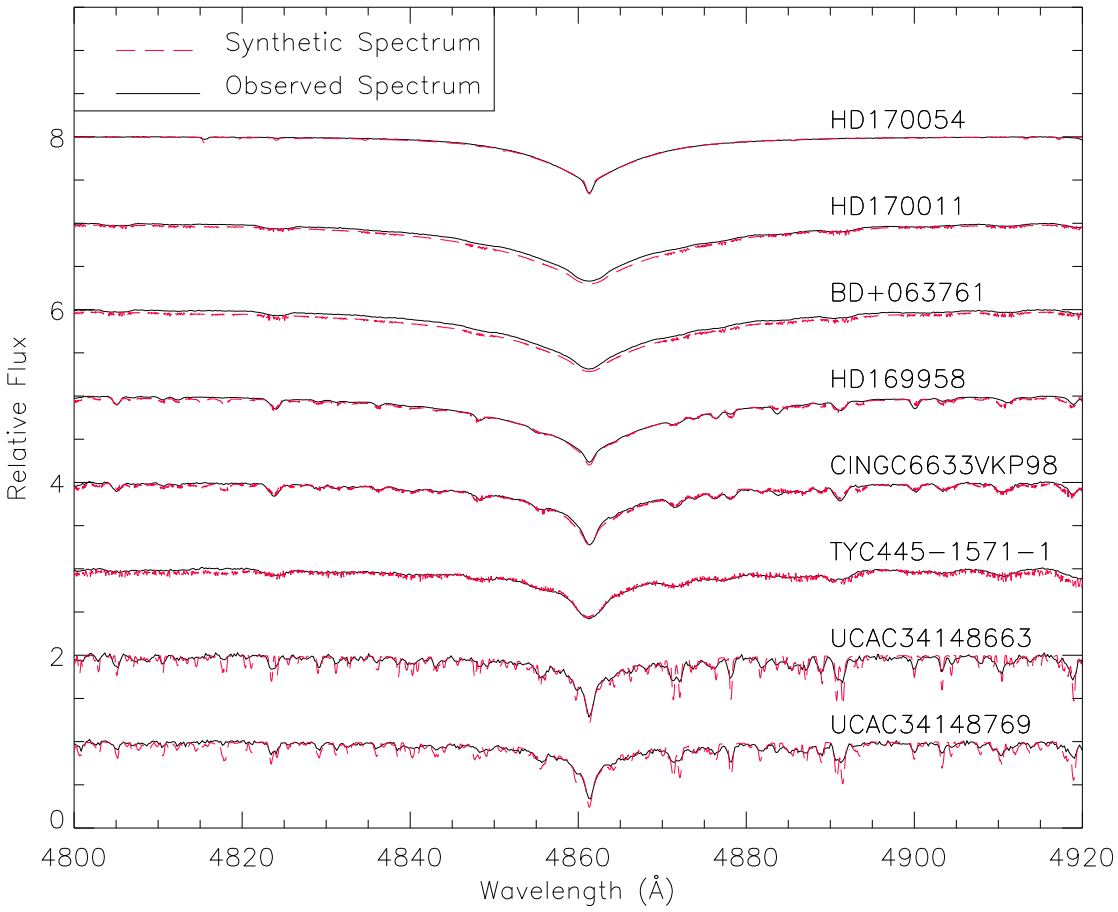

Figure A.1: A sample of the observed H_β lines.

A.2.3 Stars selection

SPARTI_SIMPLE can not be used to determine the chemical abundance of binary stars. We applied the Least Square Deconvolution (see Sect. 6.1), on the spectral region covered by the *H*525, in order to classify as probable binary stars JEF25, TYC445-1684-1 (JEF69), TYC445-1793-1, UCAC34148521 and ClNGC6633VKP129. JEF25 and TYC445-1684-1 (JEF69) were classified as binary also by Jeffries et al. (2002). Despite the LSD, it is not possible to exclude that some stars of our sample are SB1; however, it can not be determined with the current dataset. LSD profiles are reported in Fig. A.2.

We selected stars with $T_{eff} \geq 5700$ K and log g in a range 3.5 – 4.5, in order to include only main sequence stars. We analyzed only stars observed with a S/N ratio greater than 50 in all the gratings. From the starting 97 GIRAFFE and four UVES spectra, we selected 27 stars observed with GIRAFFE and two observed with UVES. Determined

values of T_{eff} and gravity $\log g$ for the selected stars are reported in Table A.4.

A.2.4 Abundance measurement

The code SPARTISIMPLE consists on an implementation of the Levenberg-Marquardt algorithm (LMA) combined with COSSAMSIMPLE. It is able to estimate chemical abundances, $v \sin(i)$, v_{mic} and v_{rad} from the minimization of the χ^2 between synthetic and observed spectra.

The search of a set of parameters which corresponds to the global minimum of an hyperspace of high number of parameters is a complicated problem of optimization. *Local* algorithms, such as the Levenberg-Marquartd, can stop into different local minima, depending on the starting value.

As initial chemical composition, we adopted the solar abundance composition given by Asplund et al. (2009). Starting $v \sin(i)$ was determined by a model fit of a short region between 5190 Å and 5240 Å and starting radial velocity v_{rad} was estimated from the cross correlation between the observed spectra and a model with the determined stellar parameters, in a region of the H_β line between 4840 Å and 4880 Å.

Landstreet et al. (2009) showed that v_{mic} goes to zero for $T_{eff} \geqslant 10000$ K and it is approximately 2 km s^{-1} for not peculiar stars with lower values of T_{eff}. Following this result, we adopted as starting value of $v_{mic} = 0.5$ km s^{-1} in the case of stars with $T_{eff} \leqslant 10000$ K and $v_{mic} = 2$ km s^{-1} in the other cases.

We estimated a lower limit of the error from the square route of diagonal elements of the covariance matrix. However, Ryabchikova et al. (2016) demonstrated that the errors computed in this way can be unrealistically small, especially in the case of spectra observed at high S/N level. Furthermore, in order to estimate realistic errors, Fossati et al. (2009) showed that uncertainties on fundamental parameters must be taken into account. For this reason, we estimated an upper value of the error of each parameter as the standard deviation of the values obtained from the inversion from starting models with $T_{eff} \pm \Delta T_{eff}$ and $\log g \pm \Delta \log g$.

A.3 Cluster's membership

The selection of the members of the cluster is a critical issue in order to select a sample of coeval stars.

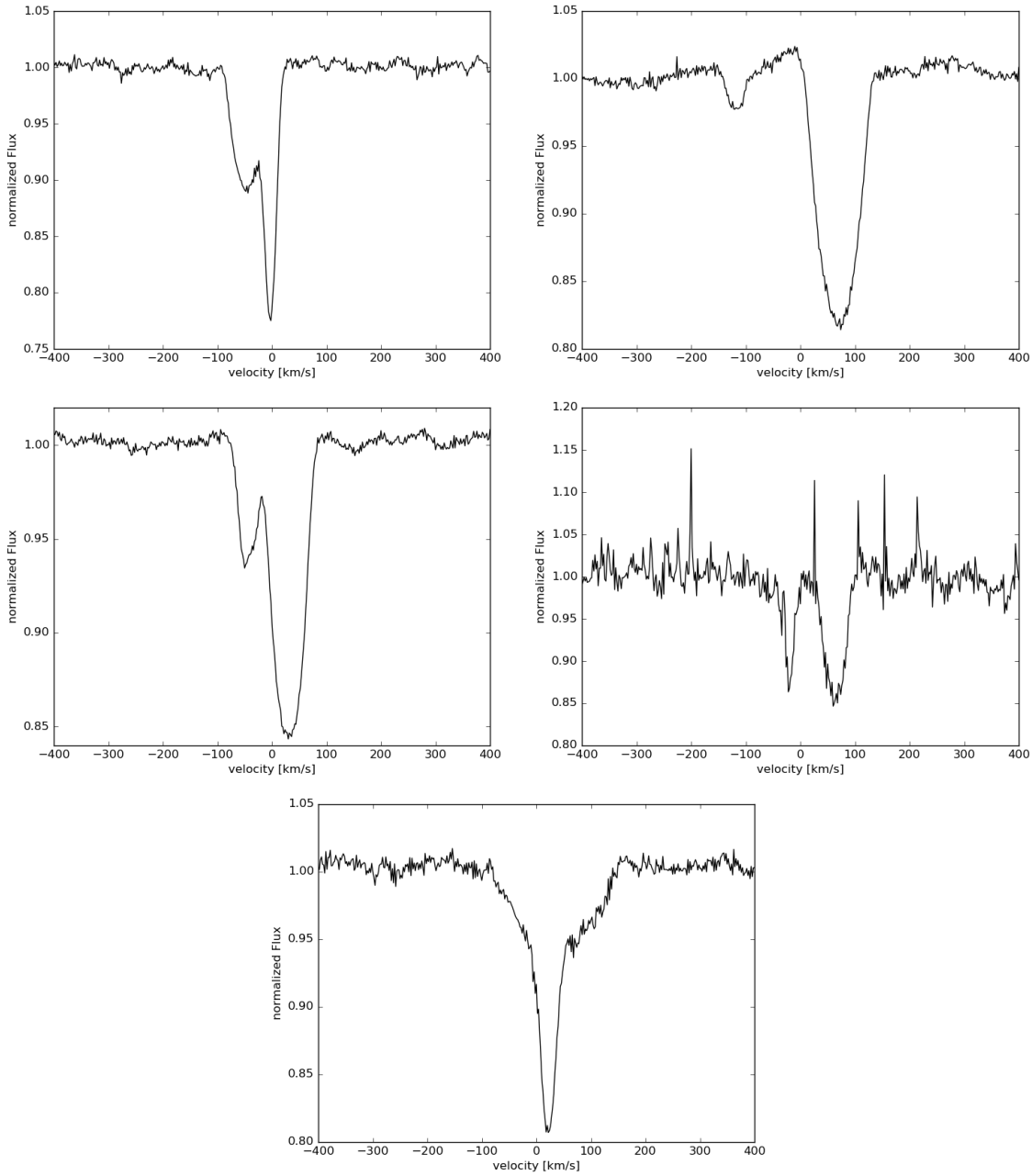

Figure A.2: LSD profiles of the possible binary stars. On the top left JEF25, on the top right TYC445-1684-1, on the center left TYC445-1793-1,on the center right UCAC34148521, on the bottom ClNGC6633VKP129.

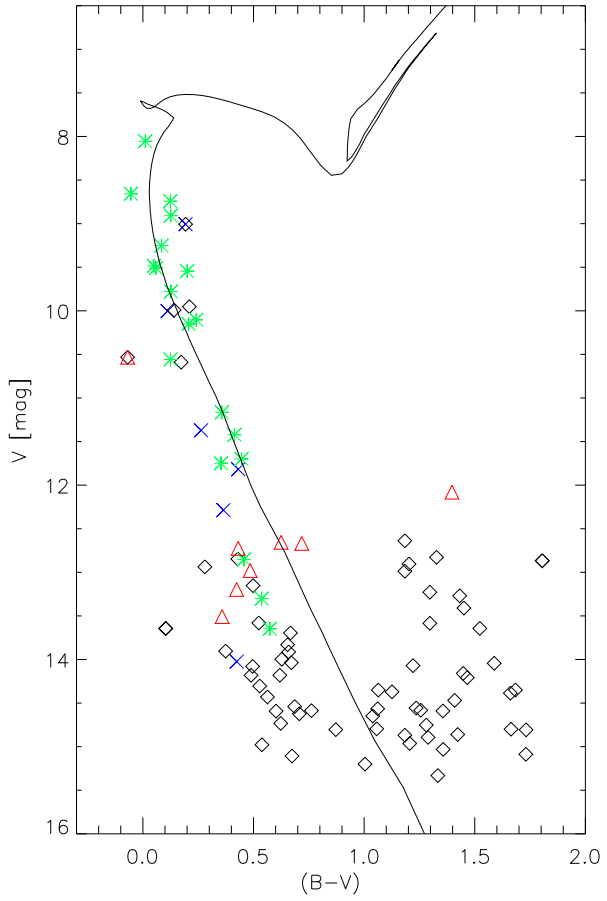

Figure A.3: Color magnitude diagram. Green asterisk are the selected cluster members, red triangles are the non members, blue cross are binary stars and black triangles are non selected stars.

Pioneering membership analyses were presented by Kopff (1943), Hiltner et al. (1958) and Vasilevskis et al. (1958). An important work was performed by Sanders (1973), who gave the membership and the associated probabilities to be member for 497 stars in the region of NGC6633, analyzing proper motions. Membership based on *BVI* photometry and radial velocity were presented by Jeffries (1997) and Jeffries et al. (2002). More recent studies, based on the proper motion of UCAC4 catalogue (Zacharias et al., 2012), were presented by Dias et al. (2014).

Despite this large literature information, it was not possible to find membership for all the stars in our sample. Jeffries et al. (2002) showed that proper motion is a poor discriminator for the membership analysis of NGC6633 because the proper motion vector ($\mu_{\rm RA}, \mu_{\rm Dec}$) of the cluster is (-2.27 $\pm$ 2.46, -4.95 $\pm$ 4.07) and the field of stars around the cluster have a mean proper motion vector of (-2.06, -5.58) with a dispersion of (20.5 ,20.8)

Table A.2: Mean kinematic values of NGC6633.

Radial Velocity [km s^{-1}]	-27.8 ± 7.5
Proper Motion RA [mas yr^{-1}]	1.0 ± 2.3
Proper Motion DEC [mas yr^{-1}]	-2.6 ± 2.0

(Dias et al., 2014). Despite this, we included also information about the proper motion for the membership analysis, taking advantage on the more precise GAIa measurements (Gaia Collaboration, 2016).

In order to assign membership to the stars sample, we considered as members all stars whose radial velocity and proper motion were in a range of 3σ from the mean kinematic values of the cluster. We computed the means in an iteratively way. At the first iteration, we included in the computation only stars whose probability to be member was grater 80% , according to Sanders (1973); at the each iteration, we removed all the stars with radial velocity or proper motions above 3σ from the means, until the number of stars was constant.

In this way we selected 19 stars as members of NGC6633; kinematic values are reported in Table A.2. It is possible to note that the mean radial velocity of -27.8 ± 7.5 km s^{-1} computed with this technique, is consistent with the value obtained by Jeffries et al. (2002) of -28.2 ± 0.3 km s^{-1}.

The radial velocity for each star is obtained from the inversion and final information about estimated membership and stars are reported in Table A.3.

Members of clusters can be estimated also analyzing the color magnitude diagrams. We reported the CMD of the observed stars in Fig. A.3; it is possible to note a general agreement between members selected with the kinematics and members that fit the isochrone. We obtained the isochrone from the code PARSEC (Bressan et al., 2012), using a value of log t = 8.75 (Williams & Bolte, 2007), a reddening of E(B-V) = 0.165 and a of metallicity [Fe/H] = -0.096 (Jeffries et al., 2002); reddening corrections were applied following Currie et al. (2010).

A.4 Results and discussion

The obtained values of v_{mic} and v sin(i) are reported on Table A.4. We reported the trend of v_{mic} respect to temperature in Fig. A.4. It is possible to note that errors of v_{mic} and v sin(i) are unrealistically small. Realistic error can be higher and they can be estimated in the order of 5% for v sin(i), as stated by (Fossati et al., 2008).

Table A.3: List of programme star of NGC6633. The probability to be member is taken from Sanders (1973). The symbol * in the spectral-type column (Column 3) means that this was estimated from our determined effective temperature according to Currie et al. (2010). The J and K magnitude are taken from 2Mass catalogue (Cutri et al., 2003). The B and V magnitude are taken from APASS catalogue (Henden et al., 2016). The symbol * in the proper motion columns means that the value are taken from Gaia Collaboration (2016), for the UCAC stars the values are taken from UCAC2 catalogue (Zacharias et al., 2004) while for all the other stars are taken from Tycho-2 catalogue (Høg et al., 2000).

Star	Memb. Prob. %	Spec. Type	μ_{RA} [mas yr^{-1}]	μ_{DEC} [mas yr^{-1}]	v_r [km s^{-1}]	SNR	B [mag]	V [mag]	J [mag]	K [mag]	Memb.
BD+063761	74	A2	0.6 ± 0.5*	-2.1 ± 0.5*	-28.6 ± 0.4	420/350/430	9.0	8.7	8.2	8.1	yes
BD+063771	92	A5	0.4 ± 1.0*	-1.0 ± 1.0*	-30.8 ± 0.3	300/400/330	10.0	9.6	9.0	8.8	yes
BD+063779	74	A3	3.1 ± 1.0*	-2.8 ± 1.0*	-24.2 ± 0.1	150[UVES]	10.0	9.6	8.9	8.7	yes
BD+063794	86	A5	2.4 ± 0.8*	-1.6 ± 0.7*	-46.0 ± 1.3	250/280/345	10.3	10.0	9.4	9.2	yes
ClNGC6633JEF25	89	F7*	3.2 ± 3.0*	-0.5 ± 2.2*		39/108/40	11.9	11.3	10.1	9.8	B
ClNGC6633VKP126	90	G0*	-12.0 ± 2.8*	-12.6 ± 2.4*	-28.3 ± 0.1	60/80/90	13.1	12.4	11.2	10.8	no
ClNGC6633VKP129	0	F4*	-1.3 ± 2.2*	-9.0 ± 1.8*		55/118/69	12.3	11.8	10.7	10.4	B
ClNGC6633VKP98	0	F2*	-1.0 ± 2.0*	3.9 ± 1.6*	-0.3 ± 0.4	176/180/170	13.1	11.6	8.7	7.8	no
HD169912	89	A3	2.3 ± 1.1	-0.7 ± 1.3	-30.8 ± 0.1	520/450/400	9.2	9.0	8.5	8.4	yes
HD169958	2	A2.5	0.0 ± 0.3*	-1.1 ± 0.4*	-30.4 ± 0.1	850/480/450	8.5	8.2	7.7	7.6	yes
HD169959	90	A0	10.4 ± 4.9	15.0 ± 4.6	-28.2 ± 0.2	140[UVES]	7.7	7.5	7.3	7.2	yes
HD170011		A	1.7 ± 0.6*	-1.9 ± 0.6*	-36.8 ± 0.4	660/400/490	9.2	9.0	8.4	8.3	yes
HD170054	70	B6	1.6 ± 0.1*	-1.8 ± 0.1*	-27.6 ± 0.1	575/400/432	8.2	8.1	8.1	8.1	yes
HD170094	69	A2	-1.2 ± 1.9	-0.9 ± 1.9	-12.6 ± 0.3	150[UVES]	9.5	9.2	8.8	8.7	yes
HD170114	91	A4	-2.5 ± 1.7	-2.3 ± 1.9		130/208/176	8.8	8.5	7.8	7.6	B
HD170135		A3	1.0 ± 0.1*	-1.5 ± 0.1*	-29.8 ± 0.2	400/350/360	8.7	8.4	7.8	7.7	yes
HD170158	92	A2	2.2 ± 0.7*	-2.6 ± 0.6*	-26.1 ± 2.0	414/320/425	9.4	9.0	8.4	8.2	yes
TYC445-1491-1	86	A3	-0.3 ± 0.8*	-1.4 ± 1.8*	-30.1 ± 0.0	220/225/280	11.2	10.6	9.7	9.4	yes
TYC445-1571-1	93	F4	-0.7 ± 2.6	-2.6 ± 2.7	-29.4 ± 0.7	150/180/195	11.5	10.9	9.8	9.5	yes
TYC445-1684-1	69	F0	-2.8 ± 2.1*	-1.2 ± 0.7*		54/106/124	11.3	10.8	10.0	9.8	B
TYC445-1686-1	89	A9	-11.1 ± 2.1*	-1.8 ± 0.7*	-22.2 ± 1.2	275/232/205	10.1	10.0	10.0	9.9	no
TYC445-1793-1	87	A3m	1.2 ± 0.9*	-1.6 ± 0.7*		99/171/137	9.8	9.5	8.9	8.8	B
TYC445-1974-1	0	F5*	7.6 ± 2.3*	-3.0 ± 1.1*	-17.0 ± 0.0	200/235/250	11.8	11.2	9.9	9.5	yes
UCAC33973380		F0*	-16.6 ± 5.9	-9.3 ± 5.9	-1.1 ± 1.1	60/80/75	13.5	13.0	11.9	11.6	no
UCAC34148324	92	F8*	-0.6 ± 3.0	-5.2 ± 2.9	10.9 ± 0.1	80/130/100	12.8	12.2	10.9	10.6	no
UCAC34148416		G6*	-5.0 ± 3.5	-67.7 ± 3.3	1.9 ± 0.1	20/50/50	13.0	12.1	10.5	10.1	no
UCAC34148423	83	F9*	-2.3 ± 3.0	-5.1 ± 2.9	-29.6 ± 0.0	95/80/90	12.9	12.3	11.1	10.8	yes
UCAC34148501		F5*	-6.3 ± 3.5	-7.3 ± 3.3	12.4 ± 0.2	122/91/80	13.3	12.7	11.5	11.2	no
UCAC34148521		F1*	-7.2 ± 5.8	1.0 ± 5.8		36/13/45	14.1	13.5	12.2	11.9	B
UCAC34148538		G8*	3.0 ± 5.8	-0.3 ± 5.8	-13.7 ± 0.1	50/65/60	13.9	13.1	11.6	11.2	yes
UCAC34148641	97	F3*	0.5 ± 1.5	-4.0 ± 3.0	-26.7 ± 0.1	260/170/190	11.7	11.2	10.2	9.9	yes
UCAC34148663	81	F9*	-1.7 ± 3.0	-5.9 ± 2.9	-28.5 ± 0.1	100/105/72	13.5	12.8	11.4	11.1	yes
UCAC34148769		F9*	-1.4 ± 3.5	-8.3 ± 3.3	-28.1 ± 0.1	125/100/90	12.9	12.1	11.0	10.6	no

The results of the chemical abundance analysis are reported in Table A.5 for non members and in Table A.6 and A.7 for members.

A.4.1 Am stars

Am stars (Conti, 1970) are peculiar early type stars that present an enhancement of Fe-peak, Y, Ba abundances and underabundance of C, N, O, Ca, and Sc (Fossati et al., 2007). In particular, the underabundance of Sc is necessary for the Am classification (Fossati, 2014).

Am stars are also slow rotators ($v \sin(i) \leq 90\,\mathrm{km\,s^{-1}}$) (Charbonneau & Michaud, 1991)

Table A.4: Stellar parameters of analysed stars.

Star	T_{eff} (K) (K)	log(g) (CGS)	v_{mic} (km s^{-1})	vsini (km s^{-1})
		Members		
UCAC34148538	5700 ± 200	4.1 ± 0.2	1.5 ± 0.2	8.9 ± 0.7
UCAC34148663	5700 ± 200	4.3 ± 0.2	0.7 ± 0.2	13.1 ± 0.2
UCAC34148423	5900 ± 200	4.3 ± 0.2	1.2 ± 0.1	8.6 ± 0.3
TYC445-1974-1	6500 ± 200	4.3 ± 0.2	1.4 ± 0.1	6.7 ± 0.2
TYC445-1571-1	6800 ± 200	4.2 ± 0.2	2.0 ± 0.1	117.9 ± 0.9
UCAC34148641	6900 ± 200	4.2 ± 0.2	2.0 ± 0.1	20.9 ± 0.3
TYC445-1491-1	7000 ± 200	4.1 ± 0.2	2.7 ± 0.1	12.1 ± 0.2
BD+063779	7700 ± 200	4.0 ± 0.2	2.8 ± 0.1	96.6 ± 0.5
BD+063794	7900 ± 200	3.6 ± 0.2	2.2 ± 0.1	193.9 ± 1.5
BD+063771	8200 ± 200	3.7 ± 0.2	2.9 ± 0.1	106.8 ± 0.4
HD170094	8300 ± 200	3.7 ± 0.2	3.0 ± 0.1	12.4 ± 0.2
HD170158	8400 ± 200	3.7 ± 0.2	2.0 ± 0.1	221.4 ± 2.2
HD169912	8600 ± 200	3.7 ± 0.2	3.4 ± 0.1	47.3 ± 0.5
HD170011	8700 ± 200	3.7 ± 0.2	3.2 ± 0.2	136.5 ± 0.9
BD+063761	8900 ± 200	3.6 ± 0.2	2.7 ± 0.2	117.8 ± 1.0
HD169958	9000 ± 200	3.7 ± 0.2	3.3 ± 0.1	35.2 ± 0.2
HD170135	9000 ± 200	3.6 ± 0.2	3.7 ± 0.2	101.8 ± 0.4
HD169959	11300 ± 200	4.1 ± 0.2	0.2 ± 0.3	84.6 ± 17.6
HD170054	14800 ± 200	4.1 ± 0.2	2.5 ± 0.1	20.9 ± 0.4
		Non Members		
UCAC34148416	5700 ± 200	4.0 ± 0.2	1.5 ± 0.1	4.3 ± 0.4
UCAC34148769	6000 ± 200	4.2 ± 0.2	0.2 ± 0.3	19.0 ± 0.6
ClNGC6633VKP126	6100 ± 200	3.9 ± 0.2	0.2 ± 0.2	15.0 ± 0.4
UCAC34148324	6200 ± 200	4.0 ± 0.2	0.6 ± 0.3	15.8 ± 0.3
UCAC34148501	6400 ± 200	4.0 ± 0.2	2.1 ± 0.2	41.1 ± 0.6
ClNGC6633VKP98	7000 ± 200	4.1 ± 0.2	2.5 ± 0.2	50.1 ± 0.6
TYC445-1686-1	7000 ± 200	3.7 ± 0.2	3.2 ± 0.2	190.1 ± 1.7
UCAC33973380	7200 ± 200	4.0 ± 0.2	2.4 ± 0.1	127.6 ± 2.4

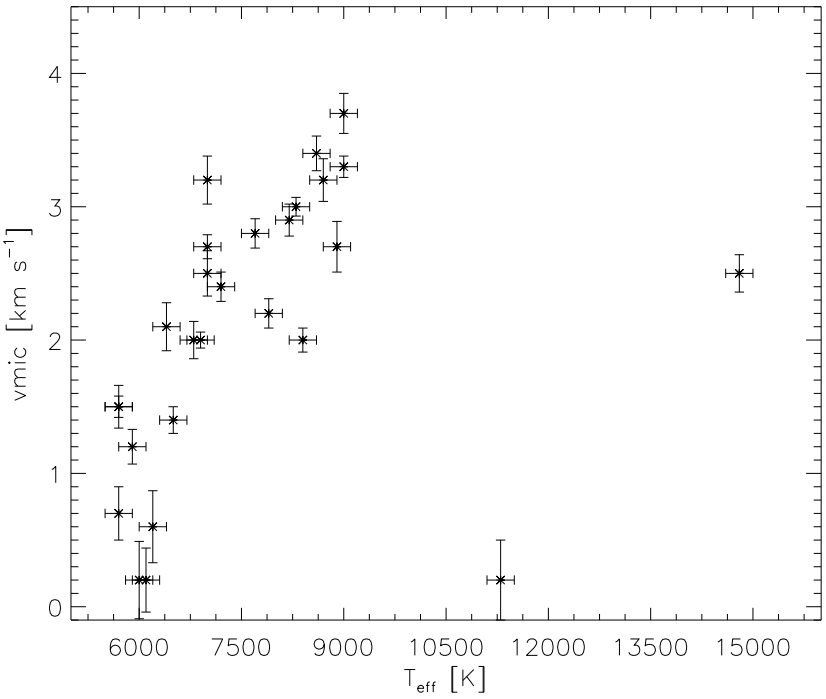

Figure A.4: v_{mic} vs T_{eff}.

and they usually have v_{mic} values larger than 3 km s^{-1} (Landstreet et al., 2009).

Among the entire sample of analyzed stars, the slow rotators HD170094 and TYC445-1491-1 show characteristics related to Am phenomenon. The abundance patterns are showed in Fig. A.5.

The Am nature of HD170094 was first reported by Levato & Abt (1977) but it was not confirmed by Renson & Manfroid (2009). The star presents underabundance of Ca, Sc and overabundance of Ni and Y.

TYC445-1491-1 is not a known Am star and it shows underabundance of C, Ca, Sc and overabundance of Ni.

A.4.2 The blue straggler HD170054

Blue stragglers are stars bluer and brighter respect to the main sequence turn-off of clusters (Fossati et al., 2010).

HD170054 was classified as blue straggler member of NGC6633 by Levato & Abt (1977). The status of member is confirmed by our membership analysis and by Landstreet et al. (2008). Abt (1985) classified the star as a peculiar star B6 IVp(Si) while Landstreet et al. (2008) considered it as a not peculiar star.

Table A.5: Abundance of elements for analysed non member stars, given in log(N/H). In parenthesis the lower and upper limit of the error. The last row gives the solar abundances from Asplund et al. (2009).

Star	$T_{\rm eff}$ [K]	vsini [km s^{-1}]	C	O	Na	Mg	Si	S
UCAC33973380	7200	127.6 ± 1.0				7.12 (05;14)		
TYC445-1686-1	7000	190.1 ± 0.7	8.37 (11;14)			7.21 (06;17)	6.73 (09;11)	7.43 (11;13)
ClNGC6633VKP98	7000	50.0 ± 0.6	8.50 (15;16)		5.94 (13;14)	7.36 (09;16)	6.93 (11;12)	7.56 (15;15)
UCAC34148501	6400	41.1 ± 0.3	8.66 (11;13)		6.08 (08;09)	7.35 (05;14)	6.98 (05;07)	7.56 (11;15)
UCAC34148324	6200	15.8 ± 0.2	8.85 (09;20)		6.34 (07;08)	7.39 (03;12)	7.05 (05;05)	
ClNGC6633VKP126	6100	15.0 ± 0.1	8.70 (09;17)		6.14 (06;07)	7.37 (03;13)	6.97 (04;04)	7.74 (08;39)
UCAC34148769	6000	19.0 ± 0.1	8.84 (07;28)		6.03 (04;06)	7.22 (02;11)	6.92 (02;04)	
UCAC34148416	5700	4.3 ± 0.3			6.75 (05;10)	7.76 (01;13)	7.41 (03;04)	
Solar	**5777**	**1.2**	**8.43**	**8.69**	**6.24**	**7.60**	**7.51**	**7.12**

Star	$T_{\rm eff}$ [K]	vsini [km s^{-1}]	Ca	Sc	Ti	V	Cr	Mn
UCAC33973380	7200	127.6 ± 1.0	5.97 (06;08)	2.69 (09;11)	4.85 (04;08)		5.47 (06;08)	5.40 (10;13)
TYC445-1686-1	7000	190.1 ± 0.7	5.97 (05;07)	2.61 (08;10)	4.42 (04;11)		5.33 (04;14)	5.08 (10;16)
ClNGC6633VKP98	7000	50.0 ± 0.6	6.15 (11;12)	3.12 (08;10)	4.83 (06;08)	4.29 (14;16)	5.62 (06;10)	5.15 (12;14)
UCAC34148501	6400	41.1 ± 0.3	6.14 (07;09)	3.03 (05;08)	4.66 (04;07)	3.74 (15;20)	5.46 (04;08)	5.08 (08;10)
UCAC34148324	6200	15.8 ± 0.2	6.31 (08;09)	3.09 (06;07)	4.98 (03;05)	4.18 (06;09)	5.75 (03;07)	5.31 (09;10)
ClNGC6633VKP126	6100	15.0 ± 0.1	6.18 (07;08)	2.93 (05;07)	4.87 (03;05)	3.95 (06;08)	5.66 (03;07)	5.30 (07;07)
UCAC34148769	6000	19.0 ± 0.1	6.06 (05;07)	2.92 (05;10)	4.79 (02;08)	3.86 (05;09)	5.54 (02;06)	5.14 (07;11)
UCAC34148416	5700	4.3 ± 0.3	6.67 (07;14)	3.28 (05;06)	5.08 (02;09)	4.21 (04;14)	5.89 (02;09)	5.64 (07;11)
Solar	**5777**	**1.2**	**6.34**	**3.15**	**4.95**	**3.93**	**5.64**	**5.43**

Star	$T_{\rm eff}$ [K]	vsini [km s^{-1}]	Fe	Ni	Zn	Y	Ba	Nd
UCAC33973380	7200	127.6 ± 1.0	7.14 (04;06)	5.86 (08;10)	5.06 (27;28)	2.30 (10;11)	2.29 (33;34)	
TYC445-1686-1	7000	190.1 ± 0.7	6.95 (05;12)	5.94 (05;11)	4.94 (21;33)		1.86 (25;43)	1.88 (09;19)
ClNGC6633VKP98	7000	50.0 ± 0.6	7.35 (07;09)	6.03 (08;11)		2.32 (10;12)	2.48 (34;36)	
UCAC34148501	6400	41.1 ± 0.3	7.20 (04;08)	5.85 (04;08)	4.05 (19;21)	1.94 (08;10)	2.22 (16;17)	
UCAC34148324	6200	15.8 ± 0.2	7.51 (03;07)	6.13 (04;05)	4.45 (35;35)	2.29 (11;12)	2.18 (14;14)	1.59 (08;13)
ClNGC6633VKP126	6100	15.0 ± 0.1	7.43 (02;07)	6.06 (03;04)	4.20 (28;28)	2.13 (09;11)	2.18 (10;22)	1.36 (08;15)
UCAC34148769	6000	19.0 ± 0.1	7.25 (01;05)	5.92 (03;05)	4.45 (26;31)	2.18 (09;15)	2.40 (06;08)	1.68 (06;21)
UCAC34148416	5700	4.3 ± 0.3	7.59 (01;08)	6.36 (03;07)	4.68 (37;37)	1.69 (13;14)	2.06 (19;20)	1.48 (09;09)
Solar	**5777**	**1.2**	**7.50**	**6.22**	**4.56**	**2.21**	**2.18**	**1.42**

Blue straggler phenomenon is not completely understood. Several scenarios tried to explain the presence of these stars, such as mass transfer in close binary (McCrea, 1964) or direct collisions between main sequence stars Hills & Day (1976). Lu et al. (2011) showed that the position of HD170054 in the color magnitude diagram can be described by a binary mass transfer model.

Chemical abundances analysis of HD170054 was presented by Andrievsky et al. (2000) who reported Mg over abundance of 0.3 dex, Si underabundance of -0.45 dex, Cr underabundance of -0.20 dex and solar values for S and Fe (respect to solar abundances of Grevesse et al. (1996)). An almost solar abundance of Fe was confirmed by Landstreet et al. (2008), that found also a lower Si underabundance of 0.2 dex. Other measures were performed by Bailey & Landstreet (2013) who reported $\log(\mathrm{Fe/H}) = -4.95$, $\log(\mathrm{Cr/H}) = -6.67$, $\log(\mathrm{SiII/H}) = -4.72$ and $\log(\mathrm{SiIII/H}) = -4.21$.

Table A.6: Abundance of elements for analysed member stars of NGC6633, given in log(N/H). In parenthesis the lower and upper limit of the error. The last row gives the solar abundances from Asplund et al. (2009).

Star	$T_{\rm eff}$ [K]	vsini [km s^{-1}]	C	O	Na	Mg	Si	S
HD170054	14800	20.9 ± 0.2					7.18 (02;02)	6.61 (02;07)
HD169959	11300	84.6 ± 0.2				8.11 (04;31)	8.31 (03;40)	
HD169958	9000	35.2 ± 0.1				7.71 (02;12)	7.52 (07;13)	
HD170135	9000	101.8 ± 0.3	8.51 (12;22)			8.12 (03;08)	7.79 (05;10)	
BD+063761	8900	117.8 ± 0.3	8.44 (14;19)			7.85 (03;05)	7.45 (27;31)	
HD170011	8700	136.5 ± 0.3				7.58 (03;10)	7.67 (23;27)	
HD169912	8600	47.3 ± 0.1				7.56 (02;11)		
HD170158	8400	221.4 ± 0.9	8.80 (08;10)			8.10 (07;16)	7.49 (10;16)	
HD170094	8300	12.3 ± 0.1					7.67 (03;07)	
BD+063771	8200	106.8 ± 0.3				7.55 (02;12)	7.71 (22;26)	
BD+063794	7900	193.9 ± 0.7	8.32 (08;11)			7.59 (05;22)	7.18 (08;16)	
BD+063779	7700	96.5 ± 0.2	8.03 (04;05)		6.79 (03;12)		7.61 (03;08)	
TYC445-1491-1	7000	12.1 ± 0.1	8.15 (09;10)		6.39 (04;07)	7.56 (03;12)	6.98 (02;05)	7.25 (09;10)
UCAC34148641	6900	20.9 ± 0.1	8.53 (05;09)		6.13 (04;05)	7.55 (03;11)	6.92 (02;05)	7.37 (06;12)
TYC445-1571-1	6800	117.9 ± 0.6				7.34 (02;13)	6.98 (08;10)	7.62 (10;12)
TYC445-1974-1	6500	6.7 ± 0.1				7.04 (03;15)	6.39 (08;08)	
Solar	**5777**	**1.2**	**8.43**	**8.69**	**6.24**	**7.60**	**7.51**	**7.12**

Star	$T_{\rm eff}$ [K]	vsini [km s^{-1}]	Ca	Sc	Ti	V	Cr	Mn
HD170054	14800	20.9 ± 0.2						
HD169959	11300	84.6 ± 0.2			5.64 (02;41)		6.47 (02;46)	
HD169958	9000	35.2 ± 0.1	6.64 (05;14)	3.14 (05;11)	5.18 (01;07)	4.68 (05;07)	5.92 (01;06)	
HD170135	9000	101.8 ± 0.3	6.97 (02;16)	3.31 (05;09)	5.18 (01;06)		5.89 (01;05)	
BD+063761	8900	117.8 ± 0.3	6.45 (08;16)		4.91 (02;04)		5.67 (02;03)	
HD170011	8700	136.5 ± 0.3	6.45 (06;15)	3.22 (05;10)	4.94 (02;06)		5.63 (02;05)	
HD169912	8600	47.3 ± 0.1	6.35 (05;16)	3.06 (05;09)	4.97 (01;07)	4.54 (05;08)	5.76 (01;06)	
HD170158	8400	221.4 ± 0.9	6.53 (12;17)		4.84 (07;09)		6.12 (06;11)	6.13 (13;17)
HD170094	8300	12.3 ± 0.1	5.54 (02;13)	1.50 (02;10)	4.60 (01;07)	4.21 (02;07)	5.52 (01;07)	5.41 (02;07)
BD+063771	8200	106.8 ± 0.3	6.09 (02;13)		4.59 (02;07)		5.35 (02;07)	
BD+063794	7900	193.9 ± 0.7	6.02 (07;12)		4.64 (04;11)		5.52 (05;15)	5.23 (15;23)
BD+063779	7700	96.5 ± 0.2	6.23 (04;06)		4.38 (02;06)		5.05 (01;05)	
TYC445-1491-1	7000	12.1 ± 0.1	5.54 (04;08)	2.53 (05;08)	4.68 (02;06)	4.19 (07;10)	5.77 (01;07)	5.31 (05;10)
UCAC34148641	6900	20.9 ± 0.1	6.09 (03;07)	2.97 (03;06)	4.79 (02;07)	4.25 (05;11)	5.54 (02;08)	5.22 (04;10)
TYC445-1571-1	6800	117.9 ± 0.6	6.11 (06;08)	2.94 (11;12)	4.67 (03;06)		5.45 (03;07)	
TYC445-1974-1	6500	6.7 ± 0.1	6.01 (04;07)	3.22 (03;07)	4.89 (02;07)	3.97 (08;16)	5.43 (02;08)	4.85 (10;14)
Solar	**5777**	**1.2**	**6.34**	**3.15**	**4.95**	**3.93**	**5.64**	**5.43**

Star	$T_{\rm eff}$ [K]	vsini [km s^{-1}]	Fe	Ni	Zn	Y	Ba	Nd
HD170054	14800	20.9 ± 0.2	7.03 (01;03)					
HD169959	11300	84.6 ± 0.2	8.28 (02;48)					
HD169958	9000	35.2 ± 0.1	7.61 (00;05)	6.80 (03;10)			2.25 (05;16)	
HD170135	9000	101.8 ± 0.3	7.57 (01;05)	6.65 (04;10)			2.33 (06;09)	
BD+063761	8900	117.8 ± 0.3	7.38 (01;04)				2.19 (07;17)	
HD170011	8700	136.5 ± 0.3	7.27 (01;05)	6.58 (05;08)			2.08 (07;13)	
HD169912	8600	47.3 ± 0.1	7.52 (01;05)	6.61 (02;11)			2.31 (07;11)	
HD170158	8400	221.4 ± 0.9	7.72 (04;08)	6.73 (09;13)				
HD170094	8300	12.3 ± 0.1	7.35 (00;08)	6.37 (01;12)		2.57 (02;26)		
BD+063771	8200	106.8 ± 0.3	7.13 (01;07)	6.07 (03;13)			2.21 (09;17)	
BD+063794	7900	193.9 ± 0.7	7.30 (04;15)	6.13 (08;15)			1.67 (32;34)	
BD+063779	7700	96.5 ± 0.2	6.91 (01;06)	5.72 (02;08)			1.77 (05;09)	
TYC445-1491-1	7000	12.1 ± 0.1	7.54 (02;07)	6.41 (02;08)	4.64 (10;13)	2.21 (03;26)	2.18 (15;19)	
UCAC34148641	6900	20.9 ± 0.1	7.30 (02;08)	5.97 (02;08)	4.12 (11;14)	2.17 (03;07)	2.18 (12;12)	
TYC445-1571-1	6800	117.9 ± 0.6	7.20 (03;06)	5.96 (05;07)	4.65 (26;28)		2.37 (18;20)	1.96 (09;17)
TYC445-1974-1	6500	6.7 ± 0.1	7.18 (02;08)	5.84 (02;07)	4.13 (12;16)	2.16 (04;07)	2.29 (08;10)	1.36 (06;10)
Solar	**5777**	**1.2**	**7.50**	**6.22**	**4.56**	**2.21**	**2.18**	**1.42**

Table A.7: Abundance of elements for analysed member stars of NGC6633, given in log(N/H). In parenthesis the lower and upper limit of the error. The last row gives the solar abundances from Asplund et al. (2009).

Star	$T_{\rm eff}$ [K]	vsini [km s^{-1}]	C	O	Na	Mg	Si	S
UCAC34148423	5900	8.6 ± 0.1				7.08 (02;15)	6.47 (08;08)	7.60 (12;13)
UCAC34148663	5700	13.1 ± 0.2				7.00 (01;14)	6.47 (09;09)	7.61 (15;16)
UCAC34148538	5700	8.9 ± 0.2			6.26 (07;08)	7.53 (04;14)	7.14 (05;05)	
Solar	**5777**	**1.2**	**8.43**	**8.69**	**6.24**	**7.60**	**7.51**	**7.12**
Star	$T_{\rm eff}$ [K]	vsini [km s^{-1}]	Ca	Sc	Ti	V	Cr	Mn
UCAC34148423	5900	8.6 ± 0.1	6.03 (05;07)	2.95 (06;08)	4.53 (02;07)		5.30 (02;09)	4.60 (12;16)
UCAC34148663	5700	13.1 ± 0.2	5.97 (05;08)	2.87 (07;10)	4.50 (03;08)		5.25 (02;11)	4.57 (13;15)
UCAC34148538	5700	8.9 ± 0.2	6.55 (08;11)	3.18 (06;08)	4.74 (03;07)	3.58 (07;14)	5.55 (03;08)	5.06 (09;11)
Solar	**5777**	**1.2**	**6.34**	**3.15**	**4.95**	**3.93**	**5.64**	**5.43**
Star	$T_{\rm eff}$ [K]	vsini [km s^{-1}]	Fe	Ni	Zn	Y	Ba	Nd
UCAC34148423	5900	8.6 ± 0.1	7.07 (02;09)	5.72 (03;07)	4.04 (19;20)	2.03 (06;08)	2.28 (08;10)	
UCAC34148663	5700	13.1 ± 0.2	7.02 (01;09)	5.69 (03;06)	4.08 (24;24)	1.90 (09;10)	2.24 (07;09)	
UCAC34148538	5700	8.9 ± 0.2	7.28 (03;07)	5.96 (04;06)	4.15 (35;36)	2.03 (11;13)	2.20 (14;15)	1.55 (08;13)
Solar	**5777**	**1.2**	**7.50**	**6.22**	**4.56**	**2.21**	**2.18**	**1.42**

Our analysis showed underabundance of Si, Cr and Fe for HD170054. The abundances of Fe and Cr agree with the values reported by Bailey & Landstreet (2013). The abundance of Si agrees with the value of Andrievsky et al. (2000).

A.4.3 Stellar metallicity

The metallicity was calculated following:

$$Z = 10^{[Fe/H]} Z_{\odot} \tag{A.1}$$

with $[Fe/H]_{\odot} = 7.50 \pm 0.04$ and $Z_{\odot} = 0.0134$ (Asplund et al., 2009).

In order to find differences between members and not members, we computed the metallicity for the two samples of stars. The iron abundance [Fe/H] was calculated as the weighted mean using the inverse square of the errors for each star. We obtained:

$$[Fe/H]_{\rm cluster} = -0.310 \pm 0.161$$
$$[Fe/H]_{\rm non-memb} = -0.073 \pm 0.176$$

that corresponds to a metallicity:

$$Z_{\rm cluster} = 0.00642 \pm 0.00238$$
$$Z_{\rm non-memb} = 0.01131 \pm 0.00458$$

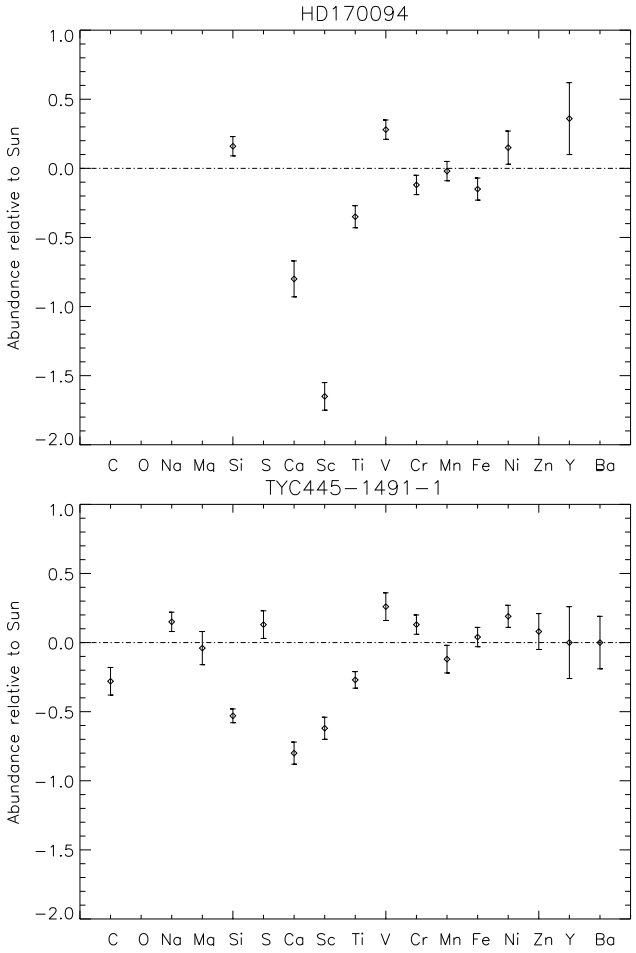

Figure A.5: Abundance patterns of the metallic stars studied in this work.

For the computation we excluded peculiar metallic stars and we used only stars until the F-type ($T_{eff} \leq 7600$ K) that are more mixed respect to hotter stars. This is because they are at the limit of temperature where the surface convection is active and they present a thin convective envelope (Nelson, 1980).

Our analysis shows that members present an abundance lower than 30% respect to not members, that are almost solar with a lower scatter.

A.4.4 HR diagrams

We computed the classical and spectroscopic HR diagram (Langer & Kudritzki, 2014) of the members of NGC6633 (Fig. A.6). Bolometric corrections are performed following Reed (1998).

Spectroscopic HR diagram has the advantage to compare the data with the evolution-

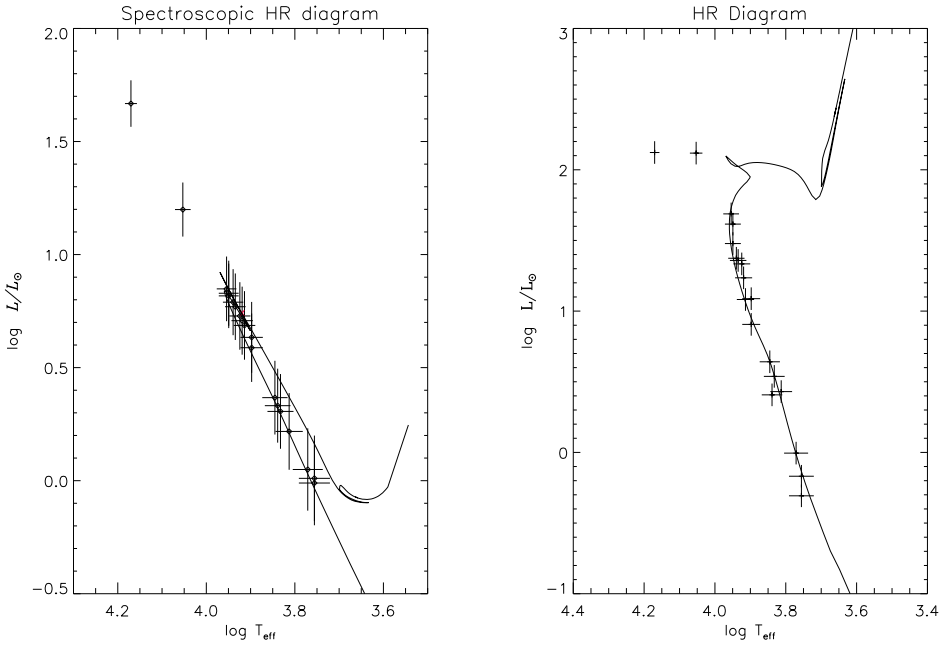

Figure A.6: Left: spectroscopic HR diagram. Right: HR diagram. The evolutionary track (Bressan et al., 2012) is computed with the age log t = 8.75 (Williams & Bolte, 2007).

ary tracks independently on the distance and on the bolometric corrections and it is also useful check for the determined values of log g. The quantity $L/L_\odot$ is given by:

$$L/L_\odot = \log\left(\frac{T_{eff}^4}{g}\right) - \log\left(\frac{T_{eff\odot}^4}{g_\odot}\right) \tag{A.2}$$

Following Landstreet et al. (2007), we fitted the evolutionary tracks (Bressan et al., 2012) (using the age log t = 8.75 reported by Williams & Bolte (2007)) and we obtained the flux-weighted luminosity, the mass and the fractional age for each stars (Table A.8).

Table A.8: $\log(\mathscr{L}/\mathscr{L}_{\odot})$, $\log(T_{eff})$, $M/M_{\odot}$ and fractional age τ for members star of NGC6633.

Star	$\log(\mathscr{L}/\mathscr{L}_{\odot})$	$\log(T_{eff})$	$M/M_{\odot}$	τ
HD170158	1.38 ± 0.15	3.92 ± 0.02	2.25 ± 0.40	0.03 ± 0.01
HD170054	1.97 ± 0.10	4.17 ± 0.01	4.00 ± 0.20	0.15 ± 0.02
BD+063794	1.38 ± 0.13	3.90 ± 0.03	2.20 ± 0.35	0.02 ± 0.01
BD+063779	0.93 ± 0.15	3.89 ± 0.03	1.65 ± 0.30	0.01 ± 0.01
UCAC34148641	0.54 ± 0.14	3.84 ± 0.03	1.30 ± 0.55	-0.00 ± 0.01
TYC445-1571-1	0.51 ± 0.17	3.83 ± 0.03	1.30 ± 0.20	-0.00 ± 0.01
UCAC34148423	0.17 ± 0.18	3.77 ± 0.03	0.90 ± 0.10	-0.02 ± 0.01
UCAC34148663	0.11 ± 0.19	3.76 ± 0.04	0.85 ± 0.05	-0.01 ± 0.01
UCAC34148538	0.31 ± 0.19	3.76 ± 0.04	0.95 ± 0.05	-0.00 ± 0.02
BD+063761	1.58 ± 0.12	3.95 ± 0.02	2.40 ± 1.40	0.03 ± 0.10
BD+063771	1.34 ± 0.15	3.91 ± 0.02	2.15 ± 0.30	0.02 ± 0.01
HD169912	1.42 ± 0.15	3.93 ± 0.02	2.30 ± 0.45	0.03 ± 0.02
TYC445-1974-1	0.34 ± 0.17	3.81 ± 0.03	1.15 ± 0.25	-0.00 ± 0.02
HD170135	1.60 ± 0.12	3.95 ± 0.02	2.60 ± 1.20	0.04 ± 0.08
HD169959	1.50 ± 0.06	4.05 ± 0.01	2.60 ± 0.40	0.04 ± 0.02
HD169958	1.50 ± 0.12	3.95 ± 0.02	2.15 ± 1.65	0.02 ± 0.11
HD170011	1.44 ± 0.12	3.94 ± 0.02	2.10 ± 0.25	0.02 ± 0.01
HD170094	1.36 ± 0.12	3.92 ± 0.02	2.20 ± 0.35	0.02 ± 0.01
TYC445-1491-1	0.67 ± 0.16	3.85 ± 0.03	1.40 ± 0.05	0.00 ± 0.01

BIBLIOGRAPHY

Abt H. A., 1985, ApJ, 294, L103

Alecian G., Stift M. J., 2004, A&A, 416, 703

Althaus L. G., Córsico A. H., Isern J., García-Berro E., 2010, A&ARv, 18, 471

Alvarado-Gómez J. D., Hussain G. A. J., Cohen O., Drake J. J., Garraffo C., Grunhut J., Gombosi T. I., 2016, A&A, 594, A95

Anderson R. I., Reiners A., Solanki S. K., 2010, A&A, 522, A81

Andrievsky S. M., Schönberner D., Drilling J. S., 2000, A&A, 356, 517

Angel J. R. P., Borra E. F., Landstreet J. D., 1981, ApJS, 45, 457

Anglada-Escudé G., Butler R. P., 2012, ApJS, 200, 15

Asplund M., Grevesse N., Sauval A. J., Scott P., 2009, ARA&A, 47, 481

Auer L. H., Heasley J. N., House L. L., 1977, ApJ, 216, 531

Aurière M., et al., 2008, A&A, 491, 499

Aurière M., et al., 2011, A&A, 534, A139

Aurière M., Konstantinova-Antova R., Petit P., Charbonnel C., Van Eck S., Donati J.-F., Lignières F., Roudier T., 2012, A&A, 543, A118

Aurière M., Konstantinova-Antova R., Espagnet O., Petit P., Roudier T., Charbonnel C., Donati J.-F., Wade G. A., 2014, in Petit P., Jardine M., Spruit H. C., eds, IAU Symposium Vol. 302, Magnetic Fields throughout Stellar Evolution. pp 359–362 (arXiv:1310.6907), doi:10.1017/S1743921314002476

Aurière M., et al., 2015, A&A, 574, A90

Avila G., Buzzoni B., Casse M., 1998, in D'Odorico S., ed., Proc. SPIEVol. 3355, Optical Astronomical Instrumentation. pp 900–904, doi:10.1117/12.316747

Babcock H. W., 1947, ApJ, 105, 105

Babcock H. W., 1949, PASP, 61, 226

Babcock H. W., 1958, ApJS, 3, 141

Babcock H. D., 1959, ApJ, 130, 364

Babcock H. W., 1960, ApJ, 132, 521

Babcock H. W., Babcock H. D., 1955, ApJ, 121, 349

Babcock H. W., Babcock H. D., 1958, in Lehnert B., ed., IAU Symposium Vol. 6, Electromagnetic Phenomena in Cosmical Physics. p. 239

Backman D., et al., 2009, ApJ, 690, 1522

Bagnulo S., Landi Degl'Innocenti E., Landolfi M., Leroy J. L., 1995, A&A, 295, 459

Bagnulo S., Landolfi M., Mathys G., Landi Degl'Innocenti M., 2000, A&A, 358, 929

Bagnulo S., Wade G. A., Donati J.-F., Landstreet J. D., Leone F., Monin D. N., Stift M. J., 2001, A&A, 369, 889

Bagnulo S., Szeifert T., Wade G. A., Landstreet J. D., Mathys G., 2002, A&A, 389, 191

Bagnulo S., Landstreet J. D., Mason E., Andretta V., Silaj J., Wade G. A., 2006, A&A, 450, 777

Bagnulo S., Landstreet J. D., Fossati L., Kochukhov O., 2012, A&A, 538, A129

Bailey J. D., Landstreet J. D., 2013, A&A, 551, A30

Baines E. K., McAlister H. A., ten Brummelaar T. A., Turner N. H., Sturmann J., Sturmann L., Goldfinger P. J., Ridgway S. T., 2008, ApJ, 680, 728

Baliunas S. L., et al., 1995, ApJ, 438, 269

Baschek B., Holweger H., Traving G., 1966, Astronomische Abhandlungen der Hamburger Sternwarte, 8, 26

Bass M., DeCusatis C., Enoch J., Lakshminarayanan V., Li G., Macdonald C., Mahajan V., Van Stryland E., 2010, Handbook of Optics, Third Edition Volume I: Geometrical and Physical Optics, Polarized Light, Components and Instruments(Set), 3 edn. McGraw-Hill, Inc., New York, NY, USA

Belopolsky A., 1913, Astronomische Nachrichten, 196, 1

Benedict G. F., et al., 2006, AJ, 132, 2206

Berdyugina S. V., 2009, in Strassmeier K. G., Kosovichev A. G., Beckman J. E., eds, IAU Symposium Vol. 259, Cosmic Magnetic Fields: From Planets, to Stars and Galaxies. pp 323–332, doi:10.1017/S1743921309030683

Bevington P., Robinson D., 2003, Data reduction and error analysis for the physical sciences. McGraw-Hill Higher Education, McGraw-Hill, `https://books.google.es/books?id=0poQAQAAIAAJ`

Bidelman W. P., 1967, in Cameron R. C., ed., Magnetic and Related Stars. p. 29

Bigelow F. H., 1891, PASP, 3, 34

Blackman E. G., Frank A., Markiel J. A., Thomas J. H., Van Horn H. M., 2001, Nature, 409, 485

Blakely R. J., 1995, Potential theory in gravity and magnetic applications.

Bonsack W. K., Pilachowski C. A., 1974, ApJ, 190, 327

Borde P., Coudé du Foresto V., Chagnon G., Perrin G., 2002, VizieR Online Data Catalog, 339

Borisova A., Aurière M., Petit P., Konstantinova-Antova R., Charbonnel C., Drake N. A., 2016, A&A, 591, A57

Borra E. F., Landstreet J. D., 1980, ApJS, 42, 421

Borra E. F., Vaughan A. H., 1976, ApJ, 210, L145

Bourges L., Mella G., Lafrasse S., Duvert G., Chelli A., Le Bouquin J.-B., Delfosse X., Chesneau O., 2017, VizieR Online Data Catalog, 2346

Bouvier J., et al., 2007, A&A, 463, 1017

Brandenburg A., 2001, ApJ, 550, 824

Brandenburg A., Subramanian K., 2005, Phys. Rep., 417, 1

Bressan A., Marigo P., Girardi L., Salasnich B., Dal Cero C., Rubele S., Nanni A., 2012, MNRAS, 427, 127

Bruntt H., et al., 2010, A&A, 512, A55

Butler R. P., et al., 2006, ApJ, 646, 505

Bychkov V. D., Bychkova L. V., Madej J., 2016, MNRAS, 455, 2567

Calamai G., Landi Degl'Innocenti E., Landi Degl'Innocenti M., 1975, A&A, 45, 297

Carolo E., et al., 2014, A&A, 567, A48

Carrington R. C., 1859, MNRAS, 19, 81

Charbonneau P., 1995, ApJS, 101, 309

Charbonneau P., 2010, Living Reviews in Solar Physics, 7, 3

Charbonneau P., 2013, Solar and Stellar Dynamos, Saas-Fee Advanced Courses, Volume 39.~ISBN 978-3-642-32092-7.~Springer-Verlag Berlin Heidelberg, 2013, p.~87, 39, 87

Charbonneau P., Michaud G., 1991, ApJ, 370, 693

Chen W., Johns-Krull C. M., 2013, ApJ, 776, 113

Chmielewski Y., 1979, Publications of the Observatoire Geneve Series B, 7, 1

Clarke D., 1965a, MNRAS, 129, 71

Clarke D., 1965b, MNRAS, 130, 75

Clarke D., 2009, Stellar Polarimetry. Wiley, https://books.google.it/books?id=lioLCB1QktQC

Clarke D., Grainger J. F., 1971, Polarized light and optical measurement [by] D. Clarke [and] J. F. Grainger, [1st ed.] edn. Pergamon Press Oxford, New York

Conti P. S., 1970, PASP, 82, 781

Covino S., et al., 2014, Astronomische Nachrichten, 335, 117

Cowling T. G., 1933, MNRAS, 94, 39

Currie T., et al., 2010, ApJS, 186, 191

Cutri R. M., et al., 2003, VizieR Online Data Catalog, 2246

D'Antona F., Ventura P., Mazzitelli I., 2000, ApJ, 543, L77

Davis J., Tango W. J., Booth A. J., 2000, MNRAS, 318, 387

De Medeiros J. R., Udry S., Burki G., Mayor M., 2002, A&A, 395, 97

Deeming T. J., 1975, Ap&SS, 36, 137

Degl'Innocenti M., Landolfi M., 2006, Polarization in Spectral Lines. Astrophysics and Space Science Library, Springer Netherlands, https://books.google.it/books?id=g8O-qhbjF88C

Dekker H., D'Odorico S., Kaufer A., Delabre B., Kotzlowski H., 2000, in Iye M., Moorwood A. F., eds, Proc. SPIEVol. 4008, Optical and IR Telescope Instrumentation and Detectors. pp 534–545, doi:10.1117/12.395512

Desidera S., et al., 2004, A&A, 420, L27

Deutsch A. J., 1970, ApJ, 159, 985

Dias W. S., Monteiro H., Caetano T. C., Lepine J. R. D., Assafin M., Oliveira A. F., 2014, VizieR Online Data Catalog, 356

Donati J.-F., Semel M., Carter B. D., Rees D. E., Collier Cameron A., 1997, MNRAS, 291, 658

Donati J.-F., Catala C., Wade G. A., Gallou G., Delaigue G., Rabou P., 1999, A&AS, 134, 149

Donati J.-F., Catala C., Landstreet J. D., Petit P., 2006, in Casini R., Lites B. W., eds, Astronomical Society of the Pacific Conference Series Vol. 358, Astronomical Society of the Pacific Conference Series. p. 362

Donati J.-F., et al., 2008, MNRAS, 386, 1234

Ducati J. R., 2002, VizieR Online Data Catalog, 2237

Durney B. R., Latour J., 1978, Geophysical and Astrophysical Fluid Dynamics, 9, 241

ESA 1997, VizieR Online Data Catalog, 1239

Fan Y., 2009, in Dikpati M., Arentoft T., González Hernández I., Lindsey C., Hill F., eds, Astronomical Society of the Pacific Conference Series Vol. 416, Solar-Stellar Dynamos as Revealed by Helio- and Asteroseismology: GONG 2008/SOHO 21. p. 489 (arXiv:0901.1822)

Feautrier P., 1964, Comptes Rendus Academie des Sciences (serie non specifiee), 258

Feigelson E. D., Montmerle T., 1999, ARA&A, 37, 363

Ferrario L., de Martino D., Gänsicke B. T., 2015, Space Sci. Rev., 191, 111

Folsom C. P., et al., 2016, MNRAS, 457, 580

Fossati L., 2014, in Mathys G., Griffin E. R., Kochukhov O., Monier R., Wahlgren G. M., eds, Putting A Stars into Context: Evolution, Environment, and Related Stars. pp 2–9 (arXiv:1311.5906)

Fossati L., Bagnulo S., Monier R., Khan S. A., Kochukhov O., Landstreet J., Wade G., Weiss W., 2007, A&A, 476, 911

Fossati L., Bagnulo S., Landstreet J., Wade G., Kochukhov O., Monier R., Weiss W., Gebran M., 2008, A&A, 483, 891

Fossati L., Ryabchikova T., Bagnulo S., Alecian E., Grunhut J., Kochukhov O., Wade G., 2009, A&A, 503, 945

Fossati L., Mochnacki S., Landstreet J., Weiss W., 2010, A&A, 510, A8

Fossati L., Folsom C. P., Bagnulo S., Grunhut J. H., Kochukhov O., Landstreet J. D., Paladini C., Wade G. A., 2011, MNRAS, 413, 1132

Foster L. V., 1938, Journal of the Optical Society of America (1917-1983), 28, 124

Foukal P. V., 2004, Solar Astrophysics, 2nd, Revised Edition

Fox G. K., 1992, MNRAS, 258, 533

Frink S., Mitchell D. S., Quirrenbach A., Fischer D. A., Marcy G. W., Butler R. P., 2002, ApJ, 576, 478

Fröhlich H.-E., 2007, Astronomische Nachrichten, 328, 1037

Fuller J., Cantiello M., Stello D., Garcia R. A., Bildsten L., 2015, Science, 350, 423

Gaia Collaboration 2016, VizieR Online Data Catalog, 1337

García-Berro E., et al., 2012, ApJ, 749, 25

Gebran M., Monier R., Richard O., 2008, A&A, 479, 189

Gebran M., Vick M., Monier R., Fossati L., 2010, A&A, 523, A71

Goodrich R. W., Cohen M. H., Putney A., 1995, PASP, 107, 179

Gray D. F., 2005, The Observation and Analysis of Stellar Photospheres

Greaves J. S., et al., 2005, ApJ, 619, L187

Gregory S. G., Jardine M., Gray C. G., Donati J.-F., 2010, Reports on Progress in Physics, 73, 126901

Grevesse N., Noels A., Sauval A. J., 1996, in Holt S. S., Sonneborn G., eds, Astronomical Society of the Pacific Conference Series Vol. 99, Cosmic Abundances. p. 117

Guenther E. W., Emerson J. P., 1997, A&A, 321, 803

Haisch B., Schmitt J. H. M. M., Rosso C., 1991, ApJ, 383, L15

Hale G. E., 1908, ApJ, 28, 315

Hale G. E., Ellerman F., 1903, Publications of the Yerkes Observatory, 3, I.1

Hale G. E., Nicholson S. B., 1925, ApJ, 62, 270

Harvey J. W., 1973, Sol. Phys., 28, 9

Hatzes A. P., Cochran W. D., 1993, ApJ, 413, 339

Hatzes A. P., et al., 2000, ApJ, 544, L145

Hatzes A. P., et al., 2006, A&A, 457, 335

Heger A., Woosley S. E., Spruit H. C., 2005, ApJ, 626, 350

Henden A. A., Templeton M., Terrell D., Smith T. C., Levine S., Welch D., 2016, VizieR Online Data Catalog, 2336

Herbig G. H., 1960, ApJS, 4, 337

Hills J. G., Day C. A., 1976, Astrophys. Lett., 17, 87

Hiltner W. A., Iriarte B., Johnson H. L., 1958, ApJ, 127, 539

Hoffleit D., Warren Jr. W. H., 1995, VizieR Online Data Catalog, 5050

Høg E., et al., 2000, A&A, 355, L27

Hough J. H., Lucas P. W., Bailey J. A., Tamura M., Hirst E., Harrison D., Bartholomew-Biggs M., 2006, PASP, 118, 1302

Hrudková M., et al., 2017, MNRAS, 464, 1018

Hsu J.-C., Breger M., 1982, ApJ, 262, 732

Hubeny I., Lanz T., 1995, ApJ, 439, 875

Hubeny I., Hummer D. G., Lanz T., 1994, A&A, 282, 151

Huber D., et al., 2013, Science, 342, 331

Hubrig S., Plachinda S. I., Hunsch M., Schroder K.-P., 1994, A&A, 291, 890

Hussain G. A. J., Alecian E., 2014, in Petit P., Jardine M., Spruit H. C., eds, IAU Symposium Vol. 302, Magnetic Fields throughout Stellar Evolution. pp 25–37 (arXiv:1402.7130), doi:10.1017/S1743921314001653

Iben Jr. I., 1965, ApJ, 141, 993

Isern J., Mochkovitch R., García-Berro E., Hernanz M., 1997, ApJ, 485, 308

Isern J., García-Berro E., Külebi B., Lorén-Aguilar P., 2017, ApJ, 836, L28

Janson M., Quanz S. P., Carson J. C., Thalmann C., Lafrenière D., Amara A., 2015, A&A, 574, A120

Jeffers S. V., Petit P., Marsden S. C., Morin J., Donati J.-F., Folsom C. P., 2014, A&A, 569, A79

Jeffries R. D., 1997, MNRAS, 292, 177

Jeffries R. D., Totten E. J., Harmer S., Deliyannis C. P., 2002, MNRAS, 336, 1109

Jofré E., Petrucci R., Saffe C., Saker L., de la Villarmois E. A., Chavero C., Gómez M., Mauas P. J. D., 2015, A&A, 574, A50

Johns-Krull C. M., 2007, ApJ, 664, 975

Johnstone C. P., Jardine M., Gregory S. G., Donati J.-F., Hussain G., 2014, MNRAS, 437, 3202

Kane S. R., Reffert S., Henry G. W., Fischer D., Schwab C., Clubb K. I., Bergmann C., 2010, ApJ, 720, 1644

Kane S. R., et al., 2016, ApJ, 820, L5

Keenan P. C., McNeil R. C., 1989, ApJS, 71, 245

Keller C. U., 2002, in Trujillo-Bueno J., Moreno-Insertis F., Sánchez F., eds, Astrophysical Spectropolarimetry. pp 303–354

Kemp J. C., Wolstencroft R. D., 1974, MNRAS, 166, 1

Kemp J. C., Swedlund J. B., Landstreet J. D., Angel J. R. P., 1970, ApJ, 161, L77

Kemp J. C., Henson G. D., Steiner C. T., Powell E. R., 1987, Nature, 326, 270

Kharchenko N. V., Piskunov A. E., Röser S., Schilbach E., Scholz R.-D., 2005, A&A, 438, 1163

Kılıçoğlu T., Monier R., Richer J., Fossati L., Albayrak B., 2016, AJ, 151, 49

Kochukhov O., Makaganiuk V., Piskunov N., 2010, A&A, 524, A5

Kochukhov O., et al., 2011, ApJ, 732, L19

Kolenberg K., Bagnulo S., 2009, A&A, 498, 543

Konstantinova-Antova R., Aurière M., Iliev I. K., Cabanac R., Donati J.-F., Mouillet D., Petit P., 2008, A&A, 480, 475

Konstantinova-Antova R., et al., 2010, A&A, 524, A57

Konstantinova-Antova R., Aurière M., Petit P., Charbonnel C., Tsvetkova S., Lèbre A., Bogdanovski R., 2012, A&A, 541, A44

Kopff E., 1943, Astronomische Nachrichten, 274, 69

Kron G. E., 1947, PASP, 59, 261

Kuhn J. R., Balasubramaniam K. S., Kopp G., Penn M. J., Dombard A. J., Lin H., 1994, Sol. Phys., 153, 143

Kurtz D. W., Martinez P., 2000, Baltic Astronomy, 9, 253

Kurtz D. W., Elkin V. G., Mathys G., 2007, MNRAS, 380, 741

Kurucz R. L., 1993a, SYNTHE spectrum synthesis programs and line data

Kurucz R., 1993b, Opacities for Stellar Atmospheres: [+0.0],[+0.5],[+1.0]. Kurucz CD-ROM No. 2. Cambridge, Mass.: Smithsonian Astrophysical Observatory, 1993., 2

Lambert D. L., Reddy A. B. S., 2016, ApJ, 831, 202

Landi Degl'Innocenti E., 1982, Sol. Phys., 77, 285

Landi Degl'Innocenti E., 1987, Transfer of Polarized Radiation, using 4 x 4 Matrices. p. 265

Landi Degl'Innocenti E., 1992, Magnetic field measurements. p. 71

Landi Degl'Innocenti M., Calamai G., Landi Degl'Innocenti E., Patriarchi P., 1981, ApJ, 249, 228

Landolfi M., Landi Degl'Innocenti E., Landi Degl'Innocenti M., Leroy J. L., 1993, A&A, 272, 285

Landolfi M., Bagnulo S., Landi Degl'Innocenti M., 1998, A&A, 338, 111

Landstreet J. D., 1982, ApJ, 258, 639

Landstreet J. D., 2004, in Arkhyz N., Glagolevskij Y. V., Kudryavtsev I. I., Romanyuk I. I., eds, Magnetic Stars. pp 11–18

Landstreet J. D., Mathys G., 2000, A&A, 359, 213

Landstreet J. D., Bagnulo S., Andretta V., Fossati L., Mason E., Silaj J., Wade G. A., 2007, A&A, 470, 685

Landstreet J. D., et al., 2008, A&A, 481, 465

Landstreet J. D., Kupka F., Ford H. A., Officer T., Sigut T. A. A., Silaj J., Strasser S., Townshend A., 2009, A&A, 503, 973

Langer N., Kudritzki R. P., 2014, A&A, 564, A52

Larmor J., 1919. pp 159–160

Lehmann L. T., Künstler A., Carroll T. A., Strassmeier K. G., 2015, Astronomische Nachrichten, 336, 258

Leone F., 2007, MNRAS, 382, 1690

Leone F., Bruno P., Cali A., Claudi R., Cosentino R., Gentile G., Gratton R., Scuderi S., 2003, in Fineschi S., ed., Proc. SPIEVol. 4843, Polarimetry in Astronomy. pp 465–475, doi:10.1117/12.458623

Leone F., Martínez González M. J., Corradi R. L. M., Privitera G., Manso Sainz R., 2011, ApJ, 731, L33

Leone F., et al., 2016, AJ, 151, 116

Leone F., Scalia C., Gangi M., Giarrusso M., Munari M., Scuderi S., Trigilio C., Stift M. J., 2017, ApJ, 848, 107

Leroy J. L., 1995, A&AS, 114, 79

Leroy J. L., Landolfi M., Landi Degl'Innocenti E., 1993, A&A, 270, 335

Levato H., Abt H. A., 1977, PASP, 89, 274

Levenberg K., 1944, Quarterly of Applied Mathematics, pp 164–168

Levy E. H., Rose W. K., 1974, ApJ, 193, 419

Lu P., Deng L.-C., Zhang X.-B., 2011, Research in Astronomy and Astrophysics, 11, 1336

Marquardt D., 1963, SIAM Journal on Applied Mathematics, pp 431–441

Martin A. J., Stift M. J., Fossati L., Bagnulo S., Scalia C., Leone F., Smalley B., 2017, MNRAS, 466, 613

Martínez González M. J., Asensio Ramos A., 2012, ApJ, 755, 96

Massarotti A., Latham D. W., Stefanik R. P., Fogel J., 2008, AJ, 135, 209

Mathys G., 1991, A&AS, 89, 121

Mathys G., 1993, in Dworetsky M. M., Castelli F., Faraggiana R., eds, Astronomical Society of the Pacific Conference Series Vol. 44, IAU Colloq. 138: Peculiar versus Normal Phenomena in A-type and Related Stars. p. 232

Mathys G., 1994, A&AS, 108

Mathys G., 2017, A&A, 601, A14

Mathys G., Hubrig S., 1997, A&AS, 124

Mathys G., Hubrig S., Landstreet J. D., Lanz T., Manfroid J., 1997, A&AS, 123

Maunder E. W., 1913, MNRAS, 74, 112

Maury A. C., Pickering E. C., 1897. pp 1–128

Mayor M., Queloz D., 1995, Nature, 378, 355

McCrea W. H., 1964, MNRAS, 128, 147

Mestel L., 2012, Stellar Magnetism: Second Edition. International Series of Monographs on Physics, OUP Oxford, https://books.google.it/books?id=eW7pS_KV-OwC

Metcalfe T. S., et al., 2013, ApJ, 763, L26

Micela G., Sciortino S., Serio S., Vaiana G. S., Bookbinder J., Golub L., Harnden Jr. F. R., Rosner R., 1985, ApJ, 292, 172

Michaud G., 1970, ApJ, 160, 641

Mizuki T., et al., 2016, A&A, 595, A79

Monaghan J. J., 1973, MNRAS, 163, 423

Moreno I., 2004, Appl. Opt., 43, 3373

Mortier A., Santos N. C., Sousa S. G., Adibekyan V. Z., Delgado Mena E., Tsantaki M., Israelian G., Mayor M., 2013, A&A, 557, A70

Nelson G. D., 1980, ApJ, 238, 659

Niedzielski A., Wolszczan A., 2008, in Sun Y.-S., Ferraz-Mello S., Zhou J.-L., eds, IAU Symposium Vol. 249, Exoplanets: Detection, Formation and Dynamics. pp 43–47 (arXiv:0712.2297), doi:10.1017/S1743921308016347

Nordhaus J., Wellons S., Spiegel D. S., Metzger B. D., Blackman E. G., 2011, Proceedings of the National Academy of Science, 108, 3135

Noyes R. W., Hartmann L. W., Baliunas S. L., Duncan D. K., Vaughan A. H., 1984, ApJ, 279, 763

Olander T., 2013, The magnetic field of ϵ Eri

Paletou F., 2012, A&A, 544, A4

Pallavicini R., Golub L., Rosner R., Vaiana G. S., Ayres T., Linsky J. L., 1981, ApJ, 248, 279

Parker E. N., 1955, ApJ, 122, 293

Pasquini L., et al., 2002, The Messenger, 110, 1

Petit P., Louge T., Théado S., Paletou F., Manset N., Morin J., Marsden S. C., Jeffers S. V., 2014, PASP, 126, 469

Piskunov N. E., Kupka F., Ryabchikova T. A., Weiss W. W., Jeffery C. S., 1995, A&AS, 112, 525

Piskunov N., et al., 2011, The Messenger, 143, 7

Pizzolato N., Maggio A., Micela G., Sciortino S., Ventura P., 2003, A&A, 397, 147

Press W. H., Teukolsky S. A., Vetterling W. T., Flannery B. P., 1992, Numerical Recipes in C (2Nd Ed.): The Art of Scientific Computing. Cambridge University Press, New York, NY, USA

Preston G. W., 1967, ApJ, 150, 547

Preston G. W., 1969, ApJ, 157, 247

Preston G. W., 1971, PASP, 83, 571

Preston G. W., 1974, ARA&A, 12, 257

Preston G. W., Sturch C., 1967, in Cameron R. C., ed., Magnetic and Related Stars. p. 111

Preusse S., Kopp A., Büchner J., Motschmann U., 2006, A&A, 460, 317

Priest E. R., 2001, in Mathys G., Solanki S. K., Wickramasinghe D. T., eds, Astronomical Society of the Pacific Conference Series Vol. 248, Magnetic Fields Across the Hertzsprung-Russell Diagram. p. 25

Queloz D., et al., 2001, A&A, 379, 279

Reed B. C., 1998, J. R. Astron. Soc. Canada, 92, 36

Rees D. E., Durrant C. J., Murphy G. A., 1989, ApJ, 339, 1093

Reiners A., 2012, Living Reviews in Solar Physics, 9

Renson P., Manfroid J., 2009, A&A, 498, 961

Richichi A., Percheron I., 2002, VizieR Online Data Catalog, 338

Richichi A., Percheron I., Khristoforova M., 2005, A&A, 431, 773

Roberts D. H., Lehar J., Dreher J. W., 1987, AJ, 93, 968

Robinson Jr. R. D., 1980, ApJ, 239, 961

Ryabchikova T., et al., 2016, MNRAS, 456, 1221

Sabine E., 1852, Philosophical Transactions of the Royal Society of London, 142, 103

Sanders W. L., 1973, A&AS, 9, 213

Sato B., et al., 2012, PASJ, 64, 135

Sbordone L., Bonifacio P., Castelli F., Kurucz R. L., 2004, Memorie della Societa Astronomica Italiana Supplementi, 5, 93

Scalia C., Leone F., Gangi M., Giarrusso M., Stift M. J., 2017, Monthly Notices of the Royal Astronomical Society, 472, 3554

Schmitt J. H. M. M., 2001, in Mathys G., Solanki S. K., Wickramasinghe D. T., eds, Astronomical Society of the Pacific Conference Series Vol. 248, Magnetic Fields Across the Hertzsprung-Russell Diagram. p. 199

Schwabe H., 1843, Astronomische Nachrichten, 20

Schwarzschild M., 1950, ApJ, 112, 222

Semel M., Li J., 1996, Sol. Phys., 164, 417

Semel M., Ramírez Vélez J. C., Martínez González M. J., Asensio Ramos A., Stift M. J., López Ariste A., Leone F., 2009, A&A, 504, 1003

Sennhauser C., Berdyugina S. V., 2010, A&A, 522, A57

Shenstone A. G., Blair H. A., 1929, Phil. Mag., 8, 765

Shu F., Najita J., Ostriker E., Wilkin F., Ruden S., Lizano S., 1994, ApJ, 429, 781

Simpson E. K., Baliunas S. L., Henry G. W., Watson C. A., 2010, MNRAS, 408, 1666

Sistla G., Harvey J. W., 1970, Sol. Phys., 12, 66

Skumanich A., 1972, ApJ, 171, 565

Smiljanic R., Gauderon R., North P., Barbuy B., Charbonnel C., Mowlavi N., 2009, A&A, 502, 267

Snik F., et al., 2011, in Kuhn J. R., Harrington D. M., Lin H., Berdyugina S. V., Trujillo-Bueno J., Keil S. L., Rimmele T., eds, Astronomical Society of the Pacific Conference Series Vol. 437, Solar Polarization 6. p. 237 (arXiv:1010.0397)

Socas-Navarro H., Trujillo Bueno J., Ruiz Cobo B., 2000, ApJ, 530, 977

Soker N., Zoabi E., 2002, MNRAS, 329, 204

Soubiran C., Le Campion J.-F., Brouillet N., Chemin L., 2016, A&A, 591, A118

Spoerer G., 1880, Publikationen des Astrophysikalischen Observatoriums zu Potsdam, 5

Spruit H. C., 2002, A&A, 381, 923

Steenbeck M., Krause F., 1969, Astronomische Nachrichten, 291, 271

Stibbs D. W. N., 1950, MNRAS, 110, 395

Stift M. J., 1974, MNRAS, 169, 471

Stift M. J., 1975, MNRAS, 172, 133

Stift M. J., 1985, MNRAS, 217, 55

Stift M. J., 1998a, (Astro)physical supercomputing: Ada95 as a safe, object oriented alternative. Springer Berlin Heidelberg, Berlin, Heidelberg, pp 128–139, doi:10.1007/BFb0055000, http://dx.doi.org/10.1007/BFb0055000

Stift M. J., 1998b, Contributions of the Astronomical Observatory Skalnate Pleso, 27, 390

Stift M. J., Dubois P. F., 1998, Computers in Physics, 12, 150

Stift M. J., Leone F., 2003, A&A, 398, 411

Stift M. J., Leone F., Cowley C. R., 2012, MNRAS, 419, 2912

Strugarek A., Brun A. S., Matt S. P., Réville V., 2015, ApJ, 815, 111

Takeda Y., Sato B., Murata D., 2008, PASJ, 60, 781

Tinbergen J., 2005, Astronomical Polarimetry

Tinbergen J., Rutten R., 1992

Trifonov T., Reffert S., Tan X., Lee M. H., Quirrenbach A., 2014, A&A, 568, A64

Tsvetkova S., Petit P., Aurière M., Konstantinova-Antova R., Wade G. A., Charbonnel C., Decressin T., Bogdanovski R., 2013, A&A, 556, A43

Tsvetkova S., Petit P., Konstantinova-Antova R., Aurière M., Wade G. A., Palacios A., Charbonnel C., Drake N. A., 2017, A&A, 599, A72

Uchida Y., Shibata K., 1984, PASJ, 36, 105

Unno W., 1956, PASJ, 8, 108

Vaiana G. S., et al., 1981, ApJ, 245, 163

Valenti J. A., Fischer D. A., 2005, ApJS, 159, 141

Valenti J. A., Marcy G. W., Basri G., 1995, ApJ, 439, 939

Vasilevskis S., Klemola A., Preston G., 1958, AJ, 63, 387

Vaughan A. H., Preston G. W., 1980, PASP, 92, 385

Vernazza J. E., Avrett E. H., Loeser R., 1981, ApJS, 45, 635

Villanova S., Carraro G., Saviane I., 2009, A&A, 504, 845

Vogt S. S., 1980, ApJ, 240, 567

Vogt S. S., Penrod G. D., 1983, PASP, 95, 565

Wade G. A., Donati J.-F., Landstreet J. D., Shorlin S. L. S., 2000, MNRAS, 313, 851

Wade G. A., Bagnulo S., Kochukhov O., Landstreet J. D., Piskunov N., Stift M. J., 2001, A&A, 374, 265

Wade G. A., Bagnulo S., Drouin D., Landstreet J. D., Monin D., 2007, MNRAS, 376, 1145

Wickramasinghe D. T., Ferrario L., 2005, in Koester D., Moehler S., eds, Astronomical Society of the Pacific Conference Series Vol. 334, 14th European Workshop on White Dwarfs. p. 153

Williams K. A., Bolte M., 2007, AJ, 133, 1490

Wilson O. C., 1978, ApJ, 226, 379

Wilson P., 2003, Solar and Stellar Activity Cycles. Cambridge Astrophysics, Cambridge University Press, https://books.google.it/books?id=0qOOkgqphYYC

Wolff S. C., 1983, The A-type stars: problems and perspectives.

Wolff S. C., Wolff R. J., 1970, ApJ, 160, 1049

Wu Y., Singh H. P., Prugniel P., Gupta R., Koleva M., 2011, A&A, 525, A71

Yokoyama Y., Yukutake T., 1991, Journal of Geomagnetism and Geoelectricity, 43, 563

Zacharias N., Urban S. E., Zacharias M. I., Wycoff G. L., Hall D. M., Monet D. G., Rafferty T. J., 2004, AJ, 127, 3043

Zacharias N., Finch C. T., Girard T. M., Henden A., Bartlett J. L., Monet D. G., Zacharias M. I., 2012, VizieR Online Data Catalog, 1322

Zechmeister M., Reffert S., Hatzes A. P., Endl M., Quirrenbach A., 2008, A&A, 491, 531

Zechmeister M., et al., 2013, A&A, 552, A78

Zeeman P., 1897, ApJ, 5, 332

Zoghbi J.-P. A., 2011, Publ. Astron. Soc. Australia, 28, 177

de Medeiros J. R., Mayor M., 1999, VizieR Online Data Catalog, 413